



# POLITECNICO DI MILANO

Facoltà di Ingegneria Industriale

Corso di Laurea Specialistica in Ingegneria Spaziale

## **“The space debris problem: collision risk assessment for perturbed orbits via rigorous global optimization”**

Relatore: Prof. Franco BERNELLI ZAZZERA

Correlatori: Ing. Sabrina CORPINO  
Dr. Roberto ARMELLIN  
Dr. Pierluigi DI LIZIA

Tesi di Laurea di:

Alessandro MORSELLI Matr. 733653

Anno Accademico 2009-2010



# *Ringraziamenti*

*Innanzitutto non posso non ringraziare chi ha contribuito a questo lavoro, ovvero il prof. Bernelli, che mi ha dato la possibilità di affrontare questo interessante argomento, insieme a Roberto Armellin e Pierluigi Di Lizia, i quali in questi mesi mi hanno sempre fornito utili consigli e supporto.*

*Un altro ringraziamento va a tutta la mia famiglia (nel senso più ampio del termine), che mi ha dato la possibilità di scegliere il corso di studi che volevo, nonostante fosse lontano da casa, e che in questi cinque anni mi ha sempre sostenuto.*

*Voglio anche ringraziare tutti gli amici della “Bassa” per tutte le uscite nei fine settimana, le partite di calcetto e gli allenamenti di atletica (che purtroppo non sono riuscito più a svolgere con continuità...).*

*Vorrei poi ringraziare tutte le persone che ho conosciuto in questi anni di università a Milano, perchè senza di loro affrontare questo corso di studi sarebbe stato due volte più difficile. Senza le battute, gli scherzi e i discorsi al limite dell’assurdo durante le pause pranzo avrei probabilmente un ricordo ben diverso di questo periodo.*



# Contents

<b>1</b>	<b>Introduction</b>	<b>5</b>
1.1	Evolution of man-made objects population around the Earth . . . . .	7
1.2	Satellite population . . . . .	9
1.3	Space debris population . . . . .	11
<b>2</b>	<b>Analytical Models</b>	<b>19</b>
2.1	Artificial satellite motion . . . . .	19
2.1.1	Orbital perturbations . . . . .	22
2.2	Model requirements . . . . .	25
2.3	Analytical models selection . . . . .	27
2.3.1	Aksnes zonal harmonics solution . . . . .	28
2.3.2	HANDE . . . . .	35
2.3.3	SGP4 . . . . .	44
2.3.4	Conclusions . . . . .	55
<b>3</b>	<b>Differential Algebra, Taylor Models and COSY</b>	<b>57</b>
3.1	The Minimal Differential Algebra . . . . .	58
3.2	The Differential Algebra $_nD_v$ . . . . .	61
3.2.1	Solution of Parametric Implicit Equations . . . . .	63
3.3	Taylor Models . . . . .	73
3.3.1	Differential Algebra and Interval Arithmetic . . . . .	73
3.3.2	Operations on Taylor Models . . . . .	75
3.4	COSY-GO . . . . .	77
<b>4</b>	<b>MOID of perturbed orbits</b>	<b>79</b>
4.1	MOID with one orbit perturbed by zonal harmonics . . . . .	81
4.2	MOID with one orbit perturbed by drag and zonal harmonics . . . . .	85
4.3	MOID with one geosynchronous orbit . . . . .	88
4.4	MOID of two perturbed orbits . . . . .	91
4.5	DA expansion of MOID . . . . .	96
<b>5</b>	<b>Debris clouds and orbital uncertainties</b>	<b>105</b>
5.1	Analogies between debris cloud and orbital uncertainties modelling . . . . .	105
5.2	Orbit propagation through Aksnes' solution . . . . .	107
5.3	Orbit propagation through HANDE . . . . .	109

---

5.4	Orbit propagation through SGP4 . . . . .	113
<b>6</b>	<b>Conclusions</b>	<b>117</b>
6.1	Future developments . . . . .	119
<b>A</b>		<b>121</b>
A.1	Greenwich sidereal time computation . . . . .	121
A.2	Moon and Sun ephemerides . . . . .	121
A.3	Global Gravity Field Model EIGEN-51C . . . . .	123
A.4	Atmospheric density model . . . . .	124
A.5	Transformations of orbital elements . . . . .	124
	A.5.1 Delaunay's variables . . . . .	125
	A.5.2 Hill's variables . . . . .	125
A.6	Smith's correction . . . . .	126
<b>B</b>		<b>127</b>
B.1	Numerical differentiation formulae . . . . .	127
B.2	Numerical integration formulae . . . . .	127
<b>C</b>		<b>129</b>
C.1	Taylor's Theorem . . . . .	129
	<b>Nomenclature</b>	<b>131</b>
	<b>Acronyms</b>	<b>135</b>
	<b>Bibliography</b>	<b>137</b>

# List of Figures

1.1	Monthly variation of in-orbit space debris . . . . .	7
1.2	Catalogued objects in orbit around the Earth . . . . .	8
1.3	Satellite divided by main function . . . . .	9
1.4	Satellite divided by orbit type . . . . .	10
1.5	Polar view of Earth’s orbiting objects . . . . .	11
1.6	Causes of known satellite breakups . . . . .	12
1.7	Proportion of catalogued satellite breakup debris remaining in orbit . . . . .	12
1.8	Sources of satellite breakup debris in orbit by object type . . . . .	13
1.9	Cumulative size distributions of the four major breakup fragment clouds since 2007 . . . . .	14
1.10	Area-to-mass ratio versus size distributions of the Fengyun-1C debris cloud . . . . .	14
1.11	Distribution of LEO catalogue objects with the semi-major axis of their orbit . . . . .	15
1.12	Distribution of super-LEO catalogued objects with the semi-major axis of their orbit . . . . .	15
1.13	Distribution of catalogued objects with the semi-major axis of their orbit . . . . .	16
1.14	Distribution of catalogued objects with the eccentricity of their orbit . . . . .	16
1.15	Distribution of catalogued objects with the inclination of their orbit . . . . .	17
2.1	Perifocal reference frame . . . . .	20
2.2	ECI reference frame . . . . .	21
2.3	Order of magnitude of the main perturbations acting on space debris orbits . . . . .	26
2.4	Molniya orbit . . . . .	31
2.5	Molniya orbit yearly variation of the argument of pericentre $\omega$ . . . . .	32
2.6	Sun-Synchronous orbit . . . . .	32
2.7	Aksnes solution: Sun-synchronous orbit RAAN yearly variation . . . . .	33
2.8	Aksnes solution: difference between analytical and numerical positions . . . . .	33
2.9	Aksnes solution: differences between numerical and analytical keplerian elements . . . . .	34
2.10	HANDE: orbital decay . . . . .	42
2.11	HANDE: numerical and analytical semi-major axis variation . . . . .	42
2.12	HANDE: numerical and analytical semi-major axis variation . . . . .	43
2.13	HANDE: Sun-synchronous orbit RAAN yearly variation . . . . .	44
2.14	SGP4: Geo-synchronous orbit . . . . .	51
2.15	SGP4: Geo-synchronous orbit mean anomaly daily variation . . . . .	52
2.16	SGP4: Geo-synchronous orbit ground-track . . . . .	52
2.17	SGP4: HOT BIRD 6 longitude drift . . . . .	53
2.18	SGP4: longitude behaviour near stable point at 70.8°E . . . . .	54
2.19	SGP4: HOT BIRD 6 yearly variation of inclination . . . . .	54

3.1	The idea behind differential algebra . . . . .	58
3.2	Position accuracy for various order of expansion . . . . .	67
3.3	Aksnes model: comparison of DA expansion and pointwise position . . . . .	68
3.4	Aksnes model: error between pointwise position and DA evaluation . . . . .	68
3.5	HANDE: comparison of DA evaluation and pointwise position of KOSMOS 2251 . . .	69
3.6	HANDE: error between KOSMOS 2251 pointwise position and DA evaluation . . .	70
3.7	SGP4: comparison of DA evaluation and punctual position of a GEO satellite . . . .	70
3.8	SGP4: error between GEO satellite pointwise position and DA evaluation . . . . .	71
3.9	Aksnes model: position accuracy for different semi-major axis . . . . .	71
3.10	Position accuracy for an eccentric orbit . . . . .	72
3.11	Aksnes model: position accuracy for different $\Delta t$ . . . . .	72
3.12	Function $f(x) = \exp(-1/x^2)$ if $x \neq 0$ ; 0 else . . . . .	73
3.13	Comparison between IA and TM . . . . .	74
4.1	Distance between two orbits . . . . .	79
4.2	MOID example: polar view of two Keplerian orbits . . . . .	80
4.3	3D contour plot of square distance search domain boundaries . . . . .	83
4.4	MOID of one orbit perturbed by zonal harmonics: first intersection . . . . .	84
4.5	MOID of one orbit perturbed by zonal harmonics: second intersection . . . . .	84
4.6	MOID of one orbit perturbed by zonal harmonics: third intersection . . . . .	84
4.7	MOID of one orbit perturbed by zonal harmonics: fourth intersection . . . . .	85
4.8	3D contour plot of square distance search domain boundaries . . . . .	86
4.9	MOID of one orbit perturbed by drag and zonal harmonics: first intersection . . . .	87
4.10	MOID of one orbit perturbed by drag and zonal harmonics: second intersection . . .	87
4.11	MOID of one orbit perturbed by drag and zonal harmonics: third intersection . . . .	87
4.12	MOID of one orbit perturbed by drag and zonal harmonics: fourth intersection . . .	88
4.13	GEO MOID: 3D representation of test case orbits . . . . .	89
4.14	GEO MOID: contour plot of square distance on search domain boundaries . . . . .	89
4.15	GEO MOID: contour plots at $\Delta t = 93.8816$ . . . . .	90
4.16	GEO MOID: contour plots at $\Delta t = 94.7894$ . . . . .	90
4.17	LEO and MEO orbits at epoch . . . . .	91
4.18	MOID between two orbits perturbed by zonal harmonics . . . . .	93
4.19	MOID between two orbits perturbed by zonal harmonics: 3D contour plot . . . . .	93
4.20	MOID between two orbits perturbed by zonal harmonics: contour plot . . . . .	94
4.21	MOID between two orbits perturbed by zonal harmonics and drag . . . . .	94
4.22	MOID between two orbits perturbed by zonal harmonics and drag: 3D contour plot	95
4.23	MOID between two orbits perturbed by zonal harmonics and drag: contour plot . .	95
4.24	Contour plot of $\nu_1$ 7-th order expansion . . . . .	98
4.25	Contour plot of $\nu_2$ 7-th order expansion . . . . .	99
4.26	Contour plot of $\Delta t$ 7-th order expansion . . . . .	99
4.27	Contour plot of $d^2$ 7-th order expansion . . . . .	101
4.28	Contour plot of $d^2$ 7-th order expansion for updated MOID . . . . .	103
5.1	Gabbard diagram of DMSP F11 satellite debris cloud 6 weeks after breakup . . . . .	106
5.2	DMSP F11, debris cloud evolution . . . . .	108
5.3	IRIDIUM 33, debris cloud evolution. . . . .	110

---

5.4	IRIDIUM 33, Node dispersion of virtual debris at time $t_0$ . . . . .	111
5.5	IRIDIUM 33, Node dispersion of virtual debris after 250 days . . . . .	111
5.6	IRIDIUM 33, Inclination dispersion fo virtual debris at time $t_0$ . . . . .	112
5.7	IRIDIUM 33, Inclination dispersion fo virtual debris after 250 days . . . . .	112
5.8	GALAXY 15, debris cloud evolution . . . . .	114
5.9	GALAXY 15, virtual debris ground track at time $t_0$ . . . . .	115
5.10	GALAXY 15, virtual debris ground track after 250 days . . . . .	115
6.1	IRIDIUM 33, area-to-mass ratio vs. diameter distribution . . . . .	120
A.1	Comparison between smoothed and non-smoothed inverse of $F(I)$ . . . . .	126



# List of Tables

1.1	Satellite score box, January 2011 . . . . .	9
1.2	Orbit classification . . . . .	10
3.1	DA map of mean anomaly . . . . .	65
3.2	DA direct map for solution of Keplerian equation . . . . .	66
3.3	DA inverse map for solution of Keplerian equation . . . . .	66
3.4	Evaluated DA inverse map . . . . .	67
3.5	Elementary properties of interval arithmetic . . . . .	74
4.1	Example of MOID computed with COSY-GO . . . . .	81
4.2	MOID zonal test case: Keplerian elements at epoch . . . . .	82
4.3	MOID of one orbit perturbed by zonal harmonics: remaining boxes . . . . .	83
4.4	MOID of one orbit perturbed by zonal harmonics: enclosure of $d^2$ . . . . .	83
4.5	MOID of one orbit perturbed by drag and zonal harmonics: remaining boxes . . . . .	86
4.6	MOID SGP4 test case: Keplerian elements at epoch . . . . .	88
4.7	MOID between two perturbed orbits: Keplerian elements at epoch . . . . .	91
4.8	MOID between two perturbed orbits, remaining boxes . . . . .	92
4.9	MOID between two perturbed orbits, remaining boxes . . . . .	92
4.10	Reference remaining boxes for MOID expansion test case . . . . .	97
4.11	Map of 3-th order MOID expansion in the variables $a$ and $I$ . . . . .	97
4.12	Values of $\nu_1$ , $\nu_2$ , and $\Delta t$ at orbit intersection obtained with MOID expansion . . . . .	100
4.13	Remaining boxes obtained with perturbed Keplerian elements at $t_0$ . . . . .	100
4.14	Map of 3-th order MOID expansion in the variables $a$ and $I$ after initial guess update	102
4.15	Values of $\nu_1$ , $\nu_2$ , and $\Delta t$ at orbit intersection obtained with updated MOID expansion	102
4.16	Keplerian elements of IRIDIUM 33 and COSMOS 2251 satellites . . . . .	103
4.17	MOID of IRIDIUM 33 and COSMOS 2251 satellites . . . . .	104
4.18	Enclosures of $\nu_1$ and $\nu_2$ obtained with MOID expansion . . . . .	104
4.19	Enclosures of $\nu_1$ and $\nu_2$ obtained with modified MOID computation . . . . .	104
5.1	DMSP F11, Keplerian elements . . . . .	107
5.2	DMSP F11, DA variables scale factors . . . . .	107
5.3	IRIDIUM 33, Keplerian elements . . . . .	109
5.4	IRIDIUM 33, DA variables scale factors . . . . .	109
5.5	GALAXY 15, Keplerian elements . . . . .	113
5.6	IRIDIUM 33, DA variables scale factors . . . . .	113

A.1	Sun's elements at epoch . . . . .	121
A.2	Moon's elements at epoch . . . . .	122
A.3	EIGEN-51C Earth's constants . . . . .	123
A.4	EIGEN-51C gravity field zonal harmonics coefficients . . . . .	123
A.5	EIGEN-51C gravity field tesseral and sectoral harmonics coefficients . . . . .	123
A.6	SGP4 tesseral and sectoral constants . . . . .	124
A.7	Density and scale height variation with altitude . . . . .	124
B.1	Points and weights of 13-points Gauss-Legendre formula . . . . .	128

---

## Sommario

Il presente lavoro di tesi è incentrato sullo studio dei detriti spaziali. L'attività umana nello spazio in prossimità del nostro pianeta ha fatto sì che nel corso del tempo una notevole quantità di materiale si sia accumulata in orbita. Satelliti non più operativi, resti di stadi superiori di lanciatori, residui di esplosioni e frammenti generati dal deterioramento dei materiali costituiscono la maggior parte degli oggetti in orbita e vengono appunto indicati con il termine di detriti spaziali. Data la loro elevata velocità orbitale, questi detriti costituiscono una minaccia per i satelliti operativi. Un impatto con oggetti di questo tipo potrebbe infatti compromettere l'esito della missione, comportando, in condizioni particolari, persino la distruzione del satellite. Negli ultimi decenni questo problema ha destato notevole interesse e si è cercato di limitare le conseguenze di questo fenomeno.

Da un lato sono state introdotte misure atte a limitare l'accumulo di materiale in orbite sensibili, come l'orbita terrestre bassa e la geostazionaria, dall'altro viene effettuata una continua sorveglianza di tutti gli oggetti osservabili, per tentare di prevedere eventuali impatti con i satelliti operativi e progettare quindi manovre per evitarli.

Lo scopo di questa tesi è di analizzare le possibilità di impatto fra oggetti in orbita. In particolare, si è utilizzato come criterio per l'identificazione di orbite a rischio il MOID, ovvero la minima distanza fra orbite. Questa quantità è stata calcolata tramite un algoritmo di ottimizzazione globale, COSY-GO. La particolarità di questo codice è quella di sfruttare i Modelli di Taylor, consentendo quindi di calcolare in modo preciso l'intervallo all'interno del quale è compresa la minima distanza. Inoltre, avendo a disposizione una formulazione analitica dell'orbita, è possibile ottenere informazioni ulteriori sul MOID, come la sua sensibilità rispetto a variazioni dei parametri iniziali. L'aspetto innovativo del presente lavoro è legato ai modelli dinamici utilizzati per la propagazione delle orbite che non vengono considerate come Kepleriane. Sono state scelte infatti opportune teorie analitiche che consentono di descrivere l'evoluzione orbitale degli oggetti sotto l'effetto delle perturbazioni, come ad esempio l'asfericità del campo gravitazionale terrestre e la resistenza atmosferica.

Il presente testo è organizzato nel seguente modo: nel primo capitolo vengono inquadrati gli aspetti principali del problema dei detriti spaziali, caratterizzando la popolazione degli oggetti in orbita. Nel secondo capitolo viene invece motivata la scelta dei modelli analitici che saranno in seguito utilizzati per il calcolo del MOID. Nel terzo capitolo sono descritte le caratteristiche fondamentali dell'algebra differenziale e dei modelli di Taylor, mentre nel quarto capitolo sono descritte le procedure adottate per il calcolo del MOID ed i risultati ottenuti. Nel quinto capitolo viene descritta un'ulteriore applicazione dell'algebra differenziale nell'ambito del problema dei detriti spaziali, ovvero come sia possibile descrivere l'evoluzione di una "nuvola" di detriti con notevoli vantaggi sui tempi di simulazione. Il lavoro si conclude col sesto capitolo nel quale vengono riportate conclusioni e possibili sviluppi futuri.

**Parole chiave:** Detriti spaziali · Modelli di Taylor · MOID · Ottimizzazione globale · Modelli analitici · Perturbazioni orbitali

---

---

## Abstract

The present work is focused on the study of space debris. Human activity in near-Earth space has led to the accumulation of a significant amount of material in orbit. Satellites no longer operational, upper stages of launch vehicles, residues of explosions, and fragments generated by materials deterioration are most of the orbiting objects nowadays. All of these are referred to as space debris. Because of their large orbital velocity, these debris represent a threat to operational satellites. An impact with such objects could compromise the payloads mission, resulting, in certain circumstances, in the breakup of the satellite. In recent decades, this problem has raised considerable interest and it was tried to limit this phenomenon.

On the one hand, the efforts were directed toward the reduction of the number of debris released in orbits such as low Earth orbit and geostationary orbit through the adoption of mitigation standards. On the other hand a continuous surveillance of all observable objects is performed in order to predict the occurrence of an impact between operative satellites and debris. This operation is necessary in order to design avoidance manoeuvres and, hence, prevent a collision.

The aim of this thesis is to assess the probability of impacts between orbiting objects. In particular, the computation of the MOID, i.e. the minimum distance between two orbits, is the criteria that is adopted to identify hazardous conjunctions. This distance is computed by means of validated global optimization algorithm COSY-GO. The peculiarity of this code is that it is based on Taylor models and thus it can compute sharp rigorous enclosures of the minimum distance. Furthermore, being based on the computation of high order Taylor expansions of the parameters of interest, additional information concerning the MOID, such as its sensibility with respect to initial conditions, are obtained. The innovative aspect of this work is that the MOID is computed for perturbed orbits instead of Keplerian orbits. Analytical theories that can describe the orbit evolution under the effect of perturbations such as non-spherical gravitational field and atmospheric drag were considered.

This thesis is organized as follows: in the first chapter the main aspects of the space debris problem are outlined and the population of orbiting objects is characterized. In the second chapter the selection of the analytical models that are subsequently used to compute the MOID is motivated. In the third chapter the main characteristics of differential algebra and Taylor models are described, whereas the procedure for MOID computation and the main results are reported in the fourth chapter. In the fifth chapter, the application of differential algebra to the modelling of a space debris cloud is described. The work ends with the sixth chapter, in which the conclusions are stated together with possible future developments.

**Keywords:** Space debris · Taylor Models · MOID · Global optimization · Analytical models · Orbital perturbations

---

# Chapter 1

## Introduction

Since the launch of the Sputnik in 1957, more than 6,000 spacecraft were launched into space. Some of them have re-entered in the atmosphere, but the large majority is still orbiting around the Earth although no more functional. In addition, the upper stages of the launchers as well as fairings can be also found in orbit. All these objects can indeed collide and consequently divide into an huge number of smaller fragments. Other fragments can be released due to material degradation, e.g. surface paintings and thermal insulation layers that are subjected to solar radiation and micro-meteoroids impacts.

All the orbiting objects that are no more functional are called *space debris*. It is clear that these objects are a threat to the operative satellites and the International Space Station, and are also hazardous for future space missions.

Anyway, the awareness of the risk of uncontrolled accumulation of man-made objects in orbit around the Earth became significant only in the late 70's. In 1978 Donald J. Kessler tackled for the first time the problem of the collision between orbiting objects [1]. He observed that, since many artificial satellites are in orbits that cross one another, there is a finite probability of collision between them. Using a statistical method developed to simulate the fragmentation within the asteroid belt, he discovered that there were the conditions necessary for the formation of a debris belt around the Earth. The occurrence of a satellite collision can indeed produce a number of fragments and some of them could be large enough to fragment another satellite, creating even more debris. The term "Kessler Syndrome" was introduced to describe this phenomenon. The cloud resulting from chain fragmentation of satellites could have dramatic effects for space exploration, even making space flight hazardous. In addition, further collision can eventually produce enough dust to create a new kind of light pollution, since solar radiation would be diffused by these particles.

The small volume occupied by artificial satellites around the Earth implies that the time-scale for the formation of the debris belt is of the order of centuries, whereas the time necessary for the cloud to disappear would be much longer. The reason is that the only natural mechanism that could remove space debris from orbit is the drag produced by the atmosphere. Because of this, only the debris at low altitude will slowly de-orbit, falling back on Earth's surface or disintegrating during re-entry.

From that year on, National Governments and Space Organisations began to keep track of all orbiting objects, including space debris and rocket bodies, while previously mainly satellites were catalogued. Facilities such as the radar and optical telescopes have been built in order to improve the accuracy of the observations and to track space debris down to small. At present, ground based

telescopes can detect debris down to 10 cm in geostationary orbit and down to a few cm in low Earth orbit.

NASA obtains information on space debris mainly from the Haystack radar in Massachusetts. Optical observation are carried out with Meter-Class Autonomous Telescope (MCAT) and Michigan Orbital DEbris Survey Telescope (MODEST). The U.S. Space Surveillance Network also collects information concerning debris and other orbiting objects through radar and optical observatories located in various part of the world. European Space Agency (ESA) operates EISCAT (European Incoherent Scatter Radar) radars, located in Tromsø (Norway) and Svalbard islands, primarily designed for ionospheric measurement, but also able to track debris down to 2 cm in low orbit. Furthermore it collaborates with Germany's TIRA (Tracking and Imaging RADar) system. A Zeiss telescope equipped with CCD camera is also used to track objects in geostationary ring. All information obtained through observation are then collected into catalogues, such as ESA's DISCOS (Database and Information System Characterising Objects in Space) and the U.S. Space Catalogue, that is maintained by the United States Department of Defense. The orbital information of the space debris are constantly maintained up-to-date. In this way avoidance manoeuvres can be designed if the impact probability between an operative satellite and a debris is high. The amount of catalogued on-orbit objects nowadays has passed by far 16,000.

In the beginning of the 90's the Inter-Agency Space Debris Coordination Committee (IADC) was created to exchange information concerning space debris and identify debris mitigation options. IADC currently comprises 11 countries (Italy, France, China, Germany, India, Japan, USA, Ukraine, Russia, United Kingdom, and Canada) and ESA.

The first space agency that issued a comprehensive set of guidelines for space debris mitigation was NASA in 1995. Two years later the Orbital Debris Mitigation Standard Practice was developed by the U.S. government [2]. ESA, Russia, Japan and other organization created their set of guidelines in the following years.

In 2002 the IADC adopted a consensus set of guidelines designed to mitigate the growth of the orbital debris. Finally, in 2007 another set of guidelines, based on the one of IADC, was developed by the Scientific and Technical Subcommittee of the United Nations' Committee on the Peaceful Uses of Outer Space (COPUOS) and endorsed by the United Nation in January 2008 [3].

Notwithstanding all these efforts, on 10 February 2009 at 16:56 GMT the first major collision between the American operative IRIDIUM 33 satellite and a Russian KOSMOS 2251 occurred.

It is indeed clear that reliable methods able to predict the possibility of impact should be developed. At present, the collisions of satellites with smaller debris are described statistically, using models such as ESA's MASTER (Meteoroid and Space Debris Terrestrial Environment Reference) and NASA's ORDEM2000 (ORbital Debris Engineering Model). Spacecraft structure and coating must be designed and sized according to the debris flux obtained with these models and materials that reduce the amount of released debris should be employed.

Anyway the events that release large amount of debris are the destructive collisions between large objects (e.g. 0.5 m diameter). Since the number of these large objects is relatively high and will continue to grow in the next years, a numerical integration of the equation of motion for all the different pairs of objects in space is both impractical and time consuming.

In the following sections the main characteristics of the space debris environment are described with the aim of motivating the hypothesis and selected solutions adopted throughout this work. In particular, the orbits with the higher number of satellites will be identified as well as the main sources of orbital debris.

## 1.1 Evolution of man-made objects population around the Earth

According to the NASA technical memorandum “History of on-orbit satellite fragmentation” [4], the objects in Earth’s orbit can be divided into the following categories:

- *Payloads/Spacecraft*, in which all operative satellites and vehicles are grouped;
- *Rocket-bodies*, that comprises launcher fairings, empty tanks, and upper stages;
- *Mission-related debris*, that includes all the intentionally released objects;
- *Fragmentation debris*, that gathers all the debris originated from destructive breakups;
- *Anomalous debris*, that incorporates everything that can not be included in one of the other categories.

The last general category was created because it was observed that satellite fragmentation could occur not only via collision, but also with release of debris from material degradation.

In Figure 1.1 the temporary evolution of the total number of objects in orbit around the Earth is reported, together with the number of objects for each category.

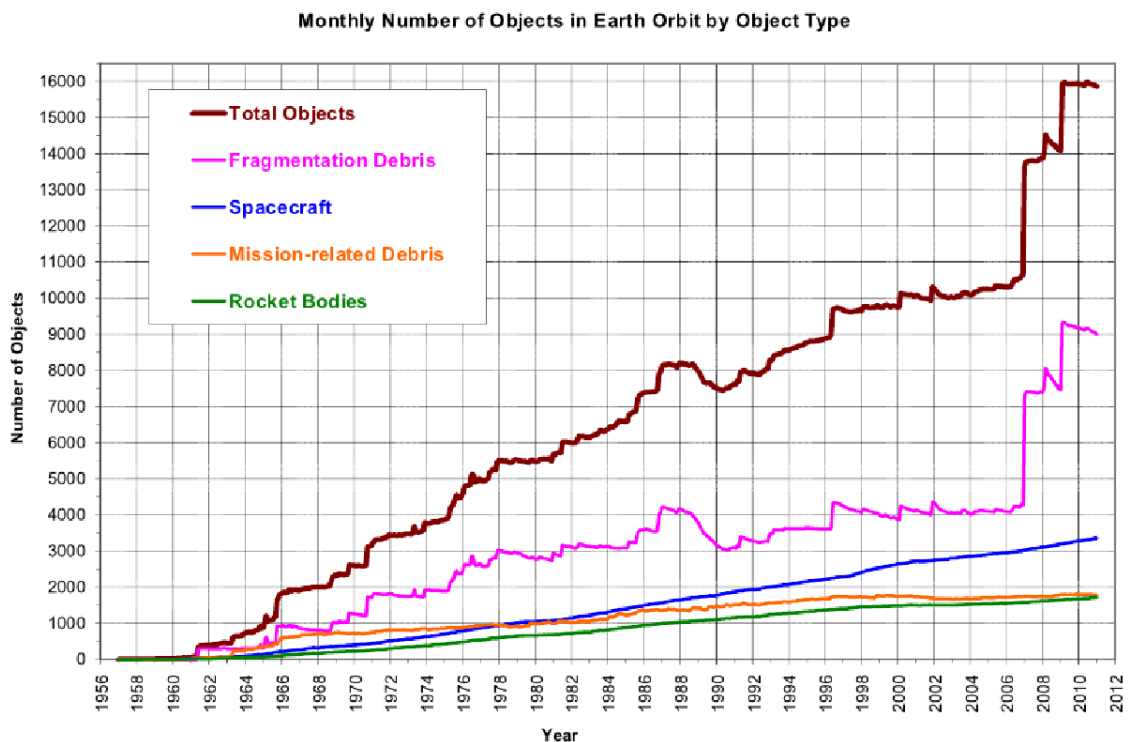


**Figure 1.1:** Monthly variation of in-orbit space debris as of January 2011 (this image is taken from [5])

Whereas the number of spacecraft and rocket bodies continues to grow steadily with a nearly constant slope, the amount of breakup debris and mission related debris is strictly related to the

occurrence of orbital collision. The reason is that a single event of that kind can originate an enormous amount of fragments. A destructive event can hence be easily identified in Figure 1.1. As an example, the deliberate destruction of the satellite Fengyun-1C on 2007 January 11 with an anti-satellite missile test performed by the Popular Republic of China has created approximately 3,000 debris [6]. The collision between the IRIDIUM 33 and KOSMOS 2251 that occurred February 2009 and at the time is the second break-up by number of debris released (more than 1,700). The Fengyun-1C breakup took place at an altitude of 850 km while the accidental collision of the two satellites happened at 790 km. As a result, nearly all the debris originated from these two events are still in orbit because at that height the effect of atmospheric drag is negligible. This statement can be also supported observing Fig. 1.1, where the total number of debris remains nearly constant after the two breakups<sup>1</sup>.

The percentage distribution of catalogued objects among these categories is represented in Figure 1.2, using the data from [4].

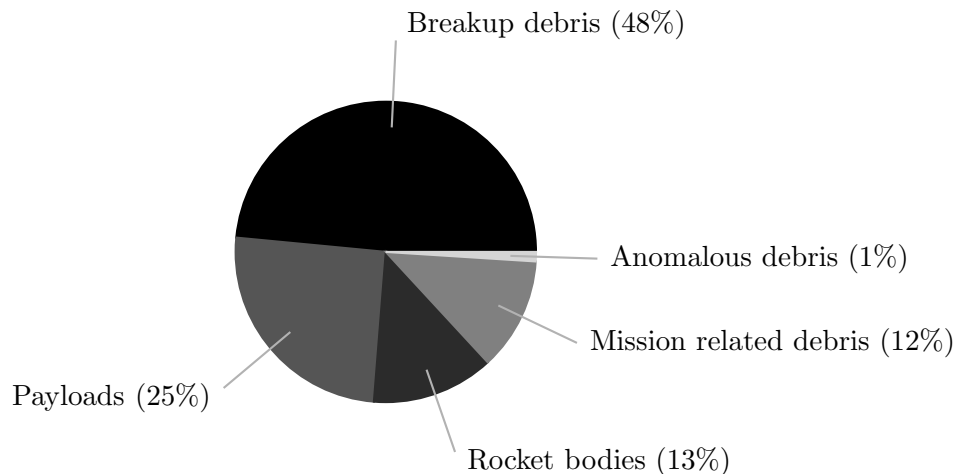


**Figure 1.2:** Catalogued objects in orbit around the Earth, April 2007

Approximately three quarter of the orbiting objects are debris while the remaining quarter are payloads. It should be emphasised that these data refer only to catalogued objects and hence the real number of debris is even higher. The reason is that with available radar and optical technologies only debris larger than 1 cm can be effectively tracked and it is estimated that there are millions of millimetre-size debris.

Another important aspect that must be taken into account when the orbiting object population is analysed is the belongings of the debris. In Table 1.1 the number of payloads and debris is listed for the main nations and international agencies.

Russia and Unites States are owner of 2548 out of 3380 operative payloads in orbit around the Earth and, as a consequence, their amount of space debris and rocket bodies is also high. An high number of debris, if compared to the amount of satellite, is associated to Popular Republic of China, as a consequence of the Fengyun-1C deliberate breakup.

<sup>1</sup>The decrease in space debris population after IRIDIUM-KOSMOS collision is related to the decay of the debris originated from KOSMOS 24121 breakup of February 2008, that occurred at 410 km of altitude

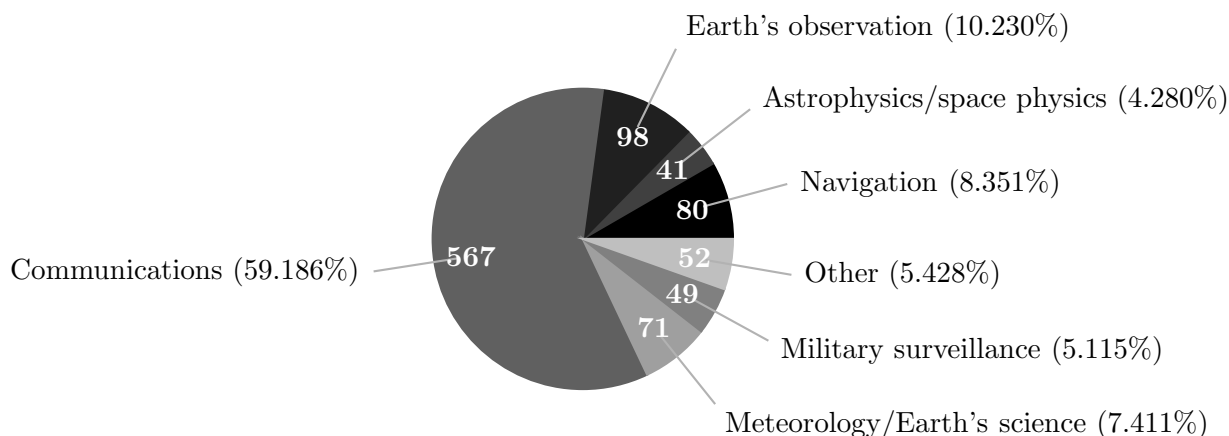
**Table 1.1:** Satellite score box, January 2011 [5]

Country/Org.	USA	Russia	China	ESA	France	India	Japan	Other
<b>Payloads</b>	1142	1406	100	39	49	41	114	489
<b>Rocket bodies &amp; debris</b>	3691	4646	3388	44	431	132	75	112
<b>Total</b>	<b>4833</b>	<b>6052</b>	<b>3488</b>	<b>83</b>	<b>480</b>	<b>173</b>	<b>189</b>	<b>601</b>

## 1.2 Satellite population

In this section the main characteristics of Earth’s artificial satellite population are analysed. In particular, the regions with the higher density of operative satellite are highlighted.

Using the data from the “UCS Satellite Catalogue” [7], the satellites can be divided into groups according to their principal function. The percentage composition of these groups is summarised in Figure 1.3.

**Figure 1.3:** Satellite divided by main function, January 2011 [7]

The majority of the satellites (59.186 %) is used for communication (e.g. television broadcasting) and another important portion is dedicated to Earth’s Observation and Meteorology (10.230% and 7.411% respectively). Navigation (e.g. Global Positioning System (GPS)) is accounted for 8.351% but the number of satellites in this category will probably grow if ESA’s Galileo constellation will be launched. Instead, the satellites designed for astrophysics and space physics observation are only 41.

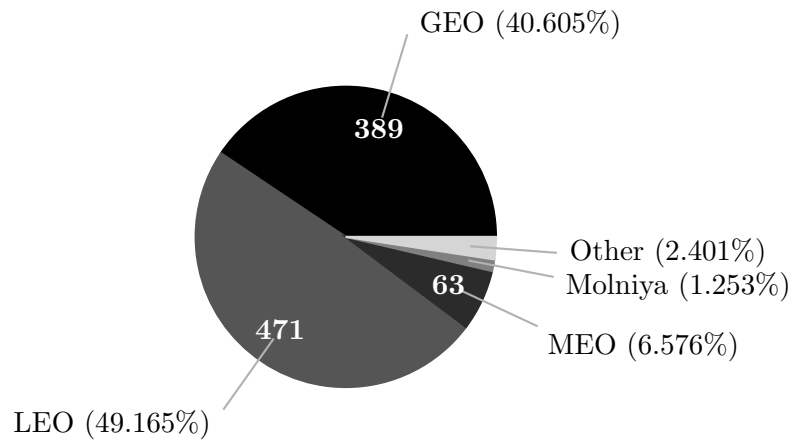
The satellites can be also grouped according to their orbit altitude. The criteria that are necessary to define each group are listed in Table 1.2.

In agreement with these definitions, in Figure 1.4 the composition of the current satellite population is represented.

Nearly 50% of the satellite listed in [7] are in LEO. The reason is that this kind of orbit is the most suitable for Meteorology, Earth’s observation, and Military surveillance and is also used by some Communication satellites. It is important to notice that 185 satellites are in Sun-synchronous

**Table 1.2:** Orbit classification

Name	Height $h$ [km]	Semi-major axis $a$ [km]
Low Earth Orbit (LEO)	$h < 800$	$a < 7,178$
Mean Earth Orbit (MEO)	$800 < h < 30,000$	$7,178 < a < 36,378$
Geostationary Earth Orbit (GEO)	$h \simeq 35,786$	$a \simeq 42,164$
Super-synchronous	$h > 37,000$	$a > 43,378$

**Figure 1.4:** Satellite divided by orbit type, January 2011 [7]

LEO orbits. The orbital plane of these orbits rotates with an angular rate of 360 deg/year and hence the time in light and shadow are constant throughout the year. For this reason most of the satellites designed for Earth's observation use this kind of orbit. Navigation satellites, instead, are maintained on the same orbital plane through station keeping manoeuvres. With respect to the Sun-synchronous satellite the probability of an impact between two navigation satellite are therefore lower.

Satellites in GEO orbit are communication satellites. Since the period of a GEO orbit is 24 hours, if the orbital plane is coincident with the equatorial plane, an observer on the Earth's surface will see it as if it occupies a steady position. Hence, a satellite in GEO will be found at the same longitude, a condition really attractive for information broadcasting since, with only one satellite, a wide area can be covered for the whole day. Because of this, all the satellites in GEO orbit are found at inclinations lower than 10 deg with respect to the equatorial plane. This fact, combined with the long period of the orbit, results in low relative velocities between objects in this orbit. As a result, the effects of a destructive collision are mitigated in this region.

Some Navigation satellites are in MEO and a few Russian communication satellites can be found in Molniya orbit, an highly eccentric MEO orbit with a period of 12 hours. Anyway, the total percentage of these two groups is below 10%.

In Figure 1.5 a polar view of the Earth surrounded by the bigger orbiting objects is represented.

The GEO orbit can be easily identified with the external circle whereas the LEO cloud covers almost completely the globe.

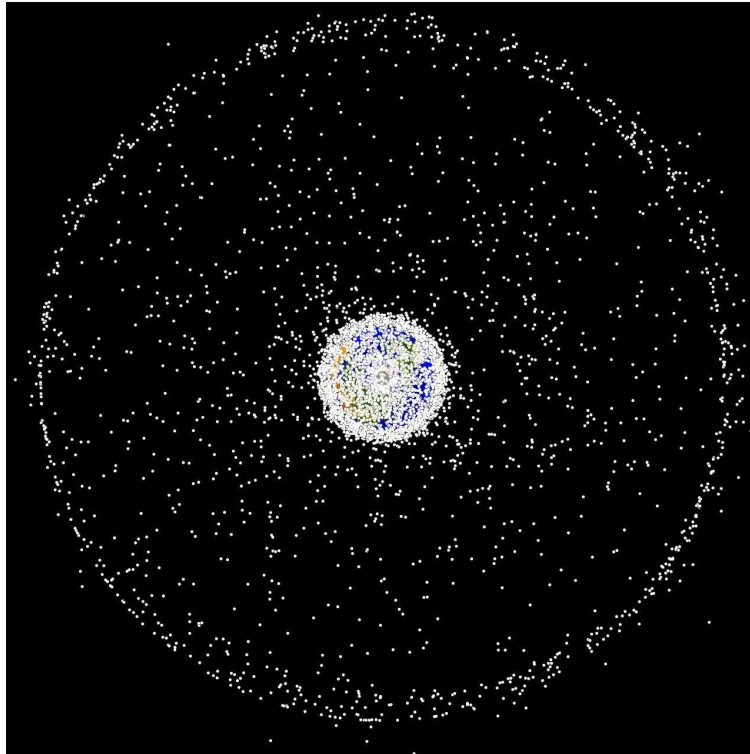


**Figure 1.5:** Polar view of Earth's orbiting objects

The high number of satellites in both LEO and GEO orbits results in higher risks of collision. Furthermore, as outlined ahead, these orbits are important for commercial purposes. For this reason it is necessary to limit the occurrence of destructive collisions, e.g. through avoidance manoeuvre, in order to limit the number of debris.

### 1.3 Space debris population

In this section the main characteristics of the space debris orbiting the Earth are described, focusing on the orbits with the largest number of debris. In addition, the sources and dimensions of the known space debris are given.

The number of orbiting debris is strictly connected to the destructive events that occurred in orbit, as already stated in Section 1.1. In Figure 1.6 the known satellite breakups are divided by fragmentation causes.

The data in Figure 1.6 are referred to April 2007. At present, the percentage of debris associated to accidental collision is higher because of the KOSMOS-IRIDIUM breakup of February 2009, that released more than 1,700 debris. A large amount of fragmentation is associated to malfunction of the propulsion system and to deliberate destruction. Another relevant part is still unknown.

In Figure 1.7 the percentage of the total number of debris associated to each cause of fragmentation that remains in orbit is represented. Even in this case the data are referred to April 2007.

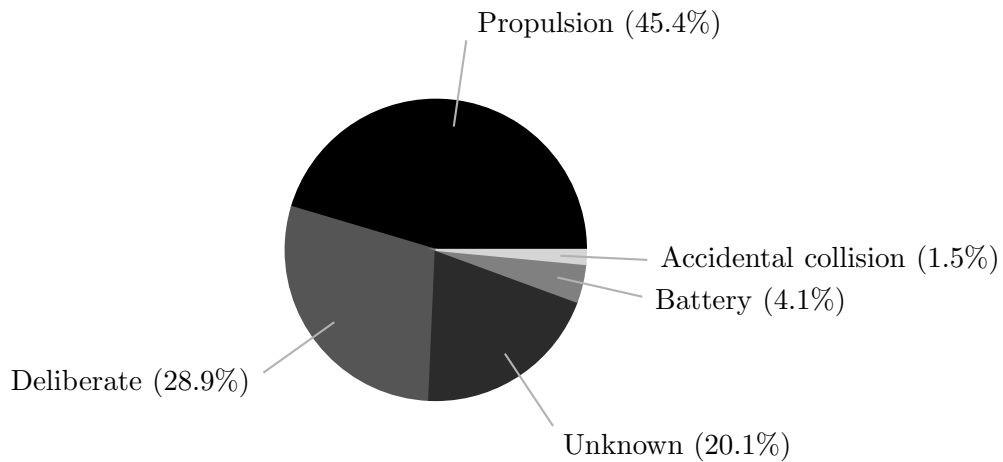


**Figure 1.6:** Causes of known satellite breakups, April 2007 [4]

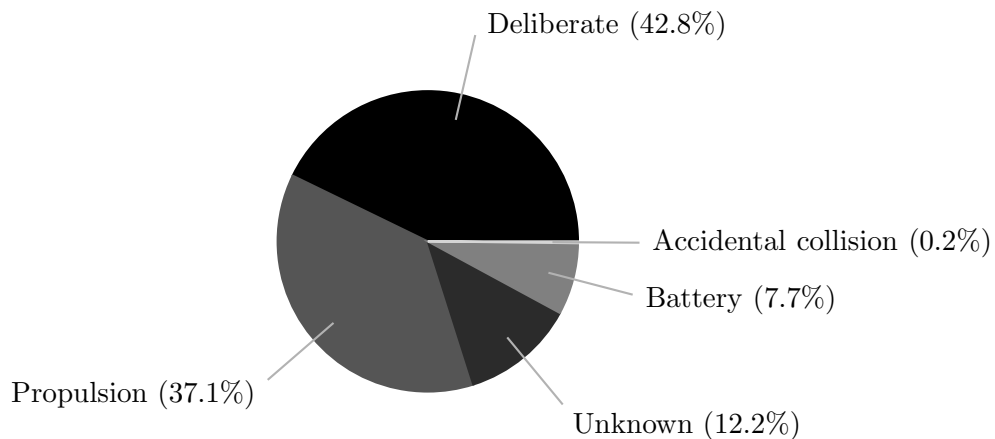


**Figure 1.7:** Proportion of catalogued satellite breakup debris remaining in orbit, April 2007 [4]

The explosion of Fengyun-1C has changed the pattern, since previously 64.4% of the in-orbit debris came from propulsion failures. The reason is that all the other deliberate breakups were executed at low altitudes, where the atmospheric drag could de-orbit most of the generated fragments in a few months. The percentage of the debris from accidental collision that is nowadays in orbit has also grown after the collision of IRIDIUM 33 and KOSMOS 2251.

The space debris can be also divided by source. The percentage associated to each of these sources is depicted in Figure 1.8.

Besides the fragments originated from payloads breakups, another important share is associated to rocket bodies. Launcher fairings and empty tanks are released after orbit injection or during stage separation. Before the release of debris mitigation guidelines there were no constraints on

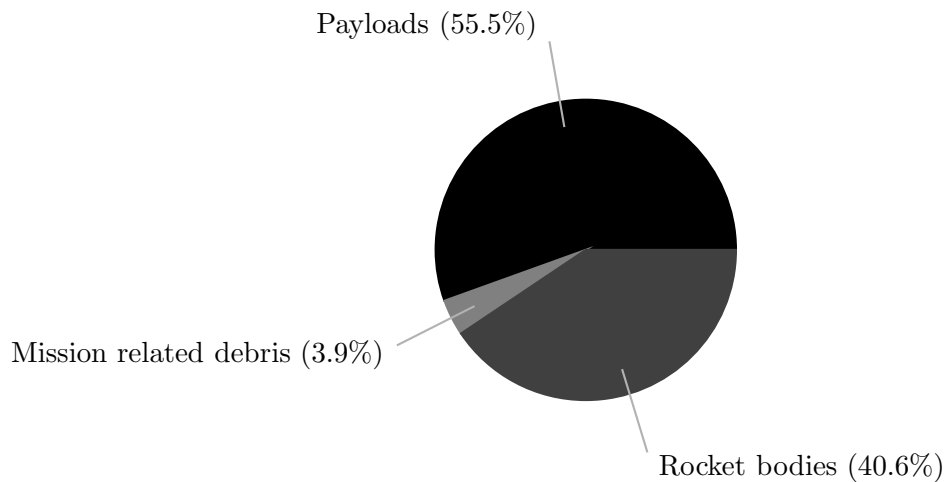


**Figure 1.8:** Sources of satellite breakup debris in orbit by object type, April 2007 [4]

these actions; thus these large debris could remain in uncontrolled orbits. Consequently, both the probability of an impact and new debris release are high.

The size distribution of the major breakup clouds is plotted in Figure 1.9. The debris size can be larger than 1 metre; anyway, the number of these bigger debris is limited.

Another important parameter is the debris area-to-mass ratio. An example of area to mass ratio versus debris size is graphed in Figure 1.10. The majority of the debris has small size and mass and hence could not cause directly a destructive breakup. Some of the larger debris have instead low area-to-mass ratios and hence a collision can release a large amount of debris.

The spatial distribution of the debris must be analysed in order to assess the risks of impact with operative satellites. In Figure 1.11 and 1.12 the distribution of the catalogued debris as of June 2003 is reported in histogram form. The debris in LEO are mainly concentrated in the region between 300 to 800 km. Another crowded region can be found just above the LEO maximum altitude, between 1,400 to 1,700 km. MEO region is much less populated, apart the semi-synchronous ring. GEO orbit sees instead a larger number of objects. A more recent detail of the LEO distribution is plotted in Figure 1.13. The number of debris has drastically increased after the Fengyun-1C explosion.

In Figure 1.14 the distribution of catalogued objects versus eccentricity is reported. Most of the satellites in orbit at the time have really low eccentricity, except a few satellites with the eccentricity typical of a Molniya orbit.

The distribution of the satellites with respect to orbital plane inclination is graphed in Figure 1.15. The majority have high inclination since are in Sun-synchronous orbits or in constellation designed for navigation. The low inclination can be mainly associated to GEO satellites. It should be noted that, under the effect of Moon and Sun gravitational forces, the inclination can grow up to 15 deg. For this reason, many debris that have inclination between 0 deg and 15 deg in Figure 1.15 are found in the geostationary ring.

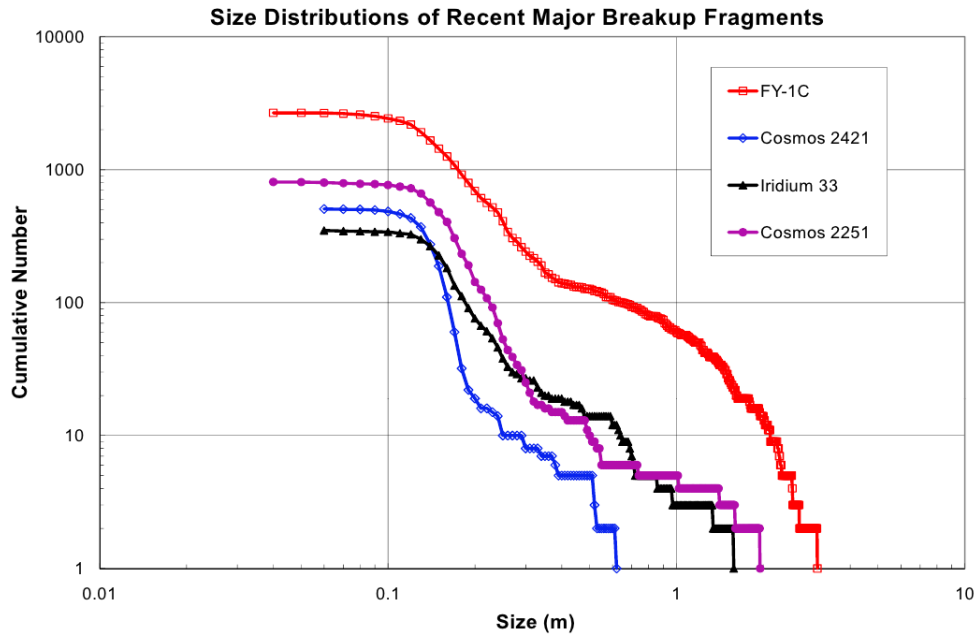


**Figure 1.9:** Cumulative size distributions of the four major breakup fragment clouds since 2007 (this image is taken from [8])

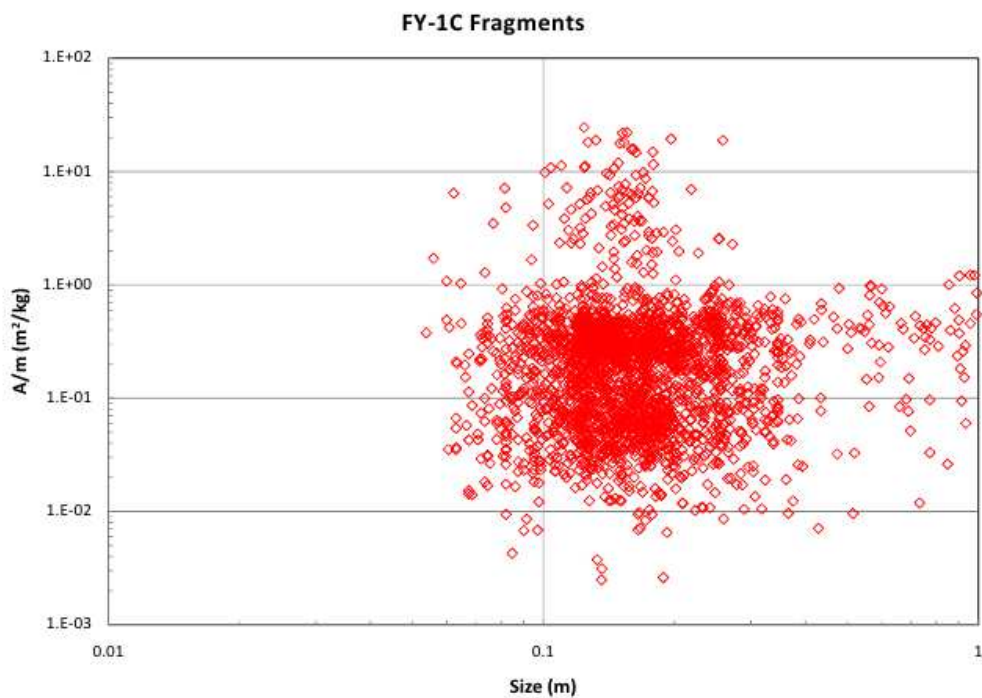


**Figure 1.10:** Area-to-mass ratio ( $A/m$ ) versus size distributions of the Fengyun-1C debris cloud (this image is taken from [8])

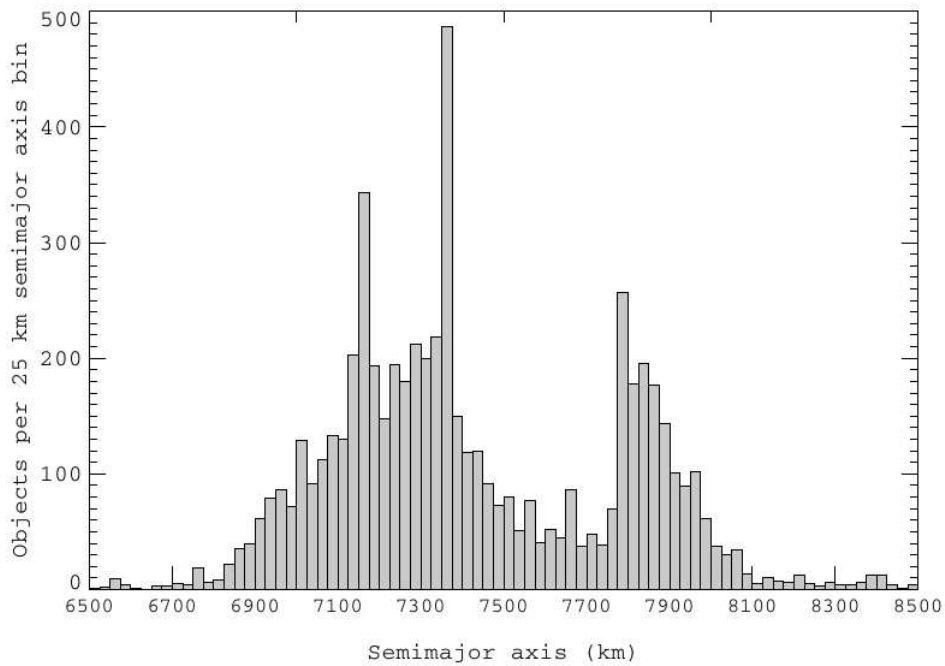


**Figure 1.11:** Distribution of LEO catalogued objects with the semi-major axis of their orbit, June 2003 (this image is taken from [9])

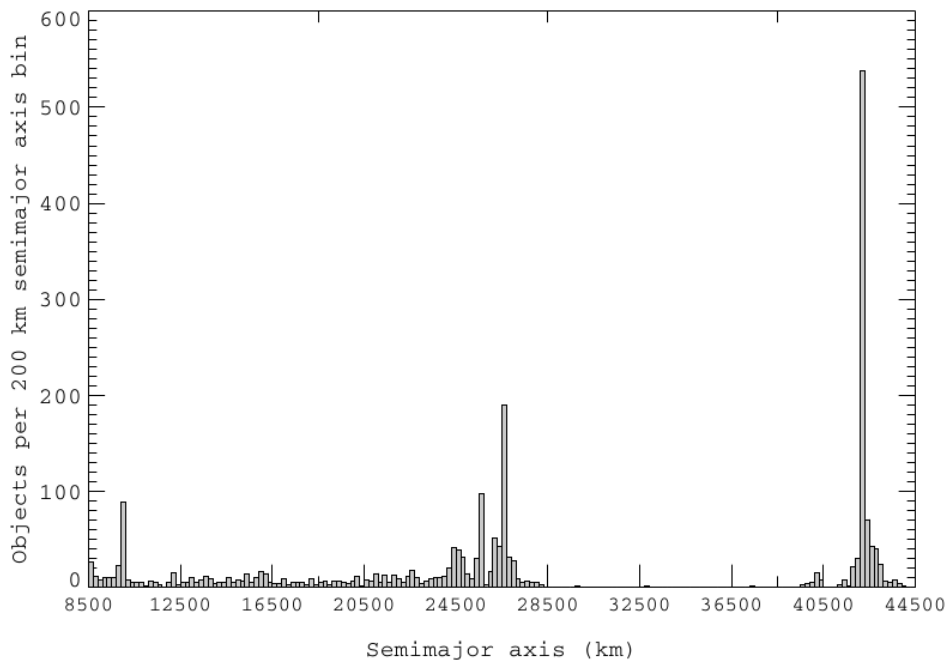


**Figure 1.12:** Distribution of LEO catalogued objects with the semi-major axis of their orbit, June 2003 (this image is taken from [9])

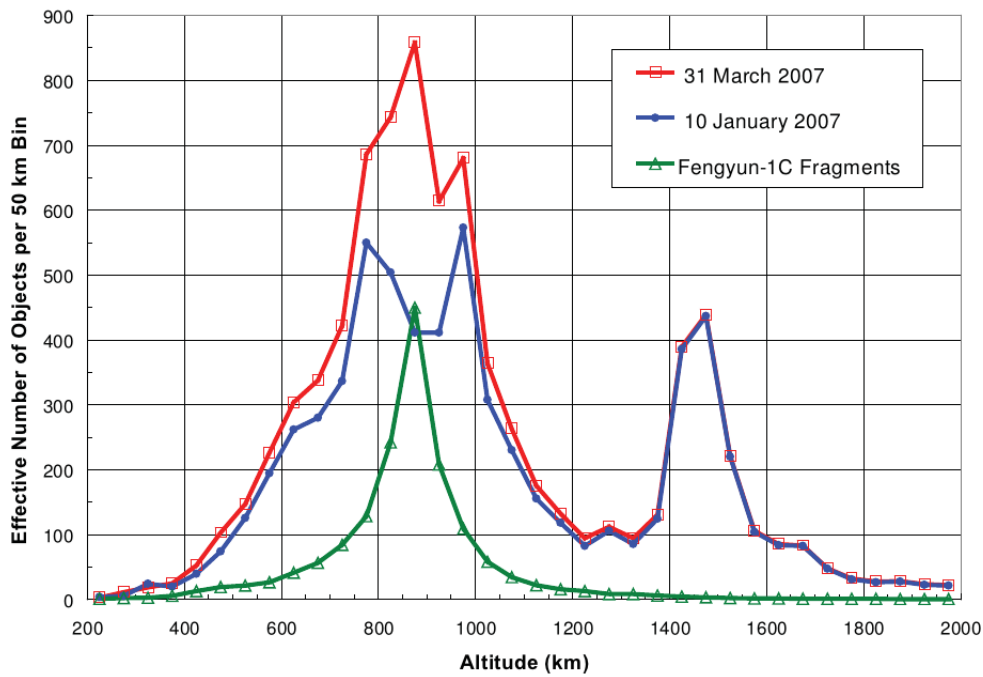


**Figure 1.13:** Distribution of catalogued objects with the semi-major axis of their orbit, March 2007 (this image is taken from [10])

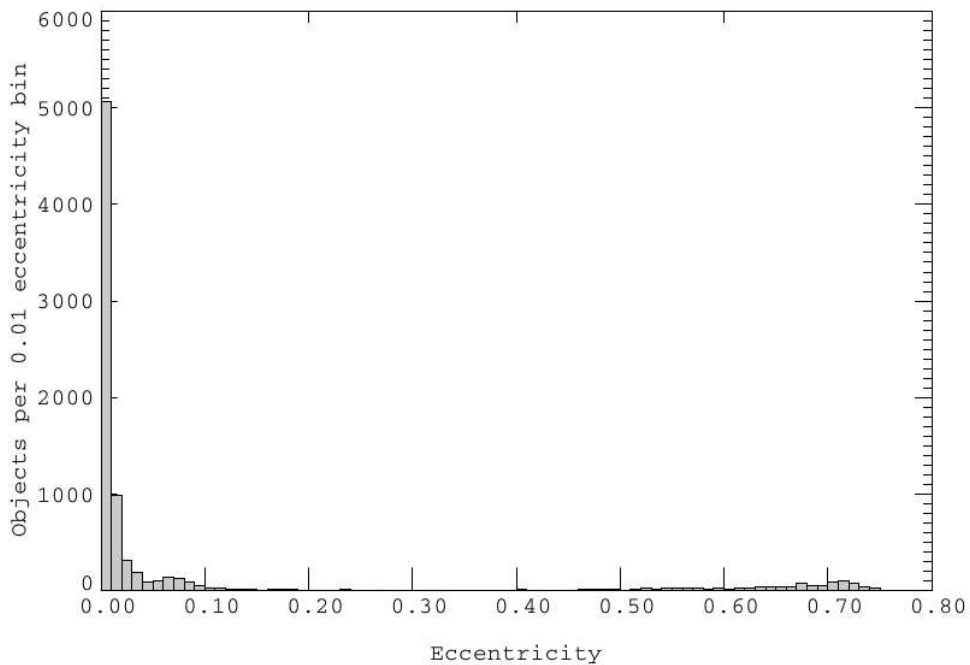


**Figure 1.14:** Distribution of catalogued objects with the eccentricity of their orbit, June 2003 (this image is taken from [9])

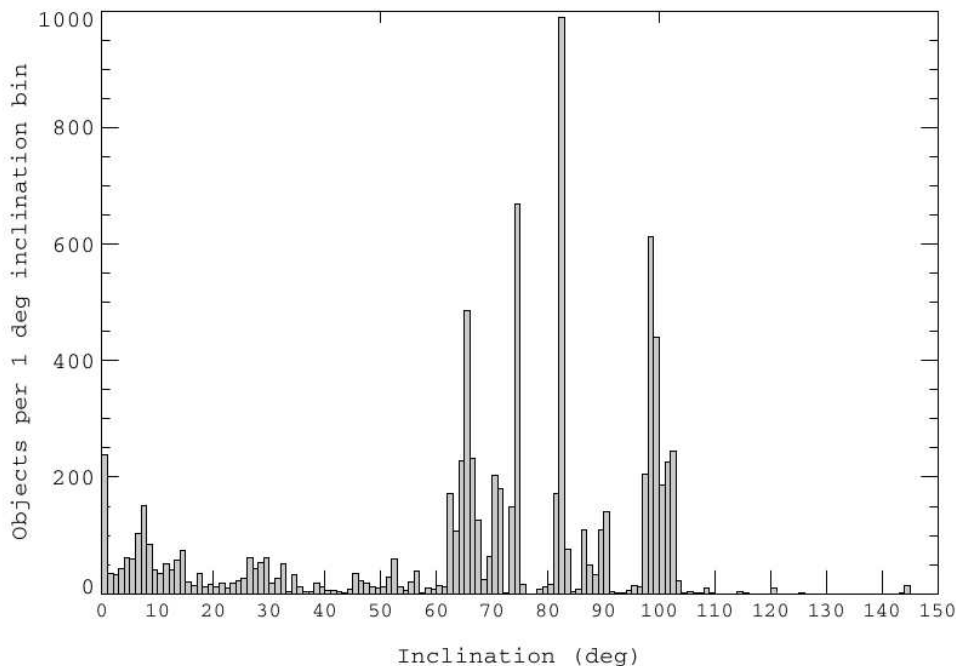


**Figure 1.15:** Distribution of catalogued objects with the inclination of their orbit, June 2003 (this image is taken from [9])

According to the general framework provided in Sections 1.2 and 1.3, it is clear how important is avoiding the collisions between orbiting objects. In particular, combining the data regarding space debris and satellite population the regions where the risk of impact is higher can be identified. These regions are clearly the geostationary ring and LEO, since both the number of active satellite and space debris are high. In addition, both regions are commercially attractive, since these orbits are suitable for communication, navigation, and surveillance satellites and the related services are already used by millions of people. For this reason, a reduction of satellites in these orbits seems unfeasible and hence *collision avoidance* manoeuvres are necessary. A *collision avoidance* manoeuvre is a manoeuvre performed by an active satellite with the aim of decreasing the probability of a collision. Since the use of thrusters is usually required to perform an avoidance manoeuvre, it can not be performed by a retired satellite or a debris. Furthermore, this strategy will reduce available fuel and satellite lifetime and so is usually applied only when the risk of collision is high.

In order to predict the occurrence of a collision, a *conjunction analysis* must be made. This means that the positions of the catalogued objects are obtained over a certain time span and are compared with the aim of identifying all close approaches. The uncertainties on the initial position of the debris and objects are also taken into account when computing the probability of a collision.

The high number of objects (more than 16,000) that must be considered during a conjunction analysis makes this task really time consuming. Using ad-hoc algorithm all the possible combinations of orbiting objects are screened, usually propagating the orbital elements provided by *Space-Track* database [11] on a time span of a week or two. Since a numerical propagation of all the object positions would require a really long time, simplified analytical models are used. An accurate analysis is then performed on the pairs of orbits that intersect in the considered time span. If the

probability of impact exceeds a certain threshold, an avoidance manoeuvre is designed.

The aim of this work is to develop a tool that can identify dangerous situations in a more efficient way. In this framework, the computation of the Minimal Orbital Intersection Distance (MOID) can be an attractive solution. The MOID provides information on the relative distance between two orbits, since it represents the minimum distance between two orbits. In addition, the points on the two orbits among which the MOID is found can be identified. In case the two orbits have a MOID above an appropriate safety distance, no numerical integration is necessary, since the two objects will not collide in the considered time interval.

At present, the methods developed for MOID computation are applied almost exclusively to Keplerian orbits [12, 13, 14]. The Keplerian orbit, anyway, is not suitable to describe the motion of an artificial satellite of the Earth. The effect of the perturbations, in particular atmospheric drag and Earth's asphericity in LEO, and Moon and Sun gravitational attraction for a GEO satellite, can change significantly the shape and orientation of the orbits. It is indeed necessary to describe the orbital evolution when computing the MOID of a real object. In this work, the procedure that are necessary to perform this operation are developed. At first, the MOID will be computed considering a mixed case, i.e. a perturbed and a Keplerian orbit. The constraint of having a Keplerian orbit will then be removed and two general orbits will be considered. The developed methods should hence distinguish the orbits that intersect each other and possibly provide information on the relative evolution of the two orbits.

The MOIDs computed throughout this work are obtained by means of the minimisation of an objective function, that is the square distance between points of the two orbits. Despite in literature many analytical, geometrical and numerical methods can be found, this approach was preferred since the use of the global optimizer COSY-GO allows further manipulation of the obtained solutions. In particular, it will be shown how the obtained MOID can be expanded through the use of Differential Algebra (DA) and hence study its variation with the uncertainties on the orbital parameters. The DA techniques will be also applied to the study of the evolution of a cloud of debris through time.

The present work is hence organised as follows: in Chapter 2 the selection of appropriate models for the computation of satellites and debris position is described. In Chapter 3 the main features of the algorithm COSY-GO, as well as the characteristics of Differential Algebra and Taylor's Models on which this algorithm is based, are outlined. The implemented procedure for MOID computation together with some interesting test cases are reported in Chapter 4. Chapter 5 comprises further application of the models for position calculation that are made possible by the use of differential algebra. Such application comprises the handling of debris orbital parameters uncertainties and MOID expansion. In Chapter 6 the results achieved are summed up and some hints for future developments are outlined.

## Chapter 2

# Analytical Models

In this chapter the selection of a model able to predict the temporary evolution of the position of an orbiting object is described.

At first, a brief description of the artificial satellite motion is given, focusing on the perturbative forces that can modify satellite or debris trajectory. For each class of orbits the main sources of perturbation are outlined.

Then, the requirements concerning model implementation are stated and the selection of analytical models is motivated. A description of the models available in literature is provided, highlighting their validity and accuracy.

At last, three analytical models are selected and, for each one, the procedure to compute the object position is given. Every implemented model has been validated through comparison with numerical integration or using ad-hoc test cases. The most relevant results are reported as well as consideration on model accuracy and validity.

### 2.1 Artificial satellite motion

The motion of a space debris or an artificial satellite around the Earth has been a problem of wide interest since the launch of Sputnik I in 1957. The general solution of the gravitational two-body problem provides an easy way to compute the position of the two bodies with respect to their common centre of mass. When one of the two bodies mass is orders of magnitude larger than the other and the force exchanged by the two bodies depends on the inverse square of their distance, the two bodies problem is called “Kepler’s problem”. The most massive body is called *primary body*, while the smaller is the *secondary body*. The equation of motion takes the form

$$\frac{d^2 \mathbf{r}}{dt^2} = \ddot{\mathbf{r}} = - \frac{G(M+m)}{r^3} \mathbf{r}, \quad (2.1)$$

where  $G$  is the universal gravitational constant,  $M$  and  $m$  are the mass of the primary and secondary body respectively, and  $r$  is the distance between them. In the case of an artificial satellite of the Earth (whose astronomical symbol is  $\oplus$ ), our planet is the primary body while the satellite can be defined as secondary body.

Since the Earth’s mass is times bigger than satellite mass the equation can be approximated as

$$\ddot{\mathbf{r}} \approx - \frac{GM_{\oplus}}{r^3} \mathbf{r} = - \frac{\mu_{\oplus}}{r^3} \mathbf{r}, \quad (2.2)$$

where  $\mu_{\oplus} = GM_{\oplus}$  is Earth's gravitational parameter, and the common centre of mass lies in the centre of mass of the primary body. For this reason, the vector  $\mathbf{r}$  describes the position of the secondary body in a reference frame with the origin in the centre of mass of the Earth.

It can be shown that both mechanical energy and angular momentum are constant. Since angular momentum remains constant in magnitude and direction it can be inferred that the trajectory belongs to a plane called orbital plane. Using this property of the motion, it can be shown that the possible trajectories are represented by the equations of a conic that has the form

$$r = \frac{a(1 - e^2)}{1 + e \cos(\nu)}, \quad (2.3)$$

where  $r$  is the orbit radius corresponding to the true anomaly  $\nu$ ,  $a$  is semi-major axis, and  $e$  is conic eccentricity. The Earth's centre of mass lies in one of the focus of this conic. The semi-major axis is a constant related to specific orbital energy<sup>1</sup>  $\mathcal{E}$  through

$$a = -\frac{\mu_{\oplus}}{2\mathcal{E}}.$$

The eccentricity  $e$  is a constant that determines the shape of the conic and can not be negative. When  $0 < e < 1$  the orbit is an ellipse, when  $e = 1$  a parabola, and when  $e > 1$  an hyperbola. The true anomaly  $\nu$  is the angle measured from the pericentre of the conic, that is the minimum value of orbit radius. A perifocal reference ( $\mathbf{P}, \mathbf{Q}, \mathbf{W}$ ) frame can be defined. This reference frame is Earth centred, orbit based, and inertial. The  $\mathbf{P}$  axis is in periapsis direction,  $\mathbf{W}$  has the same direction of angular momentum vector and the  $\mathbf{Q}$  axis belongs to the orbital plane and is mutually orthogonal to the other two vectors (Fig. 2.1).

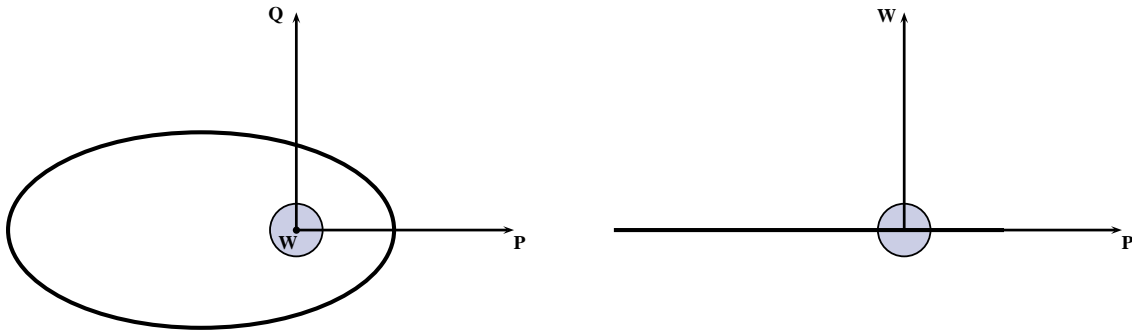


**Figure 2.1:** Perifocal reference frame

All information regarding the shape of the conic are specified with the parameters  $e$  and  $a$ , and the position along the trajectory by  $\nu$ . Three other parameters are necessary to identify the orbital plane and the position of the pericentre with respect to Earth Centred Inertial reference frame (ECI). This reference frame is centred in Earth's centre of mass and is defined by three unit vector ( $\mathbf{I}, \mathbf{J}, \mathbf{K}$ ), where  $\mathbf{I}$  is in vernal equinox ( $\mathcal{V}$ ) direction, the  $\mathbf{K}$  axis is Earth's rotation axis and  $\mathbf{J}$  is in the equatorial plane and mutually perpendicular to the two others. The three parameters can be defined as the three angles that are necessary to perform a rotation from ( $\mathbf{I}, \mathbf{J}, \mathbf{K}$ ) to ( $\mathbf{P}, \mathbf{Q}, \mathbf{W}$ ). The rotation sequence is given by the three angles

<sup>1</sup>Specific orbital energy is the sum of kinetic energy and potential energy divided by the reduced mass, that in the case of the artificial satellite can be approximated by satellite mass

- $\Omega$  around axis  $\mathbf{K}$
- $I$  around axis  $\mathbf{I}'$
- $\omega$  around axis  $\mathbf{K}'' \equiv \mathbf{W}$

where the two intermediate frames are identified by primed and double-primed vectors. The first angle  $\Omega$  is called *longitude of the ascending node* or Right Ascension of the Ascending Node (RAAN) as it orients the ascending node, i.e. where the orbits crosses the equatorial plane upward. The second angle  $I$  is the orbit *inclination* which is the vertical tilt of the conic with respect to equatorial plane, while the third,  $\omega$ , is the *argument of the periapsis* and is the angle on the orbital plane between the ascending node and the conic periapsis (Fig. 2.2).

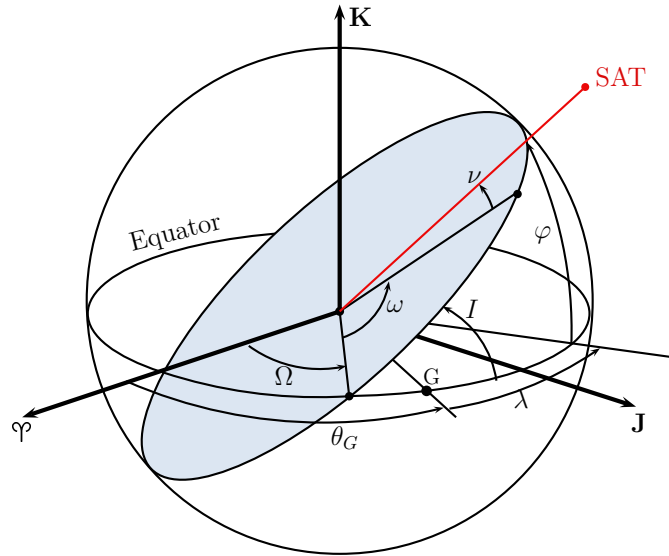


**Figure 2.2:** Earth Centered Inertial reference frame (ECI) reference frame

The six quantities  $a$ ,  $e$ ,  $I$ ,  $\Omega$ ,  $\omega$ ,  $\nu$  are known as *Keplerian elements* and can be used to obtain the position of the satellite in the inertial reference frame and the MOID. Notwithstanding this, Kepler's problem is an ideal case. In the reality there are other forces that act on the satellite. These forces are called *perturbations* or *disturbance forces* since they are orders of magnitude lower than gravitational attraction. Despite their small magnitude, they can influence the motion of artificial satellites or space debris: as a consequence the Keplerian elements are no more constants, but will vary with time. The variation of the Keplerian elements are divided in

- *secular*, when vary linearly with time
- *long period*, when exhibit an oscillatory behaviour with a period larger than the orbital one
- *short period*, when variations have periods smaller than orbital period

Hereinafter the sources of perturbation are characterized, in order to understand which ones must be retained or can be neglected when describing the motion of an orbiting object.

### 2.1.1 Orbital perturbations

The equation (2.1) is enriched by the presence of a small term  $\mathbf{a}_p$  when considering perturbations

$$\frac{d^2 \mathbf{r}}{dt^2} = -\frac{\mu_{\oplus}}{r^3} \mathbf{r} + \mathbf{a}_p. \quad (2.4)$$

For each source of disturbance forces  $i$ , a perturbative acceleration  $\mathbf{a}_{p_i}$  can be written [15], so the expression of the total perturbative acceleration is given by

$$\mathbf{a}_p = \sum_{i=1}^n \mathbf{a}_{p_i},$$

where  $n$  is the total number of perturbation sources, that can vary according to the environment in which the object moves. In the following paragraphs the main disturbance forces acting on a space debris orbiting the Earth are described, together with their qualitative effects on its Keplerian elements.

#### Inhomogeneous gravity field

The spherical gravity field used for the primary body in Eq. (2.1) is an approximation [16]. Earth's mass distribution is not uniform and, as an example, the equatorial radius is larger than the polar one. The Earth's gravitational potential  $V_{\oplus}$ , at an external point distant  $r$  from its centre of mass, can be expressed in terms of spherical harmonics [17]

$$V_{\oplus} = \frac{\mu_{\oplus}}{r} \left\{ 1 - \sum_{n=2}^{\infty} \left( \frac{R_{\oplus}}{r} \right)^n \left[ J_n P_n(\sin(\varphi)) - \sum_{m=1}^n J_{n,m} P_n^m(\sin(\varphi)) \cos(m(\lambda - \lambda_{n,m})) \right] \right\}, \quad (2.5)$$

where  $\varphi$  and  $\lambda$  are geocentric latitude and longitude respectively,  $R_{\oplus}$  is Earth's equatorial radius,  $J_n$ ,  $J_{n,m}$  and  $\lambda_{n,m}$  are constants, while functions  $P_n^m(\sin(\varphi))$  are associated Legendre's functions, defined by

$$P_n^m(x) = \frac{(1-x^2)^{m/2}}{2^n n!} \frac{d^{n+m}}{dx^{n+m}} (x^2-1)^n. \quad (2.6)$$

Constant  $J_n$  are *zonal harmonics* coefficients and are related to asymmetry of north and south hemispheres (e.g. flattening of the poles) and divide the sphere into vertical strips since they depend only on the latitude. The  $J_{n,m}$  constants are called *sectoral* harmonics when  $m = n$  and *tesseral* harmonics when  $m \neq n$ . Sectoral harmonic coefficients depend only on the longitude and their graphical representation is a sphere divided into sectors along meridians. Tesseral harmonics coefficients, instead, depend both on latitude and longitude and as a result their representation is a sphere divided into tessers.

The perturbing acceleration due to Earth is given by

$$\mathbf{a}_p = \nabla V_{\oplus} \quad (2.7)$$

The effects of the non-sphericity of Earth's gravitational field affects all six Keplerian elements and decrease if the orbit radius increases. Secular effects are generated only by even zonal harmonics, while odd harmonic cause only periodic variations. Tesseral and sectoral harmonics generate only periodic perturbations. As it can be inferred from Table A.4, the zonal harmonic  $J_2$  prevails on

the others. Its main effects are secular variation of the right ascension of the ascending node  $\Omega$  and argument of pericentre  $\omega$ . The angles rate of variations are functions of orbit inclination  $I$ . When  $I$  is below 90 deg the secular rate of  $\Omega$  is negative whereas when  $I$  exceeds 90 deg is positive. The secular rate of  $\omega$  depends on the sign of

$$F(I) = 4 - 5 \sin^2(I)$$

whose zeros are called *critical inclinations* and are respectively 64.435 deg and 116.565 deg. When  $I$  equals one of these inclinations the rate is null. When 63.435 deg  $< \omega < 116.565$  deg the secular rate is negative, while is positive in the other cases. These behaviours have been exploited to design particular orbits such as Sun-synchronous or Molniya.

The gravitational field is conservative, hence semi-major axis has no secular variation since it is related to orbital energy. All Keplerian elements exhibit long period and short period variations.

Synchronous (24 hours) and semi-synchronous (12 hours) orbits are characterized by a resonance with tesseral and sectoral harmonics, since the orbital period is related with Earth's rotation period by a ratio 1:1 or 2:1. In particular, it has been demonstrated the existence of two stable and two unstable points for satellite that orbits in GEO. The presence of these points is related to sectoral harmonics, in particular  $J_{2,2}$  and hence are found at constant longitude. The two stable points are approximately at 70.8°E and 105.3°W, while the two unstable points are at 14.7°W and 165.3°E. As a result, a GEO satellite without an east-west station keeping strategy will slowly drift from an unstable point towards the nearest stable point. Tesseral and sectoral harmonics can cause  $m$ -daily periodic oscillations, in particular in orbit semi-major axis.

### Atmospheric drag

The atmosphere around the Earth interacts with the space debris, generating an aerodynamic force. In the vast majority of the cases, the orbiting object is not designed to be a lifting body. For this reason, the resulting force acts in a direction which is nearly opposite to debris velocity, hence can be assumed to be equal to aerodynamic drag [18]. The atmospheric drag is usually written as

$$D = -\frac{1}{2}\rho A v^2 C_D, \quad (2.8)$$

in which  $\rho$  is the atmospheric density at the local altitude,  $A$  is the cross-sectional area,  $v$  is the relative velocity between the object and the atmosphere, and  $C_D$  is a dimensionless parameter, called drag coefficient. This coefficient typically ranges from 1.5-3.0. Density can be modelled using an exponential law, such as

$$\rho = \rho_0 e^{-\frac{h-h_0}{H}}, \quad (2.9)$$

where  $\rho_0$  is density at the reference altitude  $h_0$ ,  $H$  is a parameter called scale factor, and  $h$  is the local altitude.

If the atmosphere rotation is neglected the relative velocity is directly the space debris velocity along its trajectory. Instead, if the angular velocity  $\omega_a$  is considered, the relative velocity  $\mathbf{v}_a$  becomes

$$\mathbf{v}_a = \mathbf{v} - \boldsymbol{\omega}_a \wedge \mathbf{r}. \quad (2.10)$$

The perturbing acceleration due to atmospheric drag is given by

$$\mathbf{a}_{p_a} = -\frac{1}{2m}\rho A v_a^2 C_D \hat{\mathbf{v}} = -\frac{1}{2}B \rho v^2 \hat{\mathbf{v}}, \quad (2.11)$$

where  $m$  is debris mass and  $B$  is the ballistic coefficient, defined as

$$B = \frac{C_D A}{m} . \quad (2.12)$$

The effect of atmospheric drag is strongly related to body shape, dimensions and mass. Anyway, identifying these parameters can be difficult, in particular for space debris [19]. Atmospheric drag affects satellites in LEO and its effect decreases rapidly with altitude. Since it is a non-conservative force, it reduces the orbital energy and hence the semi-major axis. Eccentricity is also influenced: during perigee passage the drag decreases speed and so the apogee is lower at the following passage. The perigee height remains nearly constant until the apogee is low enough to be influenced significantly by atmosphere. Below 200 km of altitude the perturbing acceleration causes the de-orbiting of the space debris in a few days.

Periodic effects occur in all orbital elements especially on  $I$ ,  $\Omega$  and  $\omega$ .

### Solar radiation pressure

The electromagnetic radiation generated by the Sun is able to exert a force on space debris surfaces. The solar radiation pressure can be written as

$$p_{\text{sr}} = \frac{\phi_{\text{sr}}}{c_0}, \quad (2.13)$$

where  $\phi_{\text{sr}}$  is the mean solar flux and  $c_0$  the speed of light. The photons interact with object surfaces and can be reflected specularly, adsorbed or diffused. Each kind of interaction is associated to a coefficient,  $\rho_i$  for specular reflection,  $\rho_a$  for adsorbed radiation, and  $\rho_d$  for diffused radiation. The sum of these coefficients equals unity. The resulting force can hence be divided into three parts:  $\mathbf{F}_s$  is the resulting force due to specularly reflected photons and has the same direction of surface local normal  $\hat{\mathbf{n}}$ ,  $\mathbf{F}_a$  is the force due to adsorbed photons and is parallel to the photon beam direction  $\hat{\mathbf{s}}$ . The force due to diffused radiation  $\mathbf{F}_d$  is given by the sum of two terms, one in beam direction and the other in surface normal direction.

Considering a surface  $A$  and given the angle  $\alpha$  between Sun's direction and surface normal the three forces are given by

$$\mathbf{F}_a = \rho_a p_{\text{sr}} A \cos(\alpha) \hat{\mathbf{s}} \quad (2.14)$$

$$\mathbf{F}_s = 2\rho_s p_{\text{sr}} A \cos^2(\alpha) \hat{\mathbf{n}} \quad (2.15)$$

$$\mathbf{F}_d = \rho_d p_{\text{sr}} A \cos(\alpha) \left( \hat{\mathbf{s}} + \frac{2}{3} \hat{\mathbf{n}} \right) . \quad (2.16)$$

The sum of the three forces divided by space debris mass is the solar radiation perturbing acceleration [15].

A simpler expression for the perturbing force can be used under the assumption that the majority of the radiation is reflected along the direction of the vector  $\mathbf{r}_{\odot}$  that connects the Sun with the satellite. Given the space debris reflectivity coefficient  $0 < C_R < 2$ , the perturbing acceleration due to solar radiation pressure can be approximated by

$$\mathbf{a}_{\text{sr}} = \frac{p_{\text{sr}} A C_R}{m} \frac{\mathbf{r}_{\odot}}{r_{\odot}} . \quad (2.17)$$

The effect of solar radiation pressure becomes more complicated when orbiting in the proximity of the Earth because of the presence of the Earth's shadow, that can partially or totally hide the Sun. Solar pressure influences the eccentricity, in particular for those satellites with large solar arrays. This effect is connected to Earth's revolution around the Sun and hence can be classified as a long period perturbation with a period of one year. The perigee height can also be affected, and this can result in a reduced lifetime. Solar radiation pressure can exceed the effect of atmospheric drag above 500 km of altitude, depending on the area to mass ratio of the satellite or debris.

### Third body

The presence of a third body, e.g. the Sun or the Moon, generates an additional acceleration term for each additional body

$$\mathbf{a}_{3b} = -\mu_{\odot} \left( \frac{\mathbf{r}_{\odot}}{r_{\odot}^3} - \frac{\mathbf{r}_{\oplus,\odot}}{r_{\oplus,\odot}^3} \right) - \mu_{\zeta} \left( \frac{\mathbf{r}_{\zeta}}{r_{\zeta}^3} - \frac{\mathbf{r}_{\oplus,\zeta}}{r_{\oplus,\zeta}^3} \right) \quad (2.18)$$

where  $r_{\odot}$  and  $r_{\zeta}$  are the distance between the satellite and Sun and Moon respectively, while  $r_{\oplus,\odot}$  and  $r_{\oplus,\zeta}$  are the distance between Earth and the other celestial body and are functions of time. This perturbation generates secular and long period variations of  $\Omega$ ,  $\omega$  and  $M$ . The semi-major axis, eccentricity and inclination are affected only by periodic perturbation. The position of the perigee and ascending node affect these periodic perturbations.

The inclination of a GEO satellite is affected by luni-solar perturbation that generates a long-period variations with a period of approximately 54 years and an amplitude of 15 deg [18].

## 2.2 Model requirements

In this section the requirements of an algorithm that can compute space debris positions are outlined.

The prediction of future location of a satellite, a procedure which is also known as *propagation*, can be performed through three approaches: *analytical*, *numerical*, and *semi-analytical*.

Analytical theories use methods such as variation of parameters, averaging techniques and canonical transformation to simplify the equations of motion when perturbations are present, since no closed form solution of the motion can be obtained. Using this approach the Keplerian elements can be expressed as functions of time, hence reducing the computation of position to an evaluation of known functions. However, simplifications are necessary to obtain an analytical solution and, as a result, some coupling effects are sometimes neglected or, in some cases, certain perturbations are not considered.

The numerical methods, also referred to as *special perturbations*, consist in integrating numerically the equations of motion. The advantage of these approaches is that all secular and periodic perturbations are retained, as well as coupling effects between perturbations. Special perturbations are indeed more precise than analytical methods. Despite that, solving numerically perturbed equations of motion requires longer times.

Semi-analytical methods have been developed to combine the speed of analytical methods and the accuracy of special perturbations. The short periodic contribution are separated from long-periodic and secular effects, obtaining a system where three group of equations are present: equations of motion for mean elements (Keplerian elements without short period effects), equations for

short periodic coefficients (functions of the mean elements) and Fourier series (which allows the construction of short-periodic motion in the elements given short-periodic coefficients). The result is that the equation of motion written in mean elements can be integrated with large time steps (e.g. days).

The choice between these approaches is driven by COSY language and COSY-GO global optimizer. This language can manipulate code with DA Taylor series expansion, as it will be explained in details in Chapter 3. To take advantage of COSY features only analytical solutions will be taken into account in this work.

The requirements concerning perturbations that should be analytically modelled can now be formulated. In Fig. 2.3 the order of magnitude of third body, solar radiation pressure and main harmonics of gravity potential perturbations are plotted. Drag acceleration has not been drawn because it decreases rapidly with altitude and would not be visible on this scale.

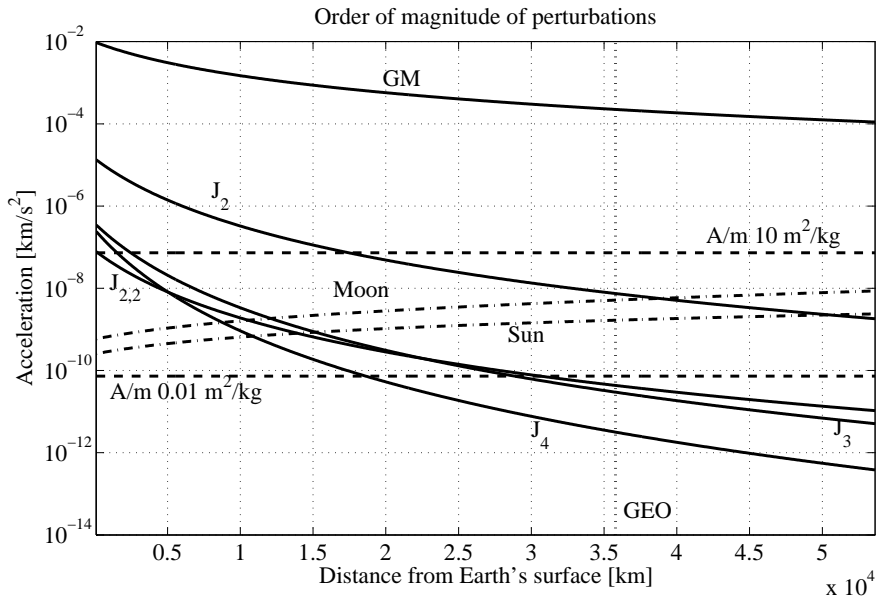


**Figure 2.3:** Order of magnitude of the main perturbations acting on space debris orbits

It is clear that the analytical model must retain at least the effect of the first zonal harmonic  $J_2$ . Since the majority of space debris are found in LEO, the atmospheric drag should be taken into account as well. Moon and Sun perturbations could be neglected for LEO satellites but their importance grows when distance from the Earth increases. Luni-solar perturbations must be modelled for synchronous and super-synchronous orbits since their magnitude overcomes zonal harmonics one. Solar radiation pressure varies with the ratio  $A/m$ , but remains constants with respect to orbit altitude. It is therefore important to have reliable information concerning shape and mass of the debris, but these properties can in general be computed only statistically, e.g. using a mean density [19]. Most of space debris area-to-mass ratio ranges between  $[0.01;10]$  m<sup>2</sup>/kg and the contribution of solar pressure in LEO is usually lower than  $J_2$ . Anyway, above 20,000 km this contribution becomes larger than the one of the first zonal harmonic, if the ratio  $A/m$  is near 10 m<sup>2</sup>/kg. An analytical model for space debris with semi-major axis above that altitude should therefore consider effects of

solar radiation pressure.

## 2.3 Analytical models selection

In this section, after a brief description of analytical solutions available in literature, the propagation models that fulfil requirements stated in the former section are described. The algorithms have been implemented in MATLAB<sup>®</sup> and subsequently validated.

The first analytical solution for the artificial satellite motion was provided in the late 1950's by Brouwer [20]. His solution was obtained using the Von Zeipel's method [21] and considered only perturbation up to the fifth zonal harmonic. Another drag free solution was obtained by Kozai [22]. However, these solutions exhibit singularities for low values of inclination and eccentricity [23] and in both theories the expression of Keplerian elements are characterized by tens of terms.

A similar model was developed by Aksnes [24, 25] that used Delaunay's variables (see § A.5.1). The same author developed a really compact theory [26] using Hill's variables (see § A.5.2). The latter theory is second-order (e.g. term  $J_2^2$  are retained as well as the interaction between zonal harmonics), it does not have singularity in eccentricity, and fails only at critical inclination. The zonal harmonics range from  $J_2$  to  $J_5$  and Kepler's equations is solved only once before applying periodic perturbations. The errors in satellite positions are limited to tens of metres during the first week of propagation.

A third order theory was developed by Kinoshita [27] and it includes all terms of Aksnes solution and additional terms obtained by the interaction of  $J_2$ ,  $J_3$  and  $J_4$ . With the development of symbolic computation [28] more accurate theories have been developed [29].

A solution for the coupled effect of zonal harmonics and atmospheric drag was developed by Brouwer and Hori [30]. They used an exponential density model under the hypothesis of a non-rotating atmosphere. Since they used the same expansion of Brouwer drag-free solution [20] there are singularities for zero inclination and eccentricity. Another model that uses a power function for density was developed by Lane and Cranford [31]. Their model eliminates division by  $e$  and  $\sin(I)$ , but remains valid for small eccentricities and inclinations. Hoots [32, 33] developed a model (Hoots ANalytic Dynamic Ephemeris (HANDE)) for zonal harmonics  $J_2$ ,  $J_3$  and  $J_4$  that does not exhibit singularities and has the flexibility of choosing the atmosphere model. This model best fits LEO satellites orbit evolution. A comprehensive list of analytical models was given by Liu [34]. Efforts in developing new theories with the help of computer algebra systems has been performed recently by Xu et al. [35].

The effects of solar radiation pressure and resonance due to tesseral harmonics have been studied in the past years but only analytical solutions for particular cases were found [36, 37, 38, 39]. For solar radiation pressure in particular the efforts were concentrated on semi-analytical models, mainly because of the presence of Earth's shadow [40, 41]. Third body perturbation have also been developed, in particular Hujsak [42] studied the problem of both Sun and Moon perturbations. More recently Xu et al. [43] obtained a new analytical solution to the same problem.

In recent years, some efforts have been made to obtain a general solution comprehensive of all sources of perturbations, anyway the number of terms that are necessary for Keplerian elements expansion becomes huge [44, 45]. A different approach has been used to create SGP4 analytical orbit propagator, developed by NORAD. The solutions of Lane and Cranford and Hujsak were in fact used to develop a comprehensive orbit propagator [46, 47]. The revised version of SGP4 [48, 49] can be used to propagate the orbits of satellite from LEO to super-synchronous orbits. In addition,

resonance effects for 12 hours and 24 hours orbits can be computed, anyway in this model Earth's atmosphere is non-rotating and a power scale density model must be used.

Since the majority of space debris is concentrated in LEO it has been decided to propagate the orbits of space debris that have perigee below 6,000 km with HANDE algorithm. At this altitude the luni-solar acceleration are still one order of magnitude lower than  $J_4$  zonal harmonic perturbation (Fig. 2.3).

The SGP4 model, instead, has been used for deep-space satellites and space debris (that have a period larger than 225 minutes), in particular for satellites in GEO. The algorithm has been simplified removing all terms related to atmospheric drag that can be neglected without any loss in accuracy at that altitude.

The second-order theory by Aksnes was also implemented. This compact, non-singular theory could be used for an operative satellite, under the hypothesis that perturbing effects of atmospheric drag, solar radiation pressure, and luni-solar perturbations are compensated with orbital manoeuvres while the zonal harmonics effects are exploited to fulfil mission objectives.

In the following sections the three analytical models are described, following their implementation scheme. To consider critically inclined orbits Smith's correction was applied (see § A.6).

### 2.3.1 Aksnes zonal harmonics solution

The present method was developed by Aksnes in 1971 [26]. In this paragraph only the terms necessary for position computation are reported.

Given the initial mean Keplerian elements ( $a_0, e_0, I_0, l_0 = M_0, g_0 = \omega_0, h_0 = \Omega_0$ ) the constants in equation (2.19) are computed

$$\begin{aligned}
 c &= \frac{H}{G} = \cos(I_0) \\
 s &= \sin(I_0) \\
 \eta &= \frac{G}{L} = \sqrt{1 - e_0^2} \\
 p &= a_0 \eta^2 \\
 n_0 &= \sqrt{\frac{\mu}{a_0^3}} \\
 \gamma &= J_2 \left( \frac{R_{\oplus}}{p} \right)^2 \\
 \gamma_j &= \frac{J_j}{J_2^2} \left( \frac{R_{\oplus}}{p} \right)^{j-4}, \quad j = 3, 4, 5.
 \end{aligned} \tag{2.19}$$

The constants for periodic perturbation in equations (2.20) are computed during the initialization step as well, together with their partial derivatives with respect to  $c^2$ , in equations (2.21).

$$\begin{aligned}
 \bar{A}_1 &= 15 \gamma_5 (1 - 14c^2 + 21c^4) (1 - 5c^2)^{-1} \\
 A_1 &= 16 \gamma_3 + \frac{4}{3} \bar{A}_1 \\
 A_2 &= [1 - 15c^2 + 5\gamma_4 (1 - 7c^2)] (1 - 5c^2)^{-1} \\
 A_3 &= -\frac{35}{18} \gamma_5 (1 - 9c^2) (1 - 5c^2)^{-1}
 \end{aligned} \tag{2.20}$$

$$\begin{aligned}
\bar{A}'_1 &= [5\bar{A}_1 - 210\gamma_5 (1 - 3c^2)] (1 - 5c^2)^{-1} \\
A'_1 &= \frac{4}{3}\bar{A}'_1 \\
A'_2 &= [5A_2 - 15 - 35\gamma_4] (1 - 5c^2)^{-1} \\
A'_3 &= \left[ 5A_3 + \frac{35}{2}\gamma_5 \right] (1 - 5c^2)^{-1} .
\end{aligned} \tag{2.21}$$

The constant rates for the variables  $l$ ,  $g$  and  $h$  are

$$\begin{aligned}
\dot{l} = n_0 \left\{ 1 - \frac{3}{4}\gamma\eta \left[ 1 - 3c^2 - \frac{1}{32}\gamma \{ 10(1 - 6c^2 + 13c^4) - 5(5 - 18c^2 + 5c^4) e_0^2 + \right. \right. \\
\left. \left. + 16\eta(1 - 6c^2 + 9c^4) - 15\gamma_4(3 - 30c^2 + 35c^4) e_0^2 \} \right] \right\}
\end{aligned} \tag{2.22}$$

$$\begin{aligned}
\dot{g} = -\frac{3}{4}\gamma n_0 \left[ 1 - 5c^2 + \frac{1}{32}\gamma \{ 2(5 + 43c^2)(1 - 5c^2) + (25 - 126c^2 + 45c^4) e_0^2 + \right. \\
\left. - 24\eta(1 - 8c^2 + 15c^4) + 20\gamma_4(3 - 36c^2 + 49c^4) + 45\gamma_4(1 - 14c^2 + 21c^4) e_0^2 \} \right]
\end{aligned} \tag{2.23}$$

$$\begin{aligned}
\dot{h} = -\frac{3}{2}\gamma c n_0 \left[ 1 - \frac{1}{16}\gamma \{ 4 - 40c^2 - (9 - 5c^2) e_0^2 + 12\eta(1 - 3c^2) + \right. \\
\left. - 5\gamma_4(3 - 7c^2)(2 + 3e_0^2) \} \right] .
\end{aligned} \tag{2.24}$$

The mean values of the Delaunay's variables  $l$ ,  $g$  and  $h$  are given by

$$\begin{aligned}
h &= h_0 + \dot{h} t \\
g &= g_0 + \dot{g} t \\
l &= l_0 + \dot{l} t ,
\end{aligned} \tag{2.25}$$

where  $t$  is time since epoch. Periodic perturbations are written using Hill's variables, that can be obtained from Delaunay's elements with (2.26)

$$\begin{aligned}
E - e \sin(E) &= l \\
r \sin(\nu) &= a\eta \sin E \\
r \cos(\nu) &= a(\cos(E) - e) \\
u &= g + \nu .
\end{aligned} \tag{2.26}$$

The periodic variations of mean Hill's variables are listed in Eqs. (2.27)-(2.31)

$$\begin{aligned}
\delta r = \frac{\gamma P}{32} \left[ 8(1 - 3c^2) \left\{ 1 + (1 + \eta)^{-1} e_0 \cos(\nu) - (A_1 + 2e_0^2 \bar{A}_1) s \cos(u) + \right. \right. \\
\left. \left. - \bar{A}_1 s e_0^2 \cos(u - 2\nu) - 3A_3 s^3 e_0^2 \cos(3u - 2\nu) \right\} \right]
\end{aligned} \tag{2.27}$$

$$\begin{aligned} \delta G = \frac{\gamma p}{32} & \left[ 8(1-3c^2) \left\{ 1 + (1+\eta)^{-1} e_0 \cos(\nu) + 2\eta \frac{r}{p} \right\} + 8s^2 \cos(2u) + \right. \\ & - 2A_2 s^2 e_0 \cos(2u - \nu) + (A_1 + 2e_0^2 \bar{A}_1) s \sin(u) - \bar{A}_1 s e_0^2 \sin(u - 2\nu) + \\ & \left. + 3A_3 s^3 e_0^3 \sin(3u - 3\nu) \right] \end{aligned} \quad (2.28)$$

$$\delta H = 0 \quad (2.29)$$

$$\begin{aligned} \delta u = -\frac{\gamma}{32} & \left[ 24(1-5c^2)(\nu - l) + 16 \left\{ 1 - 6c^2 + (1-3c^2)(1+\eta)^{-1} \right\} e_0 \sin(\nu) + \right. \\ & + 4(1-3c^2)(1+\eta)^{-1} e_0^2 \sin(2\nu) - \{4 - 28c^2 + A_2 s^2 e_0^2\} \sin(2u) + \\ & - 4(4 - 10c^2 + A_2 s^2) e_0 \sin(2u - \nu) + 8c^2 e_0 \sin(2u + \nu) + \\ & + 2(A_2' s^2 - A_2) c^2 e_0^2 \sin(2u - 2\nu) - (2A_1 + 4\bar{A}_1 e_0^2) s \cos(u) + \\ & - \left\{ (A_1 + \bar{A}_1 e_0^2) \left( -\frac{3}{2} + c^2 s^{-2} \right) - 2(A_1' + \bar{A}_1' e_0^2) c^2 + 32\gamma_3 - \frac{8}{3}\bar{A}_1 + \right. \\ & \left. + \bar{A}_1 e_0^2 \right\} s e_0 \cos(u - \nu) - 2\bar{A}_1 s e_0^2 \cos(u - 2\nu) - \frac{1}{2} (A_1 + 2\bar{A}_1 e_0^2) s e_0 \cos(u + \nu) + \\ & - \frac{1}{2} \bar{A}_1 s e_0^3 \cos(u - 3\nu) - \frac{3}{2} A_3 s^3 e_0^3 \cos(3u - \nu) - 6A_3 s^3 e_0^2 \cos(3u - 2\nu) + \\ & \left. + \left\{ \frac{1}{2} (1 - 7c^2) A_3 s + 2A_3' c^2 s^3 \right\} e_0^3 \cos(3u - 3\nu) \right] \end{aligned} \quad (2.30)$$

$$\begin{aligned} \delta h = -\frac{\gamma c}{16} & \left[ 24(\nu - l) + 24e_0 \sin(\nu) - 12 \sin(2u) - 12e_0 \sin(2u - \nu) + \right. \\ & - 4e_0 \sin(2u + \nu) + (A_2 - A_2' s^2) e_0^2 \sin(2u - 2\nu) - \left\{ (A_1' + \bar{A}_1' e_0^2) s + \right. \\ & \left. - \frac{1}{2} (A_1 + \bar{A}_1 e_0^2) s^{-1} \right\} e_0 \cos(u - \nu) + \left\{ \frac{3}{2} A_3 s - A_3' s^3 \right\} e_0^3 \cos(3u - 3\nu) \right]. \end{aligned} \quad (2.31)$$

The perturbed values of Hill's variables are obtained by adding the correspondent variations where  $u, \nu$  are function of time  $t$ . Longitude  $\tilde{\lambda}$  and latitude  $\tilde{\varphi}$ , measured respectively from the Vernal point meridian and the equator, are obtained through the following steps

$$I = \arccos \left( \frac{H}{G} \right)$$

$$\tilde{\varphi} = \arcsin (\sin(I) \cos(u))$$

$$\tilde{\lambda} = \arctan \left( \frac{\cos(I) \sin(u)}{\cos(u)} \right) + h .$$

In case the inclination  $I$  is very small, the expression of  $\delta u$  and  $\delta h$  became singular due to  $s^{-1}$

coefficients. For this reason, if  $s < \gamma$ , the periodic perturbation are applied directly to latitude and longitude using Eq. (2.32)

$$\delta \sin \tilde{\varphi} = \frac{1}{32} \gamma (A_1 + \bar{A}_1 e_0^2) e_0 \cos(\nu) \quad (2.32)$$

$$\delta \tilde{\lambda} = \delta u + \delta h ,$$

where terms factored by  $s^{-1}$  are dropped in the addition of  $\delta u$  and  $\delta h$ .

The position in ECI is obtained by means of

$$\mathbf{r} = r \hat{\mathbf{u}} , \quad (2.33)$$

where

$$\hat{\mathbf{u}} = \begin{Bmatrix} \cos(\tilde{\lambda}) \cos(\tilde{\varphi}) \\ \sin(\tilde{\lambda}) \cos(\tilde{\varphi}) \\ \sin(\tilde{\varphi}) \end{Bmatrix} . \quad (2.34)$$

### Model validation

The code derived from Asknes' analytical solution has been validated through two test-cases and also compared to numerical solution. The first test case is a Molniya orbit. This family of orbits is highly elliptical, is critically inclined ( $I \approx 63.4$  deg or  $I = 116.6$  deg), and has an orbital period of half sidereal day (Fig. 2.4). The perturbative effect of  $J_2$  on the argument of perigee at such an inclination can be neglected and hence  $\omega$  remains constant.

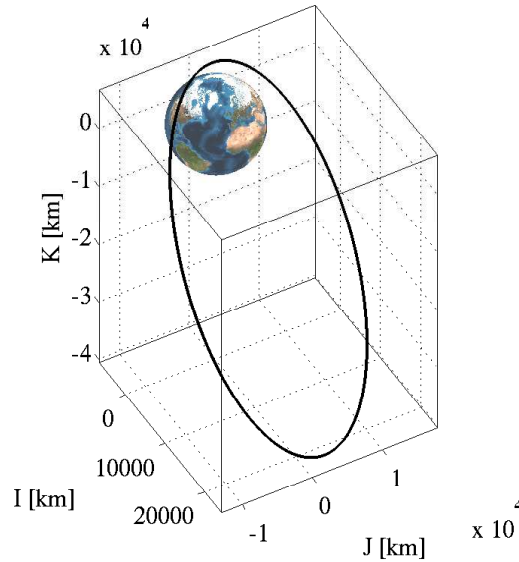


**Figure 2.4:** Molniya orbit ( $a'_0 = 26562$  km,  $e'_0 = 0.73$ ,  $I'_0 = 63.434$  deg,  $\Omega'_0 = 127$  deg,  $\omega'_0 = 80$  deg)

The temporal variation of the argument of pericentre of a Molniya orbit obtained with Aksnes model is plotted in Figure 2.5. The rate of variation is small and it is connected with the higher zonal harmonics.

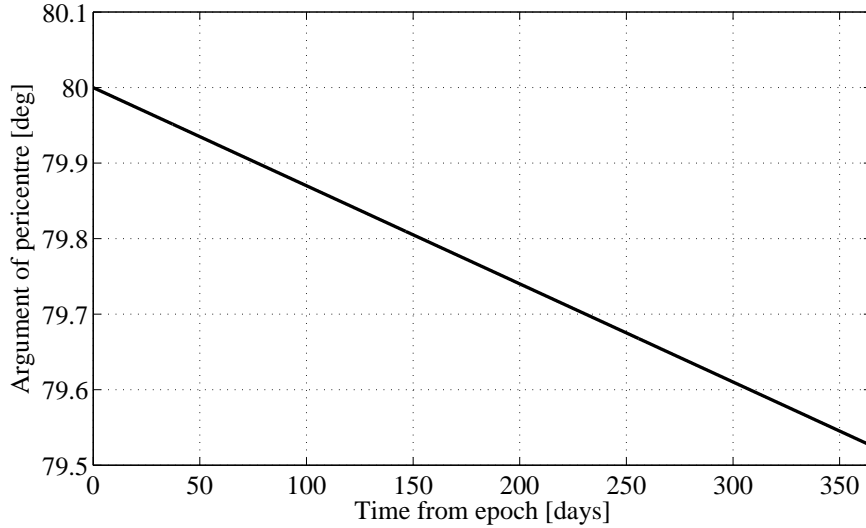


**Figure 2.5:** Molniya orbit yearly variation of the argument of pericentre  $\omega$

The second test-case is a Sun-Synchronous orbit. The perturbative effect of the second zonal harmonics is exploited to obtain a rate of 360 deg/year for the orbit RAAN. This can be achieved by choosing a proper inclination (usually around 90 deg) given semi-major axis and eccentricity of the orbit. The sun-synchronous orbit used for this validation is represented in Figure 2.6.

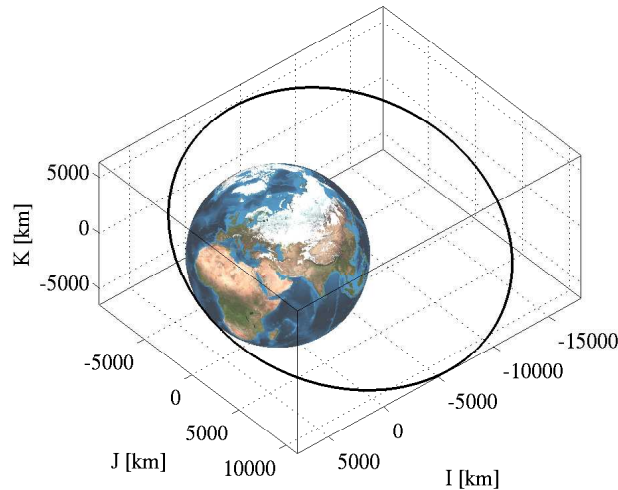


**Figure 2.6:** Sun-synchronous orbit ( $a'_0 = 12952$  km,  $e'_0 = 0.4$ ,  $I'_0 = 151.8$  deg,  $\Omega'_0 = 10$  deg,  $\omega'_0 = 20$  deg )

The behaviour of the right ascension of the ascending node for an year is graphed in Figure 2.7. As expected the RAAN variation is approximately 365 deg.

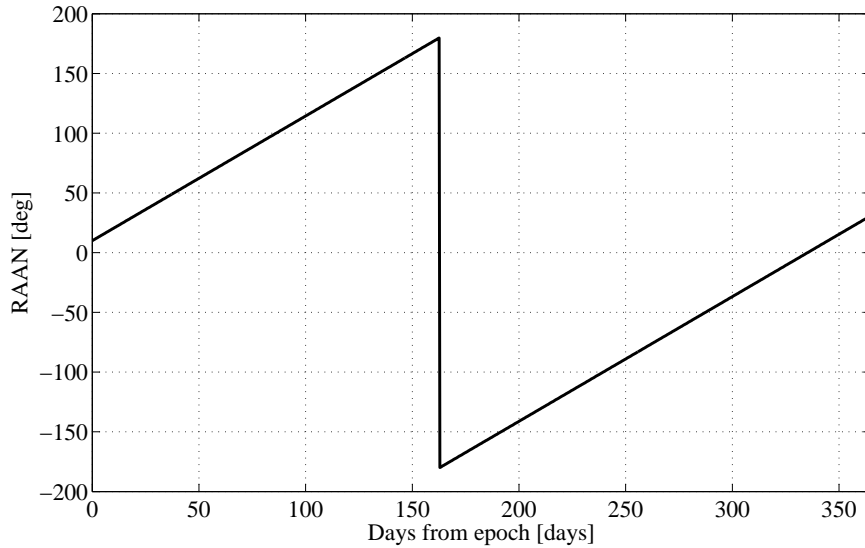


**Figure 2.7:** Aksnes solution: Sun-synchronous orbit RAAN yearly variation

The same Sun-synchronous orbit of Figure 2.6 was compared to a numerical solution obtained by means of GMAT software [50]. The error between the two computed position is graphed in Figure 2.8.

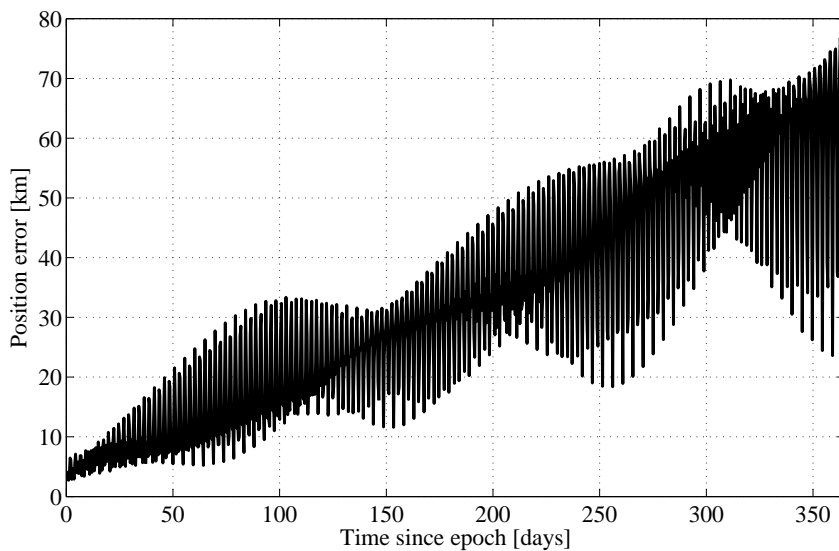
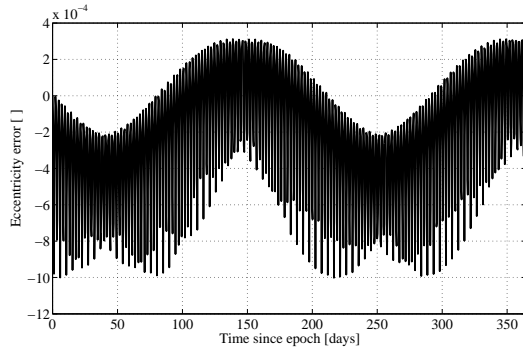


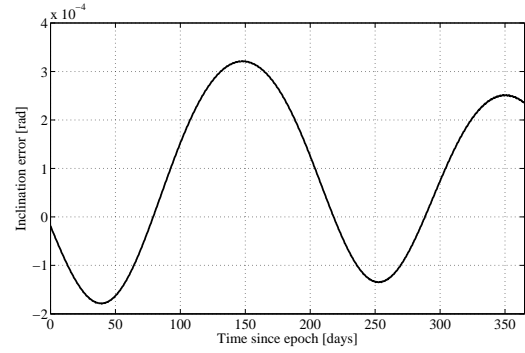
**Figure 2.8:** Aksnes solution: difference between analytical and numerical positions

The difference between the two steadily solutions grows with time, anyway the analytical solution

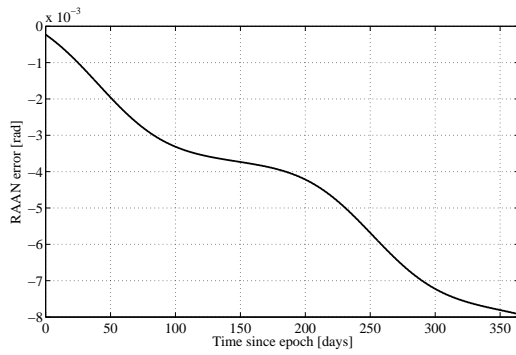
shows good accordance with the numerical one in the considered time interval (1 year). The errors of inclination, eccentricity, RAAN, argument of the pericentre and mean anomaly are reported in Figure 2.9.



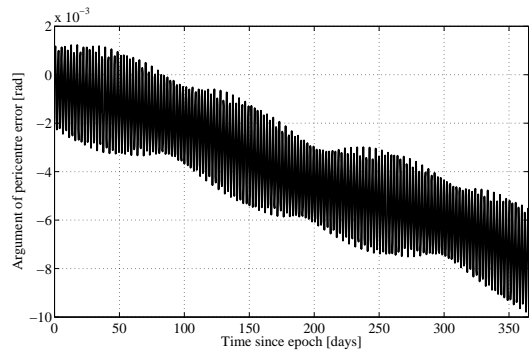
(a) Eccentricity



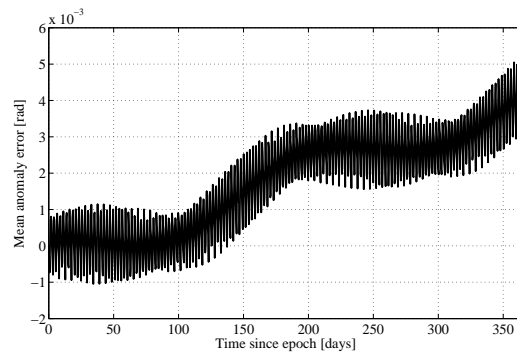
(b) Inclination



(c) RAAN



(d) Argument of pericentre



(e) Mean anomaly

**Figure 2.9:** Aksnes solution: differences between numerical and analytical keplerian elements

### 2.3.2 HANDE

The following passages can be found in [33] and [32], where the mathematical procedure for the formulation of the analytical solution can be found as well. Only the passages for position computation are reported here. The first step is the initialization of the method. To perform this operation the mean Keplerian elements at epoch are required together with satellite ballistic coefficient  $B$ . The aim of the initialization is computing the secular variations of the six Keplerian elements due to atmospheric drag as well as the derivatives of mean motion  $n$  and eccentricity  $e$ . The first derivatives of mean motion and eccentricity are equal to the following integrals, also called *drag functions*

$$f_{n,D}^{(2)} = \frac{1}{2\pi} \int_{-\pi}^{\pi} \frac{3}{2} B n \beta^{-2} \rho v \left[ 1 + e^2 + 2e \cos(\nu) - \frac{\omega_a}{n} \beta^3 \cos(I) \right] dM \quad (2.35)$$

$$f_{e,D}^{(2)} = -\frac{1}{2\pi} \int_{-\pi}^{\pi} \frac{1}{2} B \rho v \left[ 2(e + \cos(\nu)) - \frac{\omega_a}{n} \beta^3 \cos(I) \frac{(2 \cos(\nu) + e + e \cos^2(\nu))}{(1 + e \cos(\nu))^2} \right] dM ,$$

where  $\omega_a$  is the rotational velocity of Earth atmosphere,  $\beta = \sqrt{1 - e^2}$ ,  $\rho$  is the atmospheric density at the satellite altitude above Earth surface, hence a function of true anomaly  $\nu$ . The satellite velocity  $v$ , with respect to atmosphere, is given by

$$v = \frac{n a}{\beta} \sqrt{(1 + e^2 + 2e \cos(\nu)) - 2 \frac{\omega_a}{n} \beta^3 \cos(I) + \frac{\omega_a^2}{n^2} \beta^6 \frac{1 - \sin^2(I) \sin^2(u)}{(1 + e \cos(\nu))^2}} . \quad (2.36)$$

The integration is facilitated by the change of variables

$$dM = \frac{\beta^3}{(1 + e \cos(\nu))^2} d\nu .$$

The integrals are evaluated using a 13-points Gauss-Legendre formula (see § B.2). In this approach there is no constraint on the choice of the density model, that can be both mathematical (e.g power density or power function) or tabulated. Also the higher-order derivatives are obtained numerically, using a 7-points central difference formula. Hence, values of  $n$ ,  $\dot{n}$ ,  $e$ , and  $\dot{e}$  at the instants  $\pm 3\tau$ ,  $\pm 2\tau$ ,  $\pm \tau$  as well as their values at epoch are required. Denoting mean anomaly and eccentricity, as well as their first derivatives at epoch, with a subscript 0, the values at  $\pm \tau$  are

$$n_{\pm\tau} = n_0 \pm \dot{n}_0 \tau$$

$$e_{\pm\tau} = e_0 \pm \dot{e}_0 \tau .$$

Given the values of  $n$  and  $e$  at time  $\pm \tau$ , the derivatives  $\dot{n}_{\pm\tau}$  and  $\dot{e}_{\pm\tau}$  are obtained evaluating integrals (2.35) with the updated values of mean motion and eccentricity. The values at the other instants can be obtained using the same strategy. When all 7 values of eccentricity and mean motion are available the derivatives  $\dot{e}$ ,  $\ddot{e}$ ,  $\ddot{n}$  and  $\ddot{n}$  can be computed using formulae in Section B.1. To compute  $\ddot{n}$  the formula for the third derivative should be employed, using the first derivatives of  $n$  at times  $\pm 3\tau$ ,  $\pm 2\tau$ ,  $\pm \tau$ .

The secular variation of the other four Keplerian elements can be computed from the drag functions

$$f_{I,D}^{(2)} = -\frac{1}{2} \int_{-\pi}^{\pi} \frac{1}{2} B \rho v \frac{\omega_a}{n} \beta^{-1} \sin(I) \frac{r^2}{a^2} \cos^2(u) dM \quad (2.37)$$

$$f_{\omega,D}^{(2)} = \frac{1}{2} \int_{-\pi}^{\pi} \left[ \frac{1}{2} B \rho v \frac{\omega_a}{n \beta} \cos(I) \frac{r^2}{a^2} (\sin(\nu) \cos(\nu) + \sin(u) \cos(u)) \Delta M_D \right] dM \quad (2.38)$$

$$f_{\Omega,D}^{(2)} = -\frac{1}{2\pi} \int_{-\pi}^{\pi} \frac{1}{2} B \rho v \frac{\omega_a}{n} \beta^{-1} \frac{r^2}{a^2} \sin(u) \cos(u) dM \quad (2.39)$$

$$f_{M,D}^{(2)} = \frac{1}{2} \int_{-\pi}^{\pi} \left[ \frac{1}{2} B \rho v \left\{ 2e \sin(E) - \frac{2e}{1+\beta} \sin(\nu) + \right. \right. \\ \left. \left. - \frac{\omega_a}{n} \cos(I) \frac{r^2}{a^2} \left[ \frac{-2e}{\beta(1+\beta)} + \cos(\nu) \right] \sin(f) \right\} + \Delta M_D \right] dM, \quad (2.40)$$

where  $u = \nu + \omega$ ,  $E(\nu)$  is the eccentric anomaly  $r(\nu)$  the orbit radius and

$$\Delta M_D = B \rho v \left[ 1 - \frac{\omega_a}{n \beta} \cos(I) \frac{r^2}{a^2} \right] \frac{\sin(\nu)}{e}.$$

When  $e \rightarrow 0$  the values of  $\Delta M_D$  becomes singular, due to arbitrary definition of the location of perigee in circular orbits. Since this term exactly vanishes in the sum  $M + \omega$ , numerical singularities are avoided setting  $\Delta M_D = 0$  when  $e < 1 \times 10^{-6}$ .

For highly eccentric orbits density decreases rapidly away from the pericentre. In this case the integrals can be approximated by

$$I = \frac{1}{2\pi} \int_{-\pi}^{\pi} f(\nu) d\nu \simeq \frac{1}{2\pi} \int_{-b}^b f(\nu) d\nu.$$

The value  $b$  can be computed by means of

$$\cos(b) = \frac{ae(1-e) - \Delta r}{ae(1-e) + e\Delta r} \quad \text{for } \Delta r < 2ae$$

$$\cos(b) = -1 \quad \text{for } \Delta r \geq 2ae,$$

with

$$\begin{aligned}\Delta r &= q [A_0 + A_1 q + A_2 q^2 + A_3 q^3 + A_4 q^4 + A_5 q^5 + A_6 q^6] \\ q &= a_0 (1 - e_0) - R_{\oplus} \\ A_0 &= -3.1301240 \\ A_1 &= 6.1710434 \times 10^{-2} \\ A_2 &= -3.4111266 \times 10^{-4} \\ A_3 &= 8.7321429 \times 10^{-7} \\ A_4 &= -1.1225340 \times 10^{-9} \\ A_5 &= 7.1123451 \times 10^{-13} \\ A_6 &= -1.7765750 \times 10^{-16},\end{aligned}$$

where  $q$  is perigee height above Earth's mean surface in kilometres and  $\Delta r$  is the altitude change in kilometres for a drop in density by a factor 100. This approximation avoids the under-estimation of Keplerian elements secular rates that would occur computing numerically the integrals on the whole domain  $[-\pi, \pi]$ .

The total secular rates of Keplerian elements due to zonal harmonics and drag are computed using equations (2.41)-(2.44)

$$\dot{I}_0 = f_{I,D}^{(2)} \tag{2.41}$$

$$\begin{aligned}\dot{\omega}_0 &= f_{\omega,D}^{(2)} + \frac{3}{4} n_0 J_2 \left( \frac{R_{\oplus}}{p_0} \right)^2 (4 - 5 \sin^2(I_0)) + \frac{3}{16} n_0 J_2^2 \left( \frac{R_{\oplus}}{p_0} \right)^4 \left[ (4 - 5 \sin^2(I_0)) \left( 12 + \right. \right. \\ &\quad \left. \left. - \frac{43}{4} \sin^2(I_0) + 6\beta_0 \left( 1 - \frac{3}{2} \sin^2(I_0) \right) \right) + \left( 7 - \frac{9}{2} \sin^2(I_0) - \frac{45}{8} \sin^4(I_0) \right) e_0^2 \right] + \\ &\quad - \frac{15}{32} n_0 J_4 \left( \frac{R_{\oplus}}{p_0} \right)^4 \left[ 16 - 62 \sin^2(I_0) + 49 \sin^4(I_0) + \right. \\ &\quad \left. \left( 18 - 63 \sin^2(I_0) + \frac{189}{4} \sin^4(I_0) \right) e_0^2 \right] \tag{2.42}\end{aligned}$$

$$\begin{aligned}\dot{\Omega}_0 &= f_{\Omega,D}^{(2)} - \frac{3}{2} n_0 J_2 \left( \frac{R_{\oplus}}{p_0} \right)^2 \cos(I_0) - \frac{3}{8} n_0 J_2^2 \left( \frac{R_{\oplus}}{p_0} \right)^4 \cos(I_0) \left[ 9 - 10 \sin^2(I_0) + \right. \\ &\quad \left. + e_0^2 \left( 1 + \frac{5}{4} \sin^2(I_0) \right) + 6\beta_0 \left( 1 - \frac{3}{2} \sin^2(I_0) \right) \right] + \\ &\quad + \frac{15}{16} n_0 J_4 \left( \frac{R_{\oplus}}{p_0} \right)^4 \cos(I_0) (4 - 7 \sin^2(I_0)) \left( 1 + \frac{3}{2} e_0^2 \right) \tag{2.43}\end{aligned}$$

$$\begin{aligned}
\dot{M}_0 = & f_{M,D}^{(2)} + \frac{3}{2}n_0 J_2 \beta_0 \left( \frac{R_\oplus}{p_0} \right)^2 \left( 1 - \frac{3}{2} \sin^2(I_0) \right) + \\
& + \frac{3}{8}n_0 J_2^2 \beta_0^{-1} \left( \frac{R_\oplus}{p_0} \right)^4 \left[ 4\beta_0^3 \left( 1 - \frac{3}{2} \sin^2(I_0) \right)^2 + 14 - 35 \sin^2(I_0) + \right. \\
& + \frac{103}{4} \sin^4(I_0) + \left. \left( 2 - 5 \sin^2(I_0) + \frac{49}{4} \sin^4(I_0) \right) e_0^4 + \right. \\
& + \left. \left( -\frac{23}{8} + \frac{5}{8} \sin^2(I_0) + \frac{403}{64} \sin^4(I_0) \right) e_0^4 \right] + \\
& - \frac{45}{128}n_0 J_4 \left( \frac{R_\oplus}{p_0} \right)^4 e_0^2 \beta_0 (8 - 40 \sin^2(I_0) + 35 \sin^4(I_0)) .
\end{aligned} \tag{2.44}$$

The constants of the long-period periodic variation of the osculating Keplerian elements are computed as well, since they depend only on the mean elements at epoch:

$$e_{LP_1} = C_1 e_0 \beta_0^2 \sin^2(I_0) \tag{2.45}$$

$$e_{LP_2} = -C_2 \beta_0^2 \sin(I_0) \tag{2.46}$$

$$I_{LP_1} = -C_1 e_0^2 \sin(I_0) \cos(I_0) \tag{2.47}$$

$$I_{LP_2} = C_2 e_0 \cos(I_0) \tag{2.48}$$

$$\begin{aligned}
\omega_{LP_1} = & -C_1 \left( \sin^2(I_0) - e_0^2 + \frac{9}{2}e_0^2 \sin^2(I_0) \right) + \\
& - \frac{1}{8}J_2 \left( \frac{R_\oplus}{p_0} \right)^2 \frac{1}{4 - 5 \sin^2(I_0)} (e_0^2 \sin^2(I_0)) \left( 1 + 5 \frac{J_4}{J_2^2} \right)
\end{aligned} \tag{2.49}$$

$$\omega_{LP_2} = -C_2 e_0 \sin(I_0) \frac{35 \cos^2(I_0)}{4 - 5 \sin^2(I_0)} + \Delta\omega - \Delta M \tag{2.50}$$

$$\Omega_{LP_1} = -C_1 e_0^2 \cos(I_0) + \frac{5}{8}J_2 \left( \frac{R_\oplus}{p_0} \right)^2 \frac{1}{4 - 5 \sin^2(I_0)} (e_0^2 \cos(I_0) \sin^2(I_0)) \left( 3 + 7 \frac{J_4}{J_2^2} \right) \tag{2.51}$$

$$\Omega_{LP_2} = \frac{C_2}{4 - 5 \sin^2(I_0)} e_0 \sin(I_0) \left[ 15 \cos(I_0) + \frac{4}{1 + \cos(I_0)} \right] - \Delta\omega \tag{2.52}$$

$$\begin{aligned}
M_{LP_1} = & C_1 \beta_0 \sin^2(I_0) + \frac{1}{8}J_2 \left( \frac{R_\oplus}{p_0} \right)^2 \frac{1}{4 - 5 \sin^2(I_0)} (e_0^2 \beta^{-1} \sin^2(I_0)) \left( -75 + \right. \\
& + \left. \frac{127}{2} \sin^2(I_0) + 138e_0^2 - \frac{5083}{32}e_0^2 \sin^2(I_0) \right)
\end{aligned} \tag{2.53}$$

$$M_{LP_2} = \frac{27}{128}J_2 \left( \frac{R_\oplus}{p_0} \right)^2 \frac{e_0^4 \beta_0^{-1} \sin^4(I_0)}{4 - 5 \sin^2(I_0)} \tag{2.54}$$

$$M_{LP_3} = -C_2 e_0 \left[ \frac{1}{1 + \beta} + 4\beta \right] \sin(I_0) + \Delta M, \quad (2.55)$$

where the constants  $C_1$ ,  $C_2$ ,  $\Delta M$  and  $\Delta\omega$  are defined as

$$C_1 = \frac{1}{8} J_2 \left( \frac{R_\oplus}{p_0} \right)^2 \frac{1}{4 - 5 \sin^2(I_0)} \left[ 14 - 15 \sin^2(I_0) + \frac{J_4}{J_2^2} (30 - 35 \sin^2(I_0)) \right] \quad (2.56)$$

$$C_2 = \frac{1}{2} \frac{J_3}{J_2} \left( \frac{R_\oplus}{p_0} \right) \quad (2.57)$$

$$\begin{cases} \Delta M = \frac{\sin(I_0)}{e_0} & \text{if } e_0 \geq 1 \times 10^{-6} \\ \Delta M = 0 & \text{if } e_0 < 1 \times 10^{-6} \end{cases} \quad (2.58)$$

$$\begin{cases} \Delta\omega = C_2 \frac{4e_0}{\sin(I_0)} \frac{1}{4 - 5 \sin^2(I_0)} & \text{if } I_0 \geq 1 \times 10^{-6} \\ \Delta\omega = 0 & \text{if } I_0 < 1 \times 10^{-6}. \end{cases} \quad (2.59)$$

The last constants computed during initialization are

$$\frac{\dot{\beta}_0}{\beta_0} = -\frac{e_0 \dot{e}_0}{\beta_0^2} \quad (2.60)$$

$$\frac{\ddot{\beta}_0}{\beta_0} = -\frac{1}{\beta_0^4} (\dot{e}_0^2 + e_0 \ddot{e}_0 \beta_0^2) \quad (2.61)$$

$$D_{1,-3} = \frac{1}{2} \left( \frac{7 \dot{n}_0}{3 n_0} - 3 \frac{\dot{\beta}_0}{\beta_0} \right) \quad (2.62)$$

$$D_{1,-4} = \frac{1}{2} \left( \frac{7 \dot{n}_0}{3 n_0} - 4 \frac{\dot{\beta}_0}{\beta_0} \right) \quad (2.63)$$

$$D_{2,-3} = \frac{1}{6} \left( \frac{28 \dot{n}_0^2}{9 n_0^2} + \frac{7 \ddot{n}_0}{3 n_0} - 14 \frac{\dot{n}_0 \dot{\beta}_0}{n_0 \beta_0} + 12 \frac{\dot{\beta}_0^2}{\beta_0^2} - 3 \frac{\ddot{\beta}_0}{\beta_0} \right) \quad (2.64)$$

$$D_{2,-3} = \frac{1}{6} \left( \frac{28 \dot{n}_0^2}{9 n_0^2} + \frac{7 \ddot{n}_0}{3 n_0} - \frac{56 \dot{n}_0 \dot{\beta}_0}{3 n_0 \beta_0} + 20 \frac{\dot{\beta}_0^2}{\beta_0^2} - 4 \frac{\ddot{\beta}_0}{\beta_0} \right). \quad (2.65)$$

The second step of the method consists in applying both secular and long period periodic variation of the mean elements, through the equations

$$n' = n_0 + \dot{n}_0 t + \frac{1}{2} \ddot{n}_0 t^2 + \frac{1}{6} \dddot{n}_0 t^3 + \frac{1}{24} \ddddot{n}_0 t^4 \quad (2.66)$$

$$\omega_{\text{sec}} = \omega_0 + \dot{\omega}_0 t \quad (2.67)$$

$$e' = e_0 + \dot{e}_0 t + \frac{1}{2} \ddot{e}_0 t^2 + \frac{1}{6} \dddot{e}_0 t^3 + e_{LP_1} (\cos^2(\omega_{\text{sec}}) - \cos^2(\omega_0)) + e_{LP_2} (\sin(\omega_{\text{sec}}) - \sin(\omega_0)) \quad (2.68)$$

$$I' = I_0 + \dot{I}_0 t + I_{LP_1} (\cos^2(\omega_{\text{sec}}) - \cos^2(\omega_0)) + I_{LP_2} (\sin(\omega_{\text{sec}}) - \sin(\omega_0)) \quad (2.69)$$

$$\begin{aligned} \Omega' = \Omega_0 + \dot{\Omega}_0 t + \Omega_{LP_1} (\sin(\omega_{\text{sec}}) \cos(\omega_{\text{sec}}) - \sin(\omega_0) \cos(\omega_0)) + \\ + \Omega_{LP_2} (\cos(\omega_{\text{sec}}) - \cos(\omega_0)) - \frac{3}{2} n_0 J_2 \left( \frac{R_{\oplus}}{p_0} \right)^2 \cos(I_0) (D_{1,-4} t^2 + D_{2,-4} t^3) \end{aligned} \quad (2.70)$$

$$\begin{aligned} M' = M_0 + (n_0 + \dot{M}_0) t + \frac{1}{2} \dot{n}_0 t^2 + \frac{1}{6} \ddot{n}_0 t^3 + \frac{1}{24} \ddot{n}_0 t^4 + \frac{1}{120} \ddot{n}_0 t^5 + \\ + M_{LP_1} (\sin(\omega_{\text{sec}}) \cos(\omega_{\text{sec}}) - \sin(\omega_0) \cos(\omega_0)) + \\ + M_{LP_2} (\sin(\omega_{\text{sec}}) \cos^3(\omega_{\text{sec}}) - \sin(\omega_0) \cos^3(\omega_0)) + M_{LP_3} (\cos(\omega_{\text{sec}}) - \cos(\omega_0)) + \\ + \frac{3}{2} n_0 J_2 \beta_0 \left( \frac{R_{\oplus}}{p_0} \right)^2 \left( 1 - \frac{3}{2} \sin^2(I_0) \right) (D_{1,-3} t^2 + D_{2,-3} t^3) \end{aligned} \quad (2.71)$$

$$\omega' = \omega_{\text{sec}} + \omega_{LP_1} (\sin(\omega_{\text{sec}}) \cos(\omega_{\text{sec}}) \sin(\omega_0) \cos(\omega_0)) + \omega_{LP_2} (\cos(\omega_{\text{sec}}) - \cos(\omega_0)) . \quad (2.72)$$

From the primed variables computed above the following change of variables are made

$$a' = \left( \frac{\mu_{\oplus}}{n'^2} \right)^{\frac{1}{3}} \quad (2.73)$$

$$\beta' = \sqrt{1 - e'^2} \quad (2.74)$$

$$p' = a' \beta'^2 \quad (2.75)$$

$$u' = \nu' + \omega' \quad (2.76)$$

$$r' = \frac{a' \beta'^2}{1 + e' \cos(\nu')} , \quad (2.77)$$

where  $\nu'$  is the true anomaly corresponding to  $M'$  and  $e'$ .

The osculating state is obtained adding short period variation to primed variables

$$\begin{aligned} r &= r' + \delta r \\ u &= u' + \delta u \\ I &= I' + \delta I \\ \Omega &= \Omega' + \delta \Omega , \end{aligned} \quad (2.78)$$

where

$$\delta r = -\frac{1}{2} J_2 \frac{R_{\oplus}^2}{p'} \left( 1 - \frac{3}{2} \sin^2(I') \right) \left[ 1 + \frac{2r'}{a' \beta'} + \frac{e' \cos(\nu')}{1 + \beta'} \right] + \frac{1}{4} J_2 \frac{R_{\oplus}^2}{p'} \sin^2(I') \cos(2u') \quad (2.79)$$

$$\begin{aligned}
\delta u = & \frac{1}{2} J_2 \left( \frac{R_{\oplus}}{p'} \right)^2 \left( 1 - \frac{3}{2} \sin^2(I') \right) (1 - \beta') \left[ \frac{e'}{1 + \beta'} + \cos(\nu') \right] + \\
& + \frac{1}{8} J_2 \left( \frac{R_{\oplus}}{p'} \right)^2 \left[ (-6 + 7 \sin^2(I')) \sin(2u') + 2e' (-3 + \right. \\
& \left. + 5 \sin^2(I')) \sin(\nu' + 2\omega') - 2e' \cos^2(I') (3\nu' + 2\omega') \right] + \\
& + \frac{3}{4} J_2 \left( \frac{R_{\oplus}}{p'} \right)^2 (4 - 5 \sin^2(I')) (\nu' - M' + E' \sin(\nu'))
\end{aligned} \tag{2.80}$$

$$\delta I = \frac{1}{4} J_2 \left( \frac{R_{\oplus}}{p'} \right)^2 \sin(I') \cos(I') \left[ 3 \cos(2\nu') + 3e' \cos(\nu' + 2\omega') + e' \cos(3\nu' + 2\omega') \right] \tag{2.81}$$

$$\begin{aligned}
\delta \Omega = & -\frac{1}{4} J_2 \left( \frac{R_{\oplus}}{p'} \right)^2 \cos(I') \left[ 6 (\nu' - M' + e' \sin(\nu')) - 3 \sin(2u') \right. \\
& \left. - 3e' \sin(\nu' + 2\omega') - e' \sin(3\nu' + 2\omega') \right] .
\end{aligned} \tag{2.82}$$

The position in Earth centred inertial reference frame is given by

$$\mathbf{r} = r \hat{\mathbf{u}} , \tag{2.83}$$

where

$$\hat{\mathbf{u}} = \left\{ \begin{array}{l} -\sin(\Omega) \cos(I) \sin(u) + \cos(\Omega) \cos(u) \\ \cos(\Omega) \cos(I) \sin(u) + \sin(\Omega) \cos(u) \\ \sin(I) \sin(u) \end{array} \right\} . \tag{2.84}$$

### Model validation

The HANDE algorithm was tested on two LEO orbits to observe orbital decay. The orbit altitude variation during a time interval of one year is plotted in Figure 2.10. The density model used for this simulation is exponential, with a reference altitude of 550 km (Tab. A.7).

The secular trend of semi-major axis variation was extracted from these data and compared with a numerical simulation performed with numerical integrator HPOP embedded in STK software. The density model selected in STK is Jacchia-Roberts [51]. The trends are compared in Figure 2.11.

The analytical model under-estimates the orbital decay and this is mainly due to the different density representations. The difference anyway is limited to a maximum of two kilometres in one year. The effect of the atmosphere rotation is negligible as a consequence of satellite nearly polar inclination. It can be noted anyway that the atmosphere decreases satellite lifetime for orbits with inclination above 90 deg.

It is important to highlight that the difference in semi-major axis between numerical and analytical solution, although small, could result in large position error. The mean anomaly displacement between the numerical and analytical orbit increases quadratically with time and so the position error.

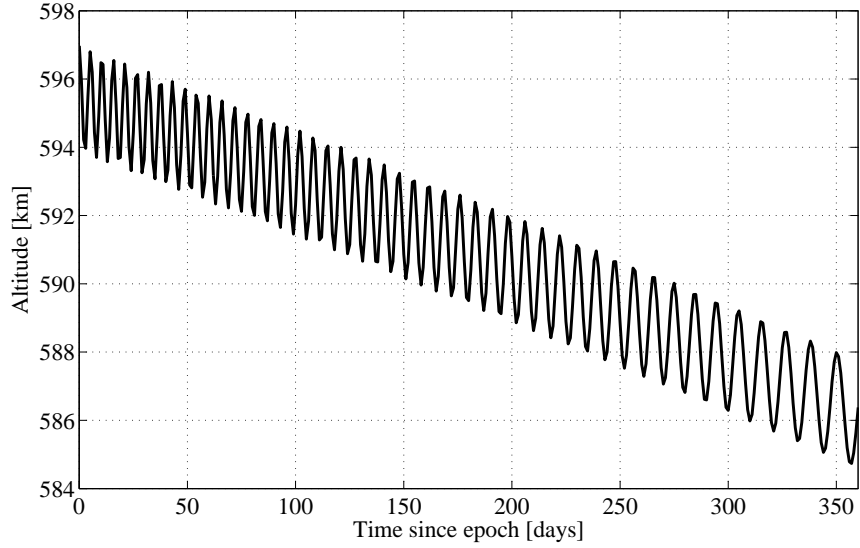


**Figure 2.10:** HANDE: orbit decaying ( $a'_0 = 6969.08$  km,  $e'_0 = 0$ ,  $I'_0 = 97.79$  deg,  $\Omega'_0 = 100.65$  deg,  $\omega'_0 = 0$  deg,  $B = 0.02$  m<sup>2</sup>/kg )

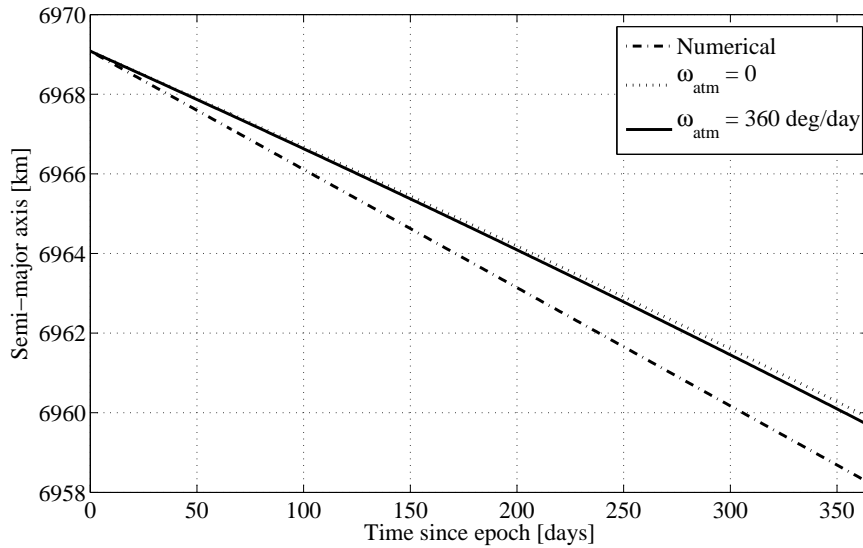


**Figure 2.11:** HANDE: numerical and analytical semi-major axis variation ( $a'_0 = 6969.08$  km,  $e'_0 = 0$ ,  $I'_0 = 97.79$  deg,  $\Omega'_0 = 100.65$  deg,  $\omega'_0 = 0$  deg,  $B = 0.02$  m<sup>2</sup>/kg )

Another comparison of numerical and analytical semi-major axis trend for a LEO eccentric orbit is graphed in Figure 2.12.

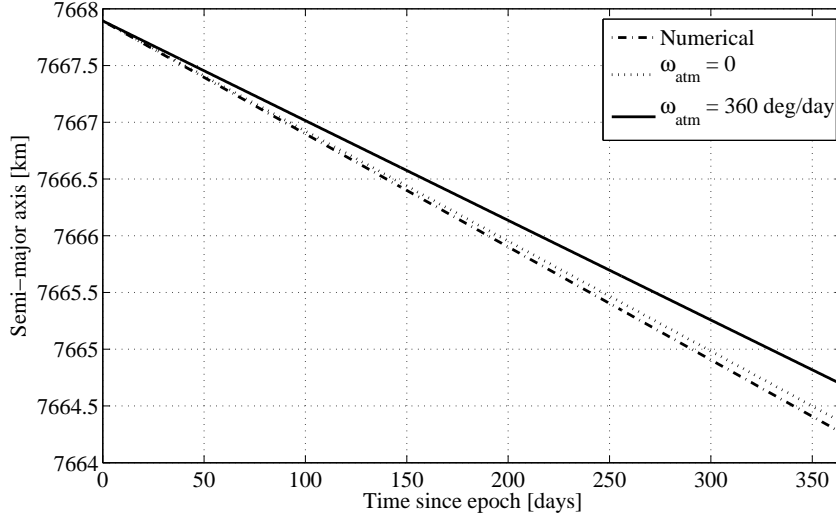


**Figure 2.12:** HANDE: numerical and analytical semi-major axis variation ( $a'_0 = 7667.89$  km,  $e'_0 = 0.1$ ,  $I'_0 = 40.0$  deg,  $\Omega'_0 = 101.0$  deg,  $\omega'_0 = 197.0$  deg,  $B = 0.02$  m<sup>2</sup>/kg )

In this case, the difference between the non-rotating analytical model and the numerical one is limited to a few tens of metres. The atmosphere rotation plays an important role at such inclination since it is subtracted from satellite velocity and hence satellite lifetime is higher.

In Figure 2.13 the RAAN variation on a time span of one year is reported. As expected, the RAAN covers nearly 360 deg. HANDE can indeed represents both the perturbative effect of zonal harmonics and drag. The errors on semi-major axis are limited to a few kilometres over one year, whereas the errors on inclination, RAAN, and argument of pericentre are of the order of  $10^{-3}$  rad. The error on eccentricity is of  $10^{-3}$ . These differences are of the same order of magnitude of Aksnes solution. Anyway, as explained above, the mean anomaly is reliable only on a time span of one month, because of the phase displacement due to the small error on semi-major axis.

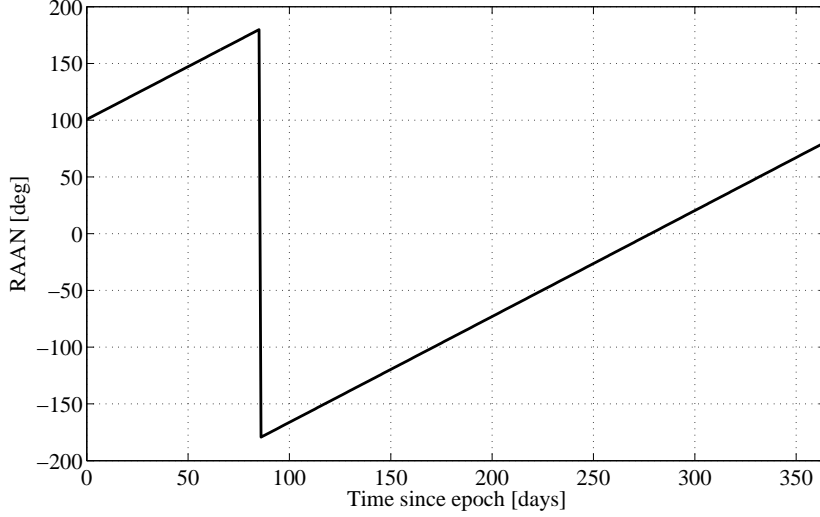


**Figure 2.13:** HANDE: Sun-synchronous orbit RAAN yearly variation ( $a'_0 = 6969.08$  km,  $e'_0 = 0$ ,  $I'_0 = 97.79$  deg,  $\Omega'_0 = 100.65$  deg,  $\omega'_0 = 0$  deg,  $B = 0.02$  m<sup>2</sup>/kg )

### 2.3.3 SGP4

The SGP4 method is described in detail in [46, 48, 47, 42, 49]. The method is optimized to work with Two-Lines Elements (TLE) maintained by the NORAD and available at Celes-Track [52] and Space-Track [11] websites. The algorithm presented in this paragraph is a simplified version of the SGP4 algorithm. All terms related to atmospheric drag have been dropped as well as effects of 12 hour resonance. This version is thus intended to be used with space debris with orbital periods larger than 225 minutes or orbiting in GEO.

The elements provided by the NORAD two line elements are written using Kozai mean motion. The first step is to recover Brower mean motion through the equations

$$a_k = \left( \frac{\mu_\oplus}{n_k^2} \right)^{\frac{1}{3}} \quad (2.85)$$

$$\delta_1 = \frac{3}{2} \frac{k_2}{a_k^2} \frac{3 \cos^2(I_0) - 1}{(1 - e_0^2)^{3/2}} \quad (2.86)$$

$$a_2 = a_1 \left( 1 - \frac{1}{3} \delta_1 - \delta_1^2 - \frac{134}{81} \delta_1^3 \right) \quad (2.87)$$

$$\delta_0 = \frac{3}{2} \frac{k_2}{a_2^2} \frac{3 \cos^2(I_0) - 1}{(1 - e_0^2)^{3/2}} \quad (2.88)$$

$$n_0 = \frac{n_k}{1 + \delta_0} \quad (2.89)$$

$$a_0 = \left( \frac{\mu_\oplus}{n_0^2} \right)^{\frac{1}{3}} . \quad (2.90)$$

where coefficient  $k_2$  is related to second zonal harmonics and is defined in Eq. (A.15).

The next step is computing the secular effects of Earth's zonal harmonics

$$\dot{M}_z = \left[ \frac{3}{2} k_2 \frac{-1 + 3 \cos^2(I_0)}{a_0^2 \beta_0^3} + \frac{3}{16} k_2^2 \frac{13 - 78 \cos^2(I_0) + 137 \cos^4(I_0)}{a_0^4 \beta_0^7} \right] n_0 \quad (2.91)$$

$$\begin{aligned} \dot{\omega}_z = & \left[ -\frac{3}{2} k_2 \frac{1 - 5 \cos^2(I_0)}{a_0^2 \beta_0^4} + \frac{3}{16} k_2^2 \frac{7 - 114 \cos^2(I_0) + 395 \cos^4(I_0)}{a_0^4 \beta_0^8} + \right. \\ & \left. + \frac{5}{4} k_4 \frac{3 - 36 \cos^2(I_0) + 49 \cos^4(I_0)}{a_0^4 \beta_0^8} \right] n_0 \end{aligned} \quad (2.92)$$

$$\dot{\Omega}_z = \left[ -3k_2 \frac{\cos(I_0)}{a_0^2 \beta_0^2} + \frac{3}{2} k_2^2 \frac{4 \cos(I_0) - 19 \cos^3(I_0)}{a_0^2 \beta_0^8} + \frac{5}{2} k_4 \cos(I_0) \frac{3 - 7 \cos^2(I_0)}{a_0^4 \beta_0^8} \right] n_0, \quad (2.93)$$

in which  $k_4$  is related to fourth zonal harmonics and is defined in Eq. (A.17). The secular effects of luni-solar perturbations are also computed during initialization. To compute these quantities the orbital elements of Sun and Moon at epoch are required. Following the procedure in appendix A.2 Moon's RAAN  $\Omega_{\mathcal{L}}$ , inclination  $I_{\mathcal{L}}$ , and argument of pericentre  $\omega_{\mathcal{L}}$  are computed. Sun's RAAN  $\Omega_{\odot}$  and argument of pericentre  $\omega_{\odot}$  are treated as constants instead.

For both the Sun and the Moon the following coefficients are calculated

$$\begin{aligned} a_{1x} &= \cos(\omega_x) \cos(\Omega_0 - \Omega_x) + \sin(\omega_x) \cos(I_x) \sin(\Omega_0 - \Omega_x) \\ a_{3x} &= -\sin(\omega_x) \cos(\Omega_0 - \Omega_x) + \cos(\omega_x) \cos(I_x) \sin(\Omega_0 - \Omega_x) \\ a_{7x} &= -\cos(\omega_x) \sin(\Omega_0 - \Omega_x) + \sin(\omega_x) \cos(I_x) \cos(\Omega_0 - \Omega_x) \\ a_{8x} &= \sin(\omega_x) \sin(I_x) \\ a_{9x} &= \sin(\omega_x) \sin(\Omega_0 - \Omega_x) + \cos(\omega_x) \cos(I_x) \cos(\Omega_0 - \Omega_x) \\ a_{10x} &= \cos(\omega_x) \sin(I_x) \\ a_{2x} &= a_{7x} \cos(I_0) + a_{8x} \sin(I_0) \\ a_{4x} &= a_{9x} \cos(I_0) + a_{10x} \sin(I_0) \\ a_{5x} &= -a_{7x} \sin(I_0) + a_8 \cos(I_0) \\ a_{6x} &= -a_{9x} \sin(I_0) + a_{10x} \cos(I_0) \end{aligned} \quad (2.94)$$

$$\begin{aligned} X_{1x} &= a_{1x} \cos(\omega_0) + a_{2x} \sin(\omega_0) \\ X_{2x} &= a_{3x} \cos(\omega_0) + a_{4x} \sin(\omega_0) \\ X_{3x} &= -a_{1x} \sin(\omega_0) + a_{2x} \cos(\omega_0) \\ X_{4x} &= -a_{3x} \sin(\omega_0) + a_{4x} \cos(\omega_0) \\ X_{5x} &= a_{5x} \sin(\omega_0) \\ X_{6x} &= a_{6x} \sin(\omega_0) \\ X_{7x} &= a_{5x} \cos(\omega_0) \\ X_{8x} &= a_{6x} \cos(\omega_0) \end{aligned} \quad (2.95)$$

$$\begin{aligned}
Z_{31x} &= 12X_{1x}^2 - 3X_{3x}^2 \\
Z_{32x} &= 24X_{1x}X_{2x} - 6X_{3x}X_{4x} \\
Z_{33x} &= 12X_{2x}^2 - 3X_{4x}^2 \\
Z_{1x} &= 6(a_{1x}^2 + a_{2x}^2) + (1 + e_0^2) Z_{31x} \\
Z_{3x} &= 6(a_{3x}^2 + a_{4x}^2) + (1 + e_0^2) Z_{33x} \\
Z_{11x} &= -6a_{1x}a_{5x} + e_0^2(-24X_{1x}X_{7x} - 6X_{3x}X_{5x}) \\
Z_{13x} &= -6a_{3x}a_{6x} + e_0^2(-24X_{2x}X_{8x} - 6X_{4x}X_{6x}) \\
Z_{21x} &= 6a_{2x}a_{5x} + e_0^2(24X_{1x}X_{5x} - 6X_{3x}X_{7x}) \\
Z_{23x} &= 6a_{4x}a_{6x} + e_0^2(24X_{2x}X_{6x} - 6X_{4x}X_{8x}) \\
Z_{22x} &= 6a_{4x}a_{5x} + 6a_{2x}a_{6x} + e_0^2(24X_{2x}X_{5x} + 24X_{1x}X_{6x} - 6X_{4x}X_{7x} - 6X_{3x}X_{8x}) \\
Z_{12x} &= -6a_{1x}a_{6x} - 6a_{3x}a_{5x} - e_0^2(24X_{2x}X_{7x} + 24X_{1x}X_{8x} + 6X_{3x}X_{6x} + 6X_{4x}X_{5x}) ,
\end{aligned} \tag{2.96}$$

where subscript  $x$  stands for the considered perturbing body, while subscript 0 indicates the satellite mean elements at epoch. The secular rate for each body are given by

$$\dot{a}_x = 0 \tag{2.97}$$

$$\dot{e}_x = -15 C_x n_x \frac{e_0 \beta_0}{n_0} (X_{1x} X_{3x} + X_{2x} X_{4x}) \tag{2.98}$$

$$\dot{I}_x = -\frac{C_x n_x}{2 n_0 \beta_0} (Z_{11x} + Z_{13x}) \tag{2.99}$$

$$\dot{M}_x = -\frac{C_x n_x}{n_0} (Z_{1x} + Z_{3x} - 14 - 6e_0^2) \tag{2.100}$$

$$\dot{\Omega}_x = \begin{cases} \frac{C_x n_x \beta_0}{2 n_0 \beta_0 \sin(I_0)} (Z_{21x} + Z_{23x}) & \text{if } |I_0| \leq 3 \text{ deg} \\ 0 & \text{if } |I_0| > 3 \text{ deg} \end{cases} \tag{2.101}$$

$$\dot{\omega}_x = \frac{C_x n_x \beta_x}{n_0} (Z_{31x} + Z_{33x} - 6) - \dot{\Omega}_x \cos(I_0) . \tag{2.102}$$

where  $C_{\mathcal{L}}$  and  $C_{\odot}$  are lunar and solar perturbation coefficients and are listed in Sect. A.2. For a nearly geosynchronous satellite or debris, whose period in minutes is in the interval [1200, 1800], it is necessary to calculate the functions of inclination  $F(I)$

$$F_{220} = \frac{3}{4} (1 + \cos(I_0))^2 \tag{2.103}$$

$$F_{311} = \frac{15}{16} \sin^2(I_0) (1 + 3 \cos(I_0)) - \frac{3}{4} (1 + \cos(I_0)) \tag{2.104}$$

$$F_{330} = \frac{15}{8} (1 + \cos(I_0))^3 , \quad (2.105)$$

and eccentricity function  $G(e)$

$$G_{200} = 1 - \frac{5}{2}e_0^2 + \frac{13}{16}e_0^4 \quad (2.106)$$

$$G_{310} = 1 + 2e_0^2 \quad (2.107)$$

$$G_{300} = 1 - 6e_0^2 + \frac{423}{64}e_0^4 , \quad (2.108)$$

The coefficients of the resonance terms are subsequently computed:

$$\delta_{S1} = 3 \frac{n_0^2}{a_0^3} F_{311} G_{310} Q_{31} \quad (2.109)$$

$$\delta_{S2} = 6 \frac{n_0^2}{a_0^2} F_{220} G_{200} Q_{22} \quad (2.110)$$

$$\delta_{S3} = 9 \frac{n_0^2}{a_0^3} F_{330} G_{300} Q_{33} , \quad (2.111)$$

where  $Q$  coefficients are listed in Table A.6.

To compute the resonance effect a numerical integration scheme is required. The 1-day period initial conditions are computed during initialization and are given by

$$\lambda_{i_0} = M_0 + \omega_0 + \Omega_0 - \theta_{G0} \quad (2.112)$$

$$n_{i_0} = n_0 \quad (2.113)$$

$$\dot{\lambda}_{i_0} = \dot{M}_z + \dot{M}_\odot + \dot{M}_\zeta + \dot{\Omega}_z + \dot{\Omega}_\odot + \dot{\Omega}_\zeta + \dot{\omega}_z + \dot{\omega}_\odot + \dot{\omega}_\zeta - \omega_\oplus \quad (2.114)$$

$$\dot{n}_{i_0} = \delta_{S1} \sin(\lambda_{i_0} - \lambda_{31}) + \delta_{S2} \sin(2\lambda_{i_0} - \lambda_{22}) + \delta_{S3} \sin(3\lambda_{i_0} - \lambda_{33}) \quad (2.115)$$

$$\ddot{\lambda}_{i_0}/2 = \dot{n}_{i_0}/2 \quad (2.116)$$

$$\ddot{n}_{i_0}/2 = \left( \dot{\lambda}_{i_0}/2 \right) [\delta_{S1} \sin(\lambda_{i_0} - \lambda_{31}) + 2\delta_{S2} \sin(2\lambda_{i_0} - \lambda_{22}) + 3\delta_{S3} \sin(3\lambda_{i_0} - \lambda_{33})] , \quad (2.117)$$

where  $\theta_{G0}$  is Greenwich Sidereal Time (GST) angle (Fig. 2.2) measured at epoch. The formulae for computation of GST are given in Section A.1.

Once all constants are defined, the mean Keplerian elements can be updated in order to find osculating elements. The secular variation due to zonal harmonics and luni-solar attraction is given by

$$M_{\text{sec}} = M_0 + n_0 t + \left( \dot{M}_z + \dot{M}_\odot + \dot{M}_\zeta \right) t \quad (2.118)$$

$$\omega_{\text{sec}} = \omega_0 + (\dot{\omega}_z + \dot{\omega}_\odot + \dot{\omega}_\zeta) t \quad (2.119)$$

$$\Omega_{\text{sec}} = \Omega_0 + \left( \dot{\Omega}_z + \dot{\Omega}_\odot + \dot{\Omega}_\zeta \right) t \quad (2.120)$$

$$I_{\text{sec}} = I_0 + \left( \dot{I}_\odot + \dot{I}_\zeta \right) t \quad (2.121)$$

$$e_{\text{sec}} = e_0 + (\dot{e}_\odot + \dot{e}_\zeta) t . \quad (2.122)$$

The next step is computing resonance effect of Earth gravity through numerical integration. The equations to integrate with an Euler-Maclaurin scheme are

$$\lambda_i = \lambda_{i-1} + \dot{\lambda}_i \Delta t + \left( \ddot{\lambda}_i/2 \right) \Delta t \quad (2.123)$$

$$n_i = n_{i-1} + \dot{n}_i \Delta t + \left( \ddot{n}_i/2 \right) \Delta t , \quad (2.124)$$

where  $n$  is debris mean motion and  $\lambda$  is defined as

$$\lambda = M + \Omega + \omega - \theta_G . \quad (2.125)$$

The time step  $\Delta t$  is 12h. At the first step the values  $\lambda_{i_0}$  and  $n_{i_0}$  and their derivatives computed during initialization are used. At each step the derivatives of  $\lambda_i$  and  $n_i$  are updated with the relations

$$\dot{\lambda}_i = n_i + \dot{\lambda}_{i_0} \quad (2.126)$$

$$\dot{n}_i = \delta_{S1} \sin(\lambda_i - \lambda_{31}) + \delta_{S2} \sin(2\lambda_i - \lambda_{22}) + \delta_{S3} \sin(3\lambda_i - \lambda_{33}) \quad (2.127)$$

$$\ddot{\lambda}_i = \dot{n}_i/2 \quad (2.128)$$

$$\ddot{n}_i/2 = \left( \dot{\lambda}_i/2 \right) [\delta_{S1} \sin(\lambda_i - \lambda_{31}) + 2\delta_{S2} \sin(2\lambda_i - \lambda_{22}) + 3\delta_{S3} \sin(3\lambda_i - \lambda_{33})] . \quad (2.129)$$

When  $\lambda_i$  and  $n_i$  are obtained at the time of interest the mean motion and mean anomaly are given by

$$n' = n_i \quad (2.130)$$

$$M_{\text{sec}} = \lambda_i - \Omega_{\text{sec}} - \omega_{\text{sec}} + \theta_G , \quad (2.131)$$

where  $\theta_G$  is Greenwich hour angle at time  $t$ .

The long-period periodic effects of luni-solar perturbation can now be applied, knowing the mean anomaly  $M_x$  of the body  $x$  at time  $t$ . The true anomaly of the perturbing body is approximated by

$$\nu_x = M_x + 2e_x \sin M_x \quad (2.132)$$

Defining for both the Sun and the Moon

$$F_{2x} = \frac{1}{2} \sin^2(\nu_x) - \frac{1}{4} \quad F_{3x} = -\frac{1}{2} \sin(\nu_x) \cos(\nu_x) , \quad (2.133)$$

the long period variation of the secular elements due to body  $x$  written in non-singular variables are

$$\delta e_x = - \left( 30 \beta_0 C_x \frac{e_0}{n_0} \right) [F_{2x} (X_{2x} X_{3x} + X_{1x} X_{4x}) + F_{3x} (X_{2x} X_{4x} - X_{1x} X_{3x})] \quad (2.134)$$

$$\delta I_x = -\frac{C_x}{n_0 \beta_0} [F_{2x} Z_{12x} + F_{3x} (Z_{13x} - Z_{11x})] \quad (2.135)$$

$$\delta M_x = -2 \frac{C_x}{n_0} [F_{2x} Z_{2x} + F_{3x} (Z_{3x} - Z_{1x}) - 3 e_x \sin(\nu_x) (7 + 3 e_0^2)] \quad (2.136)$$

$$(\delta \omega_x + \cos(I_x) \delta \Omega_x) = 2 \beta_0 \frac{C_x}{n_0} [F_{2x} Z_{32x} + F_{3x} (Z_{33x} - Z_{31x}) - 9 e_x \sin(\nu_x)] \quad (2.137)$$

$$\sin(I_x) \delta \Omega_x = \frac{C_x}{n_0 \beta_0} [F_{2x} Z_{22x} + F_{3x} (Z_{23x} - Z_{21x})] , \quad (2.138)$$

where the subscripts  $x$  on the right side of the equation are referred to the perturbing body. The combined contribution for the two body are applied directly to secular elements when  $I' \geq 0.2$  rad

$$e' = e_{\text{sec}} + \delta e_{\odot} + \delta e_{\zeta} \quad (2.139)$$

$$I' = I_{\text{sec}} + \delta I_{\odot} + \delta I_{\zeta} \quad (2.140)$$

$$M' = M_{\text{sec}} + \delta M_{\odot} + \delta M_{\zeta} \quad (2.141)$$

$$\Omega' = \Omega_{\text{sec}} + (\delta\Omega_{\odot} + \delta\Omega_{\zeta}) \quad (2.142)$$

$$\omega' = \omega_{\text{sec}} + (\delta\omega_{\odot} + \cos(I')\delta\Omega_{\odot} + \delta\omega_{\zeta} + \cos(I')\delta\Omega_{\zeta}) - (\delta\Omega_{\odot} + \delta\Omega_{\zeta}) \cos(I'). \quad (2.143)$$

It is important to underline that the long-period variation are usually non-null at epoch, as initial elements are mean elements. To have zero values of long-period perturbation at initial time, and hence initial perturbed values equal to mean Keplerian elements, the initial values of long period variation can be used as an offset and subtracted to  $\delta$  quantities. When  $I' < 0.2$  rad the perturbations can not be applied directly as the presence of small divisor leads to singular values. In this case the Lyddane[23] modification is applied to RAAN and argument of pericentre, while the other three elements are computed as above. The following quantities are computed when  $I' \geq 0$

$$\alpha = \sin(I') \sin(\Omega_{\text{sec}}) + \sin(I') (\delta\Omega_{\odot} + \delta\Omega_{\zeta}) \cos(\Omega_{\text{sec}}) + \cos(I') \sin(\Omega_{\text{sec}}) (\delta I_{\odot} + \delta I_{\zeta}) \quad (2.144)$$

$$\beta = \sin(I') \cos(\Omega) - \sin(I') (\delta\Omega_{\odot} + \delta\Omega_{\zeta}) \sin(\Omega_{\text{sec}}) + \cos(I') \cos(\Omega_{\text{sec}}) (\delta I_{\odot} + \delta I_{\zeta}), \quad (2.145)$$

whereas when  $I' < 0$ ,  $\alpha$  and  $\beta$  are

$$\alpha = -\sin(I') \sin(\Omega_{\text{sec}}) + \sin(I') (\delta\Omega_{\odot} + \delta\Omega_{\zeta}) \cos(\Omega_{\text{sec}}) + \cos(I') \sin(\Omega_{\text{sec}}) (\delta I_{\odot} + \delta I_{\zeta}) \quad (2.146)$$

$$\beta = -\sin(I') \cos(\Omega) - \sin(I') (\delta\Omega_{\odot} + \delta\Omega_{\zeta}) \sin(\Omega_{\text{sec}}) + \cos(I') \cos(\Omega_{\text{sec}}) (\delta I_{\odot} + \delta I_{\zeta}). \quad (2.147)$$

Then the mean longitude  $L$  is computed

$$L' = M' + \omega_{\text{sec}} + \cos(I')\Omega_{\text{sec}} - \Omega_{\text{sec}} \sin(I') (\delta I_{\odot} + \delta I_{\zeta}) + (\delta\omega_{\odot} + \cos(I')\delta\Omega_{\odot} + \delta\omega_{\zeta} + \cos(I')\delta\Omega_{\zeta}) \quad (2.148)$$

and the primed values of  $\Omega$  and  $\omega$  are given by

$$\Omega' = \arctan_2 \left( \frac{\alpha}{\beta} \right) \quad \omega' = L' - M' - \cos(I')\Omega' . \quad (2.149)$$

These passages are necessary because at zero inclination and eccentricity the argument of pericentre and right ascension of the ascending node are not defined uniquely.

Subsequently, the long-period periodic effects of Earth's gravity are added, using the quantities

$$a_{xN} = e' \cos(\omega') \quad (2.150)$$

$$IL_L = \frac{1}{8} \frac{A_{3,0} \sin(I')}{k_2 a' \beta'^2} (e' \cos(\omega')) \left( \frac{3 + 5 \cos(I')}{1 + \cos(I')} \right) \quad (2.151)$$

$$a_{yN} = e' \sin(\omega') + \frac{1}{4} \frac{A_{3,0} \sin(I')}{k_2 a' \beta'^2} \quad (2.152)$$

$$IL_T = M' + \Omega' + \omega' + IL_L, \quad (2.153)$$

where  $a'$  is the semi-major axis obtained with mean motion  $n'$  and

$$e = \sqrt{a_{xN}^2 + a_{yN}^2}.$$

Short-period periodic perturbation due to Earth's gravity are added after solving Kepler's equation for  $(E + \omega)$ . Defining

$$U = IL_T - \Omega' \quad (2.154)$$

the iteration equation for the solution of Kepler's equation is

$$(E + \omega)_{i+1} = (E + \omega)_i + \Delta(E + \omega)_i \quad (2.155)$$

with

$$\Delta(E + \omega)_i = \frac{U - a_{yN} \cos(E + \omega)_i + a_{xN} \sin(E + \omega)_i - (E + \omega)_i}{1 - a_{yN} \sin(E + \omega)_i - a_{xN} \cos(E + \omega)_i} \quad (2.156)$$

$$(E + \omega)_1 = U.$$

Once the eccentric anomaly  $E$  and the longitude  $U$  are known, the following quantities are calculated

$$e' \cos(E) = a_{xN} \cos(E + \omega) + a_{yN} \sin(E + \omega) \quad (2.157)$$

$$e' \sin(E) = a_{xN} \sin(E + \omega) - a_{yN} \cos(E + \omega) \quad (2.158)$$

$$e' = \sqrt{a_{xN}^2 + a_{yN}^2} \quad (2.159)$$

$$p_L = a' (1 - e'^2) \quad (2.160)$$

$$r' = a' (1 - e' \cos(E)) \quad (2.161)$$

$$\cos(u') = \frac{a'}{r'} \left[ \cos(E + \omega) - a_{xN} + \frac{a_{yN} e' \sin(E)}{1 + \sqrt{1 - e'^2}} \right] \quad (2.162)$$

$$\sin(u') = \frac{a'}{r'} \left[ \sin(E + \omega) - a_{yN} - \frac{a_{xN} e' \sin(E)}{1 + \sqrt{1 - e'^2}} \right] \quad (2.163)$$

$$u' = \arctan_2 \left( \frac{\sin u'}{\cos u'} \right). \quad (2.164)$$

The short period perturbations at time  $t$  are given by

$$\Delta r = \frac{1}{2} \frac{k_2}{p_L} (1 - \cos^2(I')) \cos(2u') \quad (2.165)$$

$$\Delta u = -\frac{1}{4} \frac{k_2}{p_L^2} (7 \cos^2(I') - 1) \sin(2u') \quad (2.166)$$

$$\Delta \Omega = \frac{3}{2} \frac{k_2}{p_L^2} \cos(I') \sin(2u') \quad (2.167)$$

$$\Delta I = \frac{3}{2} \frac{k_2}{p_L^2} \sin(I') \cos(2u'), \quad (2.168)$$

and are added to primed elements with equations

$$r = r' \left[ 1 - \frac{3}{2} k_2 \frac{\sqrt{1-e'^2}}{p_L^2} (3 \cos^2(I') - 1) \right] + \Delta r \quad (2.169)$$

$$u = u' + \Delta u \quad (2.170)$$

$$\Omega = \Omega' + \Delta \Omega \quad (2.171)$$

$$I = I' + \Delta I . \quad (2.172)$$

The position in Earth centred inertial reference frame is given by

$$\mathbf{r} = r \hat{\mathbf{u}} , \quad (2.173)$$

where

$$\hat{\mathbf{u}} = \left\{ \begin{array}{l} -\sin(\Omega) \cos(I) \sin(u) + \cos(\Omega) \cos(u) \\ \cos(\Omega) \cos(I) \sin(u) + \sin(\Omega) \cos(u) \\ \sin(I) \sin(u) \end{array} \right\} . \quad (2.174)$$

### Model validation

The representation in ECI frame of a geosynchronous orbit obtained with SGP4 is given in Figure 2.14.

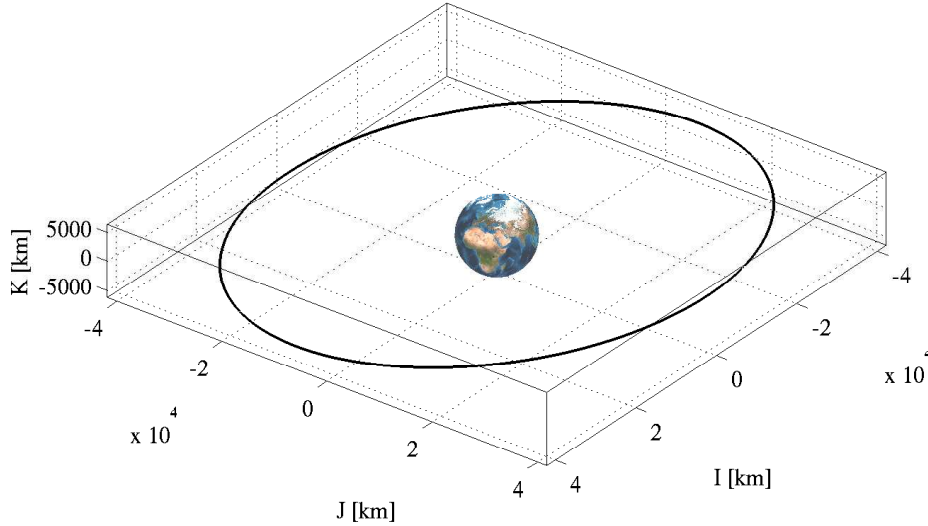


**Figure 2.14:** SGP4: Geo-synchronous orbit ( $a'_0 = 42164.50$  km,  $e'_0 = 0$ ,  $I'_0 = 7.5$  deg,  $\Omega'_0 = 334$  deg,  $\omega'_0 = 20$  deg)

The mean anomaly daily variation of the orbit in Figure 2.14 is plotted in Figure 2.15. As expected, it equals 360 deg since the orbital period is approximately 24 hours.

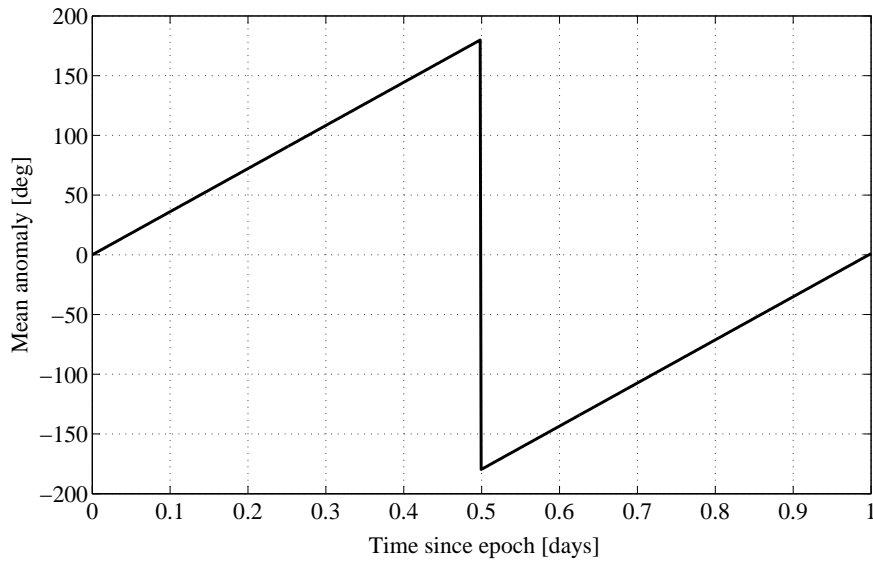
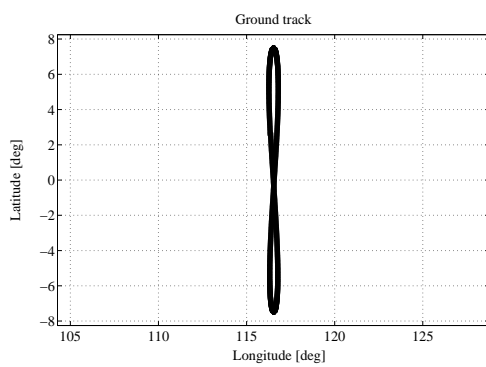
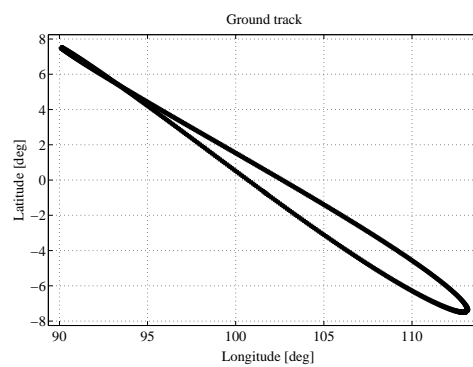


**Figure 2.15:** SGP4: Geo-synchronous orbit mean anomaly daily variation ( $a'_0 = 42164.50$  km,  $e'_0 = 0$ ,  $I'_0 = 7.5$  deg,  $\Omega'_0 = 334$  deg,  $\omega'_0 = 20$  deg)



(a)  $a'_0 = 42164.50$  km,  $e'_0 = 0$ ,  $I'_0 = 7.5$  deg,  $\Omega'_0 = 334$  deg,  $\omega'_0 = 20$  deg)



(b)  $a'_0 = 42164.50$  km,  $e'_0 = 0.1$ ,  $I'_0 = 7.5$  deg,  $\Omega'_0 = 330$  deg,  $\omega'_0 = 20$  deg)

**Figure 2.16:** SGP4: Geo-synchronous orbit ground-track

Another possible test is verifying the ground-track of two slightly inclined orbits. For a circular orbit, the ground-track has a figure-eight shape, whereas for a slightly eccentric orbit the ground-track resembles a teardrop (Figure 2.16).

The HOT BIRD 6 geostationary satellites could be used as a test case for longitude drift due to tesseral harmonics. This satellite was launched in August 2002 in a slot at 1°E. In January 2011 the satellite has drifted to 13°E. The longitude variation during this time span was computed with the SGP4 code and is represented in Figure 2.17.

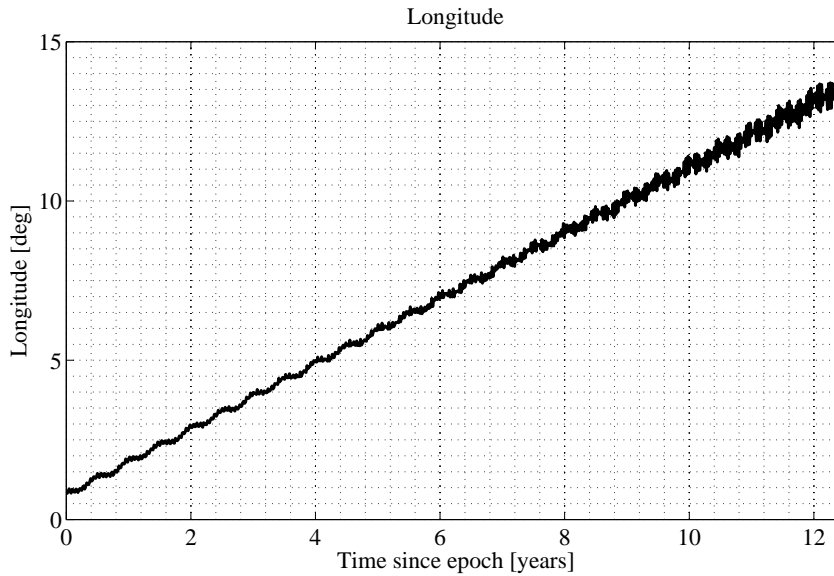


**Figure 2.17:** SGP4: HOT BIRD 6 longitude drift ( $a'_0 = 42164.50$  km,  $e'_0 = 5.65 \times 10^{-4}$ ,  $I'_0 = 0.0578$  deg,  $\Omega'_0 = 276.5$  deg,  $\omega'_0 = 4.98$  deg, epoch = JD 2452507.5)

The code was tested also in the stable points. In Figure 2.18 the longitude oscillates around the longitude value of 70.8°E.

The perturbations due to Moon and Sun attraction and Earth's  $J_2$  zonal harmonics produce an oscillation of orbit inclination. The inclination varies between  $\pm 15$  deg with a period of 54 years. The yearly variation of inclination is approximately 0.85 deg. The code can reproduce this effects as shown in Figure 2.19.

The simplified version of SGP4 for the geosynchronous orbit can indeed represent the main characteristics of this kind of orbits. The model can compute position of the satellites with a satisfactory accuracy, since the longitude shows good agreement with real world data (Fig. 2.17). The model is accurate on a time span of one or two years, as the perturbative effect of luni-solar perturbation on the inclination are obtained as a gradient at epoch (Eq. (2.97)).

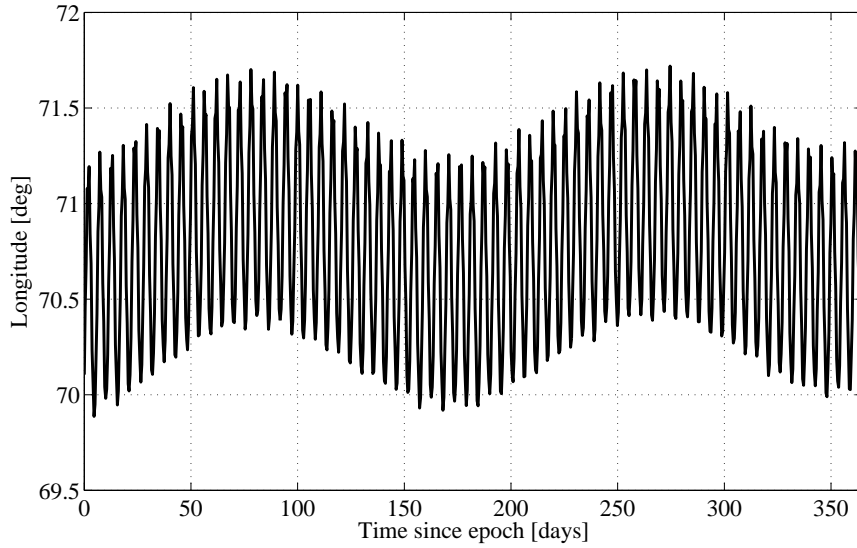


**Figure 2.18:** SGP4: longitude behaviour near stable point at  $70.8^\circ\text{E}$  ( $a'_0 = 42164.50$  km,  $e'_0 = 0$ ,  $I'_0 = 12$  deg,  $\Omega'_0 = 334$  deg,  $\omega'_0 = 4.98$  deg)

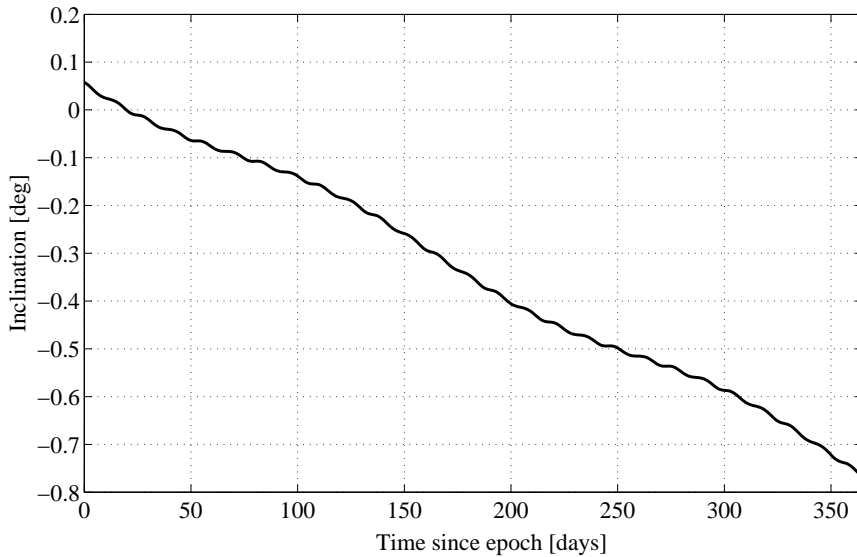


**Figure 2.19:** SGP4: HOT BIRD 6 yearly variation of inclination ( $a'_0 = 42164.50$  km,  $e'_0 = 5.65 \times 10^{-4}$ ,  $I'_0 = 0.0578$  deg,  $\Omega'_0 = 276.5$  deg,  $\omega'_0 = 4.98$  deg, epoch = JD 2455574.9)

### 2.3.4 Conclusions

Three analytical models have been selected and implemented. The model derived from Aksnes' solution, described in Section 2.3.1, considers only the perturbation due to the first five zonal harmonics. The model shows good accordance with numerical simulation that considers the same perturbations over a time span of one year. The model can be used to compute the position of satellites whose perigee is at an altitude at which the atmospheric drag can be neglected.

In Section 2.3.2 HANDE model was described. It considers both zonal harmonics and drag perturbations. The model can predict the variation of the semi-major axis as well as the effect of drag on the other Keplerian elements. It is hence suitable for modelling LEO satellites. Over long time span, the propagation of position is less accurate. The reason is the phase displacement that arise from the error on semi-major axis. Over a tens of days, even an error of a few hundreds metres on semi-major axis can result in a displacement of tens of degree on mean anomaly.

A model for GEO orbits was provided in Section 2.3.3. This model showed good accordance with real world data and can describe the main effect of resonance and luni-solar perturbations.

These models will be used in Chapter 4 to compute the MOID between perturbed orbits.



## Chapter 3

# Differential Algebra, Taylor Models and COSY

The theory of differential algebra presented in this chapter has been developed by Martin Berz in the late 80's, and the short summary given in the followings takes advantage of his book *Modern Map Methods in Particle Beam Physics* [53].

Differential Algebra (DA) techniques find their origin in the attempt to solve analytical problem by an algebraic approach. Historically, treatment of functions in numerics has been based on the treatment of numbers, and the classical numerical algorithms are based on the mere evaluation of functions at specific points. DA techniques are based on the observation that it is possible to extract more information on a function rather than its mere values. The basic idea is to bring the treatment of functions and the operations on them to the computer environment in a similar way as the treatment of real numbers. Referring to Figure 3.1, consider two real numbers  $a$  and  $b$ . In order to operate on them in a computer environment, they are usually transformed in their Floating Point (FP) representation,  $\bar{a}$  and  $\bar{b}$  respectively. Then, given any operation  $*$  in the set of real numbers, an adjoint operation  $\circledast$  is defined in the set of FP numbers such that the diagram commutes. Consequently, transforming the real numbers  $a$  and  $b$  in their FP representation and operating on them in the set of FP numbers returns the same result as carrying out the operation in the set of real numbers and then transforming the result in its FP representation. In a similar way, suppose two sufficiently regular functions  $f$  and  $g$  are given. In the framework of differential algebra, the computer operates on them using their Taylor series expansions,  $F$  and  $G$  respectively. Therefore, the transformation of real numbers in their FP representation is now substituted by the extraction of the Taylor expansions of  $f$  and  $g$ . For each operation in the function space, an adjoint operation in the space of Taylor polynomials is defined such that the corresponding diagram commutes: extracting the Taylor expansions of  $f$  and  $g$  and operating on them returns the same result as operating on  $f$  and  $g$  in the original space and then extracting the Taylor expansion of the resulting function. Differential algebra can be effectively implemented in a computer environment. In this way, the Taylor coefficients of a function can be obtained up to a specified order  $n$ , along with the function evaluation, with a fixed amount of effort. The Taylor coefficients of order  $n$  for sums and product of functions, as well as scalar products with reals, can be computed from those of summands and factors; therefore, the set of equivalence classes of functions can be endowed with well-defined operations, leading to the so-called Truncated Power Series Algebra (TPSA) [54, 55].

Similarly to the algorithms for floating point arithmetic, the algorithm for functions followed,

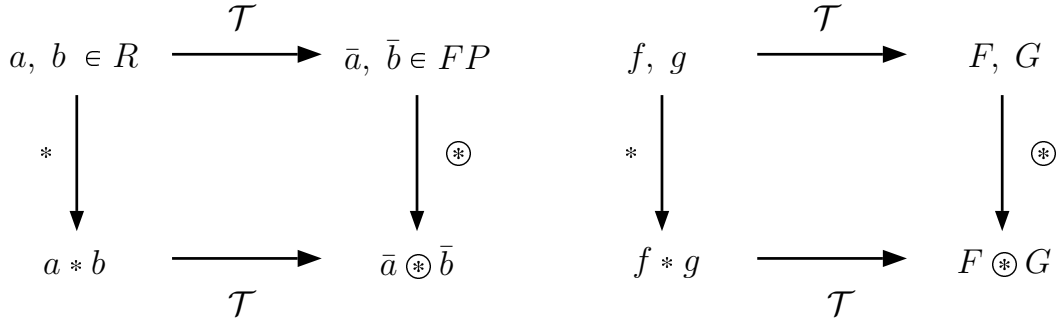


**Figure 3.1:** Analogy between the floating point representation of real numbers in a computer environment (left figure) and the introduction of the algebra of Taylor polynomials in the differential algebraic framework (right figure).

including methods to perform composition of functions, to invert them, to solve nonlinear systems explicitly, and to treat common elementary functions [56, 57]. In addition to these algebraic operations, also the analytic operations of differentiation and integration have been developed on these function spaces, defining a differential algebraic structure.

As DA represents the core of the algorithms developed in the frame of this work, some useful notes to get familiar with these techniques are given in the following. In particular, the minimal differential algebra for 1-dimensional functions and their first order expansion is explained in details, and some hints on its extension to functions of  $v$  variables and to  $n$ -th order are given. An important application of DA techniques is then presented in Section 3.2.1, pertaining the solution of parametric implicit equations. The validated extension of differential algebra into the Taylor model method concludes the chapter in Section 3.3.

### 3.1 The Minimal Differential Algebra

The simplest nontrivial differential algebra is here described. Consider all ordered pairs  $(q_0, q_1)$ , with  $q_0$  and  $q_1$  real numbers. The addition, scalar multiplication, and vector multiplication are defined as follows:

$$\begin{aligned}
 (q_0, q_1) + (r_0, r_1) &= (q_0 + r_0, q_1 + r_1) \\
 t \cdot (q_0, q_1) &= (t \cdot q_0, t \cdot q_1) \\
 (q_0, q_1) \cdot (r_0, r_1) &= (q_0 \cdot r_0, q_0 \cdot r_1 + q_1 \cdot r_0).
 \end{aligned} \tag{3.1}$$

The ordered pairs with the arithmetic (3.1) are called  ${}_1D_1$ . The first two operations are the familiar vector space structure of  $R^2$ , whereas the multiplication is similar to that in the complex numbers; except here  $(0, 1) \cdot (0, 1)$  does not equal  $(-1, 0)$ , but rather  $(0, 0)$ . The multiplication of vectors is seen to have  $(1, 0)$  as the unity element. The multiplication is commutative, associative, and distributive with respect to addition. Together, the three operations defined in (3.1) form an algebra. Furthermore, they do form an extension of real numbers, as  $(r, 0) + (s, 0) = (r + s, 0)$  and  $(r, 0) \cdot (s, 0) = (r \cdot s, 0)$ , so that the reals can be included.

However  ${}_1D_1$  is not a field, as  $(q_0, q_1)$  has a multiplicative inverse in  ${}_1D_1$  if and only if  $q_0 \neq 0$ .

If  $q_0 \neq 0$  then

$$(q_0, q_1)^{-1} = \left( \frac{1}{q_0}, -\frac{q_1}{q_0^2} \right). \quad (3.2)$$

If  $q_0$  is positive, then  $(q_0, q_1) \in {}_1D_1$  has a root

$$\sqrt{(q_0, q_1)} = \left( \sqrt{q_0}, \frac{q_1}{2\sqrt{q_0}} \right), \quad (3.3)$$

as simple arithmetic shows.

One important property of this algebra is that it has an order compatible with its algebraic operations. Given two elements  $(q_0, q_1)$  and  $(r_0, r_1)$  in  ${}_1D_1$ , it is defined

$$\begin{aligned} (q_0, q_1) < (r_0, r_1) & \text{ if } q_0 < r_0 \text{ or } (q_0 = r_0 \text{ and } q_1 < r_1) \\ (q_0, q_1) > (r_0, r_1) & \text{ if } (r_0, r_1) < (q_0, q_1) \\ (q_0, q_1) = (r_0, r_1) & \text{ if } q_0 = r_0 \text{ and } q_1 = r_1. \end{aligned} \quad (3.4)$$

As for any two elements  $(q_0, q_1)$  and  $(r_0, r_1)$  only one of the three relation holds,  ${}_1D_1$  is said totally ordered. The order is compatible with the addition and multiplication; for all  $(q_0, q_1), (r_0, r_1), (s_0, s_1) \in {}_1D_1$ , it follows  $(q_0, q_1) < (r_0, r_1) \Rightarrow (q_0, q_1) + (s_0, s_1) < (r_0, r_1) + (s_0, s_1)$ ; and  $(s_0, s_1) > (0, 0) = 0 \Rightarrow (q_0, q_1) \cdot (s_0, s_1) < (r_0, r_1) \cdot (s_0, s_1)$ .

The number  $d = (0, 1)$  has the interesting property of being positive but smaller than any positive real number; indeed

$$(0, 0) < (0, 1) < (r, 0) = r. \quad (3.5)$$

For this reason  $d$  is called an infinitesimal or a differential. In fact,  $d$  is so small that its square vanishes in  ${}_1D_1$ . Since for any  $(q_0, q_1) \in {}_1D_1$

$$(q_0, q_1) = (q_0, 0) + (0, q_1) = q_0 + d \cdot q_1, \quad (3.6)$$

the first component is called the real part and the second component the differential part.

The algebra in  ${}_1D_1$  becomes a differential algebra by introducing a map  $\partial$  from  ${}_1D_1$  to itself, and proving that the map is a derivation. Define  $\partial : {}_1D_1 \rightarrow {}_1D_1$  by

$$\partial(q_0, q_1) = (0, q_1). \quad (3.7)$$

Note that

$$\begin{aligned} \partial\{(q_0, q_1) + (r_0, r_1)\} &= \partial(q_0 + r_0, q_1 + r_1) = (0, q_1 + r_1) \\ &= (0, q_1) + (0, r_1) = \partial(q_0, q_1) + \partial(r_0, r_1) \end{aligned} \quad (3.8)$$

and

$$\begin{aligned} \partial\{(q_0, q_1) \cdot (r_0, r_1)\} &= \partial(q_0 \cdot r_0, q_0 \cdot r_1 + r_0 \cdot q_1) = (0, q_0 \cdot r_1 + r_0 \cdot q_1) \\ &= (0, q_1) \cdot (r_0, r_1) + (0, r_1) \cdot (q_0, q_1) \\ &= \partial\{(q_0, q_1)\} \cdot (r_0, r_1) + (q_0, q_1) \cdot \partial\{(r_0, r_1)\}. \end{aligned} \quad (3.9)$$

This holds for all  $(q_0, q_1), (r_0, r_1) \in {}_1D_1$ . Therefore  $\partial$  is a derivation and  $({}_1D_1, \partial)$  is a differential algebra.

The most important aspect of  ${}_1D_1$  is that it allows the automatic computation of derivatives. As an example, assume to have two functions  $f$  and  $g$ ; put their values and their derivatives at the origin in the form  $(f(0), f'(0))$  and  $(g(0), g'(0))$  as two vectors in  ${}_1D_1$ ; and consider the product

$$(f(0), f'(0)) \cdot (g(0), g'(0)) = (f(0) \cdot g(0), f(0) \cdot g'(0) + f'(0) \cdot g(0)). \quad (3.10)$$

As can be seen, if the derivative of the product  $f \cdot g$  at 0 is of interest, it has just to be looked at the second component of the resulting pair in (3.10); whereas the first component gives the value of the product of the functions. Therefore, if two vectors contain the values and the derivatives of two functions, their product contains the values and the derivatives of the product function.

Defining the operation  $[ ]$  from the space of differential functions to  ${}_1D_1$  via

$$[f] = (f(0), f'(0)), \quad (3.11)$$

it holds

$$\begin{aligned} [f + g] &= [f] + [g] \\ [f \cdot g] &= [f] \cdot [g] \end{aligned} \quad (3.12)$$

and

$$[1/g] = [1]/[g] = 1/[g] \quad (3.13)$$

by using (3.2). This observation can be used to compute derivatives of many kinds of functions algebraically by merely applying arithmetic rules on  ${}_1D_1$ , beginning from the value and the derivative of the identity function. Consider the example

$$f(x) = \frac{1}{x + \frac{1}{x}} \quad (3.14)$$

and its derivative

$$f'(x) = \frac{(1/x^2) - 1}{(x + (1/x))^2}. \quad (3.15)$$

The function value and its derivative at the point  $x = 3$  are

$$f(3) = \frac{3}{10}, \quad f'(3) = -\frac{2}{25}. \quad (3.16)$$

Within the DA framework, evaluating the function (3.14) at the ordered pair corresponding to the identity function, i.e.  $[x] = (x, 1)$ , at the point 3, i.e.  $(3, 1) = 3 + d$ , yields

$$\begin{aligned} f((3, 1)) &= \frac{1}{(3, 1) + 1/(3, 1)} = \frac{1}{(3, 1) + (1/3, -1/9)} \\ &= \frac{1}{(10/3, 8/9)} = \left( \frac{3}{10}, -\frac{8}{9} / \frac{100}{9} \right) = \left( \frac{3}{10}, -\frac{2}{25} \right). \end{aligned} \quad (3.17)$$

As can be seen, after the evaluation of the function, the real part of the result is the value of the function at  $x = 3$ , whereas the differential part is the value of the derivative of the function at

$x = 3$ . This is simply justified by applying the relations (3.12) and (3.13)

$$\begin{aligned} [f(x)] &= \left[ \frac{1}{x + 1/x} \right] = \frac{1}{[x + 1/x]} \\ &= \frac{1}{[x] + [1/x]} = \frac{1}{[x] + 1/[x]} \\ &= f([x]). \end{aligned} \tag{3.18}$$

Since, for a real  $x$ ,  $[x] = (x, 1) = x + d$ , and  $[f(x)] = (f(x), f'(x))$ , apparently

$$(f(3), f'(3)) = f((3 + d)). \tag{3.19}$$

The method can be generalised to allow the treatment of common intrinsic functions, like trigonometric or exponential functions, by setting

$$\begin{aligned} g_i([f]) &= [g_i(f)] \quad \text{or} \\ g_i((q_0, q_1)) &= (g_i(q_0), q_1 g_i'(q_0)). \end{aligned} \tag{3.20}$$

By virtue of equations (3.1) and (3.20) any function  $f$  representable by finitely many additions, subtractions, multiplications, divisions, and intrinsic functions in  ${}_1D_1$  satisfies the important relationship

$$[f(x)] = f([x]). \tag{3.21}$$

Note that  $f(r + d) = f(r) + d \cdot f'(r)$  resembles  $f(x + \Delta x) \approx f(x) + \Delta x \cdot f'(x)$ , in which the approximation becomes increasingly more refined for smaller  $\Delta x$ .

### 3.2 The Differential Algebra ${}_nD_v$

The algebra described in this section was introduced to compute the derivatives up to an order  $n$  of functions in  $v$  variables. Similarly as before, it is based on considering the space  $C^n(R^v)$ , i.e. the collection of  $n$  times continuously differentiable functions on  $R^v$ . On this space an equivalence relation is introduced. For  $f$  and  $g \in C^n(R^v)$ ,  $f =_n g$  if and only if  $f(0) = g(0)$  and all the partial derivatives of  $f$  and  $g$  agree at 0 up to order  $n$ . The relation  $=_n$  satisfies

$$\begin{aligned} f &=_n f \quad \text{for all } f \in C^n(R^v), \\ f &=_n g \Rightarrow g =_n f \quad \text{for all } f, g \in C^n(R^v), \quad \text{and} \\ f &=_n g \text{ and } g =_n h \Rightarrow f =_n h \quad \text{for all } f, g, h, \in C^n(R^v). \end{aligned} \tag{3.22}$$

Thus,  $=_n$  is an equivalence relation. All the elements that are related to  $f$  can be grouped together in one set, the equivalence class  $[f]$  of the function  $f$ . The resulting equivalence classes are often referred to as DA vectors or DA numbers. Intuitively, each of these classes is then specified by a particular collection of partial derivatives in all  $v$  variables up to order  $n$ . This class is called  ${}_nD_v$ .

If the values and the derivatives of two functions  $f$  and  $g$  are known, the corresponding values and derivatives of  $f + g$  and  $f \cdot g$  can be inferred. Therefore, the arithmetics on the classes in  ${}_nD_v$  can be introduced via

$$[f] + [g] = [f + g] \quad (3.23)$$

$$t \cdot [f] = [t \cdot f] \quad (3.24)$$

$$[f] \cdot [g] = [f \cdot g]. \quad (3.25)$$

Under this operations,  ${}_nD_v$  becomes an algebra.

For each  $k \in 1, \dots, v$ , define the map  $\partial_k$  from  ${}_nD_v$  to  ${}_nD_v$  for  $f$  via

$$\partial_k[f] = \left[ p_k \cdot \frac{\partial f}{\partial x_k} \right], \quad (3.26)$$

where

$$p_k(x_1, \dots, x_k) = x_k \quad (3.27)$$

projects out the  $k$ -th component of the identity function. It's easy to show that, for all  $k = 1, \dots, v$  and for all  $[f], [g] \in {}_nD_v$ ,

$$\partial_k([f] + [g]) = \partial_k[f] + \partial_k[g] \quad (3.28)$$

$$\partial_k([f] \cdot [g]) = [f] \cdot (\partial_k[g]) + (\partial_k[f]) \cdot [g]. \quad (3.29)$$

Therefore,  $\partial_k$  is a derivation for all  $k$ , and hence  $({}_nD_v, \partial_1, \dots, \partial_k)$  is a differential algebra.

The dimension of  ${}_nD_v$  is now assessed. Define the special numbers  $d_k$  as follows:

$$d_k = [x_k]. \quad (3.30)$$

Observe that  $f$  lies in the same class as its Taylor polynomial  $T_f$  of order  $n$  around the origin; they have the same function values and derivatives up to order  $n$ . Therefore,

$$[f] = [T_f]. \quad (3.31)$$

Denoting the Taylor coefficients of the Taylor polynomial  $T_f$  of  $f$  as  $c_{j_1, \dots, j_v}$ , it follows

$$T_f(x_1, \dots, x_v) = \sum_{j_1 + \dots + j_v \leq n} c_{j_1, \dots, j_v} \cdot x_1^{j_1} \cdots x_v^{j_v} \quad (3.32)$$

with

$$c_{j_1, \dots, j_v} = \frac{1}{j_1! \cdots j_v!} \cdot \frac{\partial^{j_1 + \dots + j_v} f}{\partial x_1^{j_1} \cdots \partial x_v^{j_v}} \quad (3.33)$$

and thus

$$\begin{aligned} [f] = [T_f] &= \left[ \sum_{j_1 + \dots + j_v \leq n} c_{j_1, \dots, j_v} \cdot x_1^{j_1} \cdots x_v^{j_v} \right] \\ &= \sum_{j_1 + \dots + j_v \leq n} c_{j_1, \dots, j_v} \cdot d_1^{j_1} \cdots d_v^{j_v}, \end{aligned} \quad (3.34)$$

where, in the last step, the properties  $[a + b] = [a] + [b]$  and  $[a \cdot b] = [a] \cdot [b]$  have been used. Therefore, the set  $\{1, d_k : k = 1, 2, \dots, v\}$  generates  ${}_nD_v$ , as any element of  ${}_nD_v$  can be obtained from 1 and the  $d_k$  via addition and multiplication. Therefore, as an algebra,  ${}_nD_v$  has  $(v + 1)$

generators, and the terms  $d_1^{j_1} \cdots d_v^{j_v}$  form a basis for the vector space  ${}_nD_v$ . It is shown in [53] that the number of basic elements is  $(n+v)!/(n!v!)$ , which is the dimension of  ${}_nD_v$ .

Similarly to the structure  ${}_1D_1$ ,  ${}_nD_v$  can be ordered, and the  $d_k$ , being smaller than any real number, are infinitely small or infinitesimal. Furthermore, a fixed point theorem for contracting operators in  ${}_nD_v$  exists, which enables the evaluation of square roots, the quotient, and the inversion of Taylor polynomials through iterative processes based on a finite number of steps [53]. Once the function composition and the elementary functions, like trigonometric or exponential functions, are introduced in  ${}_nD_v$ , the derivatives of any function  $f$  belonging to  $C^n(R^v)$  can be computed up to order  $n$  with a fixed amount of effort by applying

$$[f(x_1, \dots, x_v)] = f([x_1, \dots, x_v]) = f(x_1 + d_1, \dots, x_v + d_v). \quad (3.35)$$

The differential algebra sketched in this section was implemented by M. Berz and K. Makino in the software COSY INFINITY. The software and all the related documentations are available free of charge for non-commercial use online at [http://bt.pa.msu.edu/index\\_cosy.htm](http://bt.pa.msu.edu/index_cosy.htm).

### 3.2.1 Solution of Parametric Implicit Equations

DA techniques can be effectively used to identify the solution of parametric implicit equations. Well-established numerical techniques (e.g. Newton's method) exist, which can effectively identify the solution of a classical implicit equation

$$f(x) = 0. \quad (3.36)$$

Without loss of generality, suppose an explicit dependence on a parameter  $p$  can be highlighted in the previous function  $f$ , which leads to the parametric implicit equation

$$f(x, p) = 0. \quad (3.37)$$

Suppose the previous equation is to be solved, whose solution is represented by the function  $x(p)$  returning the value of  $x$  solving (3.37) for any value of the parameter  $p$ . Thus, the dependence of the solution of the implicit equation on the parameter  $p$  is of interest. DA techniques can effectively handle the previous problem by identifying the function  $x(p)$  in terms of its Taylor expansion with respect to  $p$ . The DA-based algorithm is presented in the following for the solution of the scalar parametric implicit equation (3.37); the generalisation to a system of parametric implicit equations is straightforward.

The solution of (3.37) is sought, where sufficient regularity is assumed to characterise the function  $f$ , i.e.  $f \in C^{n+1}$ . Thus  $x(p)$  satisfying

$$f(x(p), p) = 0 \quad (3.38)$$

is to be identified. The first step is to consider a reference value  $p^0$  of the parameter  $p$  and to compute the value of the solution  $x^0$  of the corresponding implicit equation by means of a classical numerical method, e.g. Newton's method. The variable  $x$  and the parameter  $p$  are then initialized as  $n$ -th order DA variables, i.e.,

$$\begin{aligned} [x] &= x^0 + \delta x \\ [p] &= p^0 + \delta p. \end{aligned} \quad (3.39)$$

A DA-based evaluation of the function  $f$  in (3.37) delivers the  $n$ -th order expansion of  $f$  with respect to  $x$  and  $p$ :

$$\delta f = \mathcal{M}_f(\delta x, \delta p). \quad (3.40)$$

where  $\mathcal{M}_f$  denotes the Taylor map for  $f$ . Note that the map has no constant part as  $x^0$  is the solution of the implicit equation for the nominal value of the parameter  $p^0$ ; thus,  $\delta f$  represents the deviation of  $f$  from its reference value 0, resulting from deviations of  $x$  and  $p$  from  $x^0$  and  $p^0$ . The map (3.40) is then augmented by introducing identity map on  $p$ , i.e.  $\delta p = \mathcal{I}_p(\delta p)$ , ending up with

$$\begin{pmatrix} \delta f \\ \delta p \end{pmatrix} = \begin{pmatrix} \mathcal{M}_f \\ \mathcal{I}_p \end{pmatrix} \begin{pmatrix} \delta x \\ \delta p \end{pmatrix}. \quad (3.41)$$

The  $n$ -th order map (3.41) is inverted using COSY INFINITY built-in tools, obtaining

$$\begin{pmatrix} \delta x \\ \delta p \end{pmatrix} = \begin{pmatrix} \mathcal{M}_f \\ \mathcal{I}_p \end{pmatrix}^{-1} \begin{pmatrix} \delta f \\ \delta p \end{pmatrix}. \quad (3.42)$$

As the goal is computing the  $n$ -th order Taylor expansion of the solution manifold  $x(p)$  of (3.37), the map (3.42) is evaluated for  $\delta f = 0$ :

$$\begin{pmatrix} \delta x \\ \delta p \end{pmatrix} = \begin{pmatrix} \mathcal{M}_f \\ \mathcal{I}_p \end{pmatrix}^{-1} \begin{pmatrix} 0 \\ \delta p \end{pmatrix}. \quad (3.43)$$

The first row of map (3.43) delivers

$$\delta x = \mathcal{M}_{\delta f=0}(\delta p), \quad (3.44)$$

which is the  $n$ -th order Taylor expansion of the solution manifold, i.e.

$$\delta x = \delta x(\delta p). \quad (3.45)$$

For any value of  $p$ , the approximate solution of  $f(x, p) = 0$  can be easily computed by evaluating the Taylor polynomial (3.45) at  $\delta p = p - p^0$ . Apparently, the solution obtained by means of (3.45) is a Taylor approximation of the exact solution of equation (3.37), the accuracy of the approximation depending on the order of the Taylor expansion and the displacement  $\delta p$  from the reference value  $p^0$ .

The procedure described above is necessary to compute the true anomaly  $\nu$ , needed for the evaluation of the short-period periodic terms of the analytical methods described in Sections 2.3.1, 2.3.2, and 2.3.3. For this reason, in both Aksnes zonal harmonics solution and HANDE, Kepler's equation

$$f(E) = E - e \sin E - M = 0 \quad (3.46)$$

must be solved, whereas in SGP4 algorithm a slightly different formulation in the variable  $(E + \omega)$  is used:

$$f(E + \omega) = (M + \omega) - a_{yN} \cos(E + \omega) + a_{yN} \sin(E + \omega) - (E + \omega) = 0. \quad (3.47)$$

Once the eccentric anomaly  $E$  is computed from  $e$  and  $M$  by means of one of the implicit equations above, the true anomaly is given by

$$\nu = 2 \arctan \left( \sqrt{\frac{1+e}{1-e}} \tan \left( \frac{E}{2} \right) \right). \quad (3.48)$$

The eccentric anomaly  $E$  and eccentricity  $e$  are in general both functions of time  $t$ .

If a pointwise evaluation of the space debris position at a specific time  $t$  is of interest, a classical numerical method for the solution of implicit equations, e.g. Newton's method, can be used to solve e.g. Equation (3.46). Apparently, an explicit algebraic relation between the satellite ephemerides and the epoch would be particularly useful. This means an explicit solution of Equation (3.46) is to be identified in the form of a function  $E(t)$ . Thus, Equation (3.46) must be handled in the parametric form

$$f(E, t) = 0. \quad (3.49)$$

Calling  $t_0$  the epoch at which the Keplerian elements are referred, the elapsed time  $\Delta t = t - t_0$  is initialized as a DA variable

$$[\Delta t] = t - t_0 + \delta t \quad (3.50)$$

at the beginning of one of the analytical methods described in 2.3.1, 2.3.2, and 2.3.3. A DA-based evaluation of the equations necessary to compute secular and long periodic variation of the Keplerian elements is then performed. The obtained Taylor expansions of the eccentricity and the mean anomaly with respect to the epoch

$$\begin{aligned} e(\delta t) &= \mathcal{M}_e(\delta t) \\ M(\delta t) &= \mathcal{M}_M(\delta t), \end{aligned} \quad (3.51)$$

are subsequently used to solve Kepler's equation and hence compute the corresponding eccentric anomaly  $E$ . In Table 3.1 it is reported the map of the mean anomaly obtained through DA-based evaluation of Aksnes' solution.

**Table 3.1:** DA map of mean anomaly

I	COEFFICIENT	ORDER	EXPONENTS	
			t	E
1	1.194444497404006	0	0	0
2	0.1458375887357944E-03	1	1	0

On each row the coefficients of the Taylor series are reported, together with the order of the expansions and the exponents of the variables variations. In this case the mean anomaly is a function of time  $t$  with only a linear term, notwithstanding the expansion was performed up to order 2.

Apparently, interest is not in a mere point value of  $E$  in this case, but rather in the Taylor expansion of the solution  $E$  with respect to the parameter  $t$ . Indeed, the explicit dependence of  $e$  and  $M$  on  $t$  must be kept and Kepler's equations read

$$f(E, \delta t) = E - e(\delta t) \sin E - M(\delta t) = 0 \quad (3.52)$$

$$\begin{aligned} f(E + \omega, \delta t) &= (M(\delta t) + \omega(\delta t)) - a_{yN}(\delta t) \cos(E + \omega(\delta t)) + \\ & a_{yN}(\delta t) \sin(E + \omega(\delta t)) - (E + \omega(\delta t)) = 0. \end{aligned} \quad (3.53)$$

The solution of this parametric implicit equation is attained in terms of the Taylor expansion  $E(\delta t) = \mathcal{M}_E(\delta t)$  using the techniques illustrated above.

As an example, given an eccentricity  $e = 0.1$  that is not a function of time, the Equation (3.46) is solved numerically using the constant coefficient of the mean anomaly of Table 3.1. The obtained eccentric anomaly is  $E^* = 1.290543038384026$  and it represents the zeroth-order coefficient of  $E$  DA-expansion.

The eccentric anomaly is subsequently initialized as a DA variable through

$$[E] = E^* + \delta E. \quad (3.54)$$

The equation (3.52) is then evaluated using map of the mean and eccentric anomaly and stored in the second row of a DA vector. On the first row, instead, the identity map of time variation  $\delta t$  is stored (see Eq. 3.41). The obtained DA vector is reported in Table 3.2

**Table 3.2:** DA direct map for solution of Keplerian equation

I	COEFFICIENT	ORDER	EXPONENTS	
			t	E
1	1.0000000000000000	1	1	0
1	-.1458375887357944E-03	1	1	0
2	0.9723400936098562	1	0	1
3	0.4804927049000973E-01	2	1	1

The direct map of Table 3.2 can hence be inverted as in Equation (3.42), obtaining the inverse map listed in Table 3.3.

**Table 3.3:** DA inverse map for solution of Keplerian equation

I	COEFFICIENT	ORDER	EXPONENTS	
			t	E
1	1.0000000000000000	1	1	0
1	0.1499861927881281E-03	1	1	0
2	1.028446740571455	1	0	1
3	-.1111657921288610E-08	2	2	0
4	-.1524514949712364E-04	2	1	1
5	-.5226755882786295E-01	2	0	2

The variation of eccentric anomaly is obtained as in Equation (3.43), evaluating the inverse map with a DA vector that has on the first row the identity map of  $\delta t$  and zero on the second row.

The variation  $\delta E = \delta E(\delta t)$  obtained by means of Eq. (3.43) is listed in Table 3.4. It can be noted that all terms involving the variable  $E$  have disappeared. Moreover the order of  $\delta E$  has a linear term like the mean anomaly, but a quadratic term has appeared.

The resulting eccentric anomaly is indeed obtained by adding to the order zero term  $E^*$  the second row of DA vector in Table 3.4.

**Table 3.4:** Evaluated DA inverse map

I	COEFFICIENT	ORDER	EXPONENTS	
			t	E
1	1.0000000000000000	1	1	0
1	0.1499861927881281E-03	1	1	0
2	-.1111657921288610E-08	2	2	0

Once  $E(\delta t)$  is available, the Taylor expansions of the debris position are readily obtained by carrying out the remaining algebraic manipulations in the DA framework. The resulting DA map of the variables can hence be evaluated in the surroundings of the reference value, obtaining an approximation of the function. Clearly, the accuracy of the expansions depends on the order of the DA computation as well as on the size of the interval on the epoch, i.e., on  $\delta t$ .

An example of expansion accuracy is plotted in Figure 3.2. The expansions are centred in  $\Delta t$ . The expansion is then evaluated at different times  $\delta t \in [-2000; +2000]$  sec. The obtained values are subsequently compared with the positions computed pointwise at the same instants  $\Delta t + \delta t$ .

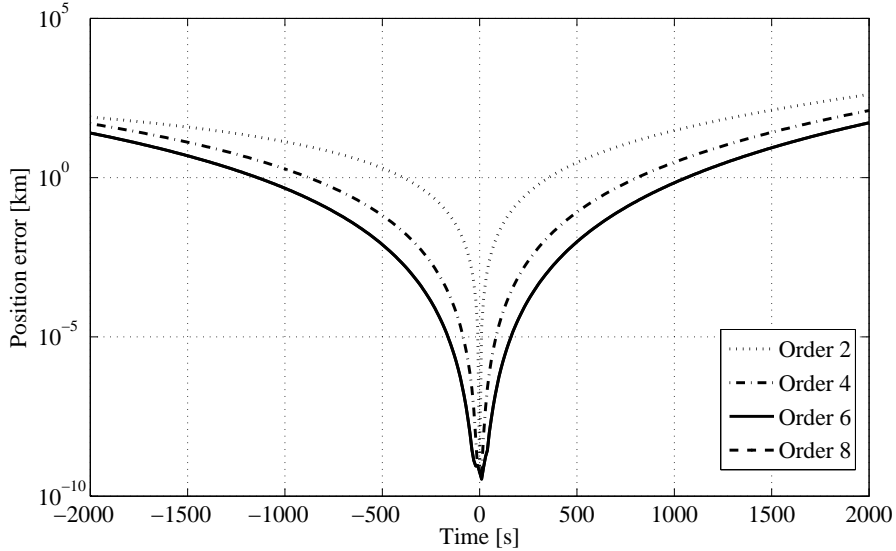


**Figure 3.2:** HANDE: position accuracy for various order of expansion ( $a'_0 = 10263.20$  km,  $e'_0 = 0.312$ ,  $I'_0 = 15.33$  deg,  $\Omega'_0 = 204.44$  deg,  $\omega'_0 = 126.40$  deg,  $\Delta t = 30$  days )

The error has a minimum in the expansion reference point and grows rapidly when  $\delta t$  increases. The accuracy increases if the order is higher. In this case, the 8-th order expansion can not be distinguished from the one at 6-th order. The reason is that the coefficients above 6-th order are too small and are thus truncated.

The expansion of the trajectory obtained with Aksnes' solution is plotted in ECI reference frame in Figure 3.3. The polynomials evaluations are marked with a cross, whereas the punctual values are circles connected with a dashed line. The reference point is at the centre of the arc. It can be

observed that the circles and the crosses coincide in the proximity of the reference point, but they diverge towards the extremities of the arc. The error for each component is graphed in Figure 3.4.

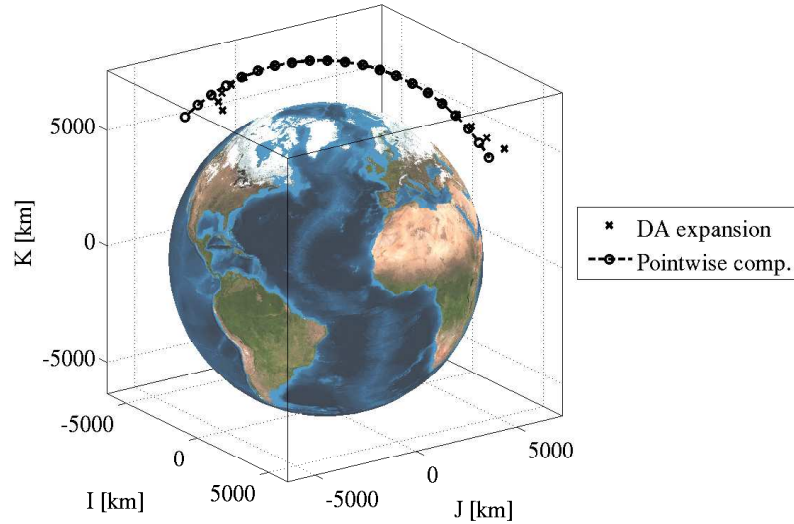


**Figure 3.3:** Aksnes model: comparison of DA expansion and pointwise computation of ECI position ( $a'_0 = 7878.14$  km,  $e'_0 = 0.03$ ,  $I'_0 = 110.0$  deg,  $\Omega'_0 = 0.0$  deg,  $\omega'_0 = 0.0$  deg,  $\Delta t = 150$  days )

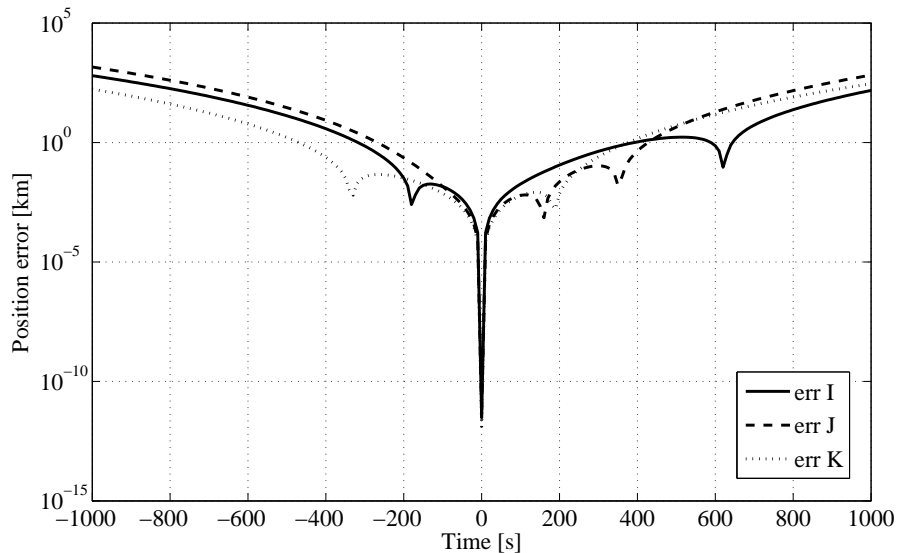


**Figure 3.4:** Aksnes model: error between pointwise and DA evaluation for different times ( $a'_0 = 7878.14$  km,  $e'_0 = 0.03$ ,  $I'_0 = 110.0$  deg,  $\Omega'_0 = 0.0$  deg,  $\omega'_0 = 0.0$  deg,  $\Delta t = 150$  days )

The same plots were obtained with HANDE on the orbit of the satellite KOSMOS 2251 satellite, using an expansion of 6-th order. The expansion and the pointwise computation in Figure 3.5 behave similarly to the previous example, and the evaluated position diverges in the last points of the arc. The error between expanded and pointwise evaluations is reported in Figure 3.6.

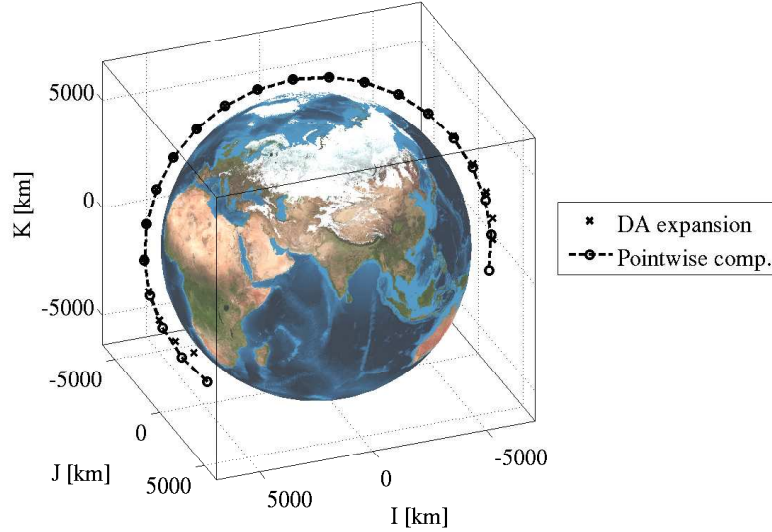


**Figure 3.5:** HANDE: comparison of DA evaluation and pointwise computation of ECI position for KOSMOS 2251 ( $a'_0 = 7168.63$  km,  $e'_0 = 0.00174$ ,  $I'_0 = 74.0$  deg,  $\Omega'_0 = 218.0$  deg,  $\omega'_0 = 194.0$  deg,  $B = 0.02$  m<sup>2</sup>/kg,  $\Delta t = 30$  days)

The same test was performed with the code SGP4, using a GEO orbit. The pointwise evaluation of the position and DA expansion are represented in Figure 3.7. The detail of the error for each component of the position vector is plotted in Figure 3.8. The order of the expansion is 6.

A few considerations can be made analysing Figures 3.2, 3.4, 3.6, and 3.8. First of all, the size of the interval for which the expansion is sufficiently accurate is related to the orbital period. For a LEO satellite like KOSMOS 2251 the maximum  $\delta t$  can be equal to a few thousands seconds. The position of a GEO satellite, instead, can be expanded using  $\delta t$  of a few hours. This behaviour is formalised in Figure 3.9, in which the size of the interval is adimensionalized taking as a reference the orbital period and by computing a proper reference length by setting  $\bar{\mu}_{\oplus} = 1$ . The error approximately has the same magnitude and trend for different values of semi-major axis. The value of  $\delta t$  that assures the desired accuracy of the expansion can indeed be defined as a proper fraction of the orbital period.

Even the eccentricity influences the maximum  $\delta t$ . When the satellite is at his perigee the expansion is less accurate, since nonlinearities increase and smaller variations of time results in larger advances of the satellite. On the contrary, when the satellite is at his apogee,  $\delta t$  can be larger. This behaviour is illustrated in Figure 3.10.

It is worth noting that the time  $\Delta t$ , in which the DA time expansion is centred, does not influences the accuracy of the expansion. In Figure 3.11 the accuracy of the expansion is plotted at different time from reference time  $t_0$  and it can be observed that the curves are nearly coincident.

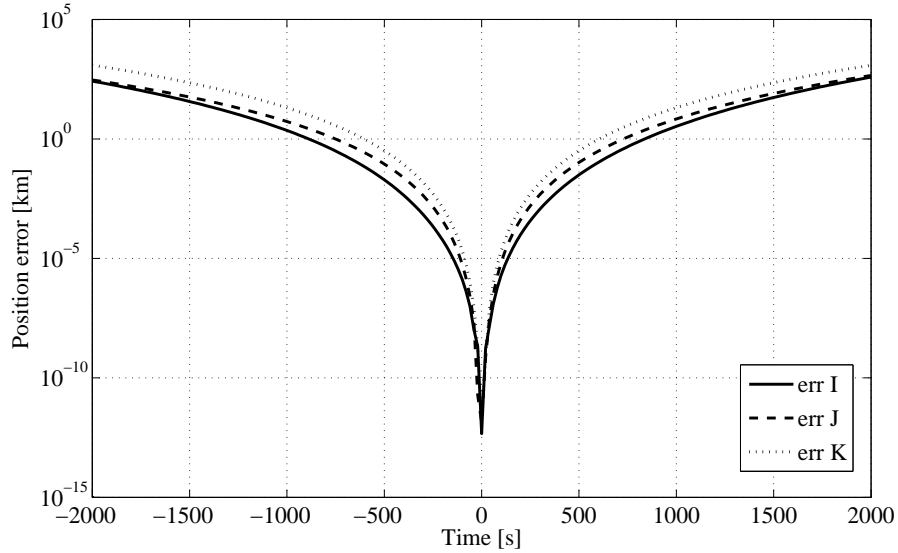


**Figure 3.6:** HANDE: error between KOSMOS 2251 pointwise position and DA evaluation for different times ( $a'_0 = 7168.63$  km,  $e'_0 = 0.00174$ ,  $I'_0 = 74.0$  deg,  $\Omega'_0 = 218.0$  deg,  $\omega'_0 = 194.0$  deg,  $B = 0.02$  m<sup>2</sup>/kg,  $\Delta t = 30$  days).

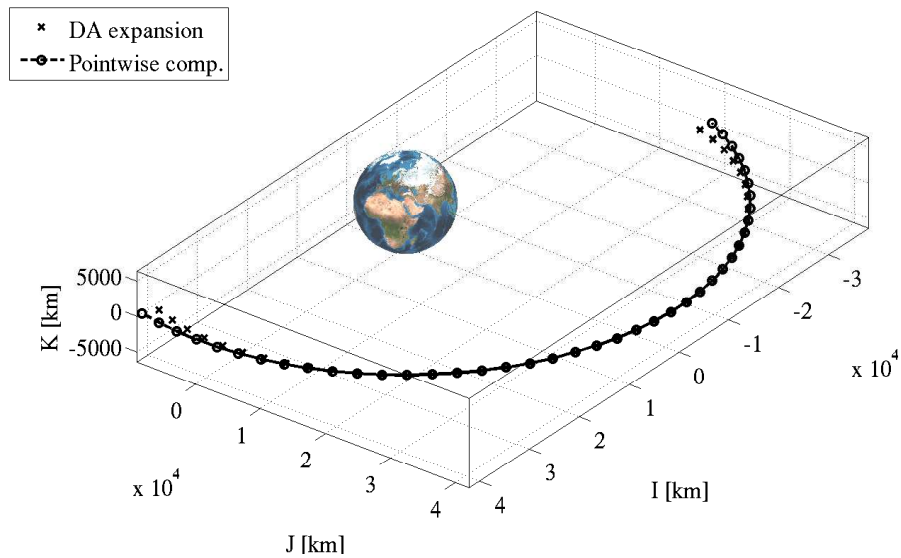


**Figure 3.7:** SGP4: comparison of DA evaluation and numerical computation of ECI position of a GEO satellite ( $a'_0 = 42164.50$  km,  $e'_0 = 5.65 \times 10^{-4}$ ,  $I'_0 = 0.0578$  deg,  $\Omega'_0 = 276.5$  deg,  $\omega'_0 = 4.98$  deg, epoch = JD 2452507.5,  $\Delta t =$  days)

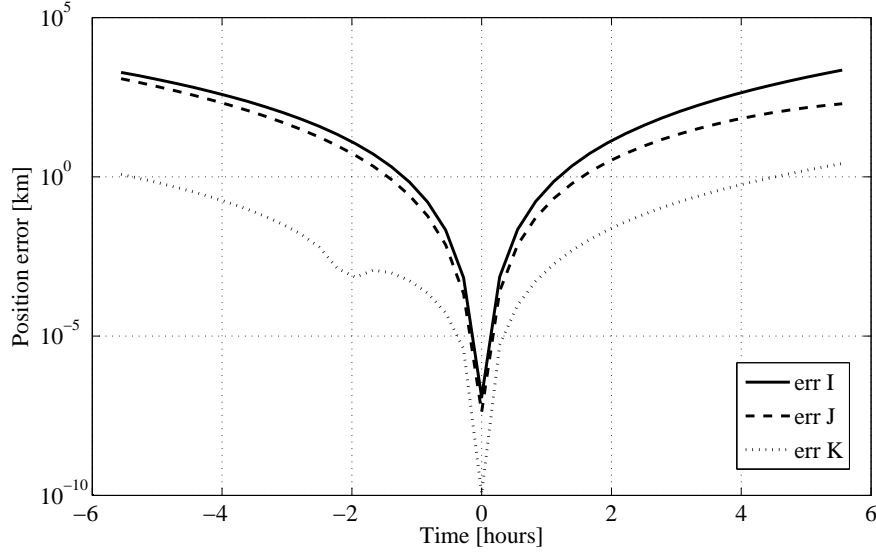


**Figure 3.8:** SGP4: error between GEO satellite pointwise position and DA evaluation for different times ( $a'_0 = 42164.50$  km,  $e'_0 = 5.65 \times 10^{-4}$ ,  $I'_0 = 0.0578$  deg,  $\Omega'_0 = 276.5$  deg,  $\omega'_0 = 4.98$  deg, epoch = JD 2452507.5,  $\Delta t = 200$  days)

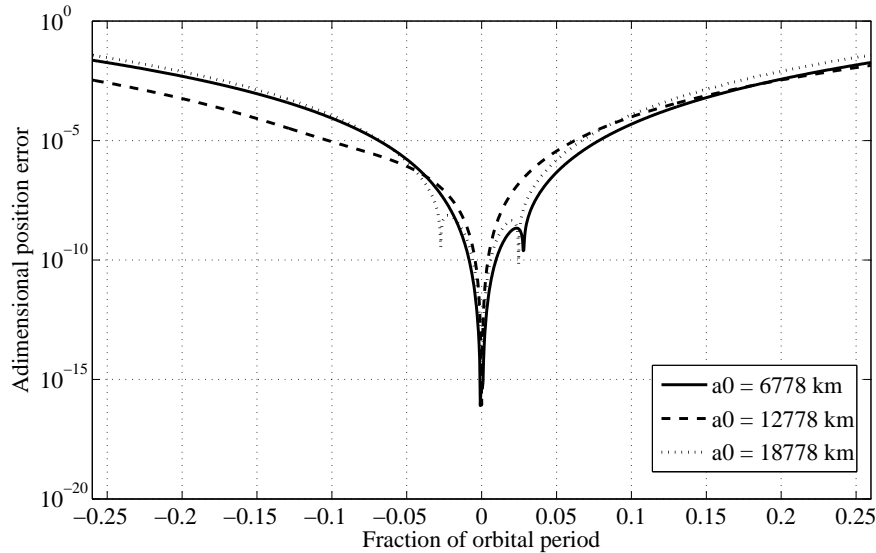


**Figure 3.9:** Aksnes model: position accuracy for different semi-major axis. The curves were adimensionalized, taking as a reference time the orbital period and computing the reference length from the relation  $\bar{\mu}_{\oplus} = 1$  ( $e'_0 = 0.002$ ,  $I'_0 = 63.45$  deg,  $\Omega'_0 = 66.99$  deg,  $\omega'_0 = 140.00$  deg,  $\Delta t = 30$  days)

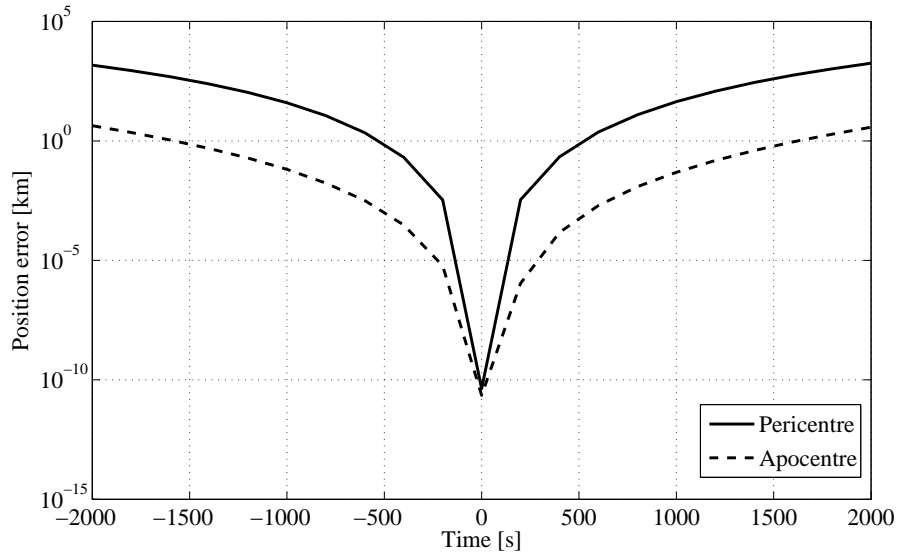


**Figure 3.10:** HANDE: position accuracy for an eccentric orbit, using 6-th order expansion ( $a'_0 = 10263.20$  km,  $e'_0 = 0.312$ ,  $I'_0 = 15.33$  deg,  $\Omega'_0 = 204.44$  deg,  $\omega'_0 = 126.40$  deg,  $\Delta t = 10$  days)

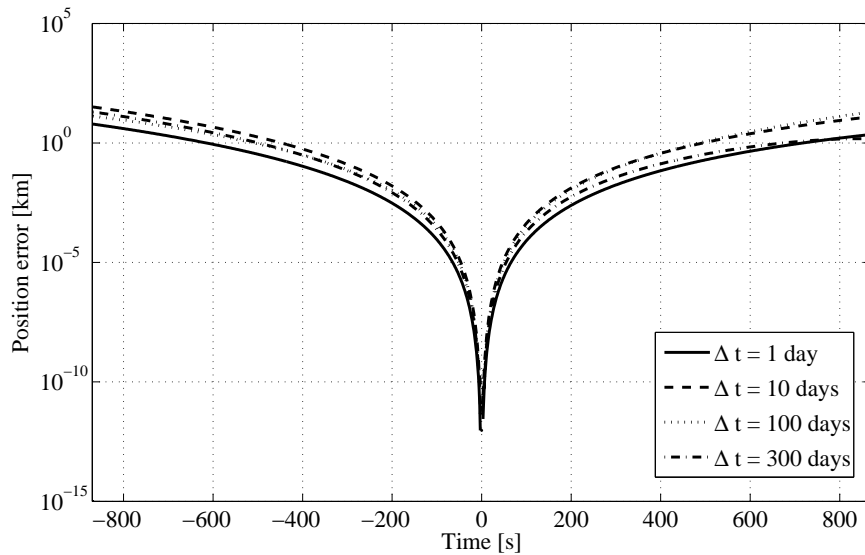


**Figure 3.11:** Aksnes model: position accuracy for different  $\Delta t$ . ( $a'_0 = 7878.136$  km,  $e'_0 = 0.030$ ,  $I'_0 = 110.00$  deg,  $\Omega'_0 = 0.0$  deg,  $\omega'_0 = 0.00$  deg)

### 3.3 Taylor Models

This section introduces the Taylor model (TM) method. Some notes on Taylor Models are presented first based on the Ph.D. thesis of Kyoko Makino [58].

#### 3.3.1 Differential Algebra and Interval Arithmetic

While DA methods can provide the derivatives of functional dependencies and the expansion of the solution of ODEs up to high orders, in a rigorous sense they fail to provide information about the range of the function. A simple example that dramatically illustrates this phenomenon is the function

$$f(x) = \begin{cases} 0 & \text{if } x = 0 \\ \exp(-1/x^2) & \text{else,} \end{cases} \quad (3.55)$$

which is shown in Figure 3.12.

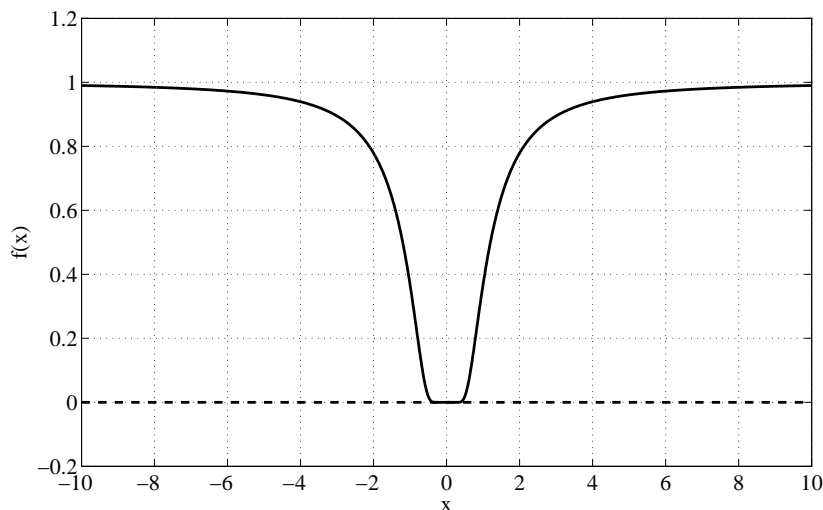


**Figure 3.12:** Function  $f(x) = \exp(-1/x^2)$  if  $x \neq 0$  ; 0 else, and its Taylor polynomial, which vanishes identically.

The value of the function and all the derivatives at  $x = 0$  are 0. Thus the Taylor polynomial at the reference point  $x = 0$  is just the constant 0. In particular, this also implies that the Taylor expansion of  $f$  converges everywhere, but it fails to agree with  $f(x)$  everywhere but at  $x = 0$ .

Rigorous bounds of the range of functions can be obtained instead using the method of Interval Arithmetic (IA) [59]. Within the IA framework, both extended domains of numbers as well as individual real numbers are represented via rigorous inclusions of floating point intervals. Arithmetic operations are introduced on intervals such that, for any two real numbers in two different intervals, a real arithmetic operation on the two real numbers always leads to a result that is contained in the interval obtained from the corresponding arithmetic operation on the two intervals. Table 3.5 lists some elementary properties of interval arithmetic.

By evaluating a function in interval arithmetic, it is thus possible to carry rigorous bounds information through the operations, and in the end obtain rigorous bounds of the function.

**Table 3.5:** Elementary properties of interval arithmetic;  $I_1 = [a_1, b_1], I_2 = [a_2, b_2]$ .

$I_1 + I_2 = [a_1 + a_2, b_1 + b_2]$ $-I_1 = [-b_1, -a_1]$ $I_1 \cdot I_2 = [\min(a_1 a_2, a_1 b_2, b_1 a_2, b_1 b_2), \max(a_1 a_2, a_1 b_2, b_1 a_2, b_1 b_2)]$ $\text{If } 0 \notin I_1, 1/I_1 = [1/b_1, 1/a_1]$
---

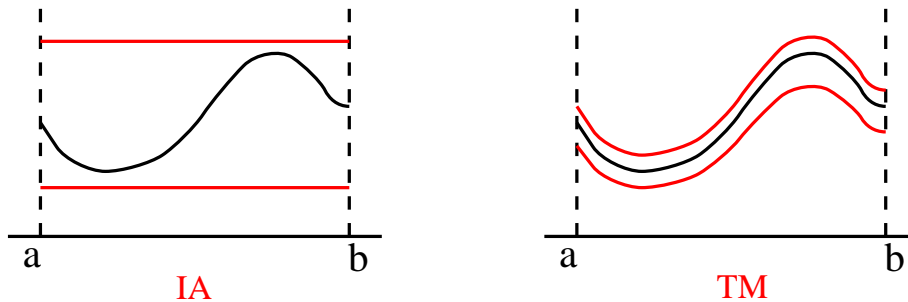
However, while reasonably fast in practice, interval methods have some severe disadvantages, which limits their applicability for complicated functions. First, the width of the resulting intervals scales with the width of the original intervals; and second, artificial blow-up usually occurs in extended calculations. To illustrate the blow-up phenomenon with a trivial example, consider the interval  $I = [a, b]$ , which has the width  $b - a$ . Compute the addition of  $I$  to itself and its subtraction from itself:

$$I + I = [a, b] + [a, b] = [a + a, b + b] = [2a, 2b]$$

$$I - I = [a, b] - [a, b] = [a, b] + [-b, -a] = [a - b, b - a].$$

In both cases the resulting width is  $2(b - a)$ , which is twice the original width, although we know that regardless of what unknown quantity  $x$  is characterized by  $I$ , certainly  $x - x$  should equal zero.

The Taylor Models (TM) method is a method that combines the advantage of rigor of the interval approach, while largely avoiding the blow-up problem through the use of DA techniques. The key idea is to describe the bulk of the functional dependence through a Taylor polynomial, and bound the deviation of the original function from the Taylor polynomial by an interval. Therefore a TM represent a hybrid between formula manipulation, interval methods, and methods of computational differentiation [60, 61] and supply a more accurate enclosure of function over an interval  $[a, b]$  with respect to IA (Figure 3.13).

**Figure 3.13:** Comparison between IA and TM

An  $n$ -th order Taylor model of a multivariate function  $f$  that is  $(n + 1)$  times continuously partially differentiable on the domain  $D$ , consists of the  $n$ -th order multivariate Taylor polynomial  $P$  expanded around a point  $\mathbf{x}_0 \in D$  representing a high order approximation of the function  $f$ , and a remainder error bound interval  $I$  for verification such that

$$\forall \mathbf{x} \in D, \quad f(\mathbf{x}) \in P(\mathbf{x} - \mathbf{x}_0) + I. \quad (3.56)$$

Thus, the Taylor model  $(P, I)$  is a functional enclosure of  $f$  over  $D$ . From Taylor's theorem (see § C.1), it is clear that the width of the remainder interval  $I$  (i.e., the accuracy of the functional enclosure) can be chosen to scale with the domain size proportional to  $|\mathbf{x} - \mathbf{x}_0|^{n+1}$ . The practical computation of  $P$  and  $I$  is based on Taylor model arithmetic, which carries  $P$  and  $I$  through all the operations comprising  $I$  [59]. By choosing the size  $|\mathbf{x} - \mathbf{x}_0|$  small and the order  $n$  sufficiently high, the size of the remainder interval  $I$  can be kept very small in practice. The bulk of the functional dependency is kept in the polynomial part  $P$  with point coefficients, and there is no interval arithmetic-associated inflation that happens in the polynomial part. Thus, the interval-related overestimation is rather optimally suppressed with the Taylor model method [62].

Altogether, the Taylor model approach has the following important properties:

1. The ability to provide enclosures of any function given by a finite computer code list by a Taylor polynomial and a remainder bound with a sharpness that scales with order  $(n + 1)$  of the width of the domain.
2. The computational expense increases only moderately with order, allowing the computation of sharp range enclosures even for complicated functional dependencies with significant dependency problem.
3. The computational expense of higher dimensions increases only very moderately, significantly reducing the "curse of dimensionality".

The implementation of the method in the code COSY Infinity [58, 63] supports binary operations and standard intrinsic functions, as well as the antiderivative operation which widens the applications of the method. In the following section a few details concerning Taylor Models operations are given.

### 3.3.2 Operations on Taylor Models

In this section, tools that allow to efficiently calculate Taylor models for all functions representable on a computer are briefly described. Similarly to differential algebra, the key is to begin with the Taylor model for the identity function, which is trivial, and then successively build up Taylor models for the total function from its pieces. This requires methods to determine Taylor models for sums and products from those of the summands or factors, as well as from intrinsics applied to functions with known Taylor models.

For illustration purposes, details about how Taylor models can be rigorously summed are reported hereafter. Let the functions  $f, g : [\mathbf{a}, \mathbf{b}] \subset \mathbb{R}^v \rightarrow \mathbb{R}$  have Taylor models

$$T_{\alpha, f} = (P_{\alpha, f}, I_{\alpha, f}) \quad \text{and} \quad T_{\alpha, g} = (P_{\alpha, g}, I_{\alpha, g}),$$

which entails that

$$\begin{aligned} \forall \mathbf{x} \in [\mathbf{a}, \mathbf{b}], \quad f(\mathbf{x}) &\in P_{\alpha,f}(\mathbf{x} - \mathbf{x}_0) + I_{\alpha,f} \quad \text{and} \\ g(\mathbf{x}) &\in P_{\alpha,g}(\mathbf{x} - \mathbf{x}_0) + I_{\alpha,g}. \end{aligned}$$

Then it is straightforward to obtain a Taylor model for  $f + g$ ; in fact, for any  $\mathbf{x} \in [\mathbf{a}, \mathbf{b}]$ ,

$$\begin{aligned} f(\mathbf{x}) + g(\mathbf{x}) &\in (P_{\alpha,f}(\mathbf{x} - \mathbf{x}_0) + I_{\alpha,f}) + (P_{\alpha,g}(\mathbf{x} - \mathbf{x}_0) + I_{\alpha,g}) \\ &= (P_{\alpha,f}(\mathbf{x} - \mathbf{x}_0) + P_{\alpha,g}(\mathbf{x} - \mathbf{x}_0)) + (I_{\alpha,f} + I_{\alpha,g}), \end{aligned}$$

so that a Taylor model  $T_{\alpha,f+g}$  for  $f + g$  can be obtained via

$$P_{\alpha,f+g} = P_{\alpha,f} + P_{\alpha,g} \quad \text{and} \quad I_{\alpha,f+g} = I_{\alpha,f} + I_{\alpha,g}. \quad (3.57)$$

Thus we define

$$T_{\alpha,f} + T_{\alpha,g} = (P_{\alpha,f} + P_{\alpha,g}, I_{\alpha,f} + I_{\alpha,g}),$$

and we obtain that  $T_{\alpha,f} + T_{\alpha,g} = (P_{\alpha,f+g}, I_{\alpha,f+g})$  is a Taylor model for  $f + g$ . Note that the above addition of Taylor models is both commutative and associative. The procedure to multiply two Taylor models is similarly introduced and it is detailed in [58].

Having introduced addition and multiplication, the computation of any polynomial of Taylor models can be performed, which turns out to be crucial when intrinsic functions are of interest. In particular, the key idea behind the computation of Taylor models for intrinsic functions is to employ Taylor's theorem of the function under consideration. As an example, consider the exponential function. Assume the Taylor model of the function  $f$ ,  $T_{\alpha,f} = (P_{\alpha,f}, I_{\alpha,f})$ , is already available. Write the constant part of the function  $f$  around  $\mathbf{x}_0$  as  $c_{\alpha,f}$ , which agrees with the constant part of the Taylor polynomial  $P_{\alpha,f}$ , and write the remaining part as  $\bar{f}$ ; that is,

$$f(\mathbf{x}) = c_{\alpha,f} + \bar{f}(\mathbf{x}).$$

A Taylor model of  $\bar{f}$  is then  $T_{\alpha,\bar{f}} = (P_{\alpha,\bar{f}}, I_{\alpha,\bar{f}})$ , where

$$P_{\alpha,\bar{f}}(\mathbf{x} - \mathbf{x}_0) = P_{\alpha,f}(\mathbf{x} - \mathbf{x}_0) - c_{\alpha,f} \quad \text{and} \quad I_{\alpha,\bar{f}} = I_{\alpha,f}.$$

Now we can write

$$\begin{aligned} \exp(f(\mathbf{x})) &= \exp(c_{\alpha,f} + \bar{f}(\mathbf{x})) = \exp(c_{\alpha,f}) \cdot \exp(\bar{f}(\mathbf{x})) \\ &= \exp(c_{\alpha,f}) \cdot \left\{ 1 + \bar{f}(\mathbf{x}) + \frac{1}{2!}(\bar{f}(\mathbf{x}))^2 + \cdots + \frac{1}{k!}(\bar{f}(\mathbf{x}))^k \right. \\ &\quad \left. + \frac{1}{(k+1)!}(\bar{f}(\mathbf{x}))^{k+1} \exp(\theta \cdot \bar{f}(\mathbf{x})) \right\}, \end{aligned}$$

where  $0 < \theta < 1$ . Taking  $k \geq n$ , where  $n$  is the order of the Taylor model, the part

$$\exp(c_{\alpha,f}) \cdot \left\{ 1 + \bar{f}(\mathbf{x}) + \frac{1}{2!}(\bar{f}(\mathbf{x}))^2 + \cdots + \frac{1}{n!}(\bar{f}(\mathbf{x}))^n \right\}$$

is a polynomial of  $\bar{f}$ , of which we can obtain the Taylor model using addition and multiplication rules. The remainder part of  $\exp(f(\mathbf{x}))$ ,

$$\exp(c_{\alpha,f}) \cdot \left\{ \frac{1}{(n+1)!}(\bar{f}(\mathbf{x}))^{n+1} + \cdots + \frac{1}{(k+1)!}(\bar{f}(\mathbf{x}))^{k+1} \exp(\theta \cdot \bar{f}(\mathbf{x})) \right\}, \quad (3.58)$$

will be bounded by an interval. The reader should refer to Makino's Ph.D. thesis [58] for further details.

Similar procedures can be used to obtain Taylor models for other elementary functions. Altogether, it is now possible to compute Taylor models for any function that can be represented in a computer environment along with the mere evaluation of the function by simple operator overloading, in much the same way as the mere computation of derivatives and Taylor polynomials in the DA framework, or interval bounds in interval arithmetic.

## 3.4 COSY-GO

In this section a few hints concerning interval based Global Optimization (GO) are given. After a brief description of Taylor-model-based bounders, the main characteristic of COSY-GO are outlined.

Verified GO needs the determination of rigorous upper and lower bounds of the objective function in order to implement a branch and bound method [64]. The commonly used interval approach has excelled in solving this problem elegantly from both a formal and an implementational viewpoint. However, as outlined in Section 3.3.1, there are situations where the method has limitations for extended or complicated calculations because of the dependency problem, which is characterized by a cancellation of various sub-parts of the function that cannot be detected by direct use of interval methods. This effect often leads to pessimism and sometimes even drastic overestimation of range enclosure. Furthermore, the sharpness of intervals resulting from calculations typically scales linearly with the sharpness of the initial discretization intervals. For complicated problems, and in particular higher dimensions, this sometimes significantly limits the sharpness of the resulting answer that can be obtained [62].

The Taylor model approach enables the computation of fully mathematically rigorous range enclosures while largely avoiding many of the limitations of the conventional interval method [58].

The structure of Taylor models naturally represents a rich resource of information. In particular, the coefficients of the polynomial part  $P$  of a Taylor model are closely related to derivatives. That means when representing a function  $f$  by a Taylor model  $(P, I)$  on a computer, we also obtain the local slope, Hessian and higher order derivatives almost free. When a task is focused on range bounding, those pieces of information become particularly useful.

While range bounding of Taylor Model with interval arithmetic in the naive sense [65] already exhibits superiority over mere interval arithmetic and the more advanced centred form [58], the active utilization of those additional pieces of information in Taylor models has a lot of potential of developing efficient range bounders. Based on this observation, various kinds of Taylor-model-based range bounders have been developed [66], and among them the Linear Dominated Bounder (LDB) and the Quadratic Fast Bounder (QFB) are the backbones of Taylor model based verified global optimizer COSY-GO.

The linear dominated bounder is based on the fact that, for Taylor models with sufficiently small remainder bound, the linear part of the Taylor model dominates the behaviour; this is also the case for range bounding. The linear dominated bounder utilizes the linear part as a guideline for iterative domain reduction to bound Taylor models. Around an isolated interior minimizer, the Hessian of a function  $f$  is positive definite, so the purely quadratic part of a Taylor model  $(P, I)$  which locally represents  $f$ , has a positive definite Hessian matrix  $H$ . The quadratic fast bounder provides a lower bound of a Taylor model cheaply when the purely quadratic part is positive definite. More details on polynomial bounders are given in [67].

COSY-GO [66, 14] is a branch-and-bound optimization code employing local domain reduction techniques exploiting the bounding performances assured by TM methods. Should the global minimum of a sufficiently regular scalar function  $f$  on a given domain  $A \subseteq \mathbb{R}^m$  wished to be evaluated, the algorithm starts with an initial value for the global optimum, the *cutoff* value, and then proceeds on analysing at each step a subdomain for possible elimination or reduction. At each step the following tasks are performed

1. A rigorous lower bound  $l$  of the objective function is obtained on the subdomain of interest using various bounding schemes hierarchically with the hope of showing that  $l$  lies above the already established cutoff value, which will allow elimination of the subdomain. A first assessment is made whether the remainder bound of the Taylor model at hand is sufficiently small; if it is not, then the underlying function exhibits too much detail for modelling by local estimators, and the subdomain is split in the direction of fastest change of the function.
2. If the remainder bound is sufficiently small, as a first test the polynomial part of the objective function is evaluated in interval arithmetic. When it fails to eliminate the box, the LDB bounder is applied. If it also fails to eliminate the box, and if the quadratic part of the polynomial representation of the objective function  $P$  is positive semi-definite, the QFB bounder is applied.
3. If the just studied subdomain of interest cannot be eliminated, but is seen to have a lower bound close to the current cutoff values, domain reduction techniques are brought to bear based on the LDB and QFB algorithms to reduce the subdomain in size. Once these methods are applicable, they will allow to cut the subdomain of interest and rapidly reduce the active volume.
4. The cutoff value is updated using various schemes. First, the linear and quadratic parts of the Taylor polynomial are utilized to obtain a potential cutoff update. In particular, if the quadratic part of the polynomial is positive definite, the minimizer of the quadratic polynomial is tested. If the quadratic part is not positive definite, the minimizer of the quadratic part in the direction of the negative gradient is tested. For objective functions of nontrivial cost, as in the example at hand, also more sophisticated local searches within and near the current subdomain may be carried out.

The algorithm continues to reduce and examine the domain until the minimum dimension allowed is reached. The result of the optimization is the validated enclosure of the minimum of the problem.

COSY-GO has been used in this work with the aim of computing MOID between a Keplerian orbit and a perturbed orbit. To achieve this result, the square distance between two points belonging to the one of the two orbits respectively was used as objective function. More details about this application are given in the following chapter, and the most relevant results are reported.

## Chapter 4

# MOID of perturbed orbits

The aim of this chapter is to describe the procedure for Minimal Orbital Intersection Distance (MOID) computation and to illustrate the most relevant results. Several methods for the computation of MOID between two Keplerian orbits exist. In [68] the close approaches of pairs of satellites are assessed analytically and the resulting equation is solved numerically. A similar but more computationally efficient method is described in [69]. An algebraic solution to the problem for two Keplerian elliptic orbits was provided in [12].

The problem was also solved using a geometrical approach in [13]. This method is divided into two phases: firstly, it is determined whether the two Keplerian orbits intersect, using a geometrical criterion. Subsequently, if there is any intersection, the collision occurrence is analysed by means of the orbital period, with the aim of obtaining the time of the collision.

In [14] the MOID is obtained by means of a global optimization, performed with the code COSYGO (see § 3.4). Even in this case, the considered orbits are Keplerian. The objective function that is processed by the global optimizer is directly the square of the Euclidean distance  $d^2$ . This distance is computed taking into account two points on the first and second orbit respectively. Since the two orbits are Keplerian, the five Keplerian elements  $a_i$ ,  $e_i$ ,  $I_i$ ,  $\Omega_i$ , and  $\omega_i$  are constants and hence  $d^2$  is a function of the true anomalies  $\nu_1$  and  $\nu_2$  (Figure 4.1).

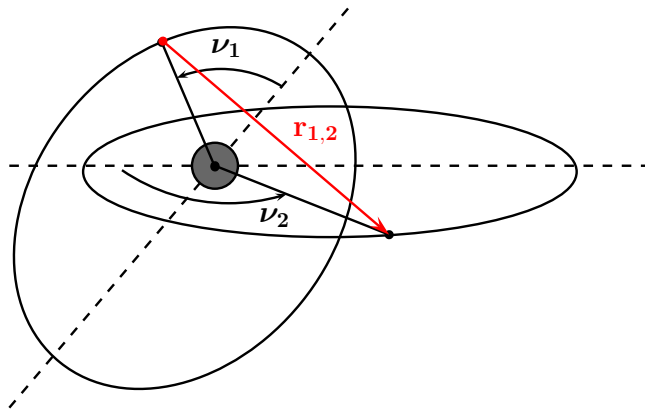


**Figure 4.1:** Distance between two orbits: given the Keplerian elements of both orbits, the distance is univoquely determined by the pair  $(\nu_1, \nu_2)$ .

The position of an object on a Keplerian orbit, written in ECI reference frame, is computed using the following equations

$$r_i = \frac{a_i (1 - e_i^2)}{1 + e_i \cos(\nu_i)}$$

$$\mathbf{r}_i = \begin{Bmatrix} r_{I_i} \\ r_{J_i} \\ r_{K_i} \end{Bmatrix} = r_i \begin{Bmatrix} \cos(\Omega_i) \cos(\omega_i + \nu_i) - \sin(\Omega_i) \cos(I_i) \sin(\omega + \nu_i) \\ \sin(\Omega_i) \cos(\omega_i + \nu_i) + \cos(\Omega_i) \cos(I_i) \sin(\omega + \nu_i) \\ \sin(I_i) \sin(\omega + \nu_i) \end{Bmatrix}. \quad (4.1)$$

It is important to notice that in this case the MOID is not time dependant: it is indeed a mere geometrical property. The square distance  $d^2$  is instead given by

$$d^2 = (r_{I_1} - r_{I_2})^2 + (r_{J_1} - r_{J_2})^2 + (r_{K_1} - r_{K_2})^2. \quad (4.2)$$

A simple test-case can be for MOID computation is represented in Figure 4.2.

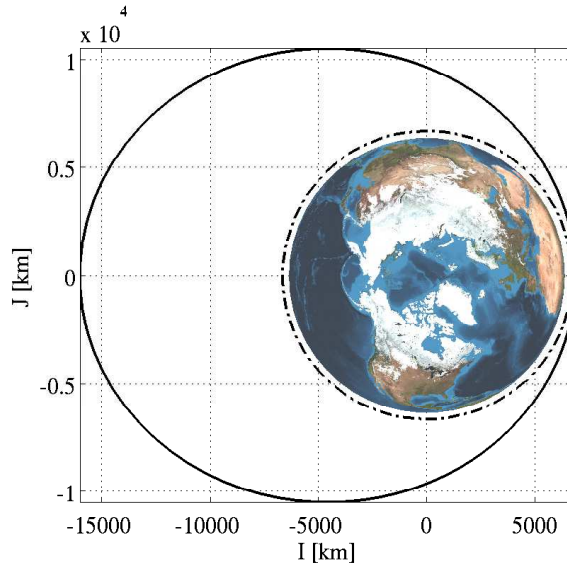


**Figure 4.2:** MOID example: polar view of two Keplerian orbits ( $h_{p_1} = 300$  km,  $h_{p_2} = 500$  km,  $e_1 = 0.0$ ,  $e_2 = 0.4$ ,  $I_1 = I_2 = 0$  deg,  $\Omega_1 = \Omega_2 = 0$  deg,  $\omega_1 = \omega_2 = 0$  deg)

It can be easily verified that the minimum distance is found in the pericentres of the two orbits and is equal to 200 km. The result obtained with COSY-GO, using the objective function defined in Eq. (4.2), is listed in Table 4.1.

The method can indeed compute the correct true anomalies and enclosure of the minimum. The sharpness of the intervals is related to the minimum box size: when the size of the residual domains computed by the optimizer are smaller than this value the iterations are stopped.

Anyway, as already observed in Chapter 2, the perturbations can modify significantly the shape and the orientation of the orbit. The analytical solutions for the artificial satellite problem have been therefore used to compute a more realistic MOID. Since the orbital elements vary with time

**Table 4.1:** Example of MOID computed with COSY-GO

$\nu_1$ [deg]	$\nu_2$ [deg]	<b>d</b> [km]
$[-0.276292\text{E-}04, 0.920974\text{E-}05]$	$[-0.917059\text{E-}05, 0.275118\text{E-}04]$	$[199.9999999, 200.0000001]$

in these analytical models, the objective function  $d^2$  is not only a function of the two anomalies  $\nu_1$  and  $\nu_2$ , but also of time  $t$ .

In Section 4.1 the Aksnes' solution is applied to the object 1 while the object 2 travels on a Keplerian orbit. This situation is similar to the one of an active satellite that performs station keeping manoeuvres, whereas the first object is uncontrolled.

In Section 4.2 HANDE solution is applied to the first orbit instead of Aksnes' one. Similarly, in Section 4.3 the first orbit is geosynchronous and hence SGP4 is used. Finally, in Section 4.4 both orbit are perturbed. The chapter ends with Section 4.5 in which the computed MOID is expanded in terms of the Keplerian elements, e.g. semi-major axis and inclination. Using this DA map the uncertainties on the initial state of the debris can be taken into account too.

## 4.1 MOID with one orbit perturbed by zonal harmonics

In this section it is described the procedure for MOID computation in the case that one of the two orbit is perturbed by Earth's zonal harmonics. The variables associated to the perturbed orbit will be indicated with a subscript 1. To compute the square distance  $d^2$  using Equation (4.2), the positions of the two objects are needed. Since the second orbit is Keplerian, the position is a function of the true anomaly  $\nu_2$  and can indeed be computed as outlined in Eq. 4.1. The position on the first orbit is instead obtained using Aksnes solution, described in Section 2.3.1. As highlighted in the previous section, the MOID is a geometrical information and for this reason it is not correlated to the real position of the object on the orbit. The equations that involves the mean anomaly and true anomaly can hence be dropped. As a result, there is no need to solve Kepler's equation during MOID computation.

With respect to the case of two Keplerian orbits, the search domain becomes three-dimensional, since the argument of the pericentre and the right ascension of the ascending node are now time-dependant. Given the Keplerian elements of both orbits at the same epoch, the square distance can be computed after a proper initialization of the variables required by Aksnes' algorithm. After this, the function  $d^2$  can be computed for any triplet  $(\nu_1, \nu_2, t)$ , belonging to the search domain, following these steps:

- update the variables  $g_1$  and  $h_1$  at time  $t$  using the secular rates  $\dot{g}_1$  and  $\dot{h}_1$ ,
- compute the true longitudes  $u_1 = g_1 + \nu_1$  and  $u_2 = \omega_2 + \nu_2$ ,
- compute the longitude  $\tilde{\lambda}_1$  and latitude  $\tilde{\varphi}_1$  and the components of vector  $\mathbf{r}_1$ ,
- compute the components of vector  $\mathbf{r}_2$ ,
- compute the square distance  $d^2$ .

It can be observed that the periodic perturbations are not applied to the final position. The reason is that these terms are strictly connected to the local position on the orbit, i.e.  $\nu_1$ , but are also dependant on the time  $t$ . Since the value of the true anomaly is merely geometrical in this case, it can not be substituted directly in the equations for the periodic perturbations. Anyway, the periodic perturbations are usually small in amplitude, thus it is sufficient to consider a safety margin of a few kilometres on the MOID to take into account these effects. This means that even small values of MOID, e.g. 1.5 km, are worth of further analytical or numerical investigation, since the occurrence of a collision can not be excluded. It is anyway important to notice that a safety margin must be considered anyway, since uncertainties affect the initial orbital elements.

As already stated, the square distance is a function of the two true anomalies  $\nu_1$  and  $\nu_2$ , and of time  $t$ . The two angles are in the enclosure  $[-180, 180]$  deg, whereas the enclosure of time  $t$  must be related to model accuracy. Since Aksnes' solution shows good accordance with numerical data on the time span of one year (see § 2.3.1), the time is taken in the domain  $\Delta t \in [0, 365]$  days. The units are chosen in order to have a search space with the same magnitude in each direction. Doing so the sharpness of the remaining boxes of each variable is similar.

The MOIDs obtained for a sun-synchronous and a Keplerian orbit are reported. The Keplerian elements of the considered orbits are listed in Table 4.2.

**Table 4.2:** MOID zonal test case: Keplerian elements at epoch

ID	Orbit type	Dynamical model	$a_0$ [km]	$e_0$ -	$I_0$ [deg]	$\Omega_0$ [deg]	$\omega_0$ [deg]
1	Sun-synchr.	Aksnes' sol.	6878.136	0.0	96.99	110.0	70.0
2	MEO	Keplerian	11130.227	0.4	6.5	300	73.0

The MOID of the two unperturbed orbits, using Keplerian elements of Table 4.2, is equal to 1880.083 km. The simulation took 116.736 seconds. According to this value, it would seem that there is no probability of an impact to occur. Anyway, the orbital plane of the sun-synchronous orbit rotates around an axis which is perpendicular to Earth's equatorial plane and, as a result, the actual MOID can be lower.

In Figure 4.3 it is represented a view of the cubical search domain. Each point belonging to one of the cube faces is coloured according to the local value of the square distance. The darker zones are associated to high distance, whereas the lighter to low distances. COSY-GO will split the domain in smaller volumes, retaining only those in which the objective function is below the cut-off value of the current iteration. The iteration are stopped when boxes volumes are smaller than the value provided by the user. The remaining boxes are listed in Table 4.3 whereas the associated enclosure of  $d^2$  is found in Table 4.4. Since COSY-GO provides the validated enclosure of the global minimum (see § 3.4), if this minimum is equal to zero the two bounds must be positive and negative respectively. This condition is verified in this case and hence the two orbits intersect in four occasions. A numerical simulation or an evaluation of the object position at four intersection times are indeed needed, in order to evaluate the occurrence of a collision. Because of the negative bound, the square root of  $d^2$  enclosure will lead to a TM arithmetic failure. Anyway, in this situation, the information provided by the enclosure of  $d^2$  are sufficient to state the the MOID is zero.

The graphical representation of the two orbits at the times listed in Table 4.3 are in the left side of Figures 4.4, 4.5, 4.6, and 4.7. On the right side of each Figure, the contour plot of  $d^2$  at the

**Table 4.3:** MOID of one orbit perturbed by zonal harmonics: remaining boxes

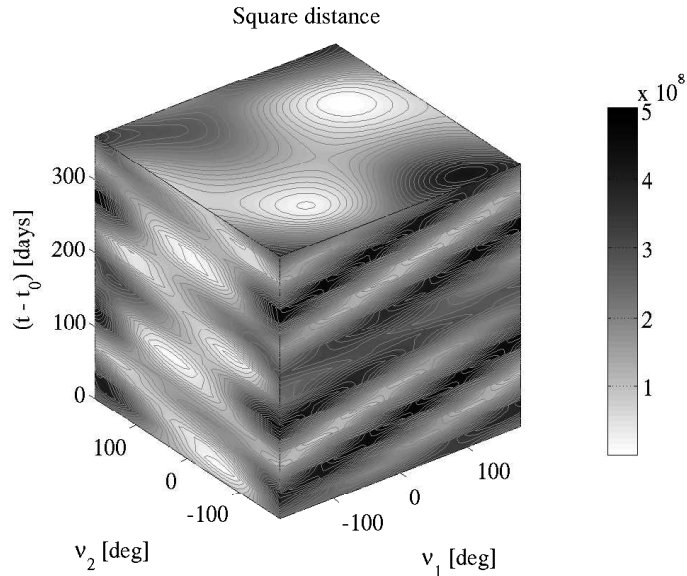
$\nu_1$ [deg]	$\nu_2$ [deg]	$\Delta t$ [days]
[-40.9823329, -40.9823327]	[-26.0738536, -26.0738534]	[61.7190874, 61.7190876]
[155.990229, 155.990231]	[26.0738534, 26.0738536]	[119.068571, 119.068573]
[118.290326, 118.290328]	[-26.0738536, -26.0738534]	[260.826736, 260.826738]
[-39.7805915, -39.7805913]	[26.0738534, 26.0738536]	[318.632662, 318.632664]

**Table 4.4:** MOID of one orbit perturbed by zonal harmonics: enclosure of  $d^2$ 

$d^2$ [km <sup>2</sup> ]
[-0.2225073858507204E-307, 0.5373688376571255E-020]

intersection time are represented. These latter plots can be seen as slices of the volume in Fig. 4.3 along planes at constant  $\Delta t$ . On each figure the corresponding MOID is represented with a cross.

The presented algorithm can compute the minimum distance between two orbits, one of which is perturbed by Earth's zonal harmonics. It has been also verified, through the presented example, that the MOID computed with the approximation of Keplerian orbits is not always sufficient to exclude the occurrence of an intersection. Anyway, since the MOIDs computed using the Aksnes' model can not be higher than the Keplerian MOID, the latter can be used as the initial cut-off value for the global optimizer COSY-GO.

**Figure 4.3:** 3D contour plot of square distance search domain boundaries

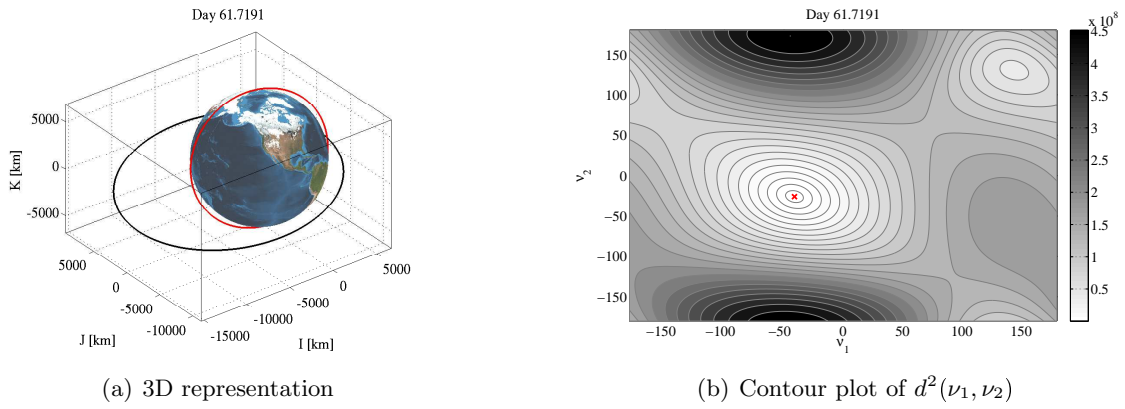


**Figure 4.4:** MOID of one orbit perturbed by zonal harmonics: first intersection

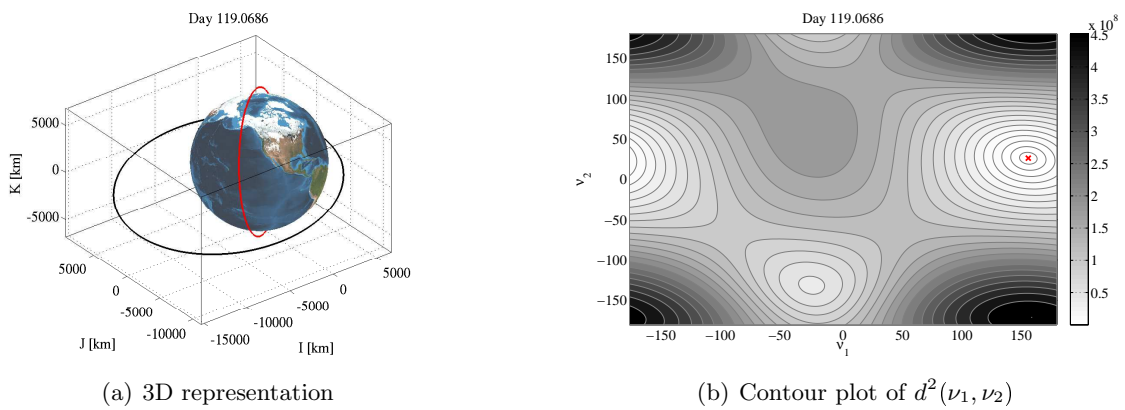


**Figure 4.5:** MOID of one orbit perturbed by zonal harmonics: second intersection

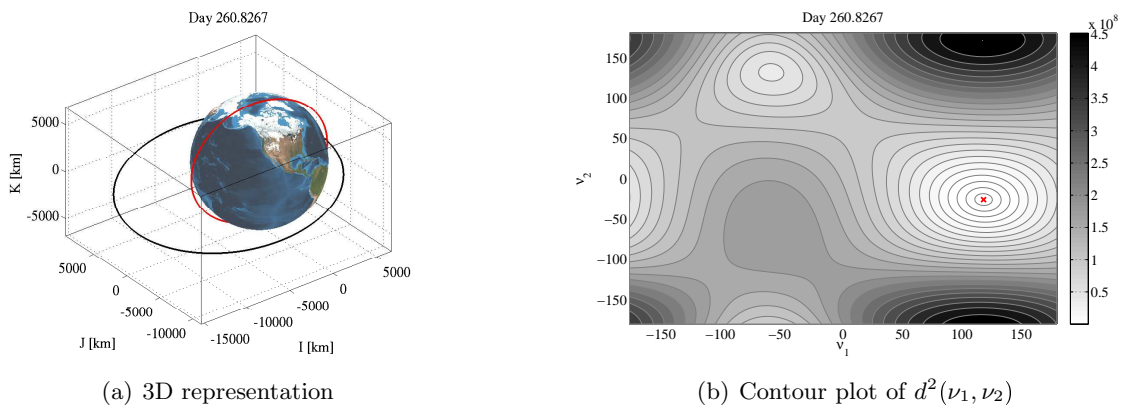


**Figure 4.6:** MOID of one orbit perturbed by zonal harmonics: third intersection

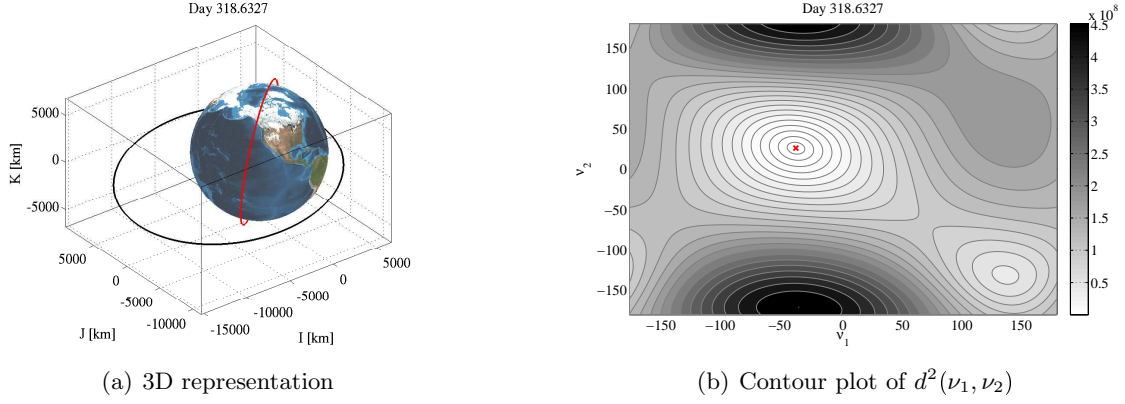


**Figure 4.7:** MOID of one orbit perturbed by zonal harmonics: fourth intersection

## 4.2 MOID with one orbit perturbed by drag and zonal harmonics

In this section the procedure presented in Section 4.1 is extended to the case of an orbit perturbed also by atmospheric drag. The solution adopted to compute the debris position on orbit 1 is HANDE, described in 2.3.2. Given the mean Keplerian elements at epoch, the algorithm can be initialized as usual, computing both secular and long-period periodic coefficients. As in the previous case, the equations involving the mean anomaly are dropped. For any triplet  $(\nu_1, \nu_2, t)$  belonging to the search domain, the procedure to compute the MOID is the following:

- compute the values of the primed variables  $n'_1(t)$ ,  $e'_1(t)$ ,  $I'_1(t)$ ,  $\Omega'_1(t)$  and  $\omega'_1(t)$  using Equations (2.66)-(2.70) and (2.72),
- compute orbit radius  $r'(t, \nu_1)$  by means of Eqs. (2.77)-(2.77),
- compute true longitudes  $u_1 = g_1 + \nu_1$  and  $u_2 = \omega_2 + \nu_2$ ,
- compute the components of the position vector  $\mathbf{r}_1$  with Eqs. (2.83) and (2.84) using primed variables,
- compute the components of the vector  $\mathbf{r}_2$  by means of Eq. (4.1),
- compute the square distance  $d^2$  with Eq. (4.2).

Even in this case the short-period periodic perturbations,  $\delta r$ ,  $\delta u$ ,  $\delta I$ , and  $\delta \Omega$  are not added, since they are function of  $\nu(t)$  and not of the geometrical position  $\nu$ . The computed MOID must hence take into account these possible variations with a proper safety margin.

The domain of the time from epoch variable was defined as  $\Delta t = [0, 365]$  days. The right bound of the interval is larger than the time span on which the full HANDE propagator is reliable, which is approximately 20 days. This is justified since the total position error in HANDE is mainly due to mean anomaly, whose equations are dropped.

The same case of Table 4.2 is considered. The sun-synchronous orbit in this case is perturbed also by atmospheric drag and hence it is expected that the MOIDs will differ from the one listed in Table 4.3.

In Figure 4.8 the value of square distance on the boundaries of the search domain is represented in grey scale. The contour lines, as expected, have the same patterns of Figure 4.3.

The MOIDs obtained in this case are listed in table 4.5. The simulation lasted 222.745 seconds. The enclosure of the true anomaly  $\nu_2$  are the same of the case of the previous section. The MOID even in this case is a really small value, of the order  $10^{-6}$  km, and hence the two orbits intersects. It is worth noting that when dealing with really small positive or null values, the objective function can be bounded with an enclosure that comprises slight negative values.

**Table 4.5:** MOID of one orbit perturbed by drag and zonal harmonics: remaining boxes

$\nu_1$ [deg]	$\nu_2$ [deg]	$\Delta t$ [days]
[-32.1646977, -32.1646975]	[-26.0738536, -26.0738534]	[64.2710642, 64.2710644]
[173.208207, 173.208209]	[26.0738534, 26.0738536]	[123.983661, 123.983663]
[155.658008, 155.658010]	[-26.0738536, -26.0738534]	[271.549212, 271.549214]
[6.05381392, 6.05381398]	[26.0738534, 26.0738536]	[331.709477, 331.709479]

Since the sun-synchronous orbit is a LEO, the effect of drag on the first orbit RAAN (that increases with rate that is slightly lower than 1 deg/day) results in higher values of  $\Delta t$ , since more time is needed to perform the same rotation. The effect is also combined to orbital decay, that reduces semi-major axis and hence changes the position of MOIDs.

The orbits at the intersections and the slices of the search domain of Figure 4.8 at the correspondent instants of time are represented in Figures 4.9, 4.10, 4.11, and 4.12. The patterns of the contour plots are similar to the ones obtained with Aksnes' solution.

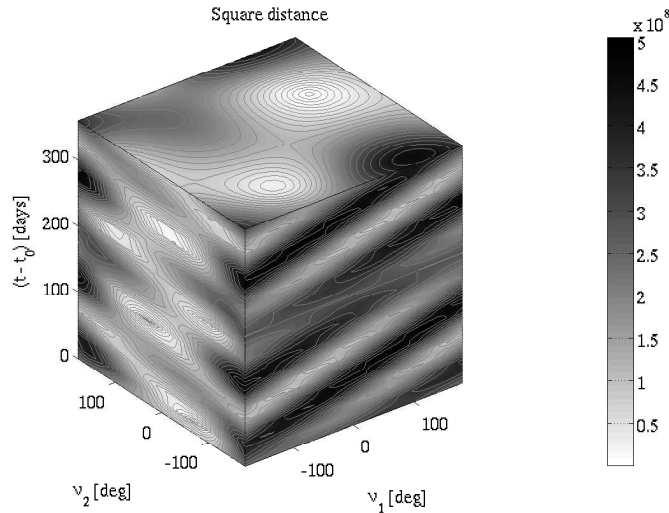


**Figure 4.8:** 3D contour plot of square distance search domain boundaries

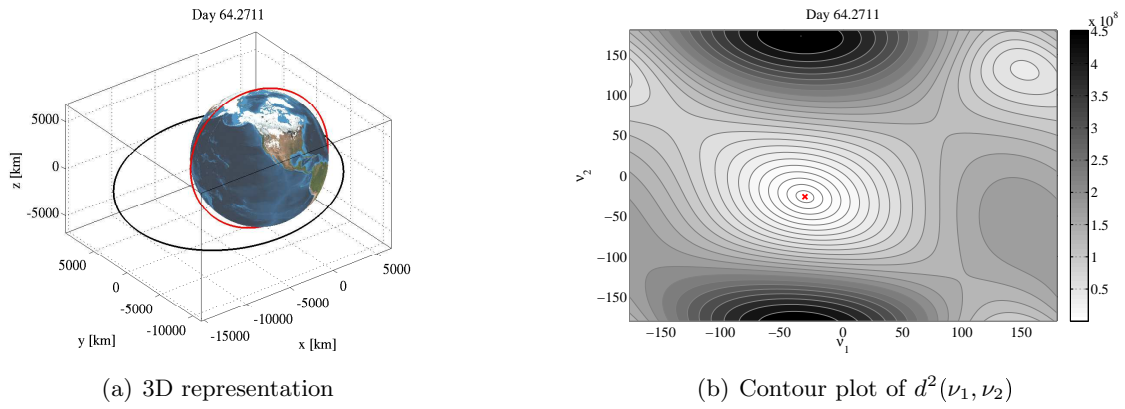


**Figure 4.9:** MOID of one orbit perturbed by drag and zonal harmonics: first intersection

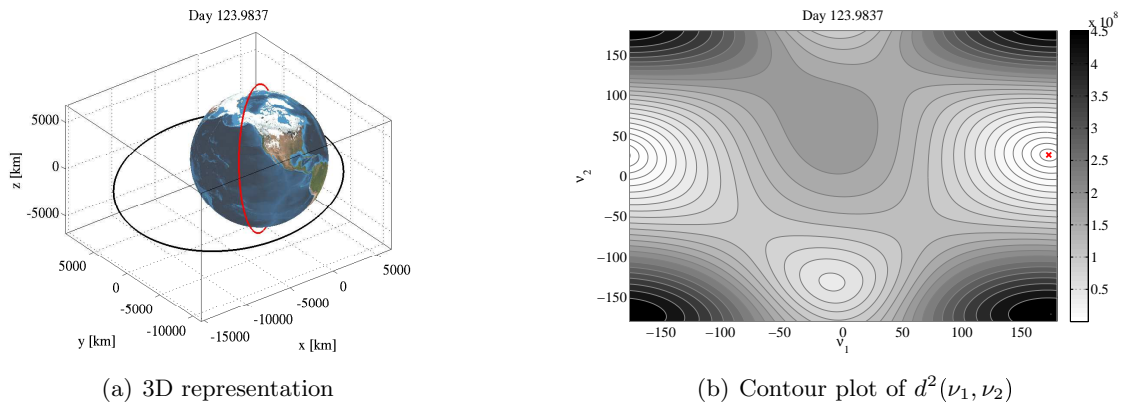


**Figure 4.10:** MOID of one orbit perturbed by drag and zonal harmonics: second intersection

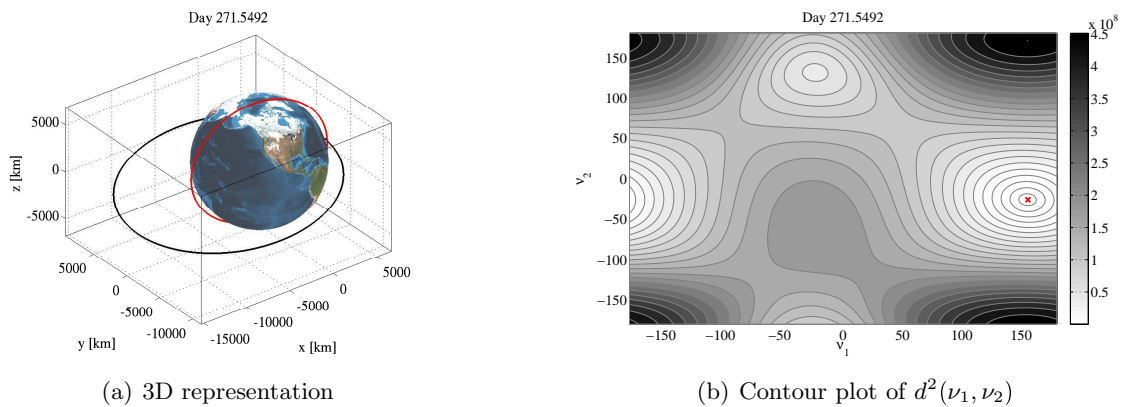


**Figure 4.11:** MOID of one orbit perturbed by drag and zonal harmonics: third intersection

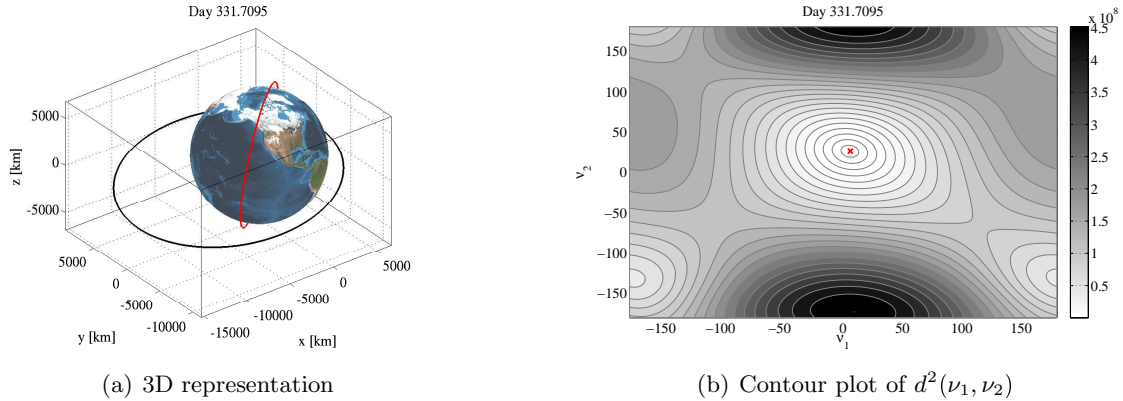


**Figure 4.12:** MOID of one orbit perturbed by drag and zonal harmonics: fourth intersection

The algorithm presented in this section computes the MOID between an orbit perturbed by drag and a Keplerian one. Through the comparison with the solution obtained in the previous section with the same orbits, it was shown that the MOID computed with HANDE is more reliable for LEO since it captures the effects of atmospheric drag.

### 4.3 MOID with one geosynchronous orbit

In this section the MOID computation between a Keplerian orbit and a geosynchronous orbit is presented. This algorithm can be applied to study the chance of impact in the geostationary ring, taking into account e.g. a functional satellite and an uncontrolled one, that is no more able to counter-act the perturbative effects. Alternatively, the satellite on the Keplerian orbit can be travelling on a Geostationary Transfer Orbit (GTO), and it is of interest the possibility of impact with a debris in geosynchronous orbit. The procedure for the computation of the objective function is similar to the one of the previous two cases, with the exception that the position on orbit 1 is computed by means of SGP4 propagator. Like before, the equation related to mean anomaly are dropped and the vector  $\mathbf{r}_1$  is computed using the primed Keplerian elements at time  $t$  and the true anomaly  $\nu_1$ .

The test case presented in this section involves two geosynchronous orbits. The Keplerian elements of each orbit are listed in Table 4.6 and are represented in Figure 4.13. The main difference among the two orbits is their inclination, whereas eccentricity and semi-major axis are nearly the same.

**Table 4.6:** MOID SGP4 test case: Keplerian elements at JD 2455574.974

ID	Orbit type	Dynamical model	$a_0$ [km]	$e_0$ -	$I_0$ [deg]	$\Omega_0$ [deg]	$\omega_0$ [deg]
1	GEO	SGP4	42164.504	$5.65 \times 10^{-4}$	0.058	276.489	4.979
2	Geo-synchr.	Keplerian	42164.136	0.0	12.605	0.0	0.0

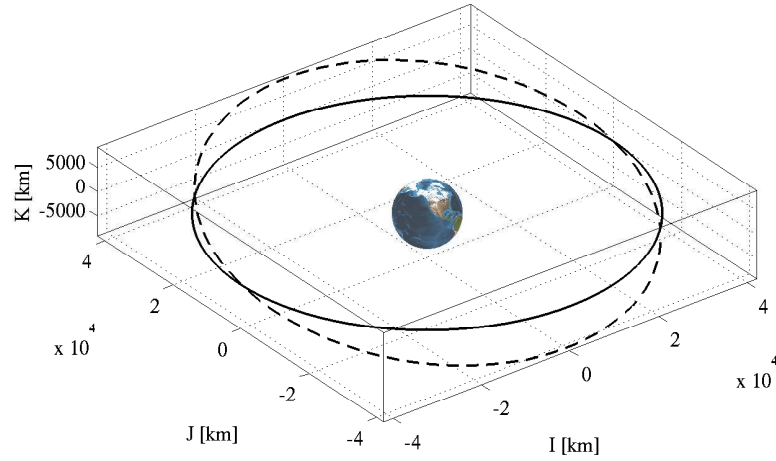


**Figure 4.13:** GEO MOID: 3D representation of test case orbits

The values of the square distance on the boundaries of the search domain are represented in Figure 4.14. Two stripes characterised by low values of the function  $d^2$  can be observed<sup>1</sup>. On the top face the contour lines identify clearly two local minima. This condition can be inferred also observing the two orbits in Figure 4.13, in which the curves nearly coincide in two points, since they have similar semi-major axis.

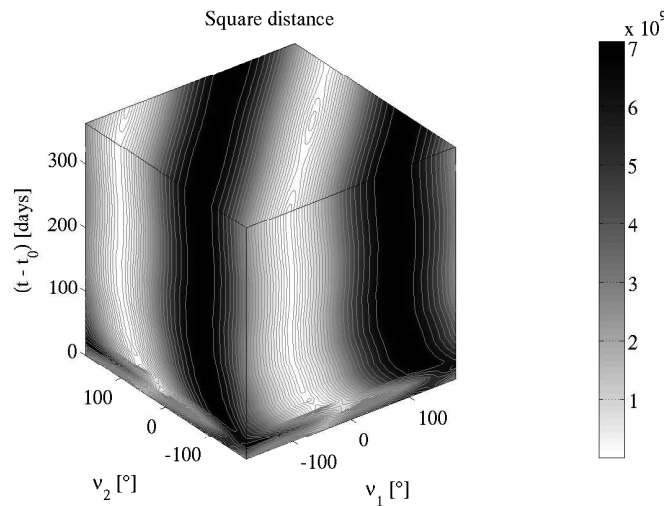
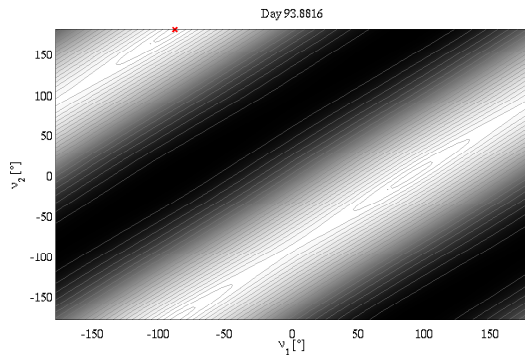


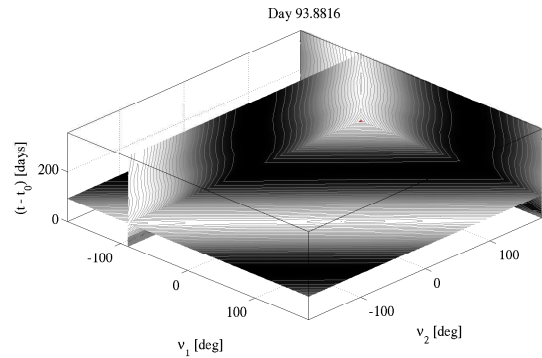
**Figure 4.14:** GEO MOID: contour plot of square distance on search domain boundaries

As a result, the number of intersections between the two orbits in the considered domain is equal to 12268. This really high number is not surprising, since an intersection is found at almost every instant of time. It should be reminded that there is no connection with the real position of the object on its trajectory and hence it is as if for each  $\Delta t$  the whole trajectories are considered to

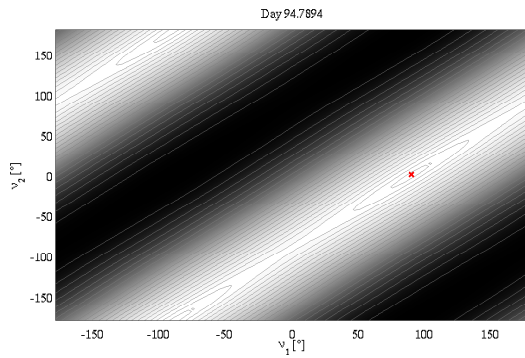
<sup>1</sup>The two stripes are actually the same stripe, because of the periodicity of the true anomalies



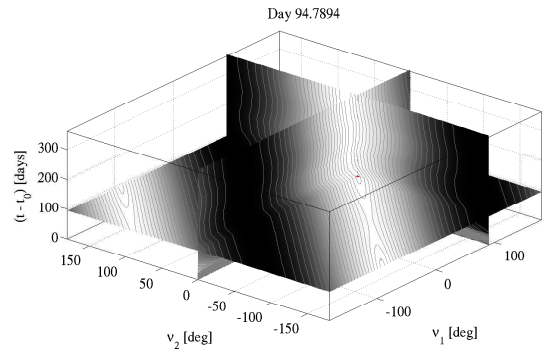
(a) Slice of search domain at constant time



(b) Slices along planes parallel to domain boundaries

**Figure 4.15:** GEO MOID: contour plots at  $\Delta t = 93.8816$ 

(a) Slice of search domain at constant time



(b) Slices along planes parallel to domain boundaries

**Figure 4.16:** GEO MOID: contour plots at  $\Delta t = 94.7894$ 

compute  $d^2$ . The simulation took 12287.074 s in this case, since the number of enclosures is higher than in cases analysed in previous sections.

Two random MOIDs are represented in Figures 4.15 and 4.16. On the right side of each figure, the domain is sliced with three planes parallel to the cube faces that cross each other in the considered MOID. Observing the contour lines that surround the red cross, i.e. the MOID, it can be inferred that the intersections are nearly piled one on each other.

## 4.4 MOID of two perturbed orbits

The natural extension of the methods described in the previous sections is to consider both orbits as perturbed. The case of two orbits under the effect of zonal harmonics and a mixed case in which one orbit is perturbed also by drag are analyzed in this section.

In the case of two orbits perturbed by zonal harmonics the position on both orbits is computed using the procedure outlined in Section 4.1. In the case of drag and zonal harmonics perturbations the algorithm presented in Section 4.2 is used to compute the position on the first orbit, whereas the position on the second one is computed using again the procedure derived from Aksnes' solution in Section 4.1.

The two codes developed have been applied to the two orbits represented in Figure 4.17.

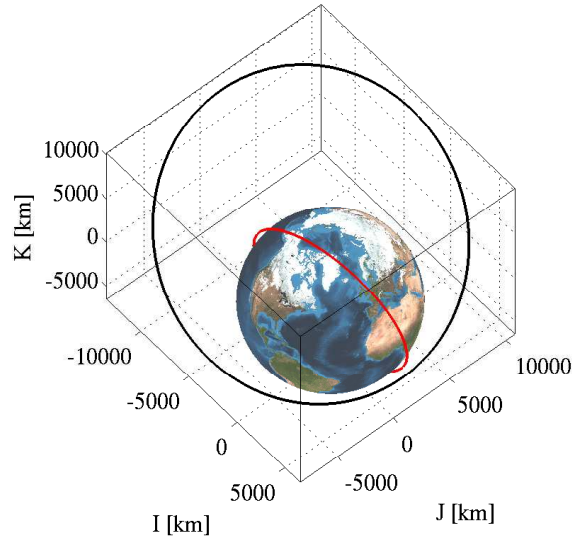


**Figure 4.17:** LEO and MEO orbits at epoch

The Keplerian elements of both orbits are listed in Table 4.7. The MOID computed using the Keplerian elements at epoch is equal to 566.078 km.

**Table 4.7:** MOID between two perturbed orbits: Keplerian elements at epoch

ID	Orbit type	Dynamical model	$a_0$ [km]	$e_0$ [ ]	$I_0$ [deg]	$\Omega_0$ [deg]	$\omega_0$ [deg]	$B$ [m <sup>2</sup> /kg]
1	LEO	Aksnes' sol./ HANDE	6878.136	0.0	96.99	10.0	70.0	0.04
2	MEO	Aksnes' sol.	11596.894	0.4	40.1	45.0	290.0	-

In the first simulation both orbit 1 and 2 have been modelled considering only the perturbations of zonal harmonics, i.e. using Aksnes' model. During the second simulation, instead, orbit 1 was modeled using HANDE solution and hence atmospheric perturbations were considered.

The conditions in which the minimum distance between orbits are reached are listed in table 4.8. On the first row the MOID obtained considering both orbits perturbed only by zonal harmonics is listed. On the second row, instead, the result obtained with the first orbit perturbed also by drag is reported. The enclosures of the square distance  $d^2$  and distance  $d$  are listed in Table 4.9.

**Table 4.8:** MOID between two perturbed orbits, remaining boxes

$\nu_1$ [deg]	$\nu_2$ [deg]	$\Delta t$ [days]
[-54.3726660, -54.3724426]	[-0.543159444E-04, 0.543107579E-04]	[232.454740, 232.454838]
[-63.8203287, -63.8202263]	[-0.819381290E-01, -0.818336669E-01]	[262.328629, 262.328701]

**Table 4.9:** MOID between two perturbed orbits, remaining boxes

$d^2$ [km <sup>2</sup> ]	$d$ [km]
[6399.999999939134, 6400.000000027399]	[79.99999571027648, 80.00000715956220]
[10002.50313857047, 10002.50313873591]	[100.0125082453246, 100.0125259603010]

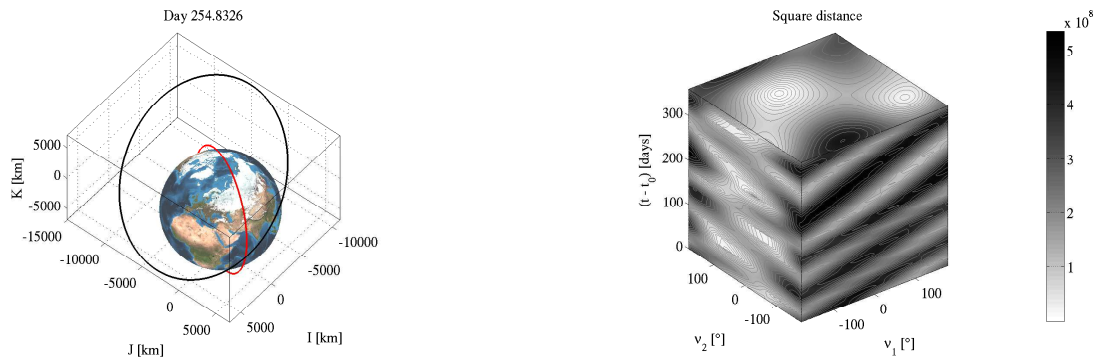
In the first case the obtained minimum distance is approximately 80 km, whereas in the second case it is 100 km. The increment is due to orbital decaying of the LEO orbit. The computational times were 165.022 s and 137.809 s respectively.

The conditions of minimum orbital distance are represented on the left side of Figures 4.18 and 4.21. On the right side of both figures, the contour plot of the square distance on the domain boundaries is represented.

The slices of the domain along the planes at constant times are represented in Figures 4.20 and 4.23. The patterns of the two figures are similar, anyway the drag has changed the position of the minimum.

In Figures 4.19 and 4.22 the search domain is sliced along planes parallel to domain boundaries whose intersection is in MOID coordinates. It can be observed that in this case there is only a lighter area that surrounds the minimum, since there is only situation in which the two orbits get closer. Since the obtained value of MOID is high in this case there is no risk of impact between the two objects. In addition, the effect of drag on the first orbit slowly increases this value.

The described code can hence be used to perform analysis concerning the occurrence of intersections between two perturbed orbits. These codes increase the combinations of orbits that can be taken into account, since the constraint of using one Keplerian orbit is removed. As an example, it is possible to consider a satellite whose orbital plane is rotating and a LEO debris that is under the effect of atmospheric drag.



(a) 3D representation of the orbits at minimum distance time (b) Contour plot of square distance function on search domain boundaries

**Figure 4.18:** MOID between two orbits perturbed by zonal harmonics

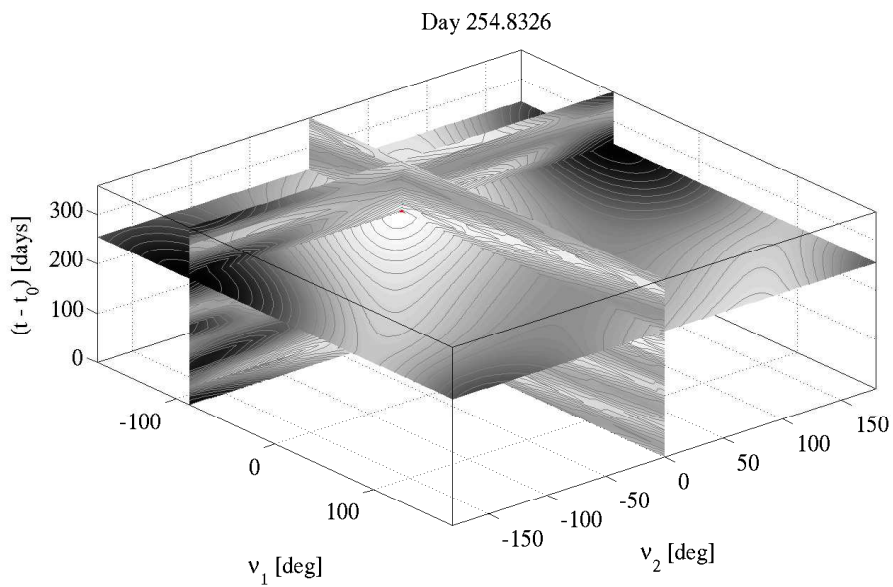


**Figure 4.19:** MOID between orbits perturbed by zonal harmonics: 3D contour plot along planes parallel to domain boundaries

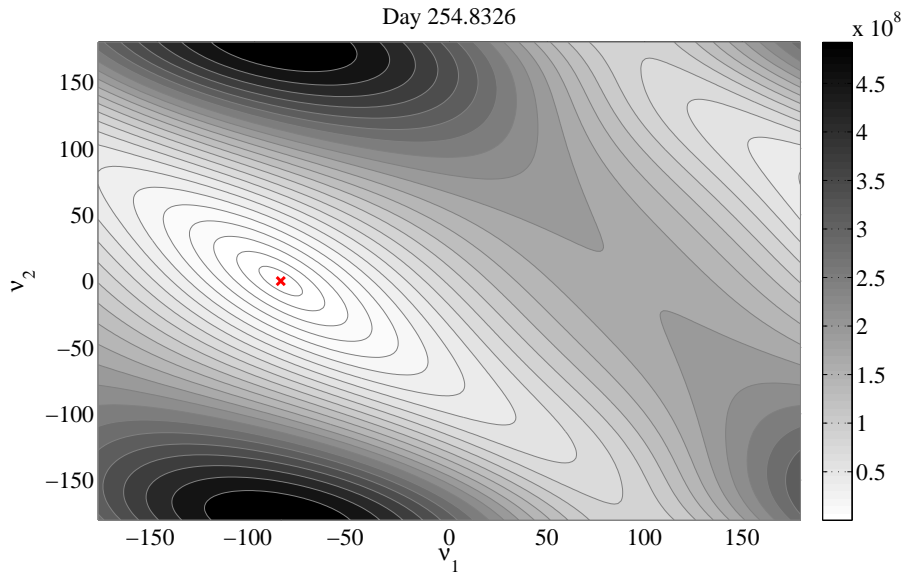
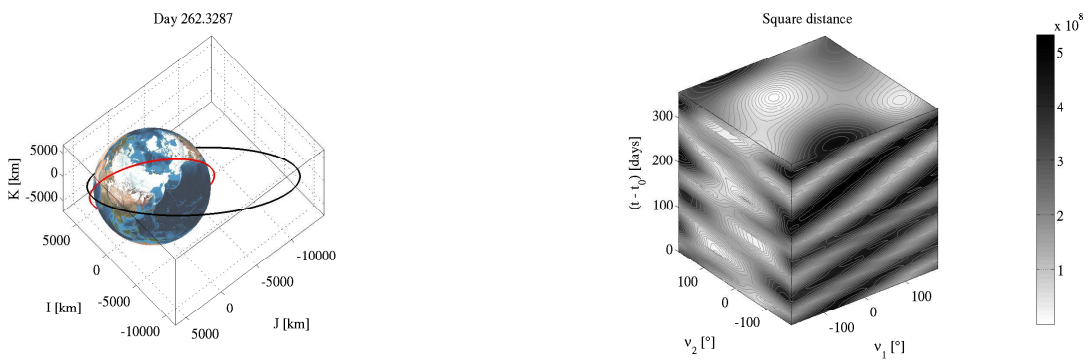


**Figure 4.20:** MOID between two orbits perturbed by zonal harmonics: contour plot of  $d^2(\nu_1, \nu_2)$  at  $\Delta t = 254.8326$  days



(a) 3D representation of the orbits at minimum distance time

(b) Contour plot of square distance function on search domain boundaries

**Figure 4.21:** MOID between two orbits perturbed by zonal harmonics and drag

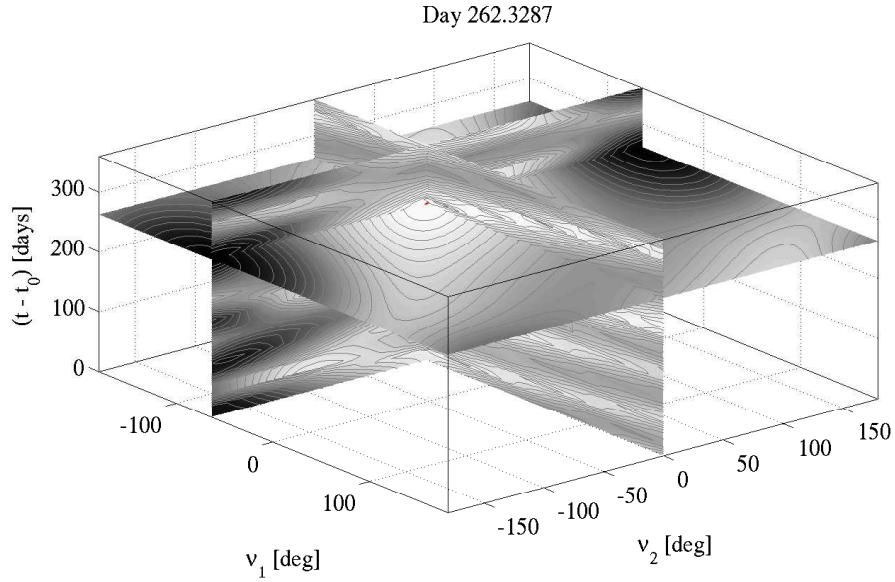


**Figure 4.22:** MOID between two perturbed orbits: 3D contour plot along planes parallel to domain boundaries

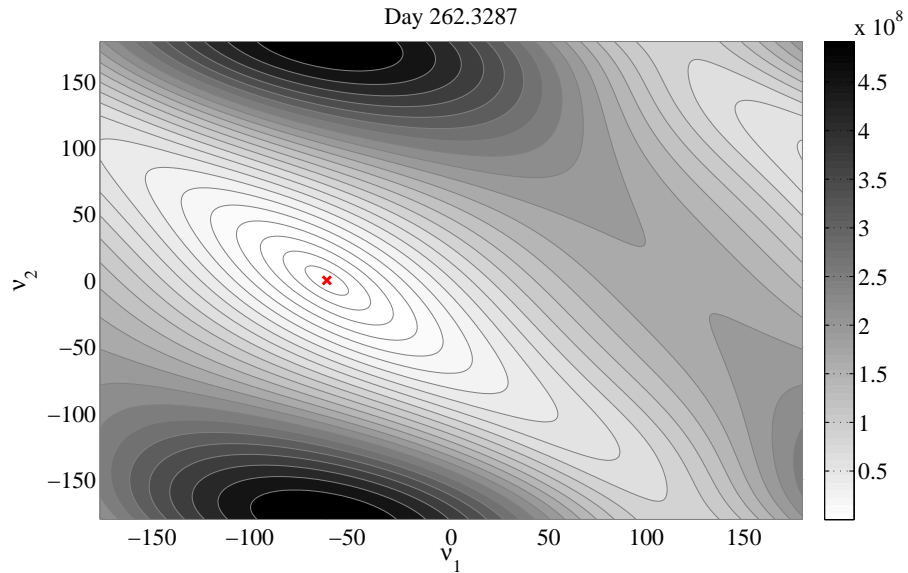


**Figure 4.23:** MOID between two orbits perturbed by zonal harmonics and drag: contour plot of  $d^2(\nu_1, \nu_2)$  at  $\Delta t = 262.3287$  days

## 4.5 DA expansion of MOID

The MOIDs presented throughout this chapter are individuated by three intervals, each one associated to one of the variables of the square distance  $d^2$ . Anyway, the Keplerian elements or, alternatively, the position and velocity vectors at epoch, are affected by uncertainties since they are obtained by orbit determination. The three intervals are indeed influenced by these uncertainties and so is the square distance.

By means of DA techniques, it is possible to obtain an expansion of the MOID in the uncertain Keplerian elements. The expansion of the solution allows a statistical propagation of the uncertainties with a mere evaluation of the polynomials, describing the deviation from the nominal Keplerian elements at epoch with a Gaussian distribution [70]. It is indeed possible to avoid a Monte-Carlo analysis, with considerable reduction of computational time. In the following, the procedure for MOID expansion is described.

Let us consider the MOID computed using the nominal Keplerian elements. The mean values of the enclosures of  $\nu_1$ ,  $\nu_2$ , and  $t$  can be initialized as  $n$ -th order DA variables and so the Keplerian elements:

$$\begin{aligned} [\mathbf{s}] &= \mathbf{s}^0 + \delta\mathbf{s} \\ [\mathbf{p}] &= \mathbf{p}^0 + \delta\mathbf{p}, \end{aligned} \tag{4.3}$$

where  $\mathbf{s}$  is an array that groups  $\nu_1$ ,  $\nu_2$  and  $t$ , whereas  $\mathbf{p}$  is a vector that comprises five Keplerian elements, i.e.  $a$ ,  $e$ ,  $I$ ,  $\Omega$ , and  $\omega$ . Using these DA variables the square distance is obtained following the same steps that are necessary for MOID computation. This DA-based evaluations of  $d^2$  delivers its  $n$ -th order expansion with respect to  $\mathbf{s}$  and  $\mathbf{p}$

$$[d^2] = f([\mathbf{s}], [\mathbf{p}]). \tag{4.4}$$

It is worth noting that the zero-order coefficient of the square distance must belong to the MOID enclosure. Using COSY INFINITY built-in function for derivation, the deviation of  $d^2$  from the MOID is given by means of

$$\delta\mathbf{g} = \nabla_{\mathbf{s}} d^2 = \mathcal{M}_{d^2} (\delta\mathbf{s}, \delta\mathbf{p}), \tag{4.5}$$

in which

$$\nabla_{\mathbf{s}} = \left[ \frac{\partial}{\partial\nu_1}, \frac{\partial}{\partial\nu_2}, \frac{\partial}{\partial t} \right]^T. \tag{4.6}$$

The following map can hence be defined

$$\begin{pmatrix} \delta\mathbf{g} \\ \delta\mathbf{p} \end{pmatrix} = \begin{pmatrix} \mathcal{M}_{d^2} \\ \mathcal{I}_p \end{pmatrix} \begin{pmatrix} \delta\mathbf{s} \\ \delta\mathbf{p} \end{pmatrix}. \tag{4.7}$$

The first three rows of the map represent the gradients of the square distance, computed in the MOID, along the three direction  $\nu_1$ ,  $\nu_2$  and  $t$ . The constant part of these gradients should be small, since this point is a minimum of the function  $d^2$ . The map can be inverted, obtaining:

$$\begin{pmatrix} \delta\mathbf{s} \\ \delta\mathbf{p} \end{pmatrix} = \begin{pmatrix} \mathcal{M}_{d^2} \\ \mathcal{I}_p \end{pmatrix}^{-1} \begin{pmatrix} \delta\mathbf{g} \\ \delta\mathbf{p} \end{pmatrix}. \tag{4.8}$$

The information regarding the deviation of the triplet  $(\nu_1, \nu_2, t)$  from its reference point can be obtained evaluating the map for  $\delta\mathbf{g} = \mathbf{0}$ :

$$\begin{pmatrix} \delta\mathbf{s} \\ \delta\mathbf{p} \end{pmatrix} = \begin{pmatrix} \mathcal{M}_{d^2} \\ \mathcal{I}_p \end{pmatrix}^{-1} \begin{pmatrix} \mathbf{0} \\ \delta\mathbf{p} \end{pmatrix}. \quad (4.9)$$

The first three rows of the map in equation (4.9) are the desired deviations, and can be written as

$$\delta\mathbf{s} = \mathcal{M}_{\delta\mathbf{g}=\mathbf{0}}^{-1}(\delta\mathbf{p}), \quad (4.10)$$

which is the  $n$ -th order Taylor expansion of the MOID triplet  $(\nu_1, \nu_2, t)$  as a function of the Keplerian elements deviations, i.e.

$$\delta\mathbf{s} = \delta\mathbf{s}(\delta\mathbf{p}). \quad (4.11)$$

This result can be used to evaluate the DA-based square distance  $[d^2]$ , retrieving the dependence of the MOID from the deviation of the nominal Keplerian elements, and hence their uncertainties.

In Table 4.11 the map resulting from the expansion of  $d^2$  is listed. To compute this map the remaining boxes on the third row of Table 4.3 were considered. These boxes are reported in Table 4.10.

**Table 4.10:** Reference remaining boxes for MOID expansion test case

$\nu_1$ [deg]	$\nu_2$ [deg]	$\Delta t$ [days]
[118.290326, 118.290328]	[-26.0738536, -26.0738534]	[260.826736, 260.826738]

The orbits taken into account are thus the ones listed in Table 4.2. The square distance was evaluated using the procedure of Section 4.1.

**Table 4.11:** Map of 3-th order MOID expansion in the variables  $a$  and  $I$

I	COEFFICIENT	ORDER	EXPONENTS	
			a	I
1	0.1625767635287872E-07	0	0	0
2	0.1200801263978590E-10	1	1	0
3	0.4134544928646733E-09	1	0	1
4	0.3637978807091713E-11	2	2	0
5	0.1164153218269348E-09	2	1	1
6	-.8642673492431641E-06	2	0	2
7	-.2770983442701436E-10	3	3	0
8	0.3491071936423396E-05	3	2	1
9	0.1583054690854624E-03	3	1	2
10	0.5034525506198406E-01	3	0	3

In this case the expansion is performed on semi-major axis  $a$  and inclination  $I$ . Evaluating this map using the variations of semi-major axis  $\delta a$  and inclination  $\delta I$  from their nominal values, the deviation of  $d^2$  is obtained. Since the magnitude of the coefficients of the expansion increase with order in this case, it can be expected that the square distance will vary considerably only with large values of  $\delta a$  and  $\delta I$ .

In Figures 4.24, 4.25, and 4.26 the deviation  $\delta\nu_1$ ,  $\delta\nu_2$ , and  $\delta t$  from the mean values of corresponding remaining boxes are represented. The contour plots are obtained evaluating the three polynomials of the variables  $\nu_1$ ,  $\nu_2$  and  $t$  obtained with Equation (4.10) on the domain  $\delta a \in [-20, 20]$  km and  $\delta I \in [-1.5, 1.5]$  deg.

The true anomaly  $\nu_2$  is less affected by the uncertainties on the nominal  $a$  and  $I$ , since the maximum deviation has a magnitude of a few degrees. On the opposite, the time of intersection  $t$  and the true anomaly of the first orbit are much more affected. The reason is that the nominal orbit 1 is Sun-synchronous and hence a variation on semi-major axis and inclination changes the rates of variation of the right ascension of the ascending node and argument of pericentre. As outlined in Chapter 2, these rates are directly connected to the inclination of the orbit. It is not surprising that the variation of true anomaly  $\nu_1$  in Figure 4.24 and time  $\Delta t$  in Figure 4.26 is higher when moving in a direction parallel to  $\delta I$  axis.

On the contrary, the true anomaly  $\nu_2$  is more affected by the variation of semi-major axis. The contour levels in Figure 4.25 are parallel to the axis  $\delta I$  in the central area of the plot, and hence the direction of maximum variation is parallel to  $\delta a$  axis.

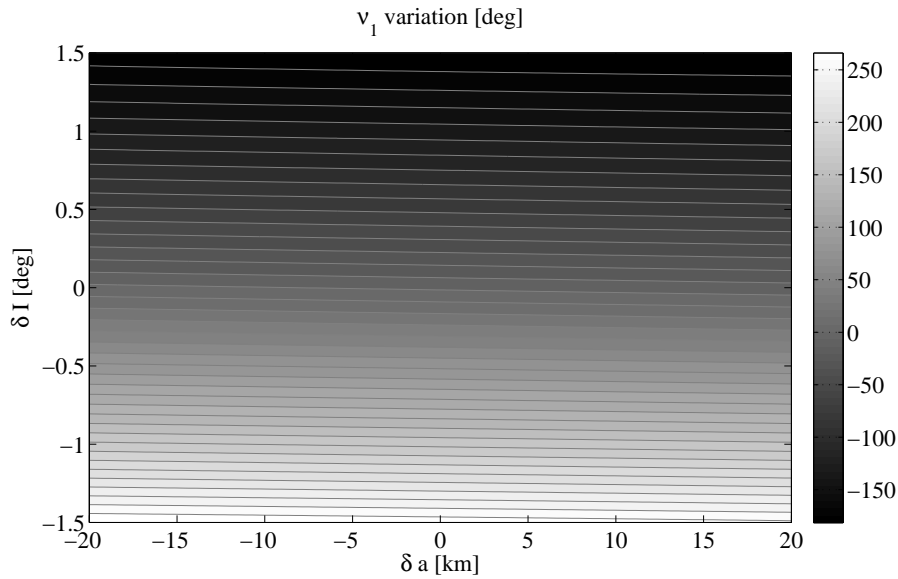


**Figure 4.24:** Contour plot of  $\nu_1$  7-th order expansion in the variables  $a$  and  $I$

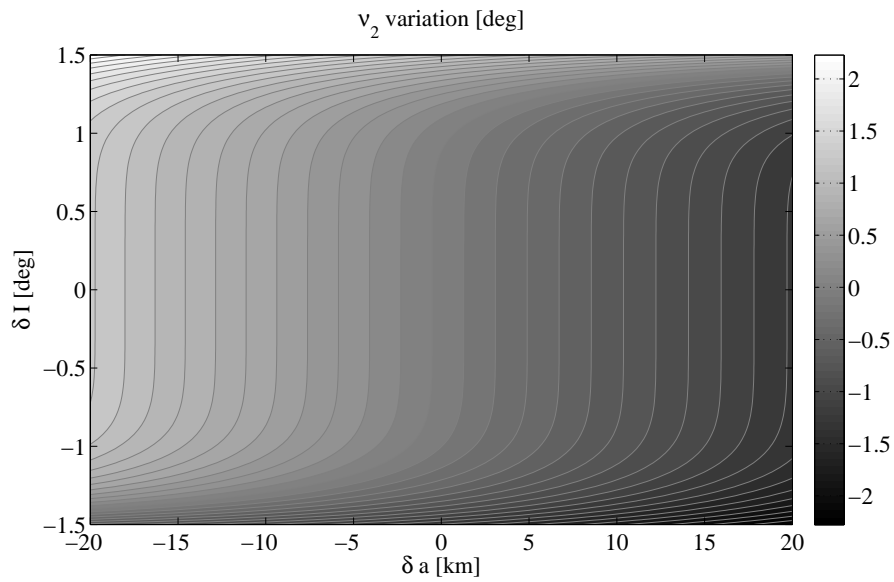


**Figure 4.25:** Contour plot of  $\nu_2$  7-th order expansion in the variables  $a$  and  $I$

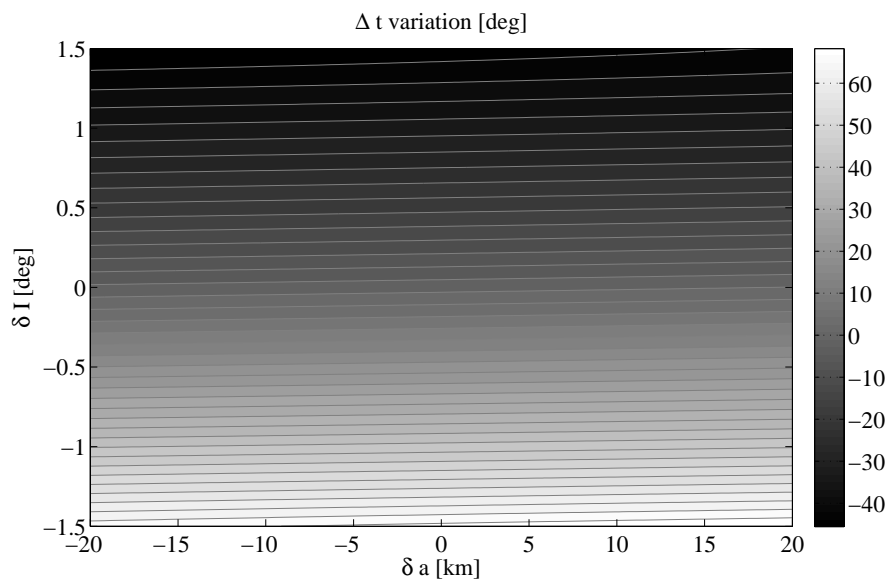


**Figure 4.26:** Contour plot of  $\Delta t$  7-th order expansion in the variables  $a$  and  $I$

The updated values of  $\bar{\nu}_1$ ,  $\bar{\nu}_2$  and  $\bar{\Delta t}$  obtained by means of MOID expansion are listed in Table 4.12. These values can be compared with those listed in Table 4.13, that groups the enclosures computed with COSY-GO initializing semi-major axis and inclination as

$$\begin{aligned}\tilde{a}_0 &= a_0 + \delta a \\ \tilde{I}_0 &= I_0 + \delta I ,\end{aligned}\tag{4.12}$$

were  $\delta a$  and  $\delta I$  are the same variation considered in the corresponding MOID expansion.

**Table 4.12:** Values of  $\nu_1$ ,  $\nu_2$ , and  $\Delta t$  at orbit intersection obtained through MOID expansion

ID	$\delta a$ [km]	$\delta I$ [deg]	$\bar{\nu}_1$ [deg]	$\bar{\nu}_2$ [deg]	$\bar{\Delta t}$ [days]
1	-15	-0.12	140.315869373514	-25.0883017102153	264.46377187495
2	-15	0.12	104.588479303045	-25.0883013063000	255.598745634253
3	15	-0.12	132.563412339712	-27.0218382649598	266.274218872641
4	15	0.12	97.1266099281829	-27.0218376510964	257.348134586662
5	2	1	-12.6932623707262	-26.1177917342817	228.614353900223
6	2	-1	-71.318128057237	-26.2780198640129	304.116603994195
7	-18	1.2	-30.4855505320096	-24.676274417113	222.231168329763

**Table 4.13:** Remaining boxes obtained with perturbed Keplerian elements at  $t_0$

$\delta a$ [km]	$\delta I$ [deg]	$\nu_1$ [deg]	$\nu_2$ [deg]	$\Delta t$ [days]
-15	-0.12	[140.315861, 140.315863]	[-25.0883035, -25.0883033]	[264.463757, 264.463759]
-15	0.12	[104.588470, 104.588472]	[-25.0883035, -25.0883033]	[255.598730, 255.598732]
15	-0.12	[132.563419, 132.563421]	[-27.0218364, -27.0218362]	[266.274235, 266.274237]
15	0.12	[97.1266150, 97.1266152]	[-27.0218364, -27.0218362]	[257.348150, 257.348152]
2	1	[-13.0321015, -13.0321013]	[-26.2023310, -26.2023308]	[228.518669, 228.518671]
2	-1	[-71.0143378, -71.0143376]	[-26.2023310, -26.2023308]	[304.202362, 304.202364]
-18	1.2	[-31.3272880, -31.3272877]	[-24.8862947, -24.8862945]	[221.993721, 221.993723]

The values obtained from the expansion are comparable with those obtained by global optimization. The difference between the enclosures and the values obtained through polynomial evaluation increases as the variation  $\delta a$  and  $\delta I$  becomes larger.

The contour plot of the  $d^2$  map is plotted in Figure 4.27. Since the variations of semi-major axis and inclination are small, the magnitude of the square distance variation is limited to  $10^{-4}$  km<sup>2</sup>. In the middle of the domain the function has a plateau, as the variation of semi-major axis

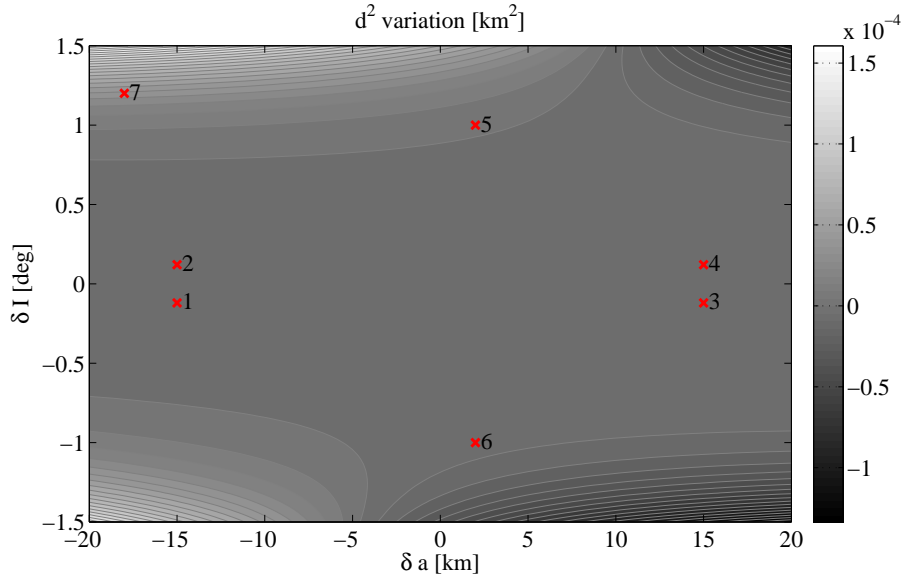


**Figure 4.27:** Contour plot of  $d^2$  7-th order expansion in the variables  $a$  and  $I$ . The red crosses represent the position of the evaluated MOIDs listed in Table 4.12

and inclination are not sufficient to avoid the intersection. In the corner of the domain the function rapidly grows. Actually the distance between orbits in that region is still null and thus the map is becoming less accurate.

Taking into account the data in Tables 4.12 and 4.13, it is interesting to note that the accuracy of the points on the plateau is higher than those of points 5 and 7. In particular, the error increases moving from point 6 to 5 and from 5 to 7, i.e. moving away from the plateau. Thus, the contour plot of the square distance function provides information on the accuracy of the MOID expansion.

In the previous example the MOID was expanded using as a reference point the mean value of the boundaries in Table 4.10. These points are not, in general, the real MOIDs. The real MOID can be anyway retrieved using the mean values of the intervals. Instead of evaluating the inverse map as in equation (4.9), the DA vector  $\delta\mathbf{g}$  can be initialized as

$$\delta\mathbf{g} = -\mathbf{g}_0 + \mathbf{0}, \quad (4.13)$$

where  $\mathbf{g}_0$  is a vector that has, on each row, the correspondent zeroth-order coefficient of the map  $\nabla_s d^2$  and  $\mathbf{0}$  is a DA null vector. Through the polynomial evaluation

$$\begin{pmatrix} \delta\mathbf{s} \\ \delta\mathbf{p} \end{pmatrix} = \begin{pmatrix} \mathcal{M}_{d^2} \\ \mathcal{I}_p \end{pmatrix}^{-1} \begin{pmatrix} \delta\mathbf{g} \\ \delta\mathbf{p} \end{pmatrix}, \quad (4.14)$$

the DA vector  $\delta\mathbf{s}$  is obtained. This vector represents the variation of the variables  $\nu_1$ ,  $\nu_2$  and  $\Delta t$  to be added to the mean values of the MOID enclosures in order to set  $d^2 = 0$ .

Using the updated values of  $\nu_1$ ,  $\nu_2$ , and  $t$  the procedure for MOID expansion is repeated from the beginning. The 3th-order expansion of  $d^2$  obtained after this procedure is listed in Table 4.14. With respect to the map in Table 4.11 the coefficients up to first order disappear. The zeroth-order coefficient are null since the square distance is computed in the intersection point, whereas the first order coefficients are null since the polynomial is evaluated in  $\delta\mathbf{g} = \mathbf{0}$ .

**Table 4.14:** Map of 3-th order MOID expansion in the variables  $a$  and  $I$  after initial guess update

I	COEFFICIENT	ORDER	EXPONENTS	
			a	I
1	-.1303851604461670E-07	2	2	0
2	-.8940696716308594E-07	2	1	1
3	-.7450580596923828E-07	2	0	2
4	0.1280568540096283E-08	3	3	0
5	-.2357410266995430E-07	3	2	1
6	0.1026783138513565E-06	3	1	2
7	0.4377216100692749E-07	3	0	3

In Table 4.15 the values obtained with the updated MOID expansion are listed. Since the enclosures of the variables  $\nu_1$ ,  $\nu_2$ , and  $\Delta t$  used to compute the MOID expansion are tight the differences between values of Table 4.12 and 4.15 are really small. As a consequence, the contour plots of the deviation  $\delta\nu_1$ ,  $\delta\nu_2$ , and  $\delta t$  from the mean values are the same of Figures 4.24, 4.25, and 4.26.

**Table 4.15:** Values of  $\nu_1$ ,  $\nu_2$ , and  $\Delta t$  at orbit intersection obtained through updated MOID expansion

ID	$\delta a$ [km]	$\delta I$ [deg]	$\bar{\nu}_1$ [deg]	$\bar{\nu}_2$ [deg]	$\bar{\Delta t}$ [days]
1	-15	-0.12	140.315860000742	-25.0883040100362	264.463770536092
2	-15	0.12	104.588472601323	-25.0883029990453	255.598745036546
3	15	-0.12	132.563418686739	-27.0218367017426	266.274221966526
4	15	0.12	97.1266175399908	-27.0218356907520	257.348138050807
5	2	1	-12.6932546389250	-26.1177894045751	228.614357429053
6	2	-1	-71.3181355366740	-26.2780214885882	304.116603197501
7	-18	1.2	-30.4855482142236	-24.6762736357758	222.231170290321

The contour plot of the square function is represented in Figure 4.28. As in Figure 4.27 there is a plateau in the middle of the domain and thus the same considerations can be made for the evaluation of the error. Anyway, since the first order coefficients of the map have disappeared after the update of the reference value, the contour levels have different shapes. It can be observed that the evaluated square distance rapidly grows for a variation of inclination above 1 deg.

In this case the maximum deviation of the MOID is of the order of  $10^{-5}$  and hence lower than the one in Figure 4.27, since the reference values are closer to the real MOID.

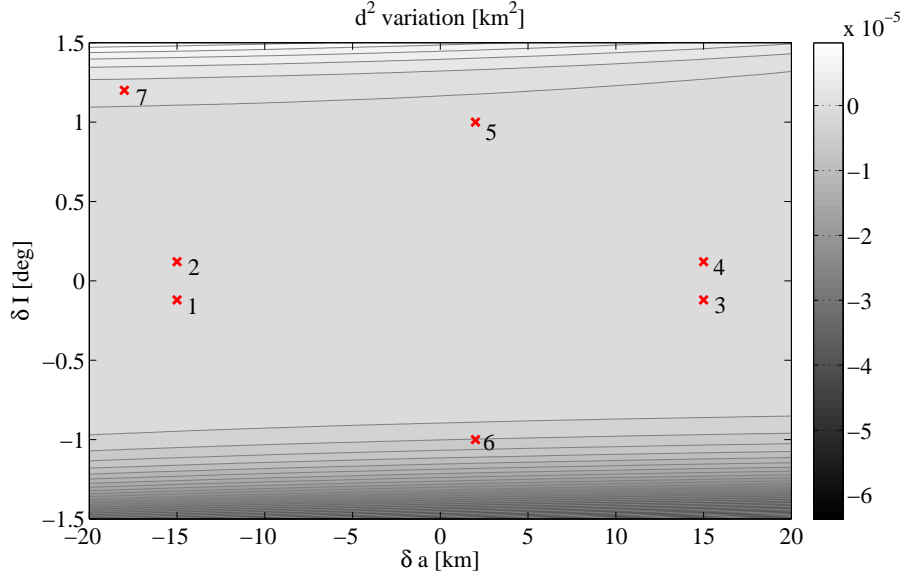


**Figure 4.28:** Contour plot of  $d^2$  7-th order expansion in the variables  $a$  and  $I$  for updated MOID. The red crosses represent the position of the evaluated MOIDs listed in Table 4.15

The uncertainties on initial orbital elements can be managed directly during global optimization. This implementation represents an alternative to MOID expansion. The number of variables taken into account during MOID computation can be increased, e.g. by adding semi-major axis. Anyway, if the search interval associated to this new variables is smaller than the minimum box size, COSYGO will not split it during iterations. By rescaling properly the domain within each objective function evaluation, the enclosures of the square distance will range from the minimum to the maximum values associated to the semi-major axis variation. At the end of the simulation, the enclosure of the variables  $\nu_1$ ,  $\nu_2$ , and  $\Delta t$  should include all the conditions in which the two orbits intersects (or are at their minimum distance), because of the variation within the scaled interval associated to semi-major axis. This approach was tested on Keplerian orbits but the LDB and QFB algorithm are at present not applicable to this kind of computation. The Naive TM and interval box splitting criteria have thus been used.

A simple test-case is reported here. In Table 4.16 the Keplerian elements of the orbits of IRIDIUM 33 and COSMOS 2251 satellites are reported.

**Table 4.16:** Keplerian elements of IRIDIUM 33 and COSMOS 2251 satellites

Satellite	Orbit type	Dynamical model	$a_0$ [km]	$e_0$ [ ]	$I_0$ [deg]	$\Omega_0$ [deg]	$\omega_0$ [deg]
IRIDIUM 33	MEO	Keplerian	7155.136	1397590E-4	86.40	230.90	0.00
COSMOS 2251	MEO	Keplerian	7168.636	1.743706E-3	74.00	217.99	194.00

The MOID obtained considering both orbit as Keplerian is reported in Table 4.17.

**Table 4.17:** MOID of IRIDIUM 33 and COSMOS 2251 satellites

$\nu_1$ [deg]	$\nu_2$ [deg]	<b>d</b> [km]
[-135.220535, -135.220531]	[32.997179, 32.997181]	[2.300096035, 2.300096195]

Using these values, an expansion of the MOID for a variation of the semi-major axis  $\delta a \in [-1, 1]$  km and inclination  $\delta I \in [-0.1, 0.1]$  deg is computed. The maximum and minimum values of  $\nu_1$  and  $\nu_2$  that are found in the domain are listed in Table 4.18.

**Table 4.18:** Enclosures of  $\nu_1$  and  $\nu_2$  on the domain  $\delta a \in [-1, 1]$  km and  $\delta I \in [-0.1, 0.1]$  deg obtained with MOID expansion

$\nu_1$ [deg]	$\nu_2$ [deg]	<b>d</b> [km]
[-135.439928, -134.999344]	[32.766791, 33.229362]	[1.270112469, 3.330493798]

As expected the variation of the distance is a bit larger than 1 km, since the variation of semi-major axis variations is  $\pm 1$  km and the one of inclination is  $\pm 0.1$  deg.

Using the procedure described above, the enclosures of the true anomalies are computed by scaling the search domain defined outside the optimization cycle to their real values at each iteration. The obtained enclosures of the angles  $\nu_1$  and  $\nu_2$  are listed in Table 4.19.

**Table 4.19:** Enclosures of  $\nu_1$  and  $\nu_2$  on the domain  $\delta a \in [-1, 1]$  km and  $\delta I \in [-0.1, 0.1]$  deg obtained with modified MOID computation

$\nu_1$ [deg]	$\nu_2$ [deg]
[-135.483399, -134.956054]	[32.728271, 33.288574]

The obtained values are really close to the ones computed by means of MOID expansion. Unfortunately, the enclosure of the square distance in this latter case is not sufficiently tight. Thus the right and left bound of the variables are overestimated. The reason is connected to the Naive TM and interval algorithms, that are less precise than QFB and LDB.

In case that in next versions of COSY-GO the applicability of LDB and QFB will be extended, the implementation of this alternative approach should be foreseen, since the results obtained are comparable with those computed through MOID expansion, with the advantage of representing validated enclosures of the MOID and true anomalies.

## Chapter 5

# Debris clouds and orbital uncertainties

In Chapter 3 it was analyzed only the dependence from time of the Keplerian elements and the position vector. Thus, only time was initialized as a DA variable. In Chapter 4 it was outlined how the computed MOIDs can be expanded in the Keplerian elements obtaining a polynomial, e.g. in the variables  $a$  and  $I$ . The evaluations of the polynomials of  $\nu_1$ ,  $\nu_2$  and  $\Delta t$  for the deviation of  $a$  and  $I$  from their nominal values delivers the variations of the MOID from its reference values. Having the Gaussian distribution of the Keplerian elements, a statistical analysis of the MOID can be indeed performed through a simple polynomial evaluation.

The uncertainties on the initial orbital elements can be taken into account when performing orbital propagation. The aim of this Chapter is to describe the procedure to obtain the DA map of the position vector. The most relevant results are also outlined.

### 5.1 Analogies between debris cloud and orbital uncertainties modelling

To recover the expansion of the position vector, the Keplerian elements at reference epoch  $t_0$  are initialized as

$$\begin{aligned} [a_0] &= a_0 + s_a \delta a \\ [e_0] &= e_0 + s_e \delta e \\ [I_0] &= I_0 + s_I \delta I \\ [\Omega_0] &= \Omega_0 + s_\Omega \delta \Omega \\ [\omega_0] &= \omega_0 + s_\omega \delta \omega \\ [M_0] &= M_0 + s_M \delta M , \end{aligned} \tag{5.1}$$

where  $s_x$  is a proper scale factor, that can be related, as an example, to the  $1\text{-}\sigma$  deviation from the mean value of each variable.

The DA variables obtained by means of Equation (5.1) can replace the initial Keplerian elements in the algorithms described in Sections 2.3.1, 2.3.2, and 2.3.3. The position vector that is obtained carrying out the whole algorithm is the desired map. In this case it is not necessary to initialize  $\Delta t$  as a DA variable, since it is of interest only the uncertainty on the position at a fixed time.

It is worth noting that the same procedure can be used to model the evolution of a debris cloud. As outlined in Section 1.3, the debris are generally originated by fragmentation of satellites or rocket bodies. This means that after a break-up a certain number of debris can be found in a small box around the orbital position of the satellite. Thus, the original orbit or, alternatively, the orbit of the larger object, can be taken as the reference or *master* orbit. The position of the surrounding debris can indeed be obtained evaluating the DA map of the position vector of the *master* orbit, using the initial deviation of each debris from the Keplerian elements of the reference orbit. The computation of the position uncertainties is indeed equivalent to the description of the evolution of a cloud of *virtual debris*. The adjective *virtual* emphasises the fact that in this case there is actually no cloud, but a single object.

If a real debris cloud has to be modelled, the scale factor  $s_x$  should be set according to the maximum variation of the Keplerian elements of the debris cloud. These information are provided in [4], where the data regarding each fragmentation are gathered. Useful information concerning object fragmentation are provided by the so called “Gabbard diagram”, named after NORAD employee John Gabbard. This scatter plot represents the perigee and apogee altitude of each debris of the cloud against their orbital period. In the resulting “X-shaped” diagram all perigee marker are located in the bottom of the diagram whereas the apogee marker are found in the upper part. In the middle of the “X” the debris have the same semi-major axis of their parent. The debris on the left have the same apogee altitude, but their perigee has lowered due to a decrease in their along-track velocity after the explosion. On the opposite, the debris on the right part have raised their apogee after the increase of their along-track velocity.

In Figure 5.1 the Gabbard diagram of the debris cloud resulting from Defense Meteorological Satellite Program (DMSP) F11 satellite fragmentation is reported. At the time of the breakup (15 April 2004) the satellite was no more operative and the assessed cause of the breakup is a failure of the propulsion system, probably related to the hydrazine reservoir that was on-board.

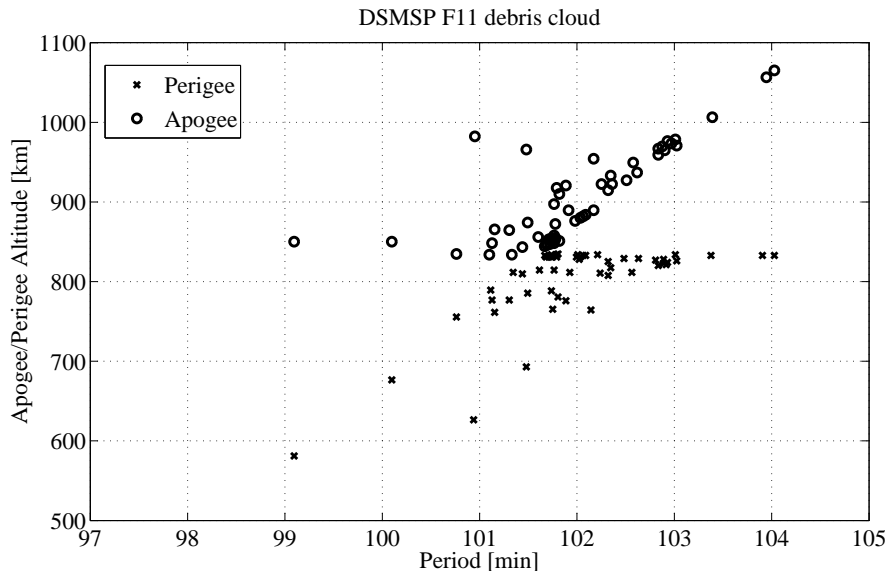


**Figure 5.1:** Gabbard diagram of DMSP F11 satellite debris cloud 6 weeks after breakup

The maximum variation of eccentricity and semi-major axis can thus be recovered from this

diagram, taking into account the perigee and apogee of each debris and their orbital period.

The out-of-plane velocity resulting from a breakup induces a variation of the orbital plane. Anyway, since large values of  $\Delta v_n$  are needed to change significantly node position and inclination, the variations of these two Keplerian elements are small.

The variation of argument of pericentre and true anomaly depend on the initial orbit eccentricity. Anyway, it can be noticed that the variation of their sum  $u$  can be neglected because the variation on  $\nu$  and  $\omega$  are nearly opposite. Since all the considered analytical models use the true longitude to avoid singularities for circular orbits, the variation of both  $\omega$  and  $M$  can be considered small. The maximum variation of inclination, semi-major axis and eccentricity for the main debris cloud are listed in [4].

In the following Sections the results obtained for the propagation of a cloud of debris are presented.

## 5.2 Orbit propagation through Aksnes' solution

The evolution of a debris cloud, whose reference objects has the same orbital elements of DMSP F11 satellite, has been studied by means of Aksnes' solution (see § 2.3.1).

The reference orbital elements are listed in Table 5.1. These orbital elements are initialized as DA variables, using the scale factors listed in Table 5.2.

**Table 5.1:** DMSP F11, Keplerian elements at JD 2453110.9733

Orbit type	Dynamical model	$a_0$ [km]	$e_0$ -	$I_0$ [deg]	$\Omega_0$ [deg]	$\omega_0$ [deg]	$M_0$ [deg]
Sun-synchr.	Aksnes' sol.	7218.692	0.001289	98.674	129.006	13.867	346.285

**Table 5.2:** DMSP F11, DA variables scale factors

$s_a$ [km]	$s_e$ -	$s_I$ [deg]	$s_\Omega$ [deg]	$s_\omega$ [deg]	$s_M$ [deg]
2	1E-2	0.3	0.1	0.1	0.1

The deviation for each Keplerian element is obtained by means of a multivariate standard Gaussian distribution. In the case of eccentricity the deviation is properly scaled in order to avoid negative eccentricities. Thus, given the map and deviation from the initial Keplerian elements, the position of each debris cloud at different propagation times are computed.

The debris cloud at time  $t_0$  is represented in Figure 5.2(a). The initial volume occupied by the debris is very small at the beginning of the propagation. The debris slowly start to spread along the orbit (Figure 5.2), due to phase displacement caused by differences in semi-major axis. In a few hundred days the debris are found on more than the half of the orbit, with an increasing risk of impact for the satellites flying nearby.

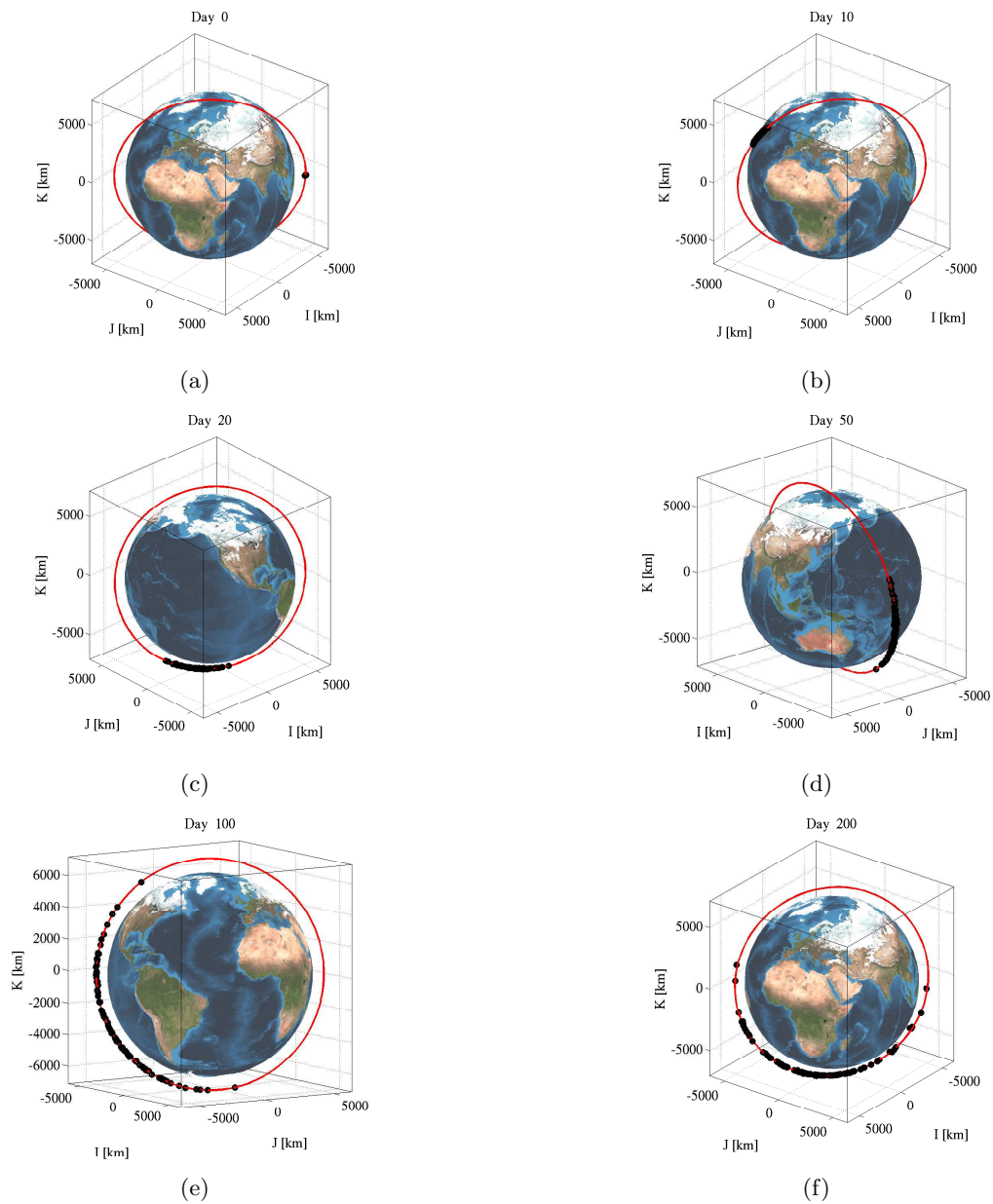


**Figure 5.2:** DMSP F11, debris cloud evolution. The red curve is the nominal orbit at that instant.

The accuracy of the propagation reduces significantly after 200 days, since the debris occupy larger portions of the orbit. However, the initial debris box can be divided into many subboxes and for each one a reference orbit can be defined. In this way the deviation from the initial Keplerian elements can be reduced. Thus, the loss in accuracy is compensated with a small additional computation effort.

### 5.3 Orbit propagation through HANDE

In this section the propagation of a fictional debris cloud originated from IRIDIUM 33 satellite is analyzed. The Keplerian elements for the reference orbit are listed in Table 5.3. The scale factor of the DA variables are reported in Table 5.4.

**Table 5.3:** IRIDIUM 33, Keplerian elements at JD 2454873.2056

Orbit type	Dynamical model	$a_0$ [km]	$e_0$ -	$I_0$ [deg]	$\Omega_0$ [deg]	$\omega_0$ [deg]	$M_0$ [deg]
MEO.	HANDE	7155.136	1.39759E-4	86.399	230.901	165.545	194.456

**Table 5.4:** IRIDIUM 33, DA variables scale factors

$s_a$ [km]	$s_e$ -	$s_I$ [deg]	$s_\Omega$ [deg]	$s_\omega$ [deg]	$s_M$ [deg]
3	1E-4	3	0.1	0.1	0.1

The evolution of the debris cloud is represented in Figure 5.3. The displacement of the debris from the initial Keplerian elements were obtained in the same way of Section 5.2. In this case the variation in the inclination is equal to 3 deg. As a result, the debris not only spread along the orbit but also in a direction perpendicular to the orbital plane. This effect is due to the different RAAN angular rates  $\dot{\Omega}$  between the debris. The differences in  $\Omega$  between the debris are represented in Figures 5.4 and 5.5 at initial time and after 250 days, respectively. On the y-axis of each figure the semi-major axis is found. Whereas at time  $t_0$  all points are concentrated in the initial box, after 250 days the values of the right ascension of the ascending node spreads from 80 to 200 deg. As a result, the swarm of debris slowly distributes on a layer that surrounds the whole planet. Note that the atmospheric drag reduces the semi-major axis of all debris of approximately by 4 km in the considered time span.

In Figures 5.6 and 5.7 semi-major axis versus inclination is plotted. In this case the values of inclination are nearly the same after 250 days.

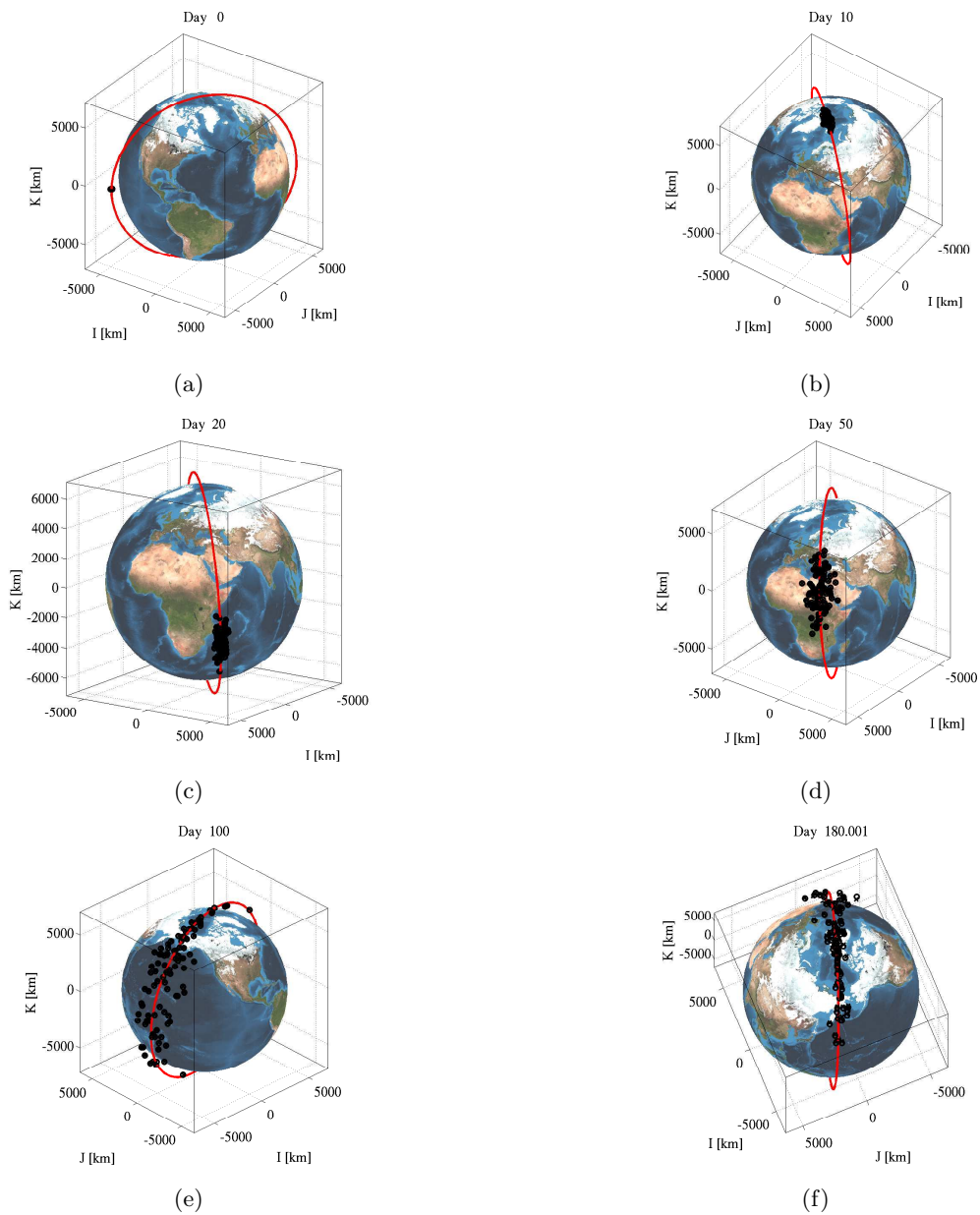


**Figure 5.3:** IRIDIUM 33, debris cloud evolution. The red curve is the nominal orbit at that instant.

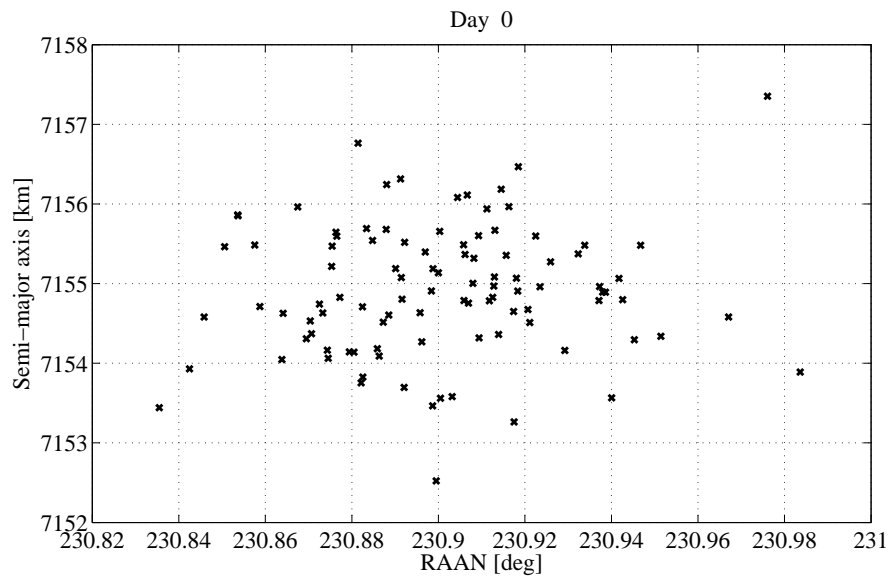


**Figure 5.4:** IRIDIUM 33, Node dispersion of virtual debris at time  $t_0$

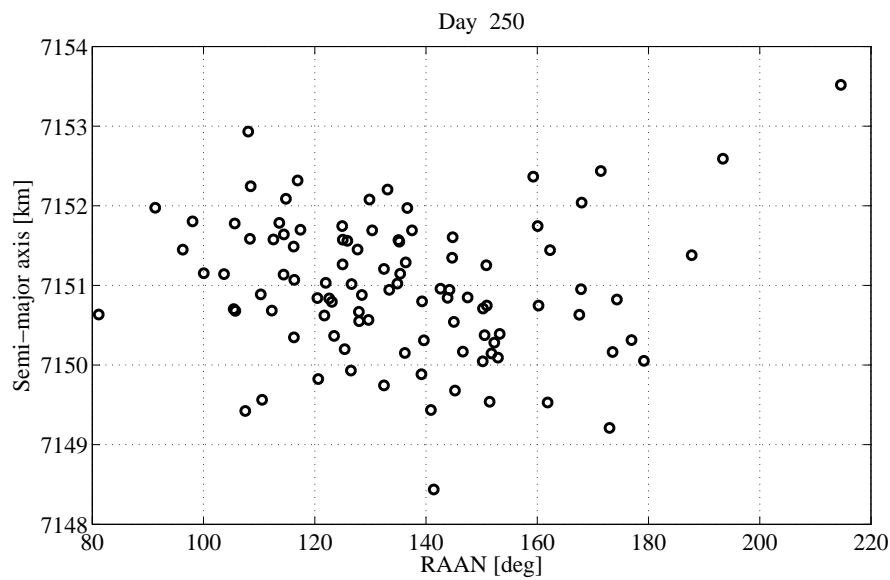


**Figure 5.5:** IRIDIUM 33, Node dispersion of virtual debris after 250 days

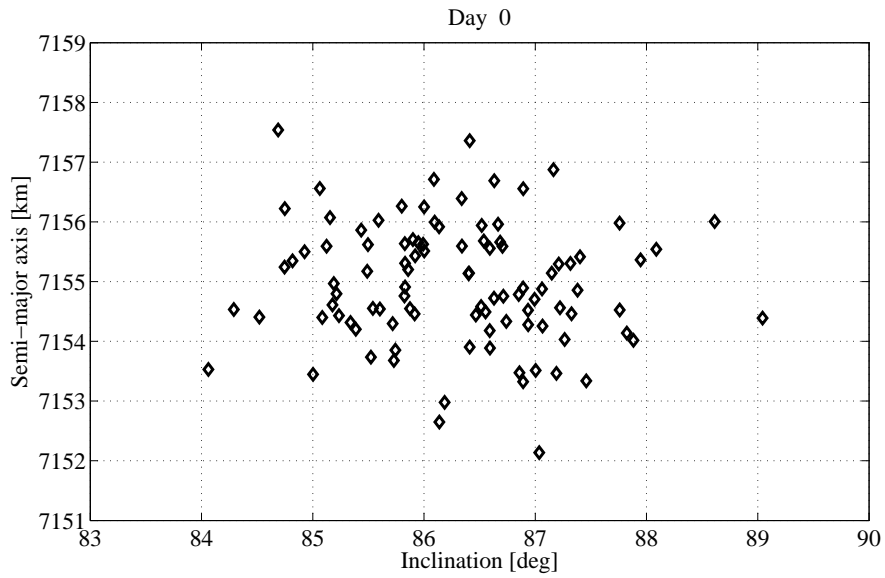


**Figure 5.6:** IRIDIUM 33, Inclination dispersion fo virtual debris at time  $t_0$

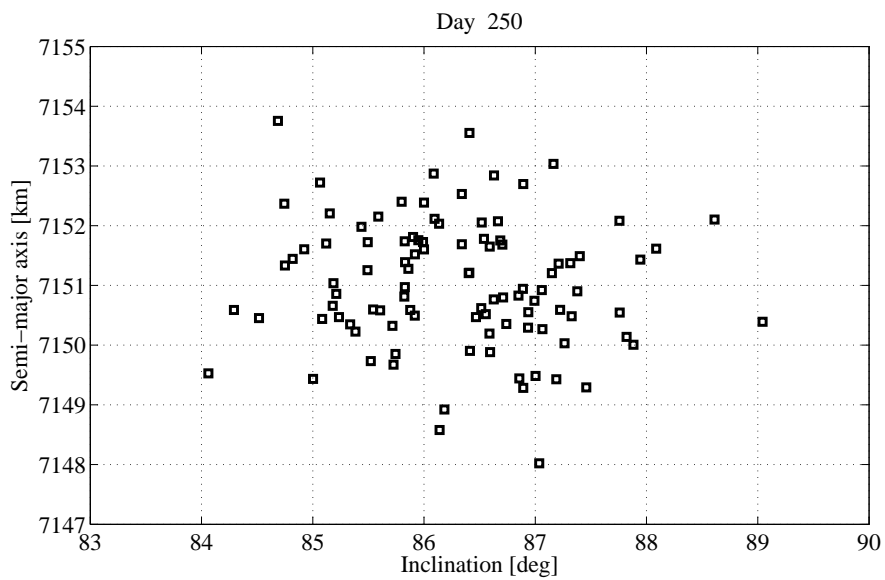


**Figure 5.7:** IRIDIUM 33, Inclination dispersion fo virtual debris after 250 days

## 5.4 Orbit propagation through SGP4

The case of a GEO cloud is analyzed in this section. The reference orbit is referred to satellite GALAXY 15, a geostationary communication satellite that was originally placed in a slot at 133°W. On April 5, 2010, the satellite experienced a failure and started to drift eastward since station keeping manoeuvres could not be performed anymore [71]. The satellite had three close approaches with other GEO satellites prior its recovery, that was successful on 23 December, 2010. The orbital elements of the satellite are listed in Table 5.5 and the DA scale factors in Table 5.6. In this simulation it is assumed that the satellite is still drifting.

**Table 5.5:** IRIDIUM 33, Keplerian elements at JD 2455618.7482

Orbit type	Dynamical model	$a_0$ [km]	$e_0$ -	$I_0$ [deg]	$\Omega_0$ [deg]	$\omega_0$ [deg]	$M_0$ [deg]
GEO.	SGP4	42231.946	2.739E-4	0.145	74.484	237.431	190.869

**Table 5.6:** IRIDIUM 33, DA variables scale factors

$s_a$ [km]	$s_e$ -	$s_I$ [deg]	$s_\Omega$ [deg]	$s_\omega$ [deg]	$s_M$ [deg]
3	1E-2	0.5	0.1	0.1	0.1

The evolution of the virtual debris is shown in Figure 5.8. The time needed for the debris to spread along the trajectory is larger than in the previous cases, since the orbital period is much larger. The main effect are phase displacement and changes in inclination due to luni-solar perturbations. These effects are recognisable if Figures 5.9 and 5.10 are compared. At time  $t_0$  the debris are grouped in a small box around the reference longitude (102.25°W) and latitude (0.11°N). After 250 the value of longitude has changed and the debris longitudes are hence comprised between 79°W and 64°W. In addition, the inclination has raised of nearly 1 deg for all debris of the cloud.

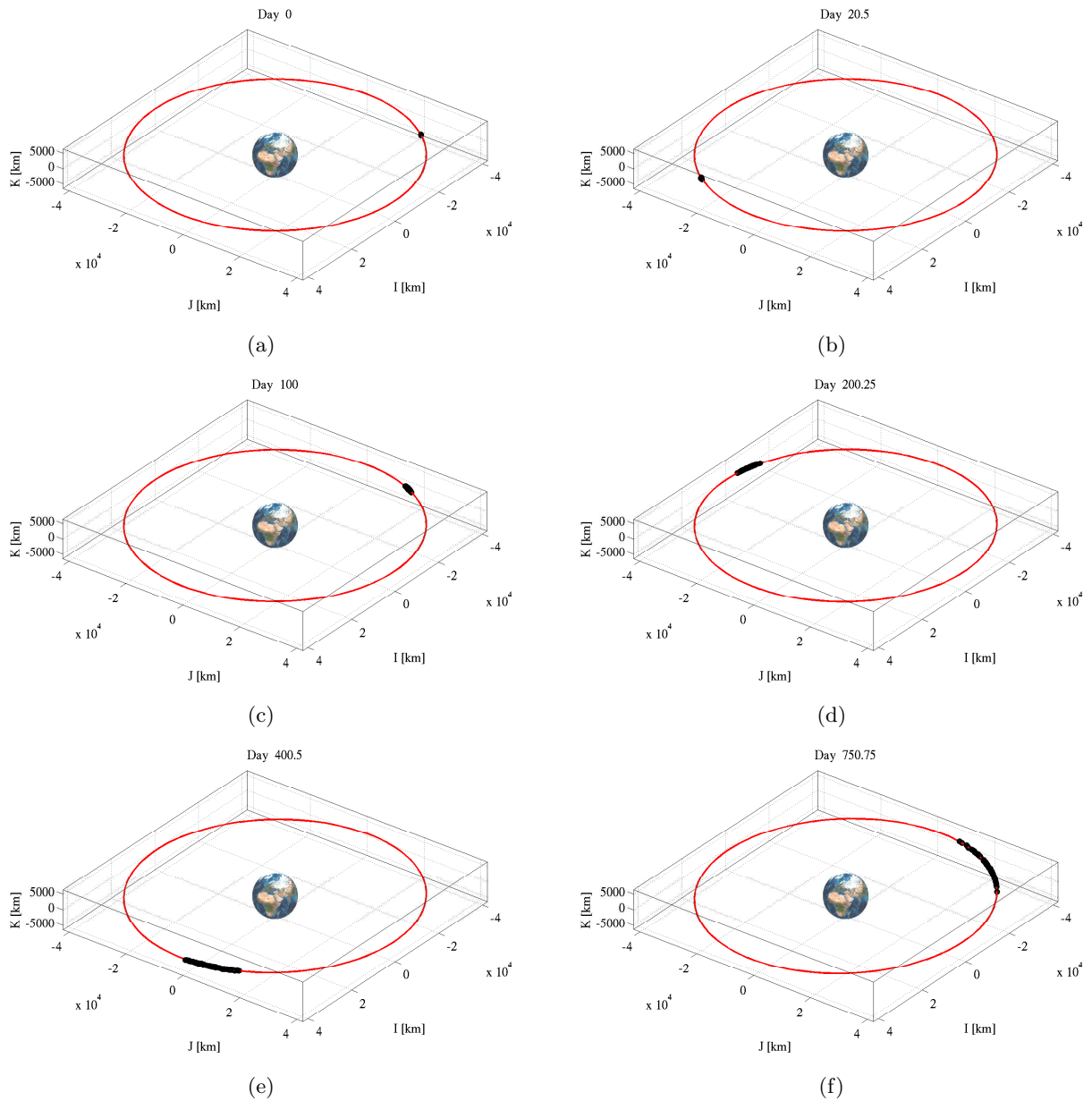


**Figure 5.8:** GALAXY 15, debris cloud evolution. The red curve is the nominal orbit at that instant.

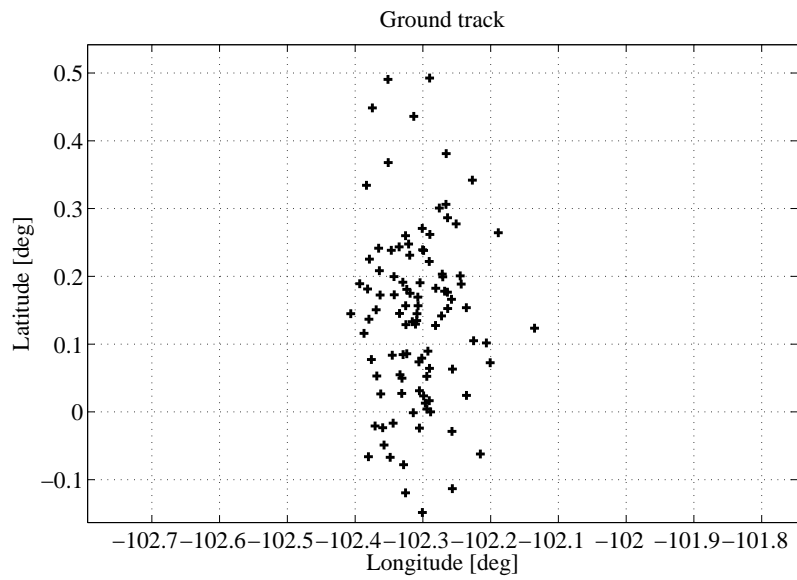


**Figure 5.9:** GALAXY 15, virtual debris ground track at time  $t_0$

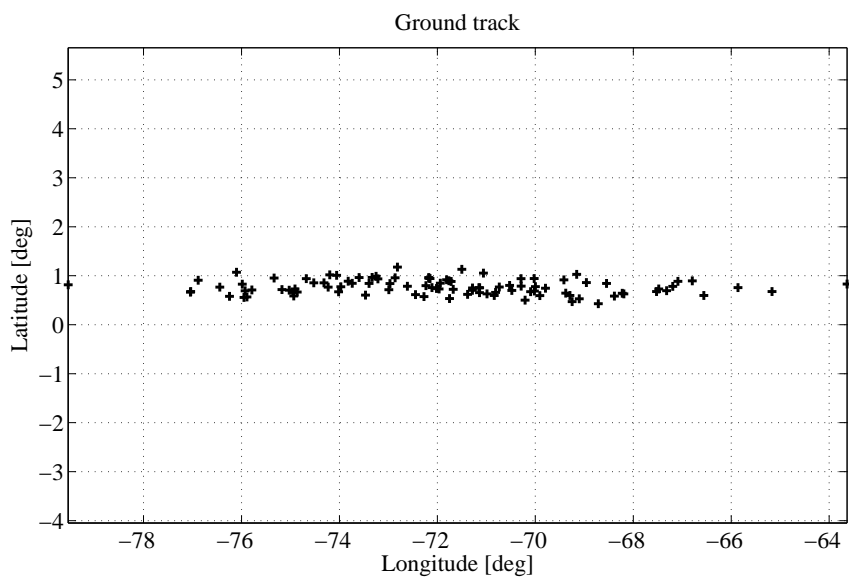


**Figure 5.10:** GALAXY 15, virtual debris ground track after 250 days



## Chapter 6

# Conclusions

In this chapter, after a brief summary of the work, the main results and objective reached are critically analyzed.

In Chapter 1 it was characterized the problem of space debris. In particular, it was highlighted that the region in which the higher concentration of debris is found are the most commercially attractive and hence more populated by satellites. It was also observed that the only natural phenomenon that could help in reducing the amount of debris is the atmospheric drag. Anyway, its effect is negligible above 600 km. For this reason mitigation standards have been developed by Space Organisations, with the aim of reducing the risks of impact, e.g identifying criteria for the safe disposal of the satellite at their end-of-life. The importance of the prediction of impacts was also stressed. In case a satellite and a debris or two satellites are found to be in collision routes a proper avoidance manoeuvres can be designed. The goal of this work was thus to develop a tool that can detect orbital intersections through validated global optimization. It was also outlined that the orbital perturbations should be taken into account since they can affect considerably the initial orbit shape and orientation.

In Chapter 2 the modelling of orbital perturbations was assessed. The main sources of perturbation were identified, and three analytical models were selected. The choice of these models was driven by the kind of orbits that they can represent. The Aksnes' solution, described in Section 2.3.1, considers the perturbation generated by the first five zonal harmonics of the Earth. It can thus be used to model the satellites that are found over LEO, where the effect of atmospheric drag is negligible and the zonal perturbations overcome the other sources of disturbance. To describe the orbital evolution of a LEO satellite, the HANDE algorithm was selected and presented in Section 2.3.2. HANDE considers both zonal harmonics and atmospheric drag perturbations and has the advantage of leaving to the user the choice of the atmosphere model. The last selected algorithm is SGP4, that has been used to model the satellites in geostationary orbit. It considers zonal harmonics up to degree four, luni-solar perturbation and resonance effects. All three analytical propagators were validated by comparison with numerical simulations or using ad-hoc test cases.

Differential Algebra (DA) and Taylor Models (TM) were described in Chapter 3. It was described how it is possible to obtain an approximation of the position by means of polynomials evaluation and the characteristics of the expansions were analyzed for all analytical models. The global optimizer COSY-GO, based on TM, was described as well. This optimizer has been used to compute the MOID between orbits.

The MOID computation is tackled in Chapter 4. At first, only one of the two orbit was perturbed

whereas the other one was Keplerian. Three codes were thus developed, one for each analytical solution that was selected in Chapter 2. Then, also the second orbit was considered as perturbed. The results obtained computing the position of both orbit by means of Aksnes' solution were compared with the case in which the first orbit was modelled through HANDE and the second through Aksnes' model. It was demonstrated that the developed codes can successfully compute the MOID of perturbed orbits. In particular, it was proved that the MOIDs computed considering only Keplerian orbits are not reliable, since cases as the Sun-synchronous orbit can not be taken into account. Intersections between orbits can occur even if at reference time the MOID is high. It was also shown that the reduction of semi-major axis caused by atmospheric drag can influence the MOID through the example reported in Section 4.4. Using this approach it is indeed possible to discriminate between orbits that can intersect or not under the effect of orbital perturbations. The advantage is that the time of computation is low if compared to numerical simulation, since all the operations are reduced to evaluation of analytical expressions. The numerical simulations are needed only in case that two orbits have a MOID close to zero, since the MOID is related only to the relative geometry of the two orbits. Thus, the position of the two objects at the time of the intersections should be computed in order to assess the occurrence of a collision. Anyway, the number of numerical propagations is drastically reduced, since these are required only in case of intersections.

The procedure for MOID expansion was presented in Section 4.5. It was demonstrated how it is possible to obtain the dependence of the MOID from the variations of the initial conditions. This allows to estimate the new coordinates in which the distance between the two orbits reaches its minimum. In this way, it is possible to obtain the uncertainties on MOID given the uncertainties on the initial parameters.

In Chapter 5 it was described how the DA allows the modelling of a debris cloud under the effect of orbital perturbations. It was also highlighted that the same procedure can be used to take into account the uncertainties of the orbital elements. It has been shown that the debris spreads along the trajectory and it was outlined how the differences in the rate of variation of RAAN between the objects can disperse the cloud around the Earth. For the GEO orbit it was found that the debris distribute along the GEO ring and their inclination can change due to luni-solar perturbations. Anyway, in the case of GEO the spreading of the debris occur in a longer period since the orbital speed is lower.

The aim of predicting the intersections between two perturbed orbits was thus met. The test cases reported in Chapter 4 demonstrated the capability of describing the most relevant effect for LEO and GEO. The computational time required, is limited to a few minutes for each simulation, apart for the case of the GEO. Note that the optimization problem for GEO can be tackled in a different way, by defining the square distance as a function of time only. This approach, described in the following Section would increase the performances in the case that two orbits intersect many times, but requires a more complex procedure for the validated solution of Kepler's equation. As an alternative, to reduce computational time it is possible to compute the MOID considering both orbit as Keplerian prior its calculation for perturbed orbits. In case the two Keplerian orbits already intersects, the risk of impact is already present and thus a numerical check of satellites position is required.

In addition, the use of DA and TM enhances the capability of the developed tool. The possibility of performing an expansion of the MOID is an important advantage, since it can cut down even more the computational time, because all variations of MOID can be computed in fractions of second by

mere polynomials evaluations.

## 6.1 Future developments

In this section the possible future developments of the work are outlined. As stated in Chapter 2 the effect of the solar radiation pressure can overcome the other sources of perturbation as the area-to-mass ratio of the debris and the semi-major axis of the orbit increase. This perturbation should thus be modelled, especially in the case of orbits above the LEO region. In the present work the analytical solutions that were selected take into account zonal harmonics, atmospheric drag, orbital resonance and luni-solar perturbations. The reason of this choice is that the analytical models for solar radiation pressure found in literature were not suitable for general applications, since they were obtained for specific problems. Anyway, if general models that take into account this perturbation together with at least that of zonal harmonics and/or drag is developed, their inclusion in the code for MOID computation could represent an important improvement. In that case all the main sources of perturbation will be available and hence the MOID would be even more reliable.

Another important development would regard the computation of the MOID of a GEO orbit. In this case the orbits are characterized by small variations of semi-major axis and inclinations, and have low eccentricities. As reported in Section 4.3 the number of MOIDs is very high in this case and computational time increases. The computation, anyway, can be tackled in a quite different way. Instead of considering all the pairs of true anomalies  $\nu_1$  and  $\nu_2$ , the true anomalies can be considered as functions of time as well, reintroducing the short period perturbations that were dropped in Section 4.3. The square distance between the orbits in that case is a function of one variable, time. Through a global optimization performed on a time interval of one or two years, the instant at which the two objects are at the minimum distance can be identified. In this way the risk of collision on the considered time span can be assessed. The computational time should be reduced since even for two coincident orbits the number of close approaches is reduced<sup>1</sup>

Further developments regards the modelling of debris cloud, analyzed in Chapter 5. In this work only the deviation from the reference Keplerian elements were considered. It is anyway possible to take into account also the deviation from the reference ballistic coefficient or area-to-mass ratio. In Figure 6.1 it is represented a distribution of area-to-mass of debris originated from a collision between two satellites. The distribution is computed following the procedure outlined in [19].

According to [19], it is also possible to compute statistically the increase of velocity resulting from a collision or an explosion. The increase can then be used to obtain the variations of the Keplerian elements. These variation are indeed correlated whereas in the simulation performed in Chapter 5 are considered as independent.

---

<sup>1</sup>In case the two objects are at the same longitude the number of close approaches can be anyway really high.

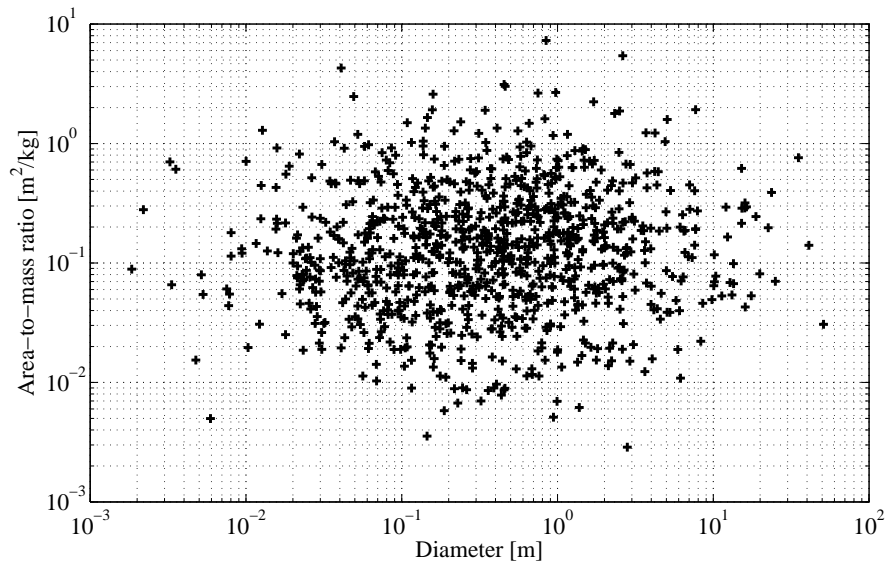


**Figure 6.1:** IRIDIUM 33, area-to-mass ratio vs. diameter distribution

# Appendix A

## A.1 Greenwich sidereal time computation

In this section the algorithm for Greenwich Sidereal Time (GST) computation is described. Given the Julian Date (JD)  $JD_{\text{UT}}$  the centuries elapsed from 2000 January 01 12:00:00.0 UT can be computed by mean of Eq. (A.1)

$$T_{\text{UT}} = \frac{JD_{\text{UT}} - 2451545.0}{36525.0} . \quad (\text{A.1})$$

The GST in radians is obtained with the following expression

$$\begin{aligned} \theta_G = & -6.2 \times 10^{-6} T_{\text{UT}}^3 + 0.093104 T_{\text{UT}}^2 + \\ & + (876600.0 \times 3600.0 + 8640184.812866) T_{\text{UT}} + 67310.54841 , \end{aligned} \quad (\text{A.2})$$

where  $\theta_G$  is Greenwich hour angle.

## A.2 Moon and Sun ephemerides

In this section the procedure for the computation of Moon and Sun position is reported. These passages are necessary for the computation of periodics luni-solar perturbations in SGP4 algorithm (see § 2.3.3) and are taken from [48].

The solar elements [72], epoched at JD 2415020.0 (0.5 January 1900), and referred to Earth's equator are listed in tables A.1.

**Table A.1:** Sun's elements at epoch

$\mathbf{n}_{0\odot}$	$\mathbf{e}_{0\odot}$	$\mathbf{I}_{0\odot}$	$\omega_{0\odot}$	$\Omega_{0\odot}$	$\mathbf{M}_{0\odot}$	$C_{\odot}$
[rad/min]	[ ]	[deg]	[deg]	[deg]	[deg]	[rad/min]
$1.19459 \times 10^{-5}$	0.01675	23.44410	281.22080	0	358.47580	$2.98648 \times 10^{-6}$

The Moon's elements with subscript  $\varepsilon$  are referred to the ecliptic plane and the variable  $u$  is the longitude of the perigee. The values of these Keplerian elements are listed in table A.2.

The first step is computing the Moon's RAAN referred to ecliptic at time  $\Delta t$ , which is the time elapsed from Moon's epoch to satellite epoch.

$$\Omega_{\mathcal{C}_\varepsilon} = \Omega_{0_\varepsilon \mathcal{C}} + \dot{\Omega}_{0_\varepsilon \mathcal{C}} \Delta t , \quad (\text{A.3})$$

**Table A.2:** Moon's elements at epoch

$\mathbf{n}_{0\mathcal{C}}$ [rad/s]	$\mathbf{e}_{0\mathcal{C}}$ [ ]	$\mathbf{I}_{0_\epsilon\mathcal{C}}$ [deg]	$\mathbf{u}_{0_\epsilon\mathcal{C}}$ [deg]	$\mathbf{\Omega}_{0_\epsilon\mathcal{C}}$ [deg]	$\mathbf{M}_{0\mathcal{C}}$ [deg]	$\mathbf{C}_{\mathcal{C}}$ [rad/min]
$1.58352 \times 10^{-4}$	0.05490	5.14540	334.32955	4.52360	270.34200	$4.79681 \times 10^{-7}$

in which the secular rate  $\dot{\Omega}_{0_\epsilon\mathcal{C}} = -9.2422029 \times 10^{-4}$  rad/day. The Moon's inclination with respect to the equatorial plane is given by

$$\cos(I_{\mathcal{C}}) = \cos(I_{\odot}) \cos(I_{0_\epsilon\mathcal{C}}) - \sin(I_{\odot}) \sin(I_{0_\epsilon\mathcal{C}}) \cos(\Omega_{\mathcal{C}_\epsilon}), \quad (\text{A.4})$$

whereas the longitude of the perigee referred to the ecliptic is

$$\gamma = u_{0_\epsilon\mathcal{C}} + \dot{u}_{0_\epsilon\mathcal{C}} \Delta t. \quad (\text{A.5})$$

The secular rate  $\dot{u}_{0_\epsilon\mathcal{C}} = 0.0019443680$  rad/day. The lunar right ascension of the ascending node referred to the equator is obtained by means of

$$\sin(\Omega_{\mathcal{C}}) = \frac{\sin(I_{0_\epsilon\mathcal{C}}) \sin(\Omega_{\mathcal{C}_\epsilon})}{\sin(I_{\mathcal{C}})} \quad (\text{A.6})$$

$$\cos(\Omega_{\mathcal{C}}) = \sqrt{1 - \sin^2(\Omega_{\mathcal{C}})}. \quad (\text{A.7})$$

The following step is computing the quantity  $\Delta$

$$\sin(\Delta) = \frac{\sin(I_{\odot}) \sin(\Omega_{\mathcal{C}_\epsilon})}{\sin(I_{\mathcal{C}})} \quad (\text{A.8})$$

$$\cos(\Delta) = \cos(\Omega_{\mathcal{C}}) \cos(\Omega_{\mathcal{C}_\epsilon}) + \sin(\Omega_{\mathcal{C}}) \sin(\Omega_{\mathcal{C}_\epsilon}) \cos(I_{\odot}) \quad (\text{A.9})$$

$$\Delta = \arctan\left(\frac{\sin(\Delta)}{\cos(\Delta)}\right), \quad (\text{A.10})$$

and subsequently the Moon's argument of the pericentre

$$\omega_{\mathcal{C}} = \gamma - \Omega_{\mathcal{C}_\epsilon} + \Delta. \quad (\text{A.11})$$

The computation of the Moon's Keplerian elements at the epoch of the space debris is concluded with the computation of the mean anomaly

$$M_{e\mathcal{C}} = M_{0\mathcal{C}} + n_{\mathcal{C}} \Delta t, \quad (\text{A.12})$$

where  $n_{\mathcal{C}}$  is converted into rad/day.

The Keplerian elements of the Sun are supposed to be constants, apart from the mean anomaly  $M_{e\odot}$  that is computed in the same way of Eq. (A.12).

The procedure described above is performed only once during SGP4 initialization. Only the fast variable, i.e. the mean anomaly, must be updated at the time  $t$  at which the space debris position is

evaluated. If  $t$  is the time in seconds measured from debris epoch, the corresponding mean anomaly of the Sun and the Moon are given by

$$M_{\zeta} = M_{e\zeta} + n_{\zeta} t \quad (\text{A.13})$$

$$M_{\odot} = M_{e\odot} + n_{\odot} t. \quad (\text{A.14})$$

In this case the mean motions  $n_{\odot}$  and  $n_{\zeta}$  are in rad/s.

### A.3 Global Gravity Field Model EIGEN-51C

The Earth's gravity field model used in this work is the EIGEN-51C [73], developed in 2010 using CHAMP and GOCE data. The equatorial Earth's radius  $R_{\oplus}$  and Earth's gravitational parameter  $\mu_{\oplus}$  according to this model are reported in table A.3.

**Table A.3:** EIGEN-51C Earth's constants

$R_{\oplus}$	$6.378136300 \times 10^6$	[m]
$\mu_{\oplus}$	$0.3986004461 \times 10^{15}$	[m <sup>3</sup> /s <sup>2</sup> ]

The coefficients of the harmonic series expansion are available at [74]. The first five zonal harmonics coefficients used in all analytical models are listed in Tab. A.4.

**Table A.4:** EIGEN-51C gravity field zonal harmonics coefficients

<b>n</b>	2	3	4	5	6
<b>J<sub>n</sub></b>	$1.082630 \times 10^{-3}$	$-2.532428 \times 10^{-5}$	$-1.619907 \times 10^{-5}$	$-2.273001 \times 10^{-7}$	$5.407118 \times 10^{-7}$

In table A.5 the coefficients of the first sectoral and tesseral harmonics are listed.

**Table A.5:** EIGEN-51C gravity field tesseral and sectoral harmonics coefficients

<b>n</b>	2	3	4	5	6
<b>m</b>	2	1	2	3	4
$J_{n,m}$	$1.815592 \times 10^{-6}$	$3.463748 \times 10^{-6}$	$3.744368 \times 10^{-7}$	$1.225020 \times 10^{-7}$	$1.050669 \times 10^{-8}$
$\lambda_{n,m}$ [rad]	-0.521115	0.885152	-0.600012	0.193638	2.118817

In SGP4 the following coefficients related to the first four zonal harmonics are defined prior code execution

$$k_2 = \frac{1}{2} J_2 R_{\oplus}^2 \quad (\text{A.15})$$

$$A_{3,0} = -J_3 R_{\oplus}^3 \quad (\text{A.16})$$

$$k_4 = -\frac{3}{8} J_4 R_{\oplus}^4 \quad (\text{A.17})$$

The coefficients for numerical integration of synchronous orbit resonance are listed in table A.6.

**Table A.6:** SGP4 tesseral and sectoral constants

<b>n</b>	2	3	
<b>m</b>	2	1	3
$Q_{nm}$	$1.7891679 \times 10^{-6}$	$2.1460748 \times 10^{-6}$	$2.2123015 \times 10^{-7}$
$\lambda_{nm}$ [rad]	2.88431980	0.13130908	0.37448087

## A.4 Atmospheric density model

The atmospheric density has been modeled throughout this work with an exponential model, whose formulation is in Eq. (A.18)

$$\rho = \rho_{\text{ref}} e^{-\frac{h-h_{\text{ref}}}{H}}, \quad (\text{A.18})$$

where  $h$  is satellite altitude. The reference density  $\rho_{\text{ref}}$  and altitude  $h_{\text{ref}}$  as well as the scale height  $H$  should be updated with altitude, in order to have a better correlation with real density. The values of reference height and density at various altitude are listed in table A.7.

<b>h</b>	<b>H</b>	<b><math>\rho</math></b>
[km]	[km]	[kg/m <sup>3</sup> ]
0	8.4	1.225
200	37.5	$2.41 \times 10^{-10}$
350	54.8	$6.66 \times 10^{-12}$
500	64.5	$4.76 \times 10^{-13}$
550	68.7	$2.14 \times 10^{-13}$
600	74.8	$9.89 \times 10^{-14}$
650	84.4	$4.73 \times 10^{-14}$
700	99.3	$2.36 \times 10^{-14}$
750	121	$1.24 \times 10^{-14}$
800	151	$6.95 \times 10^{-15}$

**Table A.7:** Density and scale height variation with altitude [75]

## A.5 Transformations of orbital elements

In this section the transformation between the orbital elements set used throughout this work are reported. These sets of variables are introduced in order to avoid the singularities that are typical

of the classical Keplerian elements  $(a, e, I, \omega, \Omega, M)$ .

### A.5.1 Delaunay's variables

The Delaunay's variables  $(L, G, H, l, g, h)$  are defined as

$$\begin{aligned}
 L &= \sqrt{\mu_{\oplus} a} \\
 G &= L\sqrt{1 - e^2} \\
 H &= G \cos(I) \\
 l &= M \\
 g &= \omega \\
 h &= \Omega
 \end{aligned} \tag{A.19}$$

where  $(a, e, I, \omega, \Omega, M)$  are the Keplerian elements of the orbit. These first three variables are related to the angular momentum of the orbit, since:

- $L$  is the conjugate momentum to mean anomaly,
- $G$  is the modulus of angular momentum vector,
- $H$  is the projection of angular momentum vector on symmetry axis.

### A.5.2 Hill's variables

The Hill's variables can be grouped in a set of six variables  $(\dot{r}, G, H, r, u, h)$  and are defined as

$$\begin{aligned}
 \dot{r} &= \mu_{\oplus} e \frac{\sin(\nu)}{G} \\
 G &= \sqrt{\mu_{\oplus} a (1 - e^2)} \\
 H &= G \cos(I) \\
 r &= \frac{a (1 - e^2)}{1 + e \cos(\nu)} \\
 u &= \omega + \nu \\
 h &= \Omega
 \end{aligned} \tag{A.20}$$

where  $\nu$  is the true anomaly and  $(a, e, I, \omega, \Omega)$  are Keplerian elements. The choice of the true longitude  $u$  avoids singularities for circular orbits and the use of  $r$ ,  $H$ , and  $G$  avoids singularities at low inclinations.

## A.6 Smith's correction

The critical inclination introduces singular terms in the analytical expressions of orbital elements. The functions

$$F(I) = 4 - 5 \sin^2(I) \quad (\text{A.21})$$

$$F(I) = 1 - 5 \cos^2(I) \quad (\text{A.22})$$

appear at the denominator of secular rates or long period periodic terms. If  $I = 63.435$  deg or  $I = 116.565$  deg these functions are equal to zero. An approximation of these terms is introduced by Smith in the analytical propagator PPT3 [48, 33]. He defines the inverse of  $F(I)$  as

$$\frac{1}{F} = C(F) = \begin{cases} \frac{1 - \exp(-100F^2)}{F} & \text{if } F \neq 0 \\ 0 & \text{else.} \end{cases} \quad (\text{A.23})$$

In this way the inverse (A.23) has its proper value away from the critical value of  $I$ , whereas the exponential term dominates within a few degrees from the singularities. The maximum amplitude of  $C(F)$  is 6.382. The function  $C(F)$  exhibits poor convergence performances when expanded in series. To avoid problems when performing DA computation the function is thus written as

$$C(F) = \frac{1}{F} [1 - \exp(-\beta F^2)] \prod_{m=0}^{10} [1 + \exp(-2^m \beta F^2)] , \quad (\text{A.24})$$

where  $\beta = 100/2^{11}$  and the first term is usually approximated as

$$\frac{1}{F} [1 - \exp(-\beta F^2)] \approx \beta F \sum_{n=0}^{12} (-1)^n \frac{\beta^n F^{2n}}{(n+1)!} . \quad (\text{A.25})$$

The non-smoothed and the smoothed inverse of  $F(I)$  are represented in Figure A.1.

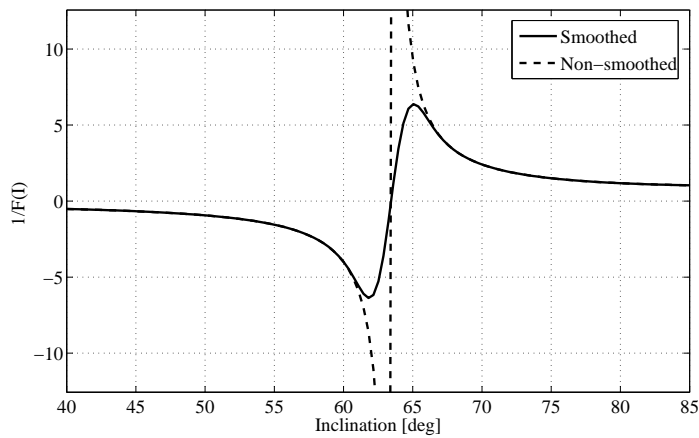


**Figure A.1:** Comparison between smoothed and non-smoothed inverse of  $F(I)$

# Appendix B

## B.1 Numerical differentiation formulae

In this section the fomulae for numerical differentiation are reported [76]. All formulae are 7-points central difference with equally spaced intervals with amplitude  $h$ . The values of the function  $f$  in the reference points is indicated with a subscript zero, whereas the values of the function in  $\pm h$ ,  $\pm 2h$  and  $\pm 3h$  are indicated with subscripts  $\pm 1$ ,  $\pm 2$  and  $\pm 3$  respectively.

The first order derivative of the function is given by

$$f'(0) = \frac{-f_{-3} + 9f_{-2} - 45f_{-1} + 45f_{+1} - 9f_{+2} + f_{+3}}{60h} . \quad (\text{B.1})$$

Second order derivative is obtained from

$$f''(0) = \frac{2f_{-3} - 27f_{-2} + 270f_{-1} - 490f_0 + 270f_{+1} - 27f_{+2} + 2f_{+3}}{180h^2} , \quad (\text{B.2})$$

while third order derivative is

$$f'''(0) = \frac{f_{-3} - 8f_{-2} + 13f_{-1} - 13f_{+1} + 8f_{+2} - f_{+3}}{8h^3} . \quad (\text{B.3})$$

## B.2 Numerical integration formulae

In this section the formula for Gauss-Legendre quadrature is reported. Given an integral of the kind

$$I = \frac{1}{2\pi} \int_{-\pi}^{\pi} g(f)df ,$$

it can be approximated numerically approximated using Gauss-Legendre formula

$$I = \frac{1}{2\pi} \int_{-\pi}^{\pi} g(f)df \approx \frac{b}{2\pi} \sum_{i=1}^k w_i g(bx_i) , \quad (\text{B.4})$$

where  $k$  is the total number of points  $x_i$  in which the function is evaluated, and  $w_i$  are their associated weights [77].

The values of  $x_i$  and  $w_i$  for a 13-points formula are listed in table B.1.

**Table B.1:** Points and weights of 13-points Gauss-Legendre formula

$x_i$	$w_i$
0	0.2325515532308739101945895
$\pm 0.2304583159551347940655281$	0.2262831802628972384120902
$\pm 0.4484927510364468528779129$	0.2078160475368885023125232
$\pm 0.6423493394403402206439846$	0.1781459807619457382800467
$\pm 0.8015780907333099127942065$	0.1388735102197872384636018
$\pm 0.9175983992229779652065478$	0.0921214998377284479144218
$\pm 0.9841830547185881494728294$	0.0404840047653158795200216

# Appendix C

## C.1 Taylor's Theorem

**Theorem (Taylor):** Suppose that a function  $f : [\mathbf{a}, \mathbf{b}] \subset R^v \rightarrow R$  is  $(n + 1)$  times continuously partially differentiable on  $[\mathbf{a}, \mathbf{b}]$ . Assume  $\mathbf{x}_0 \in [\mathbf{a}, \mathbf{b}]$ . Then for each  $\mathbf{x} \in [\mathbf{a}, \mathbf{b}]$ , there is  $\theta \in R$  with  $0 < \theta < 1$  such that

$$f(\mathbf{x}) = \sum_{\nu=0}^n \frac{1}{\nu!} ((\mathbf{x} - \mathbf{x}_0) \cdot \nabla)^\nu f(\mathbf{x}_0) + \frac{1}{(n+1)!} ((\mathbf{x} - \mathbf{x}_0) \cdot \nabla)^{n+1} f(\mathbf{x}_0 + (\mathbf{x} - \mathbf{x}_0)\theta),$$

where the partial differential operator  $(\mathbf{h} \cdot \nabla)^k$  operates as

$$(\mathbf{h} \cdot \nabla)^k = \sum_{\substack{0 \leq i_1, \dots, i_v \leq k \\ i_1 + \dots + i_v = k}} \frac{k!}{i_1! \dots i_v!} h_1^{i_1} \dots h_v^{i_v} \frac{\partial^k}{\partial x_1^{i_1} \dots \partial x_v^{i_v}}.$$

Depending on the situation at hand, the remainder term also can be cast into a variety of well-known other forms. Taylor's theorem allows a quantitative estimate of the error that is to be expected when approximating a function by its Taylor polynomial. Furthermore, it even offers a way to obtain bounds for the error in practice, based on bounding the  $(n + 1)$ st derivative, a method that has sometimes been employed in interval calculations.

For notational convenience, we introduce a parameter  $\alpha$  to describe the details of a given Taylor expansion, namely, the order of the Taylor polynomial  $n$ , and the reference point of expansion  $\mathbf{x}_0$ . For the purpose to derive bounds for the remainder, it is also necessary to include the domain interval  $[\mathbf{a}, \mathbf{b}]$  on which the function is to be considered; altogether

$$\alpha = (n, \mathbf{x}_0, [\mathbf{a}, \mathbf{b}]). \tag{C.1}$$

Consider now a  $(n + 1)$  times continuously partially differentiable function  $f : [\mathbf{a}, \mathbf{b}] \subset R^v \rightarrow R$  and write it as a sum of its Taylor polynomial  $P_{\alpha,f}$  of  $n$ -th order and a remainder  $\varepsilon_{\alpha,f}$  as

$$f(\mathbf{x}) = P_{\alpha,f}(\mathbf{x} - \mathbf{x}_0) + \varepsilon_{\alpha,f}(\mathbf{x} - \mathbf{x}_0),$$

where  $\varepsilon_{\alpha,f}(\mathbf{x} - \mathbf{x}_0)$  is continuous (even continuously differentiable) on the domain interval and thus bounded. Let the interval  $I_{\alpha,f}$  be such that

$$\forall \mathbf{x} \in [\mathbf{a}, \mathbf{b}], \quad \varepsilon_{\alpha,f}(\mathbf{x} - \mathbf{x}_0) \in I_{\alpha,f}.$$

Then

$$\forall \mathbf{x} \in [\mathbf{a}, \mathbf{b}], \quad f(\mathbf{x}) \in P_{\alpha, f}(\mathbf{x} - \mathbf{x}_0) + I_{\alpha, f}. \quad (\text{C.2})$$

Because of the special form of the Taylor remainder term  $\varepsilon_{\alpha, f}$ , in practice the remainder usually decreases as  $|\mathbf{x} - \mathbf{x}_0|^{n+1}$ . Hence, if  $|\mathbf{x} - \mathbf{x}_0|$  is chosen to be small, the interval  $I_{\alpha, f}$ , which, from now on, will be referred to as the interval remainder bound, can become so small that even the effect of considerable blow-up is not detrimental. The set  $P_{\alpha, f}(\mathbf{x} - \mathbf{x}_0) + I_{\alpha, f}$  containing  $f$  consists of the Taylor polynomial  $P_{\alpha, f}(\mathbf{x} - \mathbf{x}_0)$  and the interval remainder bound  $I_{\alpha, f}$ , and it rigorously bounds the range of the function  $f$  over the interval  $[\mathbf{a}, \mathbf{b}]$ . The pair  $(P_{\alpha, f}, I_{\alpha, f})$  of a Taylor polynomial  $P_{\alpha, f}(\mathbf{x} - \mathbf{x}_0)$  and an interval remainder bound  $I_{\alpha, f}$  is said to be a Taylor model of  $f$  if and only if (C.2) is satisfied. In this case, the Taylor model is denoted by

$$T_{\alpha, f} = (P_{\alpha, f}, I_{\alpha, f}).$$

# Nomenclature

$\Delta t$	Time elapsed from $t_0$	[s]
$\Delta v_n$	Normal velocity variation	[m/s]
$\Delta v_t$	Tangential velocity variation	[m/s]
$\ddot{\mathbf{r}}, \mathbf{a}$	Acceleration	[m/s <sup>2</sup> ]
$\dot{\mathbf{r}}, \mathbf{v}$	Velocity vector	[m/s]
$\mathbf{F}$	Force	[N]
$\mathbf{a}_p$	Perturbative acceleration	[m/s <sup>2</sup> ]
$\mathbf{r}$	Position vector	[m]
$\rho$	Atmospheric density	[kg/m <sup>3</sup> ]
$\theta$	Hour-angle	[s]
$d$	Distance between two points	[m]
$d^2$	Square distance between two points	[m <sup>2</sup> ]
$h$	Altitude above reference height	[m]
$t_0$	Reference time/epoch of Keplerian elements	[s]

## Astronomical symbols

$\varphi$	Vernal point
$\oplus$	Earth
$\ominus$	Moon
$\odot$	Sun

## Constants

$\lambda_{n,m}$	Tesseral harmonic coefficient	[rad]
-----------------	-------------------------------	-------

$\mu_{\oplus}$	Earth gravitational constant	$[\text{m}^3/\text{s}^2]$
$\mu_{\zeta}$	Moon gravitational constant	$[\text{m}^3/\text{s}^2]$
$\mu_{\odot}$	Sun gravitational constant	$[\text{m}^3/\text{s}^2]$
$\omega_a$	Earth atmosphere angular velocity	$[\text{rad}/\text{s}]$
$\phi_{\text{sr}}$	Mean solar flux	$[\text{N}/\text{m}^2]$
$\rho_0$	Atmospheric density at reference altitude	$[\text{kg}/\text{m}^3]$
$c_0$	Speed of light	$[\text{m}/\text{s}]$
$G$	Universal gravitational constant	$[\text{m}^3/\text{kg}/\text{s}^2]$
$H$	Density scale height	$[\text{m}]$
$h_0$	Reference altitude	$[\text{m}]$
$J_n$	Zonal harmonic coefficient	-
$J_{n,m}$	Tesseral harmonic coefficient	-
$M_{\oplus}$	Earth mass	$[\text{kg}]$
$p_{\text{sr}}$	Solar radiation pressure	$[\text{N}/\text{m}^2]$
$R_{\oplus}$	Earth radius	$[\text{m}]$

### Delaunay variables

$G$	Modulus of angular momentum vector	$[\text{m}^2/\text{s}]$
$g$	Argument of pericentre	$[\text{rad}]$
$H$	Projection of angular momentum vector on symmetry axis	$[\text{m}^2/\text{s}]$
$h$	Right ascension of the ascending node	$[\text{rad}]$
$L$	Conjugate momentum to mean anomaly	$[\text{m}^2/\text{s}]$
$l$	Mean anomaly	$[\text{rad}]$

### Reference frames

- (**I,J,K**) Earth Centered Inertial reference frame (ECI)  
 (**P,Q,W**) Perifocal reference frame

### Hill variables

---

$\dot{r}$	Radial velocity	[m/s]
$G$	Modulus of angular momentum vector	[m <sup>2</sup> /s]
$H$	Projection of angular momentum vector on symmetry axis	[m <sup>2</sup> /s]
$h$	Right ascension of the ascending node	[rad]
$r$	Orbit radius	[m]
$u$	True longitude	[rad]

**Notation**

$[a, b]$	Interval bounded by $a$ and $b$
$[x]$	DA variable
$\dot{x}$	Time derivation
$\mathcal{I}$	DA identity map
$\mathcal{M}$	DA map
$\nabla$	Gradient operator
$\hat{\mathbf{x}}$	Unity vector in $\mathbf{x}$ direction
$f'(x)$	Derivation with respect to $x$
$E \pm x$	Scientific notation ( $\times 10^{\pm x}$ )
$\exp(x)$	Exponentiation $e^x$

**Orbital elements**

$\mathcal{E}$	Specific orbital energy	[m <sup>2</sup> /s <sup>2</sup> ]
$\nu$	True anomaly	[rad]
$\Omega$	Right Ascension of the Ascending Node (RAAN)	[rad]
$\omega$	Argument of pericentre	[rad]
$a$	Semi-major axis	[m]
$E$	Eccentric anomaly	[rad]
$e$	Eccentricity	-
$I$	Inclination	[rad]
$M$	Mean anomaly	[rad]

---

$n$	Mean motion	[rad/s]
$u$	True longitude	[rad]

### Satellite/debris parameters

$\rho_a$	Adsorbed radiation coefficient	-
$\rho_d$	Diffused radiation coefficient	-
$\rho_s$	Specular reflected radiation coefficient	-
$A$	Effective area	[m <sup>2</sup> ]
$B$	Ballistic coefficient	[m <sup>2</sup> /kg]
$C_D$	Drag coefficient	-
$C_R$	Reflectivity coefficient	-
$m$	Mass	[kg]

### Coordinate systems variables

$\lambda$	Geocentric longitude	[rad]
$\varphi$	Geocentric latitude	[rad]
$\bar{\lambda}$	ECI longitude	[rad]
$\bar{\varphi}$	ECI latitude	[rad]

### Superscripts

'	Mean variable
---	---------------

### Subscripts

0	Value at initial time $t_0$
G	Greenwich
sec	Secular
UT	Universal time

# Acronyms

<b>DA</b>	Differential Algebra
<b>DMSP</b>	Defense Meteorological Satellite Program
<b>ECI</b>	Earth Centered Inertial reference frame
<b>ESA</b>	European Space Agency
<b>FP</b>	Floating Point
<b>GEO</b>	Geostationary Earth Orbit
<b>GO</b>	Global Optimization
<b>GPS</b>	Global Positioning System
<b>GST</b>	Greenwich Sidereal Time
<b>GTO</b>	Geostationary Transfer Orbit
<b>HANDE</b>	Hoots ANalytic Dynamic Ephemeris
<b>IA</b>	Interval Arithmetic
<b>IADC</b>	Inter-Agency Space Debris Coordination Committee
<b>JD</b>	Julian Date
<b>LDB</b>	Linear Dominated Bounder
<b>LEO</b>	Low Earth Orbit
<b>MEO</b>	Mean Earth Orbit
<b>MOID</b>	Minimal Orbital Intersection Distance
<b>NASA</b>	National Aeronautic and Space Administration
<b>QFB</b>	Quadratic Fast Bounder
<b>RAAN</b>	Right Ascension of the Ascending Node
<b>TLE</b>	Two-Lines Elements

**TM** Taylor Models

**TPSA** Truncated Power Series Algebra

**UT** Universal Time

# Bibliography

- [1] Donald J. Kessler and Burton G. Cour-Palais. Collision Frequency of Artificial Satellites: The Creation of a Debris Belt. *Journal of Geophysical Research*, 83(A6):2637–2646, June 1978.
- [2] U.S. Government Orbital Debris Mitigation Standard Practice, 1997. Website, [http://orbitaldebris.jsc.nasa.gov/library/USG\\_OD\\_Standard\\_Practices.pdf](http://orbitaldebris.jsc.nasa.gov/library/USG_OD_Standard_Practices.pdf) Last visited: 17/02/2011.
- [3] Space Debris Mitigation Guidelines, January 2008. United Nations, Comitee on the Peaceful Uses of Outer Space.
- [4] Nicholas L. Johnson, Eugene Stansbery, David O. Whitlock, Kira J. Abercromby, and Debra Shoots. *History of On-Orbit Satellite Fragmentations*. Number NASA/TM-2008-214779. June 2008.
- [5] Orbital debris quarterly news. Website, January 2011. A publication of the NASA Orbital Debris Program Office.
- [6] Orbital debris quarterly news. Website, October 2010. A publication of the NASA Orbital Debris Program Office.
- [7] UCS Satellite Database, Janaury 2011. Website <http://www.ucsusa.org/satellites> Last visited: 06/02/2011.
- [8] Orbital debris quarterly news. Website, July 2009. A publication of the NASA Orbital Debris Program Office.
- [9] H. Klinkrad. The Current Space Debris Environment and its Sources. In *Space Debris*, Springer Praxis Books, pages 5–58. Springer Berlin Heidelberg, 2006.
- [10] Orbital debris quarterly news. Website, April 2007. A publication of the NASA Orbital Debris Program Office.
- [11] Space track. Website. <http://www.space-track.org> Last visited: 30/01/2011.
- [12] K. V. Kholshchevnikov and N. N. Vassiliev. On the distance function between two Keplerian elliptic orbits. *Celestial Mechanics and Dynamical Astronomy*, 75:75–83, 1999.
- [13] Dan Xue and Juenfeng Li. Collision Criterion for two satellites on Keplerian orbits. *Celestial Mechanics and Dynamical Astronomy*, 108:233–244, September 2010.

- 
- [14] R. Armellin, P. Di Lizia, M. Berz, and K. Makino. Computing the critical points of the distance function between two Keplerian orbits via rigorous global optimization. *Celestial Mechanics and Dynamical Astronomy*, 107:377–395, 2010.
- [15] Oliver Montenbruck and Eberhard Gill. *Satellite Orbits: Models, Methods, and Applications*. Springer, 2001.
- [16] W. M. Kaula. *Theory of satellite geodesy. Applications of satellites to geodesy*. Blaisdell Publishing Company, 1966.
- [17] G. E. Cook. Perturbations of satellite orbits by tesseral harmonics in the Earth’s gravitational potential. *Planetary Space Science*, 11:797–815, 1963.
- [18] Vladimir A. Chobotov. *Orbital Mechanics*. AIAA Education series. AIAA, 3rd edition, 2002.
- [19] H. Klinkrad, P. Wegener, C. Wiedemann, J. Bendisch, and H. Krag. Modeling of the Current Space Debris Environment. In *Space Debris*, Springer Praxis Books, pages 59–114. Springer Berlin Heidelberg, 2006.
- [20] Brouwer D. Solution of the problem of artificial satellite theory without drag. *Astronomical Journal*, 64:378–396, November 1959.
- [21] Ali Hasan Nayfeh. *Perturbations Methods*. Wiley-VCH Verlag GmbH, 2007.
- [22] Kozai Y. The motion of a close Earth satellite. *Astronomical Journal*, 64:367–377, November 1959.
- [23] R. H. Lyddane. Small Eccentricities or Inclinations in the Brouwer Theory of the Artificial Satellite. *The Astronomical Journal*, 68(8):555–558, October 1963.
- [24] Kaare Aksnes. A Second-Order Artificial Satellite Theory Based on an Intermediate Orbit. *The Astronomical Journal*, 75(9), November 1970.
- [25] Kaare Aksnes. A Second-Order Artificial Satellite Theory Based on an Intermediate Orbit. Technical Report 32-1507, NASA National Aeronautics and Space Administration, Jet Propulsion Laboratory, Pasadena, California, November 1970.
- [26] Kaare Aksnes. On the use of Hill variables in Artificial Satellite Theory: Brouwer’s Theory. *Astronomy & Astrophysics*, 17:70–75, 1972.
- [27] Kinoshita H. Third-order solution of an Artificial Satellite Theory. *SAO Special Report*, 379, July 1977.
- [28] Victor A. Brumberg. *Analytical Techniques of Celestial Mechanics*. Springer-Verlag, March 1995.
- [29] Sergey M. Kudryavtsev. The fifth-order analytical solution of the equations of motion of a satellite in orbit around a non-spherical planet. *Celestial Mechanics and Dynamical Astronomy*, 61:207–215, 1995.
- [30] Dirk Brouwer and Gen-ichiro Hori. Theoretical Evaluation of Atmospheric Drag Effects in the Motion of an Artificial Satellite. *The Astronomical Journal*, 66(5):193–225, June 1961.

- 
- [31] M. H. Lane and K.H. Cranford. An Improved Analytical Drag Theory for the Artificial Satellite Problem. In *AIAA/AAS Astrodynamics Conference*, August 1969.
- [32] Felix R. Hoots. An analytical satellite theory using gravity and a dynamic atmosphere. In D. L. Gray, R. J. Cesarone, and R. E. van Allen, editors, *AIAA/AAS Astrodynamics Conference*, August 1982.
- [33] Felix R. Hoots and Richard G. France. An analytical satellite theory using gravity and a dynamic atmosphere. *Celestial Mechanics*, 40:1–18, 1987.
- [34] J. J. F. Liu. Advances in Orbit Theory for an Artificial Satellite with Drag. In *AIAA/AAS Astrodynamics Conference*. AIAA/AAS, August 1982.
- [35] G. Xu, X. Tianhe, W. Chen, and T. K. Yeh. Analytical solution of a satellite orbit disturbed by atmospheric drag. *Monthly Notices of the Royal Astronomical Society*, 410:654–662, January 2011.
- [36] R. R. Allan. On the Motion of Nearly Synchronous Satellites. *Royal Society of London Proceedings Series A*, 288:60–68, October 1965.
- [37] Segerman A. M. and Coffey S. L. An analytical theory for tesseral gravitational harmonics. *Celestial Mechanics and Dynamical Astronomy*, 76:139–156, April 2000.
- [38] No T. S. and Jung O. C. Analytical Solution to Perturbed Geosynchronous Orbit. *Acta Astronautica*, 56:641–651, April 2005.
- [39] El-Saftawy M. I., Ahmed M. K. M., and Helali Y. E. The effect of direct solar radiation pressure on a spacecraft of complex shape. *Astrophysics and Space Science*, 259:151–171, July 1998.
- [40] Harwood N. M. and Swinerd G. G. Long-periodic and secular perturbations to the orbit of a spherical satellite due to direct solar radiation pressure. *Celestial Mechanics and Dynamical Astronomy*, 62:71–80, May 1995.
- [41] Kaare Aksnes. Short-period and long-period perturbations of a spherical satellite due to direct solar radiation. *Celestial Mechanics*, 13:89–104, February 1976.
- [42] R. S. Hujsak. A Restricted Four Body Solution for Resonating Satellites With An Oblate Earth. In K. Ijichi, H. Harada, and & K. Kuriki, editors, *America Institute of Aeronautics and Astronautics Conference*, June 1979.
- [43] Xu G., Xu T., T. K. Yeh, and W. Chen. Analytical solution of a satellite orbit by lunar and solar gravitation. *Monthly Notices of the Royal Astronomical Society*, 410:645–653, January 2011.
- [44] E. Wnuk. Prediction of artificial satellite position on the basis of the second order theory of motion. *Advances in Space Research*, 30:321–330, July 2002.
- [45] Y. A. Abdel-Aziz and F.A. Abd El-Salam. An efficient algorithm for orbital evolution of artificial satellite. *Applied Mathematics and Computation*, 191:415–428, 2007.

- 
- [46] F. R. Hoots and R. L. Roehrich. Models for Propagation of the NORAD Elements Sets, Project SPACETRACK, Rept. 3. Technical report, U.S. Air Force Aerospace Defense Command.
- [47] Felix R. Hoots. Reformulation of the Brower Geopotential Theory for Improved Computational Efficiency. *Celestial Mechanics*, 24:367–375, August 1981.
- [48] Felix R. Hoots, Paul W. Schumacher Jr., and Robert A. Glover. History of Analytical Orbit Modeling in the U.S. Space Surveillance System. *Journal of Guidance, Control and Dynamics*, 27(2):174–185, March–April 2004.
- [49] David A. Vallado, Paul Crawford, Richard Hujsak, and T. S. Kelso. Revisiting SPACETRACK Report # 3: Rev. 1. In *AIAA/AAS Astrodynamics Specialist Conference and Exhibit*, August 2006.
- [50] NASA Goddard Space Flight Center. General mission analysis tool. Website <http://gmat.gsfc.nasa.gov/index.html> Last visited: 06/02/2011.
- [51] Charles E. Jr. Roberts. An analytical model for the upper atmosphere density based upon Jacchia’s 1970 models. *Celestial Mechanics*, 4(314):368–377, 1971.
- [52] T. S. Kelso. CeleTrack. Website. <http://celestrack.com/> Last visited: 06/02/2011.
- [53] M. Berz. *Modern Map Methods in Particle Beam Physics*. Academic Press, 1999.
- [54] M. Berz. The new method of tpsa algebra for the description of beam physics to high order. Technical Report AT-6:ATN-86-16, Los Alamos National Laboratory, 1986.
- [55] M. Berz. The method of power series tracking for the mathematical description of beam dynamics. *Nuclear Instruments Methods*, A258(431), 1987.
- [56] M. Berz. High-order computation and normal form analysis of repetitive systems. *Physics of Particle Accelerators*, AIP249, 1991.
- [57] M. Berz. *Handbook of Accelerator Physics and Engineering*, chapter Differential algebraic techniques. World Scientific, 1999.
- [58] K. Makino. *Rigorous Analysis of Nonlinear Motion in Particle Accelerators*. PhD thesis, Michigan State University, East Lansing, Michigan, USA, 1998.
- [59] Ramon E. Moore, R. Baker Kearfott, and Michael J. Cloud. *Introduction to Interval Analysis*. Society for Industrial and Applied Mathematics, Philadelphia, PA, USA, 2009.
- [60] M. Berz and K. Makino. Remainder Differential Algebras and their Applications. In M. Berz, C. Bischof, G. Corliss, and A. Griewank, editors, *Computational Differentiation: Techniques, Applications, and Tools*, pages 63–74, Philadelphia, 1996. SIAM.
- [61] Griewank A. and Corliss G. F. *Automatic Differentiation of Algorithms: Theory, Implementation and Application*, chapter Overloading Point and Interval Taylor Operators. SIAM, Philadelphia, 1991.
- [62] K. Makino and M. Berz. Efficient Control of the Dependency Problem Based on Taylor Model Methods. *Reliable Computing*, 5:3–12, 1999.

- 
- [63] Berz M. and Makino K. COSY INFINITY Version 9 reference manual. Technical Report MSUHEP-060803, Michigan State University, East Lansing, MI 48824, 2006.
- [64] Kearfott R. B. *Rigorous Global Saerh: Continuous Problems*. Kluwer Academic Publishers, Dordrecht, Netherlands, 1996.
- [65] K. Makino and M. Berz. Taylor models and other validated functional inclusion methods. *International Journal of Pure Applied Mathematics*, 6:239–216, 2003.
- [66] M. Berz, K. Makino, and Y. Kim. Long term stability of the tevatron by verified global optimization. *Nuclear Instruments and Methods*, A558:1–10, 2005.
- [67] K. Makino and M. Berz. verified Global Optimization with Taylor Model-based Range Bounders. *Transaction on Computers*, 11:1611–1618, 2005.
- [68] F. R. Hoots, L. L. Crawford, and L. Roehrich. An analytical method to determine the future close approaches between satellites. *Celestial Mechanics and Dynamical Astronomy*, 33:143–158, 1984.
- [69] P. A. Dybczynski, T. J. Jopek, and R. A. Seran. On the minimum distance between two keplerian orbits with a common focus. *Celestial Mechanics and Dynamical Astronomy*, 38:345–356, 1986.
- [70] R. Armellin, P. Di Lizia, F. Bernelli Zazzera, and M. Berz. Nonlinear Mapping of a Gaussian Statistics: a Differential Algebra Approach. *Celestial Mechanics and Dynamical Astronomy*, 2009.
- [71] Orbital debris quarterly news. Website, July 2010. A publication of the NASA Orbital Debris Program Office.
- [72] *Explanatory Supplement to the Astronomical Ephemeris and the American Ephemeris and Nautical Almanac*. Her Majesty’s Stationery Office, London, 1961.
- [73] Bruinsma S. L., Marty J. C., Balmino G., Biancale R., Foerste C., Abriksov O., and Neumayer H. Goce Gravity Field Recovery by Means of the Direct Numerical Method. In *ESA Living Planet Symposium*. ESA, June 2010.
- [74] EIGEN-51C. Website. <http://icgem.gfz-postdam.de/ICGEM/shms/eigen-51c.gfc> Last visited: 30/01/2011.
- [75] *U.S. Standard Atmosphere*. U.S. Government Printing Office, Washington D.C., 1976.
- [76] Bengt Fornberg. Generation of Finite Difference Formulas on Arbitrarily Spaced Grids. *Mathematics of Computation*, 51(184):699–706, October 1988.
- [77] Arnold N. Lowan, Norman Davis, and Arthur Levenson. Table of the zeros of the Legendre polynomials of order 1-16 and the weight coefficients for Gauss’ mechanical quadrature formula. *Bulletin of the American Mathematical Society*, 48(10):739–743, 1942.